

University of Louisville

## ThinkIR: The University of Louisville's Institutional Repository

---

Electronic Theses and Dissertations


---

1-2022

### Development of porous solid acid catalysts for lignocellulose and plastic upcycling.

Mohammad Shahinur Rahaman  
*University of Louisville*

Follow this and additional works at: <https://ir.library.louisville.edu/etd>

 Part of the [Catalysis and Reaction Engineering Commons](#), and the [Materials Science and Engineering Commons](#)

---

#### Recommended Citation

Rahaman, Mohammad Shahinur, "Development of porous solid acid catalysts for lignocellulose and plastic upcycling." (2022). *Electronic Theses and Dissertations*. Paper 3857.  
<https://doi.org/10.18297/etd/3857>

This Doctoral Dissertation is brought to you for free and open access by ThinkIR: The University of Louisville's Institutional Repository. It has been accepted for inclusion in Electronic Theses and Dissertations by an authorized administrator of ThinkIR: The University of Louisville's Institutional Repository. This title appears here courtesy of the author, who has retained all other copyrights. For more information, please contact [thinkir@louisville.edu](mailto:thinkir@louisville.edu).

DEVELOPMENT OF POROUS SOLID ACID CATALYSTS FOR LIGNOCELLULOSE AND  
PLASTIC UPCYCLING

By

Mohammad Shahinur Rahaman

B.S. (Engineering) Shahjalal University of Science and Technology, 2012

M.S. (Engineering) The University of Louisville, 2020

A Dissertation

Submitted to the Faculty of the

J.B. Speed School of Engineering of the University of Louisville

in Partial Fulfillment of the Requirements

for the Degree of

Doctor of Philosophy

in Chemical Engineering

Department of Chemical Engineering

University of Louisville

Louisville, Kentucky

May 2022

Copyright 2022 by Mohammad Shahinur Rahaman

All rights reserved



DEVELOPMENT OF POROUS SOLID ACID CATALYSTS FOR LIGNOCELLULOSE AND  
PLASTIC UPCYCLING

By

Mohammad Shahinur Rahaman

B.S. (Engineering) Shahjalal University of Science and Technology, 2012

M.S. (Engineering) The University of Louisville, 2020

A Dissertation Approved on

March 25, 2022

by the following Dissertation Committee:

---

Noppadon Sathitsukanoh (Dissertation Director)

---

Gerold A. Willing

---

Vance W. Jaeger

---

Lee M. Thompson

## DEDICATION

This dissertation is dedicated to my parents

Morzina Begum and Arshed Ali

who have given me invaluable educational opportunities.

## ACKNOWLEDGEMENTS

I would like to express my sincere gratitude to my advisor Prof. Noppadon Sathitsuksanoh for his guidance, support, help, and encouragement during my PhD. I also thank my advisor for providing me the opportunity to work on multiple different projects to acquire a diverse set of research skills and experience.

I would like to thank Prof. Gerold A. Willing, Prof. Vance Jaeger, and Prof. Lee Thompson for serving as members of my dissertation committee and generously offering their time, advice, and constructive feedback about this research.

I am incredibly grateful to all my colleagues and lab members in the Advance Renewable Materials (ARM) Lab, UofL for their helpfulness, advice, discussion, co-work, and friendship throughout my graduate studies, including Anwar Hossain, Dr. Thanh Khoa Phung, Dr. Sarttrawut Tulaphol, Kyle N. Mills and Ashten Molley.

I would like to thank all the CONN Center staff for their guidance and patience. Special thanks to Dr. Jacek Jasinski for his help and support for all the materials characterization facilities. I would also like to thank and acknowledge the support from all my collaborators for lending their expertise, including Prof. Shashi Lalvani (Miami University), Dr. Thana Maihom (Kasetsart University), Prof. Mark Crocker (University of Kentucky), Prof. Jie Dong (Southern Illinois University), Dr. Daniel Yelle (USDA), Dr. Ning Sun (LBNL), Prof. Scott Renneckar (University of British Columbia), Dr. Emtias Chowdhury (Intel).

I gratefully acknowledge the funding sources that made my Ph.D. work possible. First, I would like to thank the Department of Chemical Engineering, UofL, for providing me the financial support for the last 5 years. Second, I would like to thank the National Science Foundation and Office of the Executive Vice President for Research, UofL, for providing the research grant for my PhD projects. Finally, I would like to thank the UofL Graduate School for awarding me the Doctoral Dissertation Completion Award for the Spring 2022 semester.

I would like to express my deepest gratitude to Sandy and Rick, my American guardian, for their help and support from the very beginning of my UofL chapter. My time at UofL was made enjoyable in large part due to the many friends that became a part of my life. I am grateful for the time spent, and memories made with many friends, especially my travel buddies: Rocky, Anwar, Sujoy, Pradipta, Rajesh, Riyadh, Shormi, Rajib, Mouri, Sadi, Touhid, and Dip.

Lastly, I would like to thank my family members for their love, support, and encouragement, without which this dissertation and research would not have been possible.



## ABSTRACT

### DEVELOPMENT OF POROUS SOLID ACID CATALYSTS FOR LIGNOCELLULOSE AND PLASTIC UPCYCLING

Mohammad Shahinur Rahaman

March 25, 2022

My goal is to develop chemical processes for transforming waste to solve environmental problems and enhance sustainability. Environmental problems such as pollution and massive amounts of waste are the main drivers that stimulate my research ideas. I focused on creating novel, efficient catalytic processes for converting polymeric waste "feedstocks" into high-value chemicals by integrating my expertise in catalysis, materials science, and synthetic chemistry to develop porous solid catalytic materials. During my Ph.D., I focused on two polymeric feedstocks, lignocellulose, and discarded plastic.

Early in my Ph.D. journey, I focused on catalytic upcycling of lignocellulose. Lignocellulosic biomass is cost-effective, abundant, and renewable. Upcycling lignocellulose into renewable fuels and chemicals has the potential to reduce reliance on fossil fuels, mitigate global warming, and promote a sustainable bioeconomy. The major challenge in upcycling lignocellulose is the active, selective, and reusable catalysts. I developed porous solid acid catalysts by solvothermal techniques and tuned their catalytic performance through surface modifications to upcycle these lignocellulose samples.

Later part of my Ph.D. tenure, I continued to use my understanding of lignocellulose polymer and catalysis to upcycle synthetic polymers (discarded plastic). Global plastic production creates more than 400 million metric tons of plastic per year. Polyolefins account for >60% of global plastic consumption. Unfortunately, most plastics are discarded in landfills, and they pollute waterways and food chains, negatively affecting human health and the environment. In addition, most plastics are inert and designed to last a lifetime. As a result, discarded plastic ends up in landfills, pollutes waterways, and negatively affects the environment and health. The ability to upcycle plastic will mitigate plastic pollution and support a circular economy, thereby providing a financial incentive for industries to upcycle plastics instead of sending them to landfills.

I divided this dissertation into nine chapters to provide a guide in designing catalytic systems for upcycling lignocellulose and discarded plastic. Chapter One gives the background on lignocellulose and plastic and catalysis. I briefly discussed the aim and scope of this dissertation. Chapter Two explores the surface modification techniques of zeolites by organic surfactants and applies them for efficient glycerol conversion to solketal. Chapters Three, Four, Five, and Six discuss how tuning properties and structural modification of MOFs enhanced the acidity and catalytic performance. Chapter Seven combines experimental results and computational study to elucidate how Hf- and Zr-containing MOFs activate biomass-derived carbonyl compounds during transfer hydrogenation reaction.

Chapters Eight and Nine detail upcycling approaches for plastic Brønsted acid sites. Chapter Eight shows the development of the novel solid Brønsted acidic catalysts by sulfonating polypropylene for esterification of lignocellulose-derived levulinic acid. This work allowed me to translate my knowledge in lignocellulose conversion to plastic upcycling. Chapter Nine explores the use of plastic-derived Brønsted acidic catalysts for the conversion of different biomass-derived compounds and elucidates the reaction pathways for efficient conversion. Overall, the development of porous solid acid catalysts for lignocellulose and plastic upcycling will provide promising solutions to transition our society toward a circular economy.

## TABLE OF CONTENTS

|   | PAGE |
|---|------|
| ACKNOWLEDGMENTS.....  | iv   |
| ABSTRACT.....   | vi   |
| LIST OF TABLES .....  | xii  |
| LIST OF FIGURES .....   | xiv  |
| CHAPTER 1: INTRODUCTION.....  | 1    |
| 1. Introduction.....  | 1    |
| 2. Background.....  | 1    |
| 3. Aim and scope of this study.....   | 3    |
| CHAPTER 2: HYDROPHOBIC FUNCTIONALIZATION OF HY ZEOLITES FOR EFFICIENT<br>CONVERSION OF GLYCEROL TO SOLKETAL.....  | 6    |
| 1. Introduction.....  | 6    |
| 2. Materials and Methods .....  | 8    |
| 3. Results and Discussion.....  | 12   |
| 4. Conclusion.....  | 24   |
| 5. Supplementary Information.....   | 25   |
| CHAPTER 3: COOPERATIVE BRØNSTED-LEWIS ACID SITES CREATED BY<br>PHOSPHOTUNGSTIC ACID ENCAPSULATED METAL-ORGANIC FRAMEWORKS FOR<br>SELECTIVE GLUCOSE CONVERSION TO 5-<br>HYDROXYMETHYLFURFURAL..... | 31   |
| 1. Introduction.....  | 31   |
| 2. Materials and Methods .....  | 34   |
| 3. Results .....  | 39   |
| 4. Discussion.....  | 53   |
| 5. Conclusion.....  | 56   |
| 6. Supplementary Information.....   | 57   |

|  |     |
|--|-----|
| CHAPTER 4: ALUMINUM-CONTAINING METAL-ORGANIC FRAMEWORKS AS SELECTIVE AND REUSABLE CATALYSTS FOR GLUCOSE ISOMERIZATION TO FRUCTOSE.....                     | 68  |
| 1. Introduction.....   | 68  |
| 2. Materials and Methods .....   | 70  |
| 3. Results .....   | 72  |
| 4. Discussion.....   | 82  |
| 5. Conclusion.....   | 84  |
| 6. Supplementary Information.....  | 86  |
| CHAPTER 5: ALUMINUM BASED METAL-ORGANIC FRAMEWORK AS WATER-TOLERANT LEWIS ACID CATALYST FOR SELECTIVE DIHYDROXYACETONE ISOMERIZATION TO LACTIC ACID.....   | 94  |
| 1. Introduction.....   | 94  |
| 2. Experimental Section .....  | 96  |
| 3. Results .....   | 100 |
| 4. Discussion.....   | 111 |
| 5. Conclusion.....   | 115 |
| 6. Supplementary Information.....  | 116 |
| CHAPTER 6: COOPERATIVE EFFECT OF LEWIS AND BRØNSTED ACIDITY IN UIO-66(ZR) METAL-ORGANIC FRAMEWORKS FOR ESTERIFICATION OF LEVULINIC ACID WITH METHANOL..... | 128 |
| 1. Introduction.....   | 128 |
| 2. Materials and Methods .....   | 129 |
| 3. Results .....   | 134 |

|   |     |
|---|-----|
| 4. Discussion.....  | 143 |
| 5. Conclusion.....  | 144 |
| 6. Supplementary Information.....   | 145 |
| CHAPTER 7: MECHANISM OF TRANSFER HYDROGENATION OF CARBONYL COMPOUNDS<br>BY ZIRCONIUM AND HAFNIUM-CONTAINING METAL-ORGANIC FRAMEWORKS.....     |     |
| 1. Introduction.....  | 150 |
| 2. Materials and Methods .....  | 152 |
| 3. Results .....  | 156 |
| 4. Discussion.....  | 168 |
| 5. Conclusion.....  | 170 |
| 6. Supplementary Information.....   | 171 |
| CHAPTER 8: CREATION OF BRØNSTED ACID SITES ON PLASTIC FOR ESTERIFICATION<br>OF LEVULINIC ACID: A PLASTIC-TO-BIOREFINERY CIRCULAR ECONOMY..... |     |
| 1. Introduction.....  | 188 |
| 2. Materials and Methods .....  | 189 |
| 3. Results .....  | 192 |
| 4. Discussion.....  | 201 |
| 5. Conclusion.....  | 204 |
| 6. Supplementary Information.....   | 205 |
| CHAPTER 9: UPCYCLING POLYPROPYLENE TO SULFONIC ACID CATALYSTS FOR<br>CONVERSION OF BIOMASS-DERIVED COMPOUNDS TO SUSTAINABLE CHEMICALS...206   |     |
| 1. Introduction.....  | 206 |
| 2. Materials and Methods .....  | 207 |

|                                   |     |
|-----------------------------------|-----|
| 3. Results .....                  | 210 |
| 4. Discussion.....                | 220 |
| 5. Conclusion.....                | 222 |
| 6. Supplementary Information..... | 223 |
| CONCLUSION AND FUTURE WORK.....   | 224 |
| REFERENCES.....                   | 227 |
| APPENDIX.....                     | 290 |
| CURRICULUM VITAE .....            | 294 |

## LIST OF TABLES

| TABLE  | PAGE |
|--|------|
| <b>Table 2.1.</b> Surface properties and acidity of HY and OTS-HY catalysts.....   | 15   |
| <b>Table 2.2.</b> The glycerol conversion and products selectivity of investigated catalysts as a function of temperature and time.....                  | 19   |
| <b>Table 3.1.</b> Physicochemical properties of MOFs with varying PTA content.....   | 41   |
| <b>Table 3.S1.</b> List of chemicals/reagents used in this study.....  | 63   |
| <b>Table 3.S2.</b> Selected Bronsted acidic polyoxometalate-derived MOF catalysts prepared by impregnation, encapsulation, and mechanical synthesis..... | 64   |
| <b>Table 3.S3.</b> Selected MOF catalysts and solid catalysts for glucose dehydration.....   | 66   |
| <b>Table 4.1.</b> Catalyst screening for glucose isomerization.....  | 77   |
| <b>Table 4.2.</b> Catalytic activity of linker and ligands for the glucose isomerization in ethanol.....   | 79   |
| <b>Table 4.S1.</b> List of chemicals/reagents used in this study.....  | 86   |
| <b>Table 4.S2.</b> Calculated surface area, pore volume, diameter, and metal content of Al-MOFs.....   | 91   |
| <b>Table 4.S3.</b> Catalytic activity of Al-MOFs for the glucose isomerization in water.....   | 91   |
| <b>Table 4.S4:</b> Catalytic performance of selected homogeneous and heterogeneous catalysts.....  | 93   |
| <b>Table 5.S1.</b> List of chemicals/reagents used in this study.....  | 116  |
| <b>Table 5.S2.</b> Physical properties of catalysts used in this study.....  | 118  |
| <b>Table 5.S3.</b> Turnover frequency (TOF) and productivity of selected aluminum-containing catalysts toward dihydroxyacetone isomerization.....        | 118  |
| <b>Table 5.S4.</b> Catalytic performance of selected catalysts used for dihydroxyacetone isomerization to lactic acid.....                               | 126  |

|   |     |
|---|-----|
| <b>Table 6.1.</b> Molar composition of the reagents during the synthesis of UiO-66 MOFs.....  | 130 |
| <b>Table 6.2.</b> pH values of hydrated and dehydrated MOFs suspended in methanol.....  | 137 |
| <b>Table 6.S1.</b> List of chemicals/reagents used in this study.....   | 145 |
| <b>Table 6.S2.</b> Physical properties of catalysts used in this study.....   | 146 |
| <b>Table 6.S3.</b> Amount of defect and coordination number of Zr and Hf clusters in UiO-66.....  | 147 |
| <b>Table 7.1.</b> pH values of hydrated and dehydrated MOFs suspended in methanol.....  | 158 |
| <b>Table 7.S1.</b> List of chemicals/reagents used in this study.....   | 171 |
| <b>Table 7.S2.</b> Calculated surface area, pore-volume, and average pore diameter of Zr- & Hf-<br>containing MOFs.....                                       | 176 |
| <b>Table 7.S3.</b> Metal analysis of Zr- & Hf-containing MOFs by ICP-OES.....   | 177 |
| <b>Table 7.S4.</b> Amount of defect and coordination number of Zr and Hf clusters in UiO-66.....  | 183 |
| <b>Table 8.1.</b> Surface area, density, total pore volume, average pore size, carbon to sulfur ratio,<br>and pH in methanol of the PP-SO <sub>3</sub> H..... | 193 |
| <b>Table 8.S1.</b> List of chemicals/reagents used in this study.....   | 205 |
| <b>Table 9.1.</b> Surface area, density, total pore volume, average pore size, carbon to sulfur ratio, and<br>pH in methanol of the PP-SO <sub>3</sub> H..... | 211 |
| <b>Table 9.2.</b> Applications of PP-SO <sub>3</sub> H in the conversion of selected biomass-derived<br>molecules.....  | 218 |
| <b>Table 9.S1.</b> List of chemicals/reagents used in this study.....   | 223 |



## LIST OF FIGURES

| FIGURE  | PAGE |
|---|------|
| <b>Figure 2.1.</b> Solketal production from glycerol acetalization by acid.....   | 7    |
| <b>Figure 2.2.</b> TGA profiles, FTIR spectra, and DRIFT spectra of OTS-HY and HY catalysts.....  | 13   |
| <b>Figure 2.3.</b> HRTEM, contact angles, and suspension behaviour of HY and OTS-HY catalysts.....  | 14   |
| <b>Figure 2.4.</b> XRD patterns of OTS-HY and HY catalysts.....   | 15   |
| <b>Figure 2.5.</b> Suspension behaviour and Glycerol conversion by OTS-HY and HY catalysts. Changes in suspension behaviour of HY at 30 and 50°C..... | 20   |
| <b>Figure 2.6.</b> Phase transition of the glycerol-acetone mixture during the reaction.....  | 22   |
| <b>Figure 2.7.</b> Effect of catalyst loading on the glycerol conversion between 20 to 140 min.....   | 23   |
| <b>Figure 2.S1.</b> FTIR spectra of HY, OTS-HY, and OTS-OTS samples.....  | 27   |
| <b>Figure 2.S2.</b> N <sub>2</sub> -adsorption/desorption isotherms of HY and OTS-HY.....   | 27   |
| <b>Figure 2.S3.</b> Suspension of HY and OTS-HY in water-dodecane and glycerol-acetone.....   | 28   |
| <b>Figure 2.S4.</b> Water adsorption behaviour of HY and OTS-HY catalysts. ....   | 28   |
| <b>Figure 2.S5.</b> Behaviour of emulsion formation in water-dodecane and glycerol-acetone in the presence of OTS-HY or tween 60.....                 | 29   |
| <b>Figure 2.S6:</b> Suspension behaviour of OTS-HY and HY in the glycerol/acetone at 30 °C.....   | 29   |
| <b>Figure 2.S7.</b> Suspension behaviour of OTS-HY and HY in the glycerol/acetone at 50 °C.....   | 30   |
| <b>Figure 2.S8.</b> Suspension behavior of OTS-HY and HY in the glycerol/acetone at 70 °C.....  | 30   |

|   |    |
|---|----|
| <b>Figure 3.1.</b> STEM-HAADF images and elemental mapping of MIL-101(Al)-NH <sub>2</sub> and 14%PTA <sub>⊂</sub> MIL-101(Al)-NH <sub>2</sub> .....                                     | 42 |
| <b>Figure 3.2.</b> Acid properties of encapsulated PTA <sub>⊂</sub> Al-MOF catalysts measured by diffuse reflectance infrared Fourier transform spectroscopy (DRIFTS).....              | 43 |
| <b>Figure 3.3.</b> Catalytic performance of encapsulated PTA <sub>⊂</sub> MIL-101(Al)-NH <sub>2</sub> catalysts.....  | 46 |
| <b>Figure 3.4.</b> HMF selectivity of PTA <sub>⊂</sub> MIL-101(Al)-NH <sub>2</sub> at similar glucose conversion.....   | 47 |
| <b>Figure 3.5.</b> Solvent effect on glucose conversion and HMF selectivity by using 14%PTA <sub>⊂</sub> MIL-101(Al)-NH <sub>2</sub> catalyst.....                                      | 48 |
| <b>Figure 3.6.</b> Solvent effect on fructose conversion to HMF without added catalyst and catalytic performance of encapsulated 14%PTA <sub>⊂</sub> MIL-101(Al)-NH <sub>2</sub> .....  | 49 |
| <b>Figure 3.7.</b> HMF conversion in different solvents with/without 14%PTA <sub>⊂</sub> MIL-101(Al)-NH <sub>2</sub> .....  | 49 |
| <b>Figure 3.8.</b> HMF conversion by encapsulated PTA <sub>⊂</sub> MIL-101(Al)-NH <sub>2</sub> .....  | 51 |
| <b>Figure 3.9.</b> Reuse of 14%PTA <sub>⊂</sub> MIL-101(Al)-NH <sub>2</sub> for glucose dehydration.....  | 52 |
| <b>Figure 3.S1.</b> Glucose and HMF concentrations with and without 14%PTA <sub>⊂</sub> MIL-101(Al)-NH <sub>2</sub> .....   | 57 |
| <b>Figure 3.S2.</b> Gas chromatography and mass spectrometry profiles of extracted HMF.....   | 58 |
| <b>Figure 3.S3.</b> Characterization of PTA <sub>⊂</sub> MIL-101(Al)-NH <sub>2</sub> by N <sub>2</sub> adsorption-desorption and X-ray diffraction (XRD).....                           | 59 |
| <b>Figure 3.S4.</b> FTIR spectra of PTA <sub>⊂</sub> MIL-101(Al)-NH <sub>2</sub> catalysts.....   | 60 |
| <b>Figure 3.S5.</b> Thermogravimetric analysis (TGA) and Differential Thermogravimetric analysis (DTG) of bare Al-MOF and 14%PTA <sub>⊂</sub> Al-MOF catalysts.....                     | 61 |
| <b>Figure 3.S6.</b> Catalytic conversion of MIL-101(Al)-NH <sub>2</sub> treated at 80-150°C.....  | 62 |
| <b>Figure 3.S7.</b> Catalytic performance of encapsulated PTA <sub>⊂</sub> MIL-101(Al)-NH <sub>2</sub> catalysts and different PTA loading on HMF selectivity at the time on steam..... | 62 |
| <b>Figure 4.1.</b> Physicochemical properties of Al-MOFs by XRD, TGA, FTIR, HRTEM, and Al mapping.....  | 73 |
| <b>Figure 4.2.</b> DRIFTS with temperature-programmed desorption of pyridine from Al-MOFs.....  | 76 |

|   |     |
|---|-----|
| <b>Figure 4.3.</b> Glucose isomerization by selected Al-containing metal-organic framework.....   | 78  |
| <b>Figure 4.4.</b> Reusability and stability of MIL-101(Al)-NH <sub>2</sub> for the glucose isomerization.....  | 81  |
| <b>Figure 4.5.</b> Selected catalysts for glucose isomerization reaction and their reactivity.....  | 84  |
| <b>Figure 4.S1.</b> Characterization of MIL-101(Al)-NH <sub>2</sub> by N <sub>2</sub> adsorption-desorption at 77 K.....  | 90  |
| <b>Figure 4.S2.</b> Effect of solvent for glucose isomerization by MIL-101-Al-NH <sub>2</sub> .....   | 92  |
| <b>Figure 4.S3.</b> Characterization of the used Al-MOF after 4 reuse cycles by FTIR and XRD.....   | 92  |
| <b>Figure 5.1.</b> DRIFT spectra of adsorbed pyridine with $\gamma$ -Al <sub>2</sub> O <sub>3</sub> and MIL-101(Al)-NH <sub>2</sub> .....   | 102 |
| <b>Figure 5.2.</b> Catalytic activity of MIL-101(Al)-NH <sub>2</sub> and aluminum-containing homogenous and heterogeneous catalysts, conversion/yield, and TOF/productivity.....                      | 103 |
| <b>Figure 5.3.</b> Catalytic activity of blank, $\gamma$ -Al <sub>2</sub> O <sub>3</sub> , and MIL-101(Al)-NH <sub>2</sub> .....  | 104 |
| <b>Figure 5.4.</b> Comparison of catalytic activity of dihydroxyacetone (DHA) isomerization to lactic acid at 90 °C by MIL-101(Al)-NH <sub>2</sub> and $\gamma$ -Al <sub>2</sub> O <sub>3</sub> ..... | 105 |
| <b>Figure 5.5.</b> Effect of Al-MOF catalysts and reaction temperature on DHA conversion.....   | 106 |
| <b>Figure 5.6.</b> Catalytic activity of MIL-101(Al)-NH <sub>2</sub> and $\gamma$ -Al <sub>2</sub> O <sub>3</sub> using pyruvaldehyde, and lactic acid as a feed.....                                 | 107 |
| <b>Figure 5.7.</b> Stability and reusability of Al-MOFs for the dihydroxyacetone isomerization by filtration test at 90 °C and recycle of MIL-101(Al)-NH <sub>2</sub> catalyst at 120 °C.....         | 110 |
| <b>Figure 5.8.</b> Proposed chemical pathway for the DHA conversion by MIL-101(Al)-NH <sub>2</sub> .....  | 114 |
| <b>Figure 5.S1.</b> N <sub>2</sub> adsorption-desorption isotherm of MIL-101(Al)-NH <sub>2</sub> at -196.15 °C, XRD, HRTEM, Al mapping, FTIR, and TGA.....  | 117 |
| <b>Figure 5.S2.</b> Comparison of catalytic activity of dihydroxyacetone isomerization to lactic acid by MIL-101(Al)-NH <sub>2</sub> and AlCl <sub>3</sub> .6H <sub>2</sub> O.....                    | 120 |
| <b>Figure 5.S3.</b> Conversion of DHA without added catalysts at 90 °C, 105 °C, and 120 °C.....   | 121 |
| <b>Figure 5.S4.</b> Conversion of PA without added catalysts at 90°C, 105°C, and 120°C.....   | 122 |
| <b>Figure 5.S5.</b> Catalytic activity of MIL-101-Al-NH <sub>2</sub> at 90 °C, 105 °C and 120 °C.....   | 123 |
| <b>Figure 5.S6.</b> Catalytic activity of $\gamma$ -Al <sub>2</sub> O <sub>3</sub> at 90 °C, 105 °C, and 120 °C.....  | 124 |
| <b>Figure 5.S7.</b> Acid properties of spent $\gamma$ -Al <sub>2</sub> O <sub>3</sub> , spent MIL-101-Al-NH <sub>2</sub> by DRIFTS.....   | 125 |

|   |     |
|---|-----|
| <b>Figure 6.1.</b> Physicochemical structure of synthesized UiO-66 with modulators by XRD, N <sub>2</sub> -adsorption-desorption, DRIFTS, and TGA.....  | 136 |
| <b>Figure 6.2.</b> Catalytic activity of selected Zr-MOFs; time on stream of Levulinic acid conversion, methyl levulinate selectivity, and conversion over selectivity.....                         | 138 |
| <b>Figure 6.3.</b> Levulinic acid conversion Vs the number of linker defects in UiO-66 MOFs.....  | 140 |
| <b>Figure 6.4.</b> FTIR spectra of the hydroxyl-group region for modulated UiO-66 MOFs.....   | 141 |
| <b>Figure 6.5.</b> Reusability and stability of UiO-66-A130 catalysts for esterification reaction.....  | 142 |
| <b>Figure 6.S1.</b> FTIR spectrum of synthesized UiO-66 MOFs.....   | 146 |
| <b>Figure 6.S2.</b> Characterization of spent UiO-66-A130 by FTIR, and XRD.....   | 149 |
| <b>Figure 7.1.</b> Catalytic activity of selected Zr- and Hf-containing catalysts; time on stream of benzaldehyde conversion, benzyl alcohol selectivity, and conversion over selectivity.....      | 159 |
| <b>Figure 7.2.</b> Proposed mechanism of MPV reduction of benzaldehyde with 2-propanol to produce benzyl alcohol by Zr- and Hf-containing MOF-808.....  | 163 |
| <b>Figure 7.3.</b> Proposed mechanism of benzaldehyde reaction with 2-propanol over Brønsted acid sites in UiO-66(Hf) and free energies (kJ/mol).....   | 164 |
| <b>Figure 7.4.</b> Proposed chemical pathway for Meerwein–Ponndorf–Verley reduction of benzaldehyde with 2-propanol to benzyl alcohol by MOF-808(Hf).....   | 165 |
| <b>Figure 7.5.</b> Transfer hydrogenation of selected carbonyls by MOF-808(Hf).....   | 166 |
| <b>Figure 7.6.</b> Stability and reusability of MOF-808(Hf) for the MPV reduction of benzaldehyde to benzyl alcohol by filtration test at 100 °C and recycle of MOF-808(Hf) catalyst at 100 °C..... | 167 |
| <b>Figure 7.S1.</b> Cluster model of MOF-808 (a) and UiO-66 (b) used in this work.....  | 174 |
| <b>Figure 7.S2.</b> Evolution profiles of benzaldehyde conversion and selectivity to benzyl alcohol for MPV reduction of benzaldehyde with 2-propanol by metal triflates.....                       | 175 |
| <b>Figure 7.S3.</b> Characterization data for Zr- and Hf-containing MOF catalysts by N <sub>2</sub> adsorption-desorption, FTIR, TGA, and XRD.....  | 179 |
| <b>Figure 7.S4.</b> Acid properties of MOF-808(Hf), MOF-808(Zr), and UiO-66(Zr) measured by diffuse reflectance infrared Fourier transform spectroscopy (DRIFTS).....                               | 181 |
| <b>Figure 7.S5.</b> TGA analysis profiles of UiO-66(Zr), UiO-66(Hf), and modulated UiO-66(Hf).....  | 182 |

|  |     |
|--|-----|
| <b>Figure 7.S6.</b> Hydrogenation of benzaldehyde by Zr- and Hf-containing MOF-808 and UiO-66.....   | 184 |
| <b>Figure 7.S7.</b> Conversion of benzaldehyde by H <sub>2</sub> SO <sub>4</sub> . Evolution of benzaldehyde conversion and product selectivity.....                               | 185 |
| <b>Figure 7.S8.</b> Conversion of benzyl alcohol by H <sub>2</sub> SO <sub>4</sub> . Evolution of benzyl alcohol conversion and product selectivity.....                           | 185 |
| <b>Figure 7.S9.</b> Effect of the modulator on the transfer hydrogenation of benzaldehyde by UiO-66(Hf).....   | 186 |
| <b>Figure 7.S10.</b> Optimized structures of the benzaldehyde and 2-propanol co-adsorption complexes on Hf and Brønsted sites of UiO-66(Hf).....                                   | 186 |
| <b>Figure 7.S11.</b> Characterization of spent MOF-808(Hf) by FTIR, and XRD.....   | 187 |
| <b>Figure 8.1.</b> ATR-FTIR spectra and X-ray diffraction patterns of modified polypropylene with different sulfonate loading.....   | 196 |
| <b>Figure 8.2.</b> Physical characteristics of the modified polypropylene with different sulfonate loadings by suspension in water, SEM images, and contact angle.....             | 196 |
| <b>Figure 8.3.</b> Catalytic performance of PP-SO <sub>3</sub> H catalysts for levulinic acid esterification.....  | 198 |
| <b>Figure 8.4.</b> Effect of alcohols on esterification of levulinic acid.....   | 199 |
| <b>Figure 8.5.</b> Reusability and stability of PP-SO <sub>3</sub> H-0.23 for levulinic acid esterification.....   | 200 |
| <b>Figure 8.6.</b> FTIR spectra and X-ray diffraction pattern of spent PP-SO <sub>3</sub> H-0.23 catalyst.....   | 201 |
| <b>Figure 8.7.</b> Proposed chemical pathway for esterification of levulinic acid by PP-SO <sub>3</sub> H.....   | 203 |
| <b>Figure 9.1.</b> Characterization of functionalized polypropylene with sulfonate at different loading, SEM images, suspension, contact angle, XRD spectra, and FTIR spectra..... | 213 |
| <b>Figure 9.2.</b> Catalytic performance of PP-SO <sub>3</sub> H catalysts for xylose dehydration.....   | 215 |
| <b>Figure 9.3.</b> Catalyst recyclability, and stability of PP-SO <sub>3</sub> H-0.23 for xylose dehydration.....  | 216 |
| <b>Figure 9.4.</b> FTIR spectra and X-ray diffraction pattern of spent PP-SO <sub>3</sub> H-0.23 catalyst.....   | 217 |
| <b>Figure 9.5.</b> Proposed reaction pathways for conversion of biomass-derived compounds by acidic PP-SO <sub>3</sub> H catalyst.....   | 220 |

## CHAPTER 1

### INTRODUCTION

#### **1. Introduction**

The petroleum and animal farming industries are the leading contributors to greenhouse gases, including carbon dioxide (CO<sub>2</sub>), methane, and nitrous oxide [1]. Carbon dioxide emissions account for 65% of global greenhouse gases, causing a global temperature rise and climate change and negatively affecting agricultural/forest production, livestock farming, and our standard of living [2-4]. In 2014, CO<sub>2</sub> emissions were estimated at ~34.1 gigatons [5], and this quantity is projected to rise [6]. CO<sub>2</sub> emissions stem from petroleum processing to produce transportation fuels, chemicals, and plastic precursors [7]. One potential solution to mitigate greenhouse gas emissions is by transitioning to the circular economy and transforming these readily available wastes (biomass and plastics) into fuels, and chemicals [8, 9]. In doing so, we add value to these wastes and become less dependent on petroleum-derived products.

#### **2. Background**

##### **2.1. Background on biomass**

Lignocellulosic biomass is cost-effective, abundant, and renewable. It consists of three primary building blocks: cellulose, hemicellulose, and lignin [10]. Cellulose from lignocellulose is the most abundant bioresource on the planet and consists mainly of glucose building blocks [11]. Glucose can be converted into different platform molecules, for example, fructose, 5-hydroxymethylfurfural (HMF) [12], levulinic acid [13], lactic acid [14], ethanol [15], 2,5-dimethylfuran [16], ethyl levulinate [17], 5-(alkoxymethyl) furfurals, 2,5-bis(alkoxymethyl)furans [18] which can be further processed into monomers, fuel additives, paints, and a variety of fine chemicals.

## **2.2 Background on catalysts for biomass upgrading**

Catalysts can be divided into three main types – biocatalyst, homogeneous, and heterogeneous. Currently, many chemical industries such as food and pharmaceuticals paid great attention to the transformations of an aldose to ketose. They relied on the biocatalyst (i.e., enzymes) [19-21]. However, biocatalysts have some serious limitations, such as the short lifetime of enzymes and the requirement of strictly-controlled conditions, such as temperature, pH, and solvent [22]. In this perspective, chemo-catalysts would be an excellent alternative for biomass valorization. Catalysts in the homogenous form (metal salts, chloride) have been used for biomass upgrading. However, homogeneous catalysts have the classic problem of requiring catalyst separation and product purification. Therefore, it is greatly desirable to develop highly selective heterogeneous solid acid catalysts for biomass upgrading.

## **2.3. Background on metal-organic frameworks (MOFs)**

In recent years, metal-organic frameworks (MOFs) have drawn attention as heterogeneous catalysts for biomass transformation reactions. They are composed of metal clusters and organic linkers, connected by coordination networks [23, 24]. The coordinatively unsaturated metal sites and their structural defects in MOFs provide Lewis acid sites for various organic reactions, such as acetalization [25, 26], hydrogenation [27, 28], and esterification [29, 30]. MOFs' porous, high surface area provides a high density of active sites and a large contact area for reactants. These attributes make MOFs attractive catalysts [31]. MOFs' advantages as heterogeneous catalysts are that they can be tuned in different pore sizes and pore functionality by tailoring different metals and organic ligands in the framework [32]. By tuning the structure of metal-organic frameworks, we can change the functional properties and increase the catalytic activity. We can change the functional group in organic ligands, encapsulate the active species into the pores, and synthesize MOFs with modulators to increase the Lewis acid densities in their structure. The tuning properties and structural modification will provide a new perspective in the application of MOFs for biomass conversion into value-added fuels and chemicals.

## **2.4 Background on Plastics**

In our daily life, plastics materials have increasingly been used in a wide range of applications, including packaging, containers, automotive parts, and offered unique properties that are unsurpassed by other materials. With increasing demand, global plastic production is projected to rise to 1800 million tons by 2050, and every year about 8 million plastic accumulates in the ocean [33]. Around 448 million metric tons of plastics had been produced, and around 6300 Mt of plastic waste was generated in 2015. Only 9 percent of its plastic waste was recycled in the US, and another 12% was incinerated. The rest of the 79% was accumulated in the landfills or natural environment, and the amount of the landfill's waste will be around 12,000 MT by 2050 [34]. The amount of waste plastic in the ocean is rapidly increasing, and in 2050, the weight ratio of waste plastic to fish in the ocean will be outweighed (>1:1), which is very alarming [35]. As a step toward a greener and safer plastics world, it is important to find the suitable application of these waste plastics.

## **3. Aim and scope of this study**

I developed heterogeneous solid acid catalysts for lignocellulose and plastic upcycling in this work.

### **3.1 MOFs are alternative to zeolites for Biomass upgrading**

Zeolites are commonly used catalysts for petroleum processing [36, 37] and biomass upgrading [38, 39]. My initial study (**Chapter 2**) was to develop and modify the surface of zeolite with a long-chain organic surfactant which improved the contact between glycerol and acetone for glycerol acetalization and resulted in high catalytic activity. However, zeolites have mainly Brønsted acid sites with low Lewis acid sites, resulting in coke formation [40, 41]. In the zeolites, aluminum is presented in the form of a cluster which results in the low Lewis acid density. To remove the oxygen from the biomass-derived compounds, we need to develop a robust catalytic system that has a high Lewis acid density. Metal-organic frameworks (MOFs) are porous crystalline materials of metal clusters and organic linkers, connected by coordination networks [23, 24]. The exposed metal



nodes give them high Lewis acid sites, and the tunability of their ligands can enhance their ability in catalysis. Hence, I transitioned my research from zeolites to metal-organic frameworks (MOFs).

### 3.2. Tuning properties and structural modification of MOFs

In **chapter 3**, I developed the bi-functional Lewis-Brønsted acid catalysts for glucose dehydration to 5-hydroxymethylfurfural (HMF). Production of HMF from glucose involves a cascade of reactions, glucose isomerization to fructose and fructose dehydration to HMF [42]. The glucose isomerization requires Lewis acid sites [43], whereas fructose dehydration requires Brønsted acid sites [44]. MOFs have coordinatively unsaturated metal sites that provide Lewis acid sites for various organic reactions. Adding Brønsted acid sites into the pores created bi-functional solid acid catalysts. I encapsulated the Brønsted acidic phosphotungstic acid (PTA) in Al-MOFs, which provides the synergy between Lewis acid sites ( $\text{Al}^{3+}$ ) and encapsulated Brønsted acid sites, enhancing its catalytic performance in glucose dehydration to HMF.

In **chapter 4**, my study evaluated the effect of amino functionalization in aluminum (Al)-containing MOFs on glucose isomerization in ethanol. I tested three Al-MOFs for glucose isomerization. Among three Al-MOFs, MIL-101(Al)- $\text{NH}_2$  gave a high fructose selectivity of 64% at 82% glucose conversion. The presence of amino groups enhanced medium-to-strong Lewis acid strength, fructose selectivity, and glucose conversion. Moreover, MIL-101(Al)- $\text{NH}_2$  MOF was stable and reusable up to four times without losing catalytic performance. In **chapter 5**, I used this MIL-101(Al)- $\text{NH}_2$  as a water-tolerant Lewis acid catalyst for selective dihydroxyacetone isomerization to lactic acid. We obtained a high lactic acid selectivity of 91% at 96% DHA conversion at 120°C in water, and Al-MOFs were reusable four times without any decrease in catalytic performance.

In **chapter 6**, I synthesized the UiO-66(Zr) MOFs by adding acetic acid as modulators which create surface defects on the framework. Defective UiO-66 MOFs have the unsaturated metal sites ( $\text{Zr}^{4+}$ ) created by missing linkers which acted as Lewis acid sites, and the Brønsted acidity induced from the surface hydroxyl group. Later, I studied the cooperative effect of Lewis and Brønsted acidity for

the esterification of levulinic acid with methanol. The cooperative Brønsted-Lewis acid sites are responsible for the superior catalytic performance of defective UiO-66 MOFs and showed high methyl levulinate selectivity (93%).

In **chapter 7**, I evaluated the catalytic performance of Zr- and Hf-containing MOF-808 and UiO-66 catalyst for transfer hydrogenation of benzaldehyde in 2-propanol. Next, I combined experimental results and density functional theory to elucidate the mechanism by which Hf- and Zr-containing MOFs activate carbonyl compounds during transfer hydrogenation. The Lewis acidic MOF-808(Hf) was the most active and selective to transfer hydrogenation (MPV) of benzaldehyde to benzyl alcohol. This study provided an insight into the development of active and selective Lewis acidic MOF catalysts for the transfer hydrogenation of biomass-derived carbonyl compounds.

### **3.3. Creation of Brønsted acid sites on plastic**

Polypropylene is the second-most used plastic and one of the most versatile types of plastics. The utilization of polypropylene-derived catalysts for the chemical industry potentially would increase plastic recycling rates and mitigate plastic pollution. In **chapter 8**, I developed the novel solid Brønsted acidic catalysts by sulfonating polypropylene to create sulfonated polypropylene (PP-SO<sub>3</sub>H). The PP-SO<sub>3</sub>H catalyst had an excellent catalytic performance for esterification of levulinate with methanol. We obtained high ester selectivity (96%) at 94% conversion of levulinic acid.

Moreover, the PP-SO<sub>3</sub>H catalyst was stable and reusable up to 4 times without compromising the esterification performance. In **chapter 9**, I used this PP-SO<sub>3</sub>H catalyst for xylose dehydration to furfural and obtained high selectivity to furfural (88%) at 85% conversion of xylose. I also applied these PP-SO<sub>3</sub>H catalysts to transform selected biomass-derived molecules (i.e., glycerol, fructose) and elucidated the reaction pathways for the conversion of biomass-derived compounds.

CHAPTER 2  
HYDROPHOBIC FUNCTIONALIZATION OF HY ZEOLITES FOR EFFICIENT CONVERSION OF  
GLYCEROL TO SOLKETAL<sup>1</sup>

**1. Introduction**

The petroleum and animal farming industries are the leading contributors to greenhouse gases, including carbon dioxide (CO<sub>2</sub>), methane, and nitrous oxide [1, 45]. Carbon dioxide emissions account for 65% of global greenhouse gases, causing a global temperature rise and climate change and negatively affecting agricultural/forest production, livestock farming, and our standard of living [2, 4, 46]. In 2014, CO<sub>2</sub> emissions were estimated at ~34.1 gigatonnes [47], and this quantity is projected to rise [6]. CO<sub>2</sub> emissions stem from fossil fuel processing and methane release from shale oil extraction and natural gas development [48]. Production of biofuels and bioproducts from renewable plant biomass can reduce CO<sub>2</sub> emissions, mitigating global warming and climate change.

Glycerol is a by-product of processing vegetable oils to produce biodiesel. In 2017, the biodiesel production volume was ~ 1.6 billion gallons, and production is projected to reach 4 billion gallons by 2022 [49]. Biodiesel production generates ~10 wt.% glycerol [50]. As our society slowly moves to a sustainable future, the ability to convert glycerol to high-value products will accelerate its commercial use and the fight against global warming.

---

<sup>1</sup> This chapter has been published in *Applied Catalysis A: General* (Rahaman et al., 2020, *Applied Catalysis A: General*, 592, 117369.). The copyright clearance from the publisher has been included in the "APPENDIX" section.

Glycerol can be upgraded to valuable compounds such as propanediol, acrolein, glycerol carbonate, glyceric acid, tartronic acid, syngas, and solketal [51-59], thereby providing opportunities for additional revenue for the biodiesel industry and the agricultural sector. Glycerol acetalization is catalyzed by acid sites and produces cyclic acetals with 5- and 6-membered rings (4-hydroxymethyl-2,2-dimethyl-1,3-dioxane (solketal) and 5-hydroxy-2,2-dimethyl-1,3-dioxane (acetal)) (**Fig. 2.1**). Solketal is of particular interest because (1) it is a 100% bio-based chemical, produced from glycerol conversion with acetone. Acetone can be derived from hemicellulose from biorefineries [60]; (2) the reaction operates under mild conditions [61-63]; and (3) solketal can be used in many applications including fuel additives [64, 65], solvents in paint and ink industries [66-68], cleaning products [69], additives for the pharmaceutical industry [70, 71], and co-initiators for polymerization [69, 72].

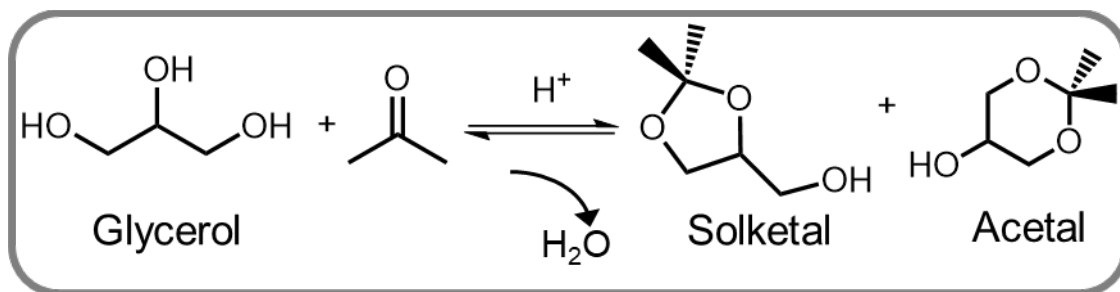


**Figure 2.1.** Solketal production from glycerol acetalization by acid.

Although homogeneous acid catalytic systems work for glycerol acetalization, their use is complicated by the need to separate catalysts from products. Thus, heterogeneous zeolite catalysts have been popular choices for glycerol acetalization [73, 74]. However, the low glycerol solubility in acetone (5 wt.% or ~ 0.03 glycerol/acetone molar ratio) causes the two reactants to be immiscible, presenting a mass transfer limitation. Immiscibility greatly limits the joint contact between the two reactants and catalysts' active sites, and, therefore, impairs catalysis [75-77]. Mass transfer limitation is unavoidable in multiphase reactions, including glycerol acetalization, but it can be minimized [78, 79].

The objective of this study was to develop a multifunctional, solid acid catalyst modified with a surfactant to improve the contact between glycerol and acetone. We hypothesized that grafting an organosilane surfactant onto a solid HY zeolite catalyst would generate interface-active materials that would create an emulsion in which catalysis would occur. The emulsion would enhance the interfacial mass transfer by increasing the contact surface between the two immiscible reactants. We tested the foregoing conjecture by grafting an organosilane surfactant, n-octadecyltrichlorosilane (OTS), onto an HY zeolite catalyst and evaluated the performance of this OTS-grafted HY (OTS-HY) at 30°C. We selected OTS because it has a long alkyl chain to provide substantial hydrophobicity. Moreover, we selected HY zeolite (Si/Al = 2.6) as our catalyst because (1) it is widely used in the chemical industry, (2) it has a large pore dimension (7.3 nm), and (3) it has a low Si/Al ratio, providing a high acidity (578  $\mu\text{mol NH}_3/\text{g catalyst}$ ) [80] for glycerol acetalization. We found that the OTS-HY catalyst produced a higher glycerol conversion than did the HY catalyst. The OTS-HY catalyst enabled emulsion formation, increasing contact between the two reactants. This catalytic system addresses the fundamental limitation of the low contact between a catalyst's active sites and the two immiscible reactants in glycerol acetalization.

## **2. Materials and Methods**

### **2.1 Functionalization of zeolites with surfactant**

HY zeolite (CBV600, Si/Al ratio = 2.6) was obtained from Zeolyst® International (Conshohocken, PA, USA). We chose this HY zeolite with 2.6 Si/Al ratio because it has a high acid site density with the hydrophilic characteristic, enabling us to observe (1) the negative effect of water formation on catalytic activity and (2) the benefit of adding surface hydrophobicity. The as-received HY zeolite was calcined at 500 °C for 1 h to remove residual impurities before use. The surface functionalization of the zeolite was performed as described [81]. In short, 1 g of zeolite was dispersed in 20 mL of toluene in a capped 250 mL flask using a sonicator at room temperature for 1 h. The organosilane reagent (n-octadecyltrichlorosilane (OTS), 95%, Alfa Aesar) at an organosilane/zeolite ratio of 0.5 mmol/g zeolite (theoretical OTS loading on zeolite) was mixed with 50 mL toluene at room temperature. The hydrolyzable Cl ions of the OTS underwent hydrolysis

and formed a stable condensation with silanol groups (-Si-OH) on the surface of HY. The organofunctional group (octadecyl) is a nonhydrolyzable organic radical and adds chemical characteristics. The organosilane solution was added to the zeolite suspension, and the resulting mixture was stirred for 24 h at 500 rpm at room temperature. The surface-modified zeolite was then filtered and washed with ethanol five times and vacuum dried at 80 °C overnight. This functionalized zeolite was named OTS-HY.

## **2.2 Characterization of catalytic materials**

The degree of hydrophobicity of zeolites was determined by the contact angle measurement using water droplets. Zeolite samples were compressed into a 1 cm disc (OD) with a thickness of 2 mm. A 1  $\mu$ L water droplet was placed on the external surface of the disc using Optical contact angle measurement and drop contour analysis (OCA15, DataPhysics Instruments USA Corp., Charlotte, NC, USA). Infrared spectra of the zeolites were recorded on a JASCO Fourier transform infrared (FTIR) spectrometer (Easton, MD, USA), equipped with an attenuated total reflection stage (ATR). High-resolution transmission electron microscopy (HRTEM) was performed on catalysts using a 200 kV-operated field emission gun FEI Tecanai F20 transmission electron microscope. Low-intensity illumination conditions were used to minimize the amorphization of zeolites.

To confirm the changes in surface functionality after grafting OTS onto HY catalysts, the diffuse reflectance infrared Fourier transformation spectroscopy (DRIFT) was performed using the JASCO FTIR equipped with high-temperature DiffuseIR™ cell (PIKE Technology, WI, USA). The sample treatment and temperature program were described elsewhere with a slight modification [81]. In short, all experiments were performed after heating 5mg catalyst sample in situ up to 230 °C under a flow of N<sub>2</sub> (20 mL/min) with a heating rate of 10 °C/min. Then the temperature was maintained at 230°C for 30 min. A background spectrum was recorded prior to each run and the 512 scans of spectra were collected in the range between 4000–1000 cm<sup>-1</sup> at a 4 cm<sup>-1</sup> resolution.

The surface area and pore volume of zeolites were measured using N<sub>2</sub> adsorption/desorption by a Tristar Micromeritics (Norcross, GA, USA) instrument. Prior to the measurement, the samples were pretreated at 160 °C for 2 h using a Micromeritics FlowPrep with sample degasser (Norcross, GA, USA). The surface area, S<sub>BET</sub>, was determined by N<sub>2</sub> isotherms using the Brunauer–Emmett–Teller equation (BET) on the basis of overall mass of the catalysts. The desorption cumulative pore volume was estimated according to the Barrett–Joyner–Halenda (BJH) model. The moisture and organic compounds on the catalysts were determined by thermogravimetric analysis (TGA) using a SDT Q600 TA instrument (New Castle, DE, USA). In short, ~20 mg of the sample was placed in a cylindrical alumina crucible and heated in the air from room temperature to 500 °C with a heating rate of 10 °C/min under N<sub>2</sub> flow (100 ml/min). The moisture content of catalyst was calculated from the weight loss below 150 °C. X-ray diffraction (XRD) analysis was performed on a Bruker D8 Discover diffractometer (Bellerica, MA, USA) using CuK<sub>α</sub> radiation and 2θ ranging from 10° to 60° with 0.2 sec/step [81]. This 2θ range revealed the diffraction intensity of (220), (311), (331), (511), (440), (533), (642), and (555), respectively [82-84].

The total acidity of zeolites was determined by ammonia-temperature programmed desorption (NH<sub>3</sub>-TPD). The NH<sub>3</sub>-TPD experiments were performed using a Micromeritics ChemiSorb 2720 instrument equipped with a thermal conductivity detector (TCD) (Norcross, GA, USA). The samples were dried in a vacuum oven overnight prior to NH<sub>3</sub>-TPD. About 20-40 mg of sample was pretreated at 250 °C for 1 h under flowing He gas to remove adsorbed water. The sample was then cooled to 100 °C and saturated with ammonia (10% NH<sub>3</sub>/He). Next, the samples were flushed with 40 mL/min He flow at 100 °C for 1 h to remove physically adsorbed ammonia. TPD profiles were recorded by heating the samples to 700 °C at a rate of 10 °C/min in 40 mL/min He flow. In the case of OTS-HY catalysts, we ran the TPD experiment without pre-adsorption of NH<sub>3</sub> to evaluate the OTS decomposition temperature ranges and its contribution during the NH<sub>3</sub>-TPD. To determine the acid site density of OTS-HY catalyst, we subtracted the OTS decomposition peak area from the NH<sub>3</sub>-TPD peak area.

### 2.3 Study of glycerol acetalization

Reactions were performed in 15 mL glass pressure vials in an oil bath. Typically, glycerol, acetone, and catalysts were added to the pressure vial which was sealed and stirred at the desired temperature. We ran this reaction for different times (10-60 min), at different temperatures (30 and 50°C), with different catalyst loading (5 and 15 wt.%), and a fixed glycerol/acetone molar ratio of 1/12 (12 wt.% glycerol), unless otherwise noted. The OTS-HY catalyst was loaded at an amount that provided a number of active sites comparable to that of HY. Dodecane was used as an internal standard. The glycerol conversion and product yield were calculated based on the internal standard. The reaction was stopped by quenching in a cold-water bath followed by adding ethanol (2 mL ethanol per 0.25 g glycerol) to dissolve the remaining glycerol and acetone. The solution was centrifuged, and the solid catalyst was removed. The liquid sample was then diluted with ethanol prior to analysis.

The reactants and products were analyzed using a gas chromatograph (7890B GC) (Agilent Technologies, Santa Clara, CA, USA) equipped with a mass spectrometer and flame ionization detector (FID) for product identification and quantification, respectively. A DB-1701 column (30 m x 0.25 mm x 0.25 µm, Agilent Technologies, Santa Clara, CA, USA) was used for product separation with the following parameters: injection temperature 275 °C and FID detector temperature 300 °C; split ratio 1:50. The temperature program started at 50 °C with a heating rate of 8°C/min to 200 °C. The glycerol conversion, product yield, and product selectivity were calculated as follows:

$$\text{Glycerol conversion (\%)} = \frac{\text{mole of glycerol reacted}}{\text{initial mole of glycerol}} \times 100$$

$$\text{Product yield (\%)} = \frac{\text{mole of product generated}}{\text{initial mole of glycerol}} \times 100$$

$$\text{Product selectivity (\%)} = \frac{\text{Product yield}}{\text{Glycerol conversion}} \times 100$$



### 3. Results and Discussion

We first confirmed the successful grafting of the OTS surfactant onto the HY catalyst and characterized changes in the surface properties. These analyses were performed with Fourier-transform infrared spectroscopy (FTIR), Thermal gravimetric analysis (TGA), High-resolution transmission electron microscope (HRTEM), X-ray diffraction (XRD), and N<sub>2</sub>-adsorption/desorption. Then we evaluated the effect of OTS grafting onto the HY catalyst in the glycerol acetalization reaction with various conditions.

#### 3.1 Characterization of the organosilane-grafted HY zeolites

The FTIR and DRIFT spectra of the OTS-HY catalyst confirmed the successful grafting of OTS onto the HY catalyst. The skeletal FTIR spectra of the unmodified HY catalyst presented an asymmetric stretching of the T-O-T bridges at 1056 and 1198 cm<sup>-1</sup> (**Fig. 2.2B**), where T is tetrahedrally coordinated Si or Al atoms [85, 86]. Upon OTS grafting onto HY catalyst, the characteristic T-O-T band at 1056 cm<sup>-1</sup> shifted to 1050 cm<sup>-1</sup> because of the formation of the Si-O bond on the tetrahedral T-O-T. We observed a similar down-shift of the zeolite's characteristic T-O-T band in the silane grafted SAPO-34 zeolites, suggesting the formation of linkages between silane and zeolites [87]. We observed bands at 2919 and 2851 cm<sup>-1</sup>, associated with the CH symmetric ( $\nu_s(\text{CH})$ ) and asymmetric ( $\nu_a(\text{CH})$ ) stretching vibrations for CH<sub>2</sub> groups of the OTS, respectively (**Fig. 2.S1A**). The band at 1198 cm<sup>-1</sup> was due to the formation of Si-O-Si linkages between OTS and HY catalyst [88, 89]. We did not observe the characteristic band of the self-condensed OTS product at 1014 cm<sup>-1</sup>, suggesting that its formation was negligible (see Supplementary Information, **Fig. 2.S1B**).

We further confirmed the successful OTS grafting by DRIFT and observed changes in the OH vibrational region (3500–3800 cm<sup>-1</sup>) of HY and OTS-HY catalysts. We detected a significant decrease in band intensity at 3740 cm<sup>-1</sup> after OTS grafting onto HY catalysts (**Fig. 2.2C**). Whereas the two bands at 3627 and 3562 cm<sup>-1</sup> remained relatively unchanged. The band at 3740 cm<sup>-1</sup> was attributed to the free silanol groups on the external surface of HY catalysts [90]. So the decrease

in this band intensity indicated a reduction in density of silanol groups after OTS grafting. The bands at 3627 and 3562  $\text{cm}^{-1}$  were attributed to the structural hydroxyl groups, the high-frequency (HF) OH groups at the supercages and low frequency (LF) at the sodalite cages, respectively [91]. These OH groups are responsible for the Brønsted acidity of the zeolites [92, 93]. After OTS grafting, intensities of these bands remained relatively unchanged, suggesting that grafted OTS did not block the active sites. Consistent with our results, Zapata et al also observed negligible changes in intensities of these OH stretching bands after silylation of HY catalysts [81]. The retention of the active sites in OTS-HY catalysts was helpful for the acetalization reaction. Hence, alterations of FTIR bands in the fingerprint region and the reduction of the silanol density observed by DRIFT confirmed the formation of linkages between OTS and HY catalysts.

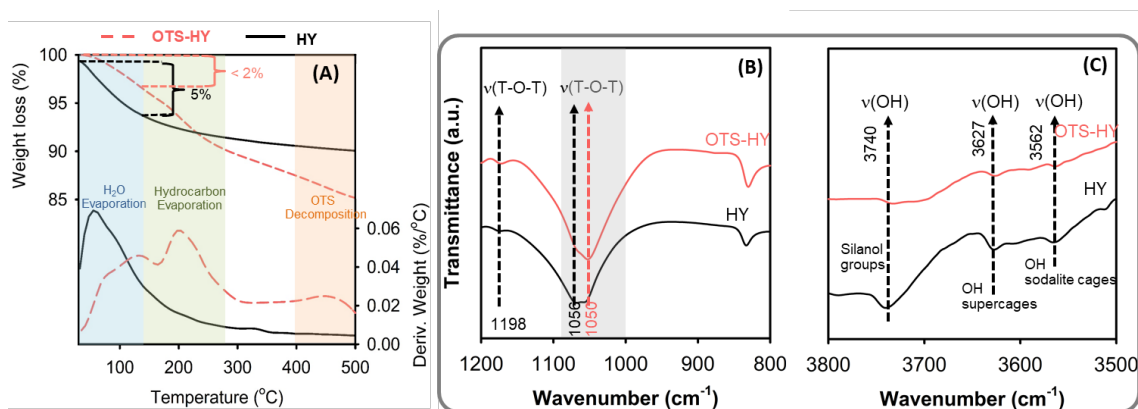


**Figure 2.2.** TGA profiles (A), FTIR spectra (B), and DRIFT spectra (C) of OTS-HY and HY catalysts.

We used TGA to assess the stability of the OTS-HY and quantify the amount of OTS grafted onto the HY (**Fig. 2.2A**). Below 150 °C, HY incurred an initial weight loss (~5%) that was attributed to breaking hydrogen-bond networks and desorption of water. OTS-HY's weight loss was lower (~2%). The sharper decrease in weight of HY indicated higher water adsorption (~5%) compared with that of OTS-HY (~2%). These results suggested that OTS-HY catalyst was more hydrophobic than HY catalyst because the surface of HY catalyst consists of portions of free silanols (-Si-OH) that adsorb water molecules [94-96]. The weight loss of the OTS-HY occurred in three steps: (1) ambient to 150°C, (2) 150-270°C and (3) 400-500°C. The weight losses in the first and second

steps were from the evaporation of moisture and residue organic solvent during synthesis, respectively. The total weight loss for OTS-HY was higher than that of HY, which we attributed to the slow decomposition of OTS at a higher temperature ( $> 400^{\circ}\text{C}$ ). Zapata et al. reported OTS decomposition from OTS-functionalized silica and SBA-15 in the range of  $350\text{-}600^{\circ}\text{C}$ , corroborating our OTS decomposition findings. We estimated that the amount of grafted OTS on HY was  $\sim 16\%$  (w/w).

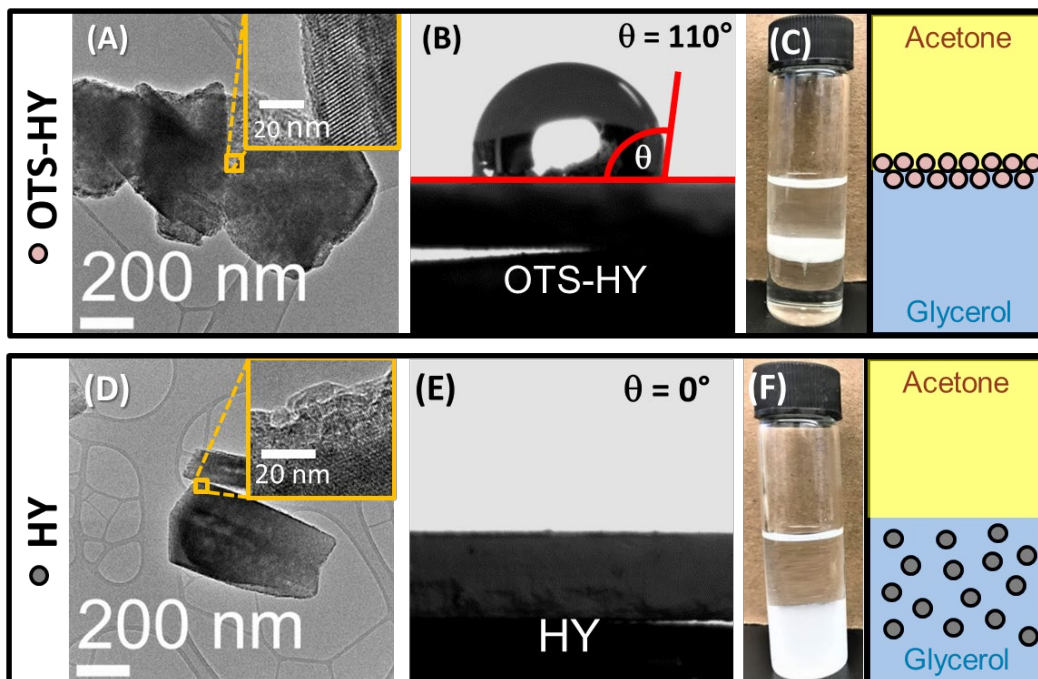


**Figure 2.3.** HRTEM images of HY and OTS-HY catalysts (A & D) and their contact angles (B & E). The suspension behavior of HY and OTS-HY catalysts in the glycerol-acetone system (C & F).

The crystallinity of HY was preserved after grafting with OTS. The HRTEM image (**Fig. 2.3A & D**) of OTS-HY catalyst illustrated (1) the cubic crystalline structure of the FAU zeolites [83, 97], and (2) an unchanged crystalline structure after grafting OTS. Likewise, the XRD spectrum of OTS-HY catalyst confirmed the presence of a highly crystalline HY zeolite [98] (**Fig. 2.4**). The HRTEM and XRD results suggested a negligible loss of crystallinity after grafting OTS onto HY.

| Table 2.1. Surface properties and acidity of HY and OTS-HY catalysts |   |  |   |                                      |   |        |       |
|--|---|--|---|--------------------------------------|---|--------|-------|
| Catalyst   | $S_{\text{BET}}$<br>( $\text{m}^2/\text{g}$ ) | Pore<br>volume<br>( $\text{cm}^3/\text{g}$ ) | Micropore<br>volume<br>( $\text{cm}^3/\text{g}$ ) | Pore<br>diameter<br>( $\text{\AA}$ ) | Acidity<br>( $\mu\text{mol NH}_3/\text{g catalyst}$ ) |        |       |
|  |   |  |   |                                      | Weak  | Strong | Total |
| HY   | 513   | 0.36   | 0.22  | 7.3                                  | 265   | 313    | 578   |
| OTS-HY   | 347   | 0.23   | 0.14  | 6.5                                  | 286   | 267    | 552   |

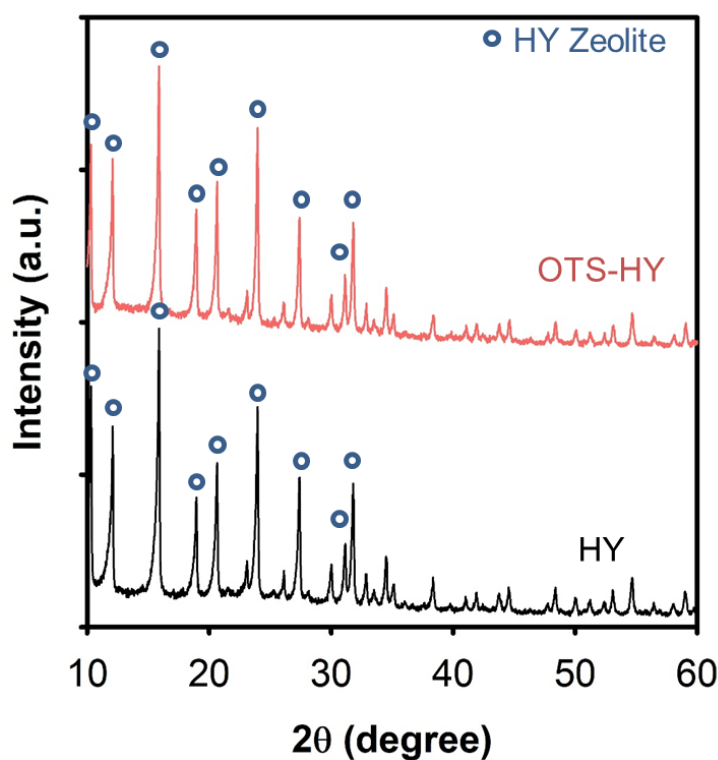


**Figure 2.4.** XRD (A) and N<sub>2</sub>-adsorption-desorption isotherms (B) of OTS-HY and HY catalysts.

To evaluate how grafting OTS onto HY affected the catalyst's acid sites, we measured changes in surface area, pore-volume, and acidity by N<sub>2</sub>-adsorption/desorption and NH<sub>3</sub>-TPD. The N<sub>2</sub> adsorption/desorption isotherms of HY and OTS-HY catalysts exhibited the type IV isotherm [83], indicating that both catalysts were microporous (**Fig. 2.S2**). The estimated surface area and pore volume of HY zeolite were 513 m<sup>2</sup>/g and 0.36 cm<sup>3</sup>/g (**Table 2.1**), consistent with reported values

[80]. Previous investigators reported that grafting organosilanes onto zeolites reduced the surface area and pore volume because some portion of the pores was occupied by the organosilanes [81]. In addition, we speculated that the decrease in the surface area and pore volume of our OTS-HY catalysts might be partly because of the dilution contributed from the grafted OTS. Moreover, our results revealed a slight decrease in the total acidity of OTS-HY catalysts ( $552 \mu\text{mol NH}_3/\text{g catalyst}$ ), measured by  $\text{NH}_3$ -TPD, compared with that of HY catalyst ( $578 \mu\text{mol NH}_3/\text{g catalyst}$ ), and this behavior is consistent with previous observations [81, 99]. The slight change in the total acidity of the OTS-HY catalysts agreed with our DRIFT results, showing comparable skeleton OH groups (i.e., at  $3627$  and  $3562 \text{ cm}^{-1}$ ) and suggesting the retention of acidity after the OTS grafting. We found that the grafting OTS onto HY took place mostly on the external surface of the HY catalysts, leaving the Brønsted and Lewis acid sites intact.

### **3.2 Emulsion formation by modified catalysts in two-phase systems**

Typically, the HY catalyst contains many free silanols, making it hydrophilic and limiting its suspension in the less polar acetone phase. Thus, we investigated the catalyst suspension behaviour by placing HY and OTS-HY in two liquid systems, (1) water-dodecane, and (2) glycerol-acetone. We chose the water-dodecane system to represent the polar-nonpolar solvent system. In the water-dodecane system, the OTS-HY catalyst was suspended in dodecane, whereas the HY was suspended in water (**Fig. 2.S3A & B**). These visual observations were consistent with the expectation that grafting OTS onto HY would add a hydrophobic layer to the HY surface, enabling it to be suspended in the nonpolar dodecane phase. These results agreed Zapata et al. who showed that, in a water-decalin system, a pristine hydrophilic catalyst settled in the water phase [99], whereas an organosilane-grafted catalyst dispersed in the decalin phase.

To determine the degree of hydrophobicity of our OTS-HY catalyst, we measured its contact angle and observed its behaviour in the two-phase systems. The OTS-HY had a contact angle of  $\sim 110^\circ$ , suggesting that OTS-HY was hydrophobic [100] (**Fig. 2.3B**). The water droplet for HY adsorbed into the disc, i.e., the contact angle was  $\sim 0^\circ$  (**Fig. 2.3E**). Our contact angle results agreed with

another study by Zapata et al. [81] that showed a high degree of hydrophobicity of OTS-grafted HY catalyst (126-135°). In addition, we conducted the water adsorption experiments using the OTS-HY and HY catalysts in a closed container with 100 mL DI water in a 200 mL beaker and measured the water absorption during 12h. The pristine HY catalyst had ~3 times higher water adsorption capacity than the OTS-HY catalyst (**Fig. 2.S4**), an observation that corresponded with the TGA results. These results confirmed the high degree of hydrophobicity of OTS-HY and the hydrophilicity of HY. Nonetheless, these water adsorption results suggested that OTS-HY was not completely hydrophobic because water could still adsorb onto its surface.

The locations of the OTS-HY and HY catalysts in the reaction vessel further confirmed the difference in the catalysts' surface properties. The glycerol-acetone system was a two-phase system due to low glycerol solubility in acetone. The OTS-HY catalyst was suspended at the interface between glycerol and acetone (**Fig. 2.3C & F**) because, although acetone is a polar solvent, it is less polar than glycerol. Hence, OTS-HY did not disperse in the acetone. Conversely, the pristine HY catalyst was suspended only in the glycerol phase because of its abundant silanol groups; the confinement of HY to the glycerol was another indication of its hydrophilicity. Previous work has shown that hydrophobic solid particles (contact angle > 90°) stabilize the formation of water-in-oil emulsions [81, 101]. We hypothesized that the high degree of hydrophobicity of OTS-HY catalysts would stabilize an emulsion between glycerol and acetone.

Thus, we investigated emulsion formation by placing the OTS-HY catalyst in the aforesaid same two liquid systems: (1) water-dodecane; and (2) glycerol-acetone. First, we used a non-ionic surfactant, Tween 60, as a control. For the water-dodecane system, we added 1 wt.% Tween 60 and vortexed for one min. The microscopic images, taken after leaving this system for 30 min, showed water droplets dispersed in the dodecane, indicating the formation of a stable emulsion layer (**Fig. 2.S5C**). Similarly, OTS-HY also stabilized the formation of the emulsion layer in the water-dodecane system (**Fig. 2.S5A**). These results suggested that the OTS-HY catalyst assisted in the formation of Pickering emulsion in the water-dodecane system [102-105]. In contrast, in the

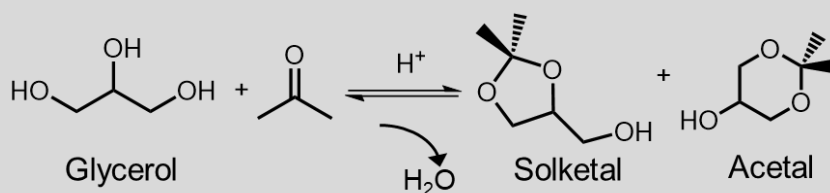
glycerol-acetone system, after adding either Tween 60 or OTS-HY and vortexing for one min, we initially observed the formation of emulsion layer. However, this emulsion layer broke and separated back into two phases after stopping agitation (**Fig. 2.S5B & D**)

The formation of Pickering emulsion has many benefits in two-phase reaction systems in which mass transfer limitation (limited contact between reactants) inhibits reactivity. For example, the use of solid particles, such as OTS-HY, to stabilize the emulsion enables easy breaking of the emulsion and recovery of the two phases. Moreover, this approach improves the contact between the two immiscible reactants without adding surfactants. Although adding surfactants in two-phase reactions can improve the contact between immiscible liquid reactants, adding surfactants complicates the downstream product purification and adds to the carbon footprint of the process [106].

### **3.3 Catalytic activity of OTS-HY catalysts in glycerol acetalization**

Next, we demonstrated the benefit of the emulsion formation by OTS-HY in glycerol acetalization under reaction conditions. At 30°C upon agitation after 10 sec, OTS-HY began dispersing in the glycerol (bottom phase) and forming an emulsion. Conversely, the HY only stayed in the glycerol phase regardless of the reaction time (**Fig. 2.S6**). An increase in reaction temperature to 50°C improved the glycerol solubility in acetone and enabled the emulsion formation by OTS-HY after 10 sec (**Fig. 2.S7**). Moreover, a 50°C reaction temperature caused a larger HY suspension area compared with the area at 30°C, indicating that increasing reaction temperature increased glycerol solubility in acetone and enabled more contact area between catalyst active sites and the two reactants. After 1 min, HY was well-dispersed in both phases (**Fig. 2.S7C**). A further increase in reaction temperature to 70°C enabled the higher glycerol solubility in acetone caused HY to be well-dispersed in both phases after 10 sec (**Fig. 2.S8**). These results suggested that the OTS-HY catalysts itself assisted in emulsion formation, thus eliminating the need for higher reaction temperatures.

**Table 2.2.** The glycerol conversion and products selectivity of investigated catalysts as a function of temperature and time. Reaction condition: 5 wt.% catalyst loading, acetone/glycerol molar ratio of 12/1.



| Catalyst | Temperature (°C) | Time (min) | Glycerol conversion (%) | 5-MR selectivity (%) | 6-MR selectivity (%) |
|----------|------------------|------------|-------------------------|----------------------|----------------------|
| HY       | 30               | 10         | 7                       | 83                   | 17                   |
|          |                  | 20         | 10                      | 87                   | 13                   |
|          |                  | 60         | 28                      | 88                   | 12                   |
|          |                  | 480        | 85                      | 92                   | 8                    |
|          |                  | 600        | 89                      | 98                   | 2                    |
| HY       | 50               | 10         | 60                      | 93                   | 7                    |
|          |                  | 20         | 65                      | 94                   | 6                    |
|          |                  | 60         | 88                      | 98                   | 2                    |
|          |                  | 480        | 88                      | 98                   | 2                    |
|          |                  | 600        | 88                      | 98                   | 2                    |
| OTS-HY   | 30               | 10         | 73                      | 88                   | 12                   |
|          |                  | 20         | 78                      | 92                   | 8                    |
|          |                  | 60         | 89                      | 95                   | 5                    |
|          |                  | 120        | 89                      | 96                   | 4                    |
|          |                  | 480        | 89                      | 98                   | 2                    |



The emulsion formation resulted in better contact between reactants with active sites of catalysts, leading to an improvement in the catalyst activity (**Fig. 2.5A & B**). We applied OTS-HY catalyst to glycerol acetalization at 30°C and 12 wt.% glycerol for 10 h. We arbitrarily chose the 12 wt.% glycerol in acetone to provide excess acetone. We performed similar experiments with HY catalyst as control. Solketal was the main reaction product with a trace amount of 6-MR (**Table 2.2**). Glycerol conversion increased with increasing reaction time and leveled off at 89% after 60 min for OTS-HY catalyst at 30°C (**Fig. 2.5C**). This plateau suggested that the reaction equilibrium was approached after 60 min. Our equilibrium conversion of 89% over the OTS-HY catalyst at 30°C was consistent with the previously reported value [107].

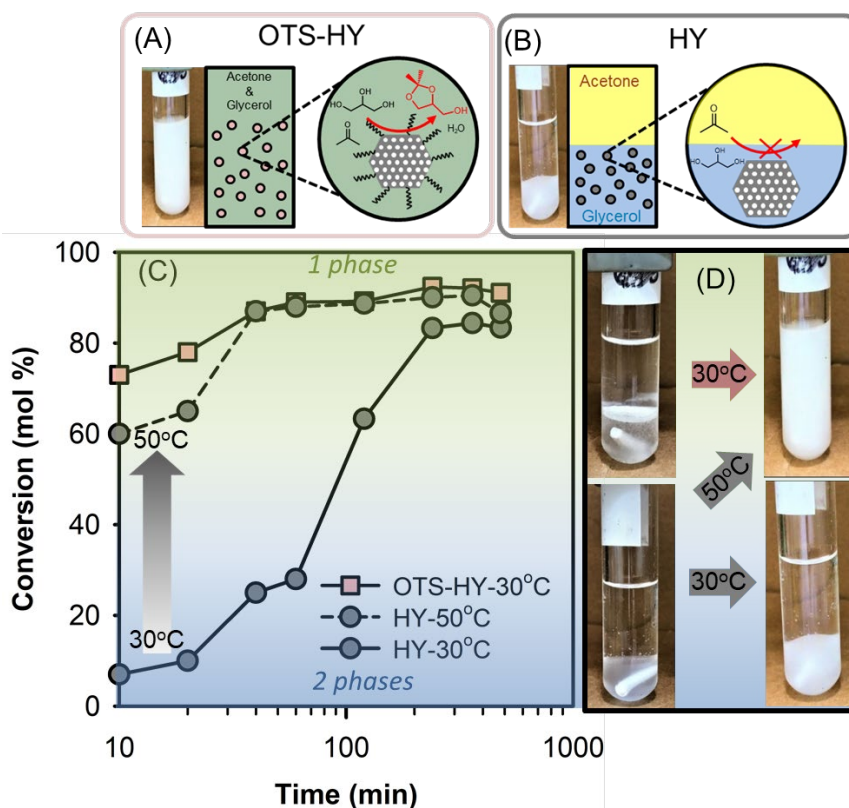


**Figure 2.5.** Suspension behaviour of OTS-HY and HY catalysts in the glycerolacetone system (A & B). Glycerol conversion by OTS-HY and HY catalysts over time (C). Changes in suspension behaviour of HY at 30 and 50 °C (D).

In the case of HY catalyst at 30°C, the reaction conversion reached 89% after 10h. An increase in reaction temperature to 50°C yielded the glycerol conversion of 88% after 60 min. These results suggested that using OTS-HY catalysts reached equilibrium faster than HY catalysts at 30°C. Moreover, glycerol acetalization is an exothermic reaction. We observed the equilibrium conversion decreased slightly with increasing temperature using HY catalysts at 12h (**Fig. 2.5C**). This slight decrease in equilibrium conversion (<2%) at elevated temperature was consistent with previous studies in both flow reactor with ethanol as a solvent and solvent-free batch reactor [107-109]. An increase in reaction temperature from 30 to 50°C simply improved the reaction rates. We observed the evolution of the phases during the course of the reaction. At 12 wt.% glycerol in acetone, the system was a two-phase system. At 30°C, the two-phase glycerol-acetone system became one phase after 60 min using OTS-HY catalysts, consistent with the 89% glycerol conversion. In the case of HY catalyst at 30°C, the reaction system remained two phases even after 60 min, consistent with the 28% glycerol conversion. Consistent with the glycerol conversion results, these findings suggested the faster reaction rate was achieved by OTS-HY catalysts.

An increase in reaction temperature from 30 to 50°C raised the catalytic activity of HY to nearly that of OTS-HY catalyst at 30°C (**Fig. 2.5D**). One reason for this increased activity of HY was that an increase in temperature increased the glycerol solubility in acetone, enhancing the contact between HY's active sites and both reactants. Yu et al. reported a similar behaviour for SDS surfactants adsorbed on the surface of multi-wall carbon nanotubes (MWCNTs) that enhanced suspension of MWCNTs in aqueous solution [110].

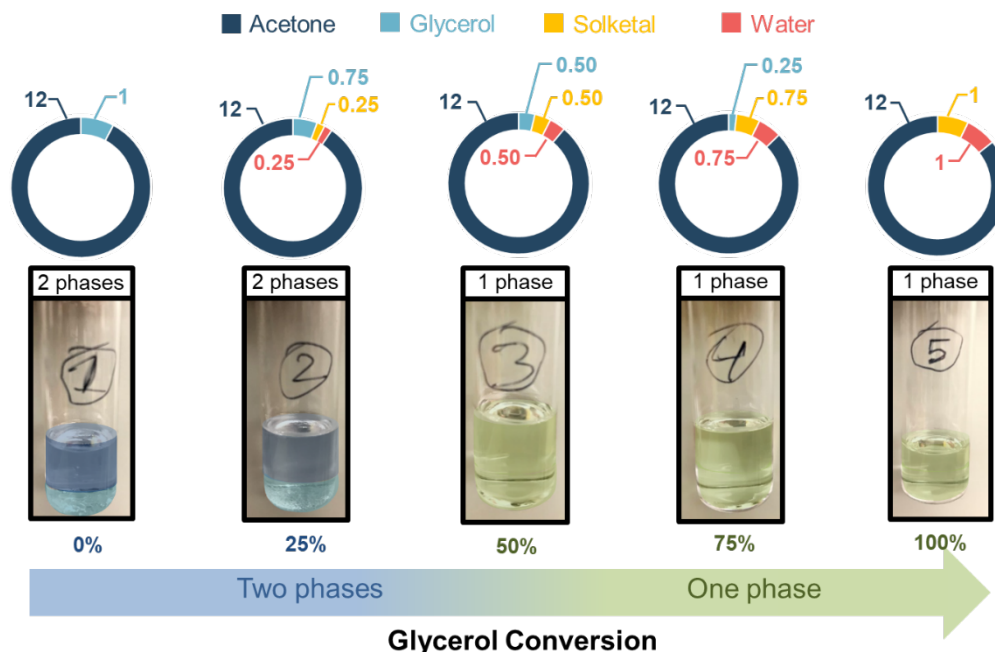


**Figure 2.6.** Phase transition of the glycerol-acetone mixture during the course of reaction.

### 3.4 Phase transition in glycerol acetalization due to the formation of solketal

Another important consideration was whether the formation of the product, solketal, affected the transition from two immiscible phases to one single phase during the reaction. We performed a series of experiments to demonstrate the behavior of the reaction mixture at varying reactants (glycerol and acetone) and products (solketal and water) concentration (i.e., simulated glycerol conversion between 0 to 100%) (**Fig. 2.6**). On the existence of the two immiscible phases, a slow mass transfer of acetone to glycerol phase was indicated at the beginning of the reaction because of a small supply of acetone. Upon the emulsion formation, the accumulation of the acetone in the glycerol phase promoted an increase in the overall rate. During the reaction, solketal is formed and accumulated. When the solketal yield exceeded 25%, it behaved as a solubilizing agent to make a homogenous mixture between glycerol and acetone, followed by a rapid conversion of glycerol because the interfacial mass transfer was eliminated.

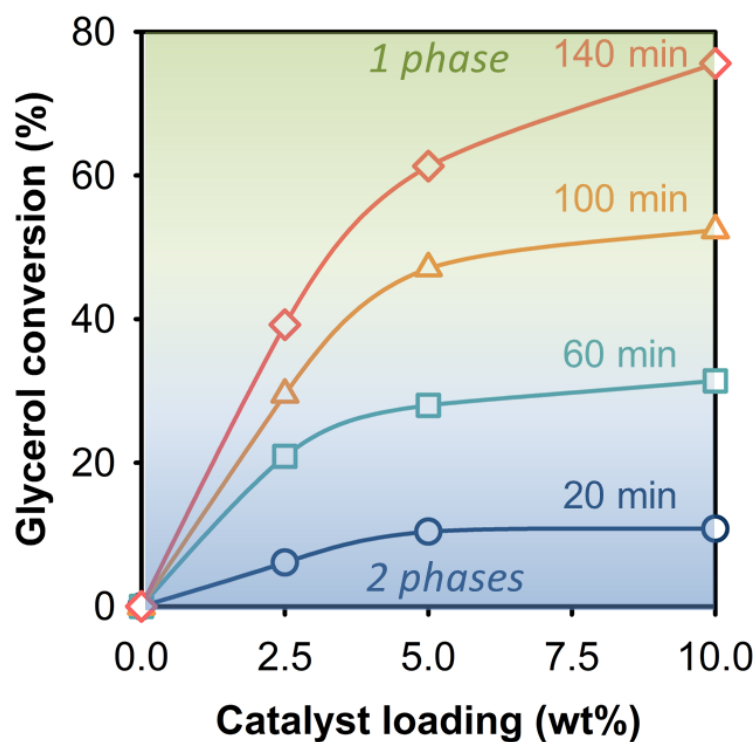


**Figure 2.7.** Effect of catalyst loading on the glycerol conversion between 20–140 min.

We further explored how this phase transition affected the interfacial mass transfer limitations in glycerol acetalization over HY catalysts at 30°C. When we performed the reaction under two-phase system (i.e., conversion < 25%, see **Fig. 2.7**), the glycerol conversion increased with increasing the catalyst loading only up to 5 wt.%. The higher amount of catalyst loading did not increase the glycerol conversion, suggesting that the reaction was controlled by the mass transfer of the reactant from one phase to the other (i.e., the mass transfer of acetone to the glycerol phase). However, when the reaction proceeded and conversion is >50%, the glycerol conversion continuously increased with increasing catalyst loading because the interfacial mass transfer limitation was minimized (i.e., the initial two-phase system became homogenous (a single-phase) and the reaction became kinetically-controlled. These findings supported the existence of interfacial mass transfer limitations. Moreover, these results are consistent with the phase change behavior over the course of the reaction time (**Fig. 2.6**), affecting the apparent reaction rates.

Previous investigators have proposed the use of solvent (methanol, ethanol, and/or dichloromethane) to improve miscibility of glycerol and acetone, overcoming the mass transfer limitation of the glycerol acetalization [111, 112]. Glycerol conversion reached 73% at 40°C because the reaction rate was increased by both reactants being in the same phase [112]. However, the use of solvents to enhance the miscibility of glycerol and acetone complicates downstream processing because of additional unit operations for product separation/purification. Our hydrophobically modified zeolite catalysts had higher catalytic activity for glycerol acetalization than that of HY catalysts at low temperature because OTS-HY catalysts possessed two key advantages. First, the grafted hydrophobic layers of OTS-HY catalysts form emulsion between two immiscible reactants, minimizing the mass transfer limitation by improving contacts between the two immiscible reactants without added solvents. Second, the OTS-HY catalysts still had the comparable acid site density to that of HY, enabling the glycerol acetalization at the interface of two immiscible reactants. The high catalytic activity of OTS-HY at low temperatures makes it a promising candidate for glycerol acetalization and other acid-catalyzed two-phase reactions. The alkyl chain length of the organosilane surfactant affects the degree of hydrophobicity of the catalysts. We are currently correlating the degree of hydrophobicity of the modified catalyst with its catalytic activity in glycerol acetalization.

#### **4. Conclusion**

Acetalization of glycerol with acetone is an acid-catalyzed reaction. The poor miscibility between glycerol and acetone results in an initial two-phase mixture and presents a considerable interfacial mass transfer limitation between liquid phases and catalyst's active sites. Initially, the poor miscibility of acetone in glycerol phase caused a slow supply of acetone for the formation of solketal. When the solketal content exceeded 25%, it acted as a solubilizing agent and the reaction mixture became homogeneous, followed by a rapid production of solketal. We proposed to overcome this initial interfacial mass transfer limitation by grafting the n-octadecyltrichlorosilane (OTS) onto an HY catalyst. The modified HY catalyst was hydrophobic and assisted the emulsion formation during agitation. The emulsion formation improved the contact between the ordinarily

immiscible reactants and active sites of the OTS-HY catalyst, yielding 89% glycerol conversion, compared with 28% for unmodified HY, at 30°C. In addition, we revealed that the formation of reaction product, solketal, beyond 25% acted as a solvent to solubilize glycerol and acetone into a single phase. Hydrophobic zeolites of this type are promising for other acid-catalyzed reactions to upgrade by-product glycerol from biodiesel industry, such as esterification, dehydration to acrolein, and etherification with alcohols to produce fuel additives.

### **Acknowledgment**

A part of this material is based upon work supported by the National Science Foundation under Cooperative Agreement No. 1355438. This work was performed in part at the Conn Center for Renewable Energy Research at the University of Louisville, which belongs to the National Science Foundation NNCI KY Manufacturing and Nano Integration Node, supported by ECCS-1542174. The authors would like to thank Dr. Howard Fried for his valuable comments and suggestions on the manuscript.

## **5. Supplementary Information**

### **Characterization of hydrolysis and condensation products of octadecyltrichlorosilane (OTS)**

The formation of the self-condensed OTS product (OTS-OTS) was negligible as evidenced by the FTIR. First, we synthesized the OTS-OTS product by adding a small amount of water (~100  $\mu\text{L}$ ) in the 0.5 mmol OTS in 50 mL toluene and agitated for 24h at room temperature. We observed the condensed OTS-OTS product as white solid precipitates. We collected the solid OTS-OTS product by filtration, wash with ethanol, and dry in the oven at 80°C overnight. Secondly, we analyzed the OTS-OTS product by FTIR and compared its spectra with the OTS-HY catalyst. We used the HY catalyst as a control. We found that the OTS-OTS product had similar characteristic bands at 2851 and 2919  $\text{cm}^{-1}$  to those of the OTS-HY catalyst (**Fig. 2.S1A**). These bands were associated with the CH symmetric ( $\nu_s(\text{CH})$ ) and asymmetric ( $\nu_a(\text{CH})$ ) stretching vibrations for  $\text{CH}_2$  groups of the

OTS, respectively. However, we did not observe these two bands on the HY catalysts. The presence of these two bands suggested the presence of OTS in the OTS-HY catalyst and OTS-OTS sample. Hence, we further analyzed the FTIR fingerprint region.

Changes in the characteristic bands of OTS are pronounced in the range of 900 to 1200  $\text{cm}^{-1}$  due to the silane grafting extension [113]. The OTS has a unique Si-Cl band at  $\sim 425\text{-}625 \text{ cm}^{-1}$ . In the presence of water, OTS underwent hydrolysis. The hydrolysis products of OTS can condense with each other. From the FTIR analysis, we confirmed that OTS underwent hydrolysis in the presence of moisture because of the occurrence of Si-OH band at  $\sim 950 \text{ cm}^{-1}$  from the hydrolysis product. Moreover, we observed the band at  $1014 \text{ cm}^{-1}$ , associated with Si-O-Si stretching from the self-condensation reaction between OTS hydrolysis products (**Fig. 2.S1B**). However, the unique Si-O-Si band of the self-condensed OTS products at  $1014 \text{ cm}^{-1}$  was not observed in the both OTS-HY and HY samples, suggesting negligible formation of self-condensed OTS products. Consistent with previous findings, the HY catalyst showed the asymmetric stretching T-O-T band at  $\sim 1056 \text{ cm}^{-1}$  (T is tetrahedrally coordinated Si or Al atom) [98, 114, 115]. Upon grafting HY with OTS, the T-O-T band shifted to  $1050 \text{ cm}^{-1}$  because of the formation of the Si-O bond on the tetrahedral T-O-T. A similar down-shift of the zeolite's characteristic T-O-T band was observed in silane grafted SAPO-34 zeolites, suggesting the formation of linkages between silane and zeolites [87].

Additional evidence to support this claim is the high catalytic activity of OTS-HY catalysts. The formation of condensed OTS products in the pores of HY zeolites should have blocked reactant accessibility. Instead, we observed an increase in the catalytic activity using OTS-HY catalysts over HY catalysts. In addition, previous studies indicate that the pore size of the HY zeolites is  $\sim 0.74 \times 0.74 \text{ nm}$  [116]. The size of OTS is larger than the HY pore dimensions [117]. Hence, OTS was grafted on the external surface, leaving the internal surface accessible to reactants.

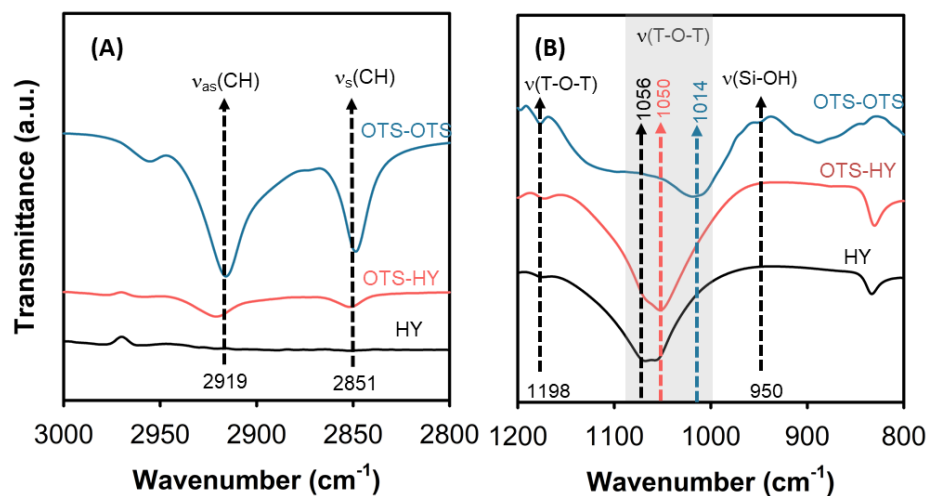


**Figure 2.S1.** FTIR spectra of HY, OTS-HY, and OTS-OTS samples: (A) 3000-2800  $\text{cm}^{-1}$ ; and (B) 1200-800  $\text{cm}^{-1}$ . The OTS-OTS sample indicated the condensed product of OTS.

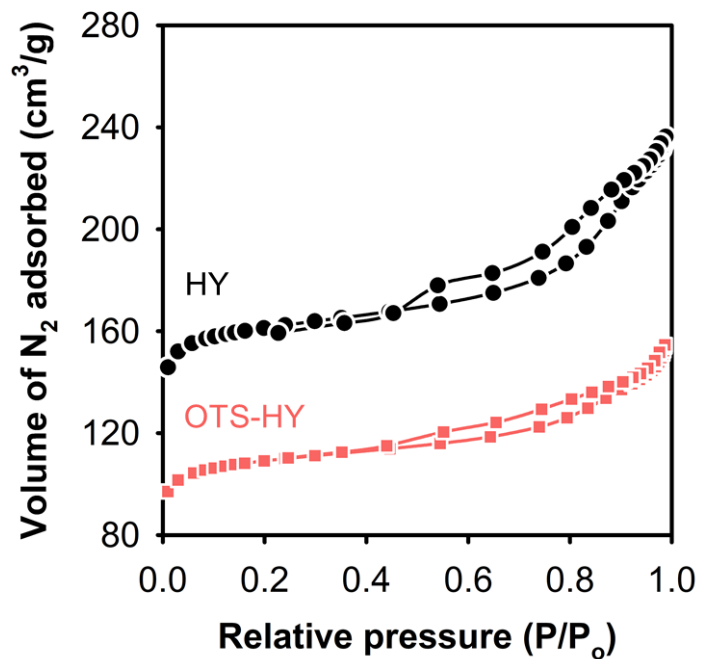


**Figure 2.S2.**  $\text{N}_2$ -adsorption/desorption isotherms of HY and OTS-HY.



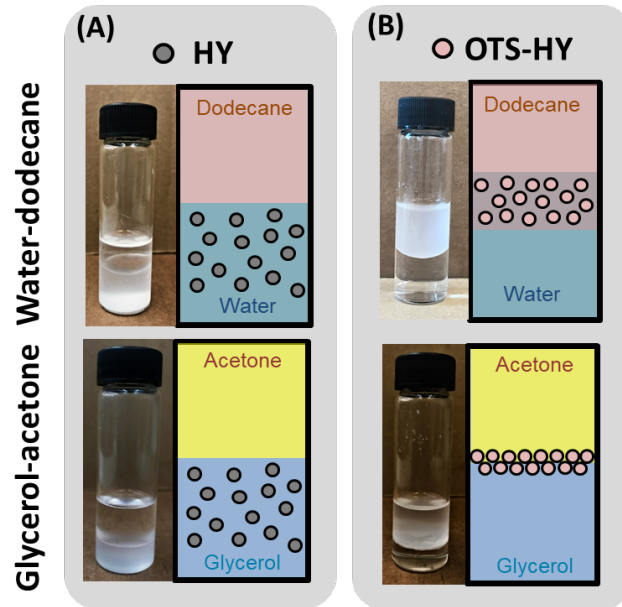


**Figure 2.S3.** Suspension behavior of (A) HY or (B) OTS-HY in water-dodecane and glycerol-acetone.

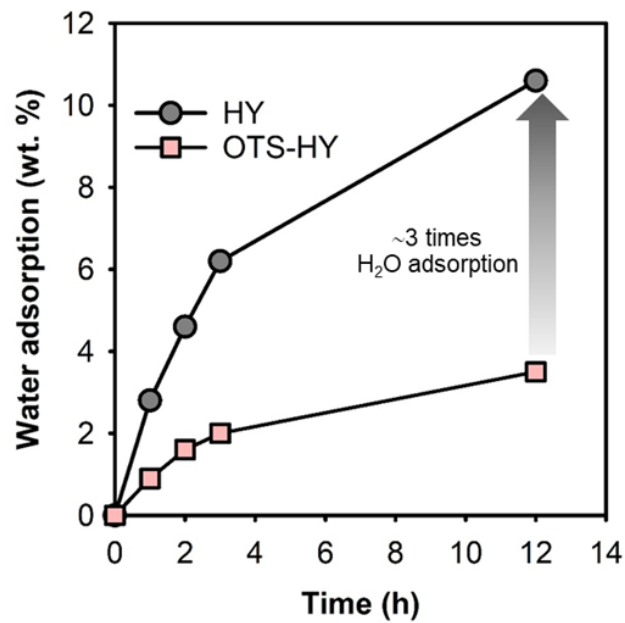


**Figure 2.S4.** Water adsorption of HY and OTS-HY. OTS has a higher degree of hydrophobicity

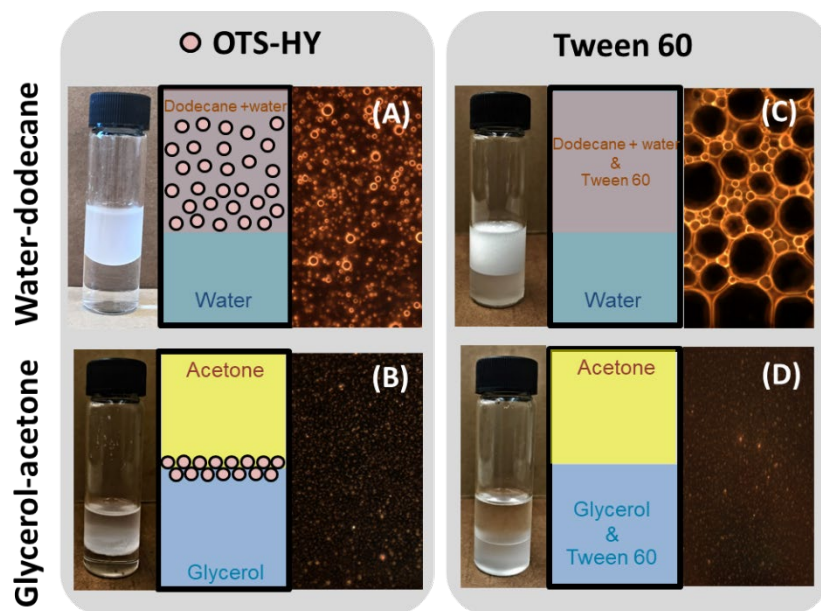


**Figure 2.S5.** Behaviour of emulsion formation in water-dodecane and glycerol-acetone in the presence of OTS-HY or tween 60 (A) OTS-HY in dodecane-water (B) OTS-HY in acetone-glycerol (C) Tween 60 in dodecane-water and (D) Tween 60 in acetone-glycerol.

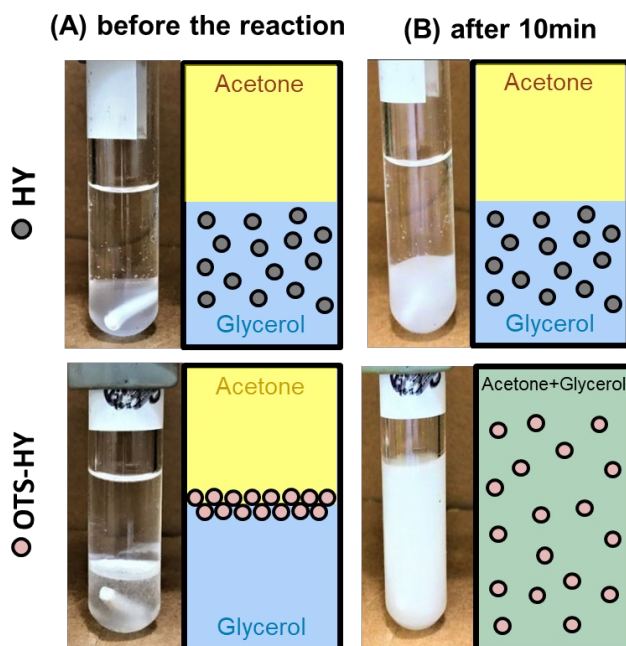


**Figure 2.S6.** Suspension behavior of OTS-HY and HY in the glycerol/acetone mixture at 30°C

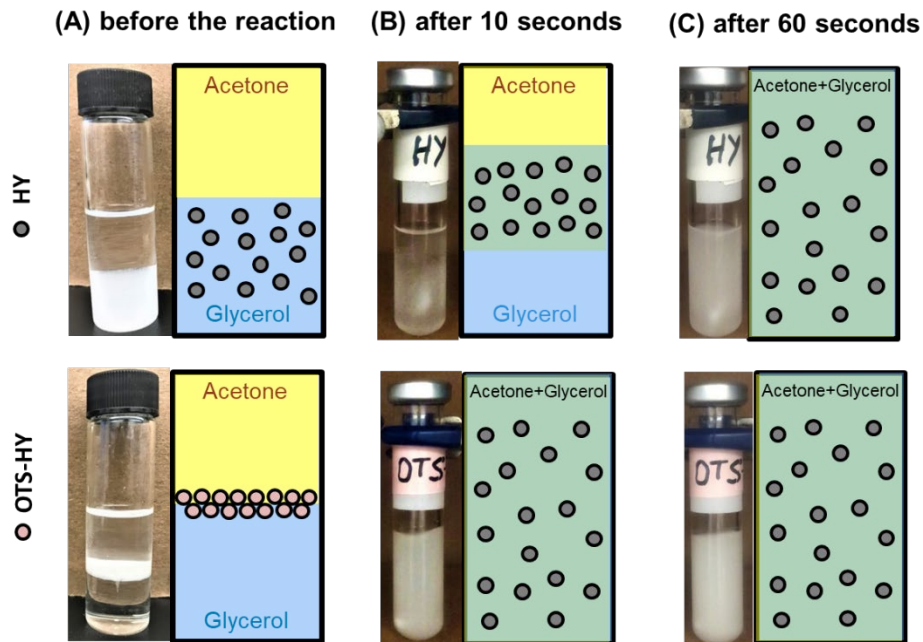


**Figure 2.S7.** Suspension behavior of OTS-HY and HY in the glycerol/acetone mixture at 50°C

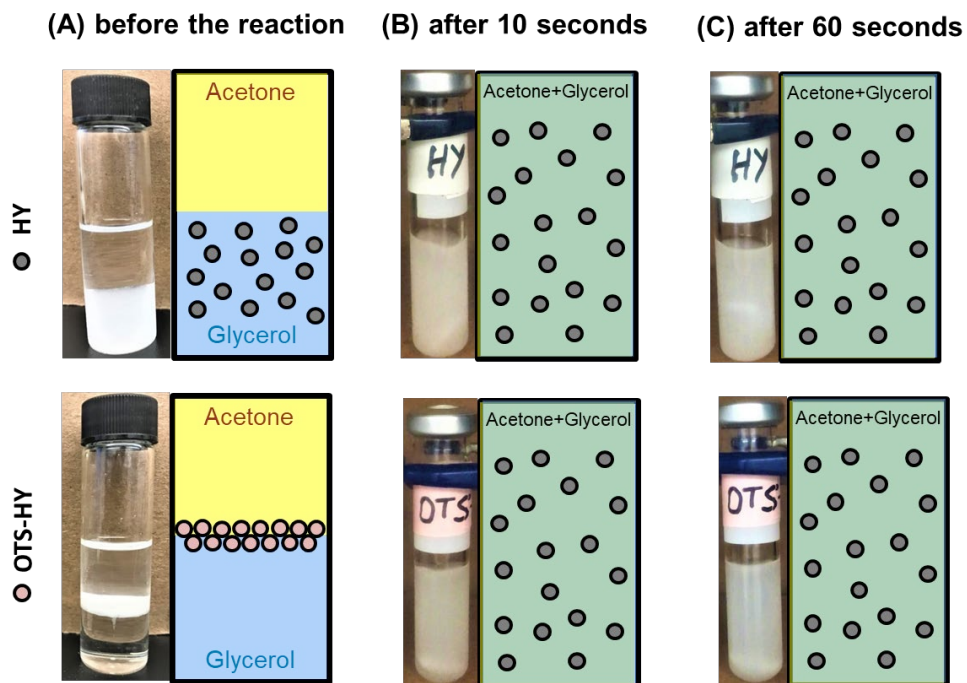


**Figure 2.S8.** Suspension behavior of OTS-HY and HY in the glycerol/acetone mixture at 70°C

CHAPTER 3  
COOPERATIVE BRØNSTED-LEWIS ACID SITES CREATED BY PHOSPHOTUNGSTIC ACID  
ENCAPSULATED METAL-ORGANIC FRAMEWORKS FOR SELECTIVE GLUCOSE  
CONVERSION TO 5-HYDROXYMETHYLFURFURAL<sup>2</sup>

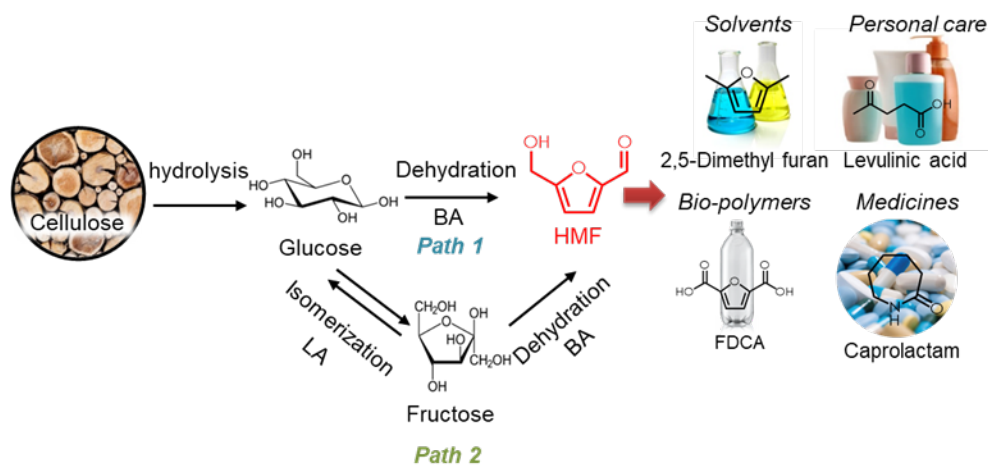
### 1. Introduction

Negative consequences of fuel and chemical production from petroleum, especially sizeable greenhouse gas emissions, price volatility [118], and non-renewability [119], have propelled the production of commodity chemicals from renewable plant biomass. Hydroxymethylfurfural (HMF) is a versatile platform chemical derived from biomass with potential applications for fuels, chemicals, plastics, and pharmaceuticals [120-122]. The challenge of glucose dehydration to HMF is to obtain high HMF selectivity. Although the glucose dehydration reaction has been studied extensively, its mechanism is still being debated [123, 124].

In general, glucose dehydration to HMF can occur by two chemical pathways (**Scheme 1**), direct dehydration (path 1) and tandem isomerization-dehydration reactions (path 2). The direct dehydration of glucose to HMF by Brønsted acid catalysts is slow, and HMF selectivity is low because of side reactions such as cross-condensation with formation of undesired humins [42, 125-127]. Tandem isomerization-dehydration reactions in one-pot afford opportunities to transform glucose to HMF selectively [128]. Selective production of HMF from glucose requires cooperation between Lewis and Brønsted acid catalysts for glucose isomerization to fructose and subsequent fructose dehydration to HMF [42-44, 128].

---

<sup>2</sup> This chapter has been published in *Fuel* (Rahaman, Mohammad Shahinur, et al. *Fuel* 310 (2022): 122459). The copyright clearance from the publisher has been included in the "APPENDIX" section.



**Scheme 1.** Reaction network of HMF production (BA = Brønsted acid, LA = Lewis acid)

Lewis acid promotes the isomerization of glucose to fructose and then dehydration of fructose to HMF by Brønsted acid [129-131]. Swift et al. demonstrated this concept of tandem isomerization-dehydration reactions by incorporating a Lewis acid ( $\text{CrCl}_3$ ) with a Brønsted acid (HCl) catalyst, an approach that enhanced both catalytic activity for glucose dehydration and HMF selectivity [132]. Vieira et al. used the combination of Lewis acid  $\text{Nb}_2\text{O}_5$  and Brønsted acid HCl in a water/tetrahydrofuran (THF) biphasic system. They found that the Brønsted acid HCl was necessary to improve HMF selectivity from 7.6% to 51% and glucose conversion from 49% to 93%, compared with  $\text{Nb}_2\text{O}_5$  alone [131]. Nikolla et al. used the combination of Sn-containing  $\beta$ -zeolite and HCl in  $\text{H}_2\text{O}/\text{THF}$  biphasic system to reach 72% HMF selectivity at 79% glucose conversion [133]. However, all these studies were conducted with homogeneous Brønsted acid catalysts that complicate product purification [134] and catalyst recycling. Therefore, it would be most useful to have solid catalysts that possess both Brønsted and Lewis acid active sites for selective glucose conversion to HMF. In answer to this need, this report describes metal-organic frameworks that have both Brønsted and Lewis acid sites for selective glucose conversion to HMF.

Metal-organic frameworks (MOFs) are porous crystalline materials that consist of metal ions or clusters coordinated with organic linkers to form highly uniform solid networks [23, 24, 135-138]. The coordinated unsaturated metal sites (cus) endow MOFs with Lewis acidity [139, 140]. Lewis

acid sites of MOFs have been used to catalyze various reactions, such as aldol condensation [141], deacetalization-Knoevenagel condensation [142, 143], Meinwald rearrangement [144], and CO oxidation [145]. The porosity of MOFs enables incorporation of large Brønsted acidic molecules to create bifunctional acid catalysts for various acid-catalyzed organic reactions [23, 24, 146-149].

Polyoxometalates (POMs) are versatile catalysts because of their many active sites [150, 151]. The Keggin family of POMs ( $[XM_{12}O_{40}]^{n-}$  anions (X = Si and P, M = Mo and W) with protons as the only counterions are heteropolyacids; examples include phosphotungstic acid, silicotungstic acid, silicomolybdic acid, and phosphomolybdic acid. These heteropolyacids have high acid strength and they are less corrosive compared with ordinary mineral acids (HBr, H<sub>2</sub>SO<sub>4</sub>, HNO<sub>3</sub>, and HCl) [152, 153]. Although these properties make heteropolyacids attractive in acid-catalyzed reactions [154-158], they are soluble in water and many organic solvents. Thus, they are difficult to recycle, and their presence complicates purification of soluble products.

Trapping heteropolyacids in MOF pores generates bifunctional catalysts with both Lewis and Brønsted acids, which are important for selective glucose conversion to HMF [128, 159]. Indeed, as reported in **Table 3.S2**, the Keggin-type heteropolyacids have been encapsulated successfully in the pores of MOFs [160-163]. For example, phosphotungstic acid (PTA)-encapsulated MIL-101(Cr) was used for various catalytic reactions such as the esterification of *n*-butanol with acetic acid [164], dehydration of methanol [164], oxidative desulfurization of dibenzothiophene [165], carbohydrate dehydration to 5-hydroxymethylfurfural [163], and oxidation of the alkenes [166]. Zhang et al. synthesized PTA<sub>c</sub>MIL-101(Cr) by encapsulating PTA in MIL-101(Cr) for sugar dehydration [163]. Fructose dehydration by PTA<sub>c</sub>MIL-101(Cr) was selective for HMF (77% HMF selectivity at 82% fructose conversion). However, PTA<sub>c</sub>MIL-101(Cr) was not selective for HMF in glucose dehydration (10% HMF selectivity at 21% glucose conversion). Moreover, the use of fructose as a feedstock is not cost-effective because glucose is less expensive than fructose [167]. In addition, the chromium in PTA<sub>c</sub>MIL-101(Cr) catalysts is harmful to humans, animals, and the environment [168]. Therefore, there is a need to develop heterogeneous chromium-free acid

catalytic systems that possess both Brønsted and Lewis acid sites to regulate the HMF selectivity in glucose dehydration.

Here, this work describes encapsulation of phosphotungstic acid in the pores of MIL-101(Al)-NH<sub>2</sub> to form PTA-MIL-101(Al)-NH<sub>2</sub>. The effect of PTA encapsulation on catalytic performance in glucose dehydration with [C<sub>4</sub>C<sub>1</sub>im]Cl as solvent was evaluated. The [C<sub>4</sub>C<sub>1</sub>im]Cl was selected as the reaction solvent because our previous studies established that the alkyl imidazolium chloride ionic liquids, such as [C<sub>2</sub>C<sub>1</sub>im]Cl and [C<sub>4</sub>C<sub>1</sub>im]Cl, can dissolve cellulose and enable hydrolysis of cellulose to sugars [169-171]. The MIL-101(Al)-NH<sub>2</sub> was selected because it is chemically and thermally stable [143]. Moreover, Brønsted acidic PTA was used as the heteropolyacid because it has a high acid strength compared with other heteropolyacids [172]. The encapsulated PTA in MIL-101(Al)-NH<sub>2</sub> was uniformly dispersed and stable in NH<sub>2</sub>-MIL-101(Al) pores, and it provided Brønsted acid sites that rendered the catalyst selective for HMF production. These results reveal the unrecognized catalytic performance of the PTA-MIL-101(Al)-NH<sub>2</sub> catalysts for selective glucose dehydration.

## 2. Materials and Methods

### 2.1 Materials

The following chemicals were purchased and used as received: D-glucose, 1-butyl-3-methylimidazolium chloride ([C<sub>4</sub>C<sub>1</sub>im]Cl), 2-aminoterephthalic acid (2-ATA), aluminum chloride hexahydrate, phosphotungstic acid (PTA), and *N,N*-dimethylformamide (DMF), methanol, ethanol, *n*-propanol, 2-propanol, *n*-butanol, 2-butanol, *p*-dioxane, ethyl acetate (EA), *N,N*-dimethylformamide (DMF), *N,N*-dimethylacetamide (DMA), dimethyl sulfoxide (DMSO), and tetrahydrofuran (THF). **Table 3.S1** summarizes the list of chemicals/reagents, their supplier, purity, and CAS number. All other chemicals, solvents, and gases were of the highest purity available from commercial sources.

## **2.2 Synthesis of metal-organic frameworks**

### **2.2.1 Synthesis of MIL-101(Al)-NH<sub>2</sub>**

MIL-101(Al)-NH<sub>2</sub> was synthesized by the solvothermal method with a slight modification [173]. Typically, a mixture of aluminum chloride hexahydrate (0.51 g, 2 mmol) and 2-aminoterephthalic acid (0.56 g, 3 mmol) in DMF (30 mL) was kept in a Teflon-lined autoclave reactor without stirring at 130 °C for 72 h. Then the reactor was cooled to ambient temperature, and the solids were separated from the solution by centrifugation (6000 RPM, 5 min). The solids were washed with DMF under sonication for 10 min. Finally, the solid catalysts were washed three times with methanol at room temperature followed by washing with hot (70 °C) methanol for 5 h and dried overnight under vacuum at 80 °C.

### **2.2.2 Synthesis of encapsulated PTA in MIL-101(Al)-NH<sub>2</sub> (PTA@MIL-101(Al)-NH<sub>2</sub>)**

PTA@MIL-101(Al)-NH<sub>2</sub> was synthesized by incorporating phosphotungstic acid (PTA) hydrated during the synthesis of MIL-101(Al)-NH<sub>2</sub>. In short, aluminum chloride hexahydrate (0.51 g, 2.1 mmol), 2-amino terephthalic acid (0.56 g, 3.1 mmol), and different amounts of PTA hydrate (0.1-2.0 g) in DMF (30 mL,  $\rho = \sim 0.9$  g/mL) were kept in a Teflon-lined autoclave reactor without stirring, and the mixture was heated at 130 °C for 72 h. After cooling to ambient temperature, the resulting solids were separated by centrifugation (6000 RPM, 5 min), washed with DMF, then washed with hot methanol (70°C), and finally washed with acetone, and dried under vacuum at 80 °C overnight.

## **2.3 Catalyst characterization**

### **2.3.1 Transmission electron microscopy and energy-dispersive X-ray spectroscopy analysis**

The microstructure and elemental distribution of the metal-organic frameworks (MOFs) were analyzed using transmission electron microscopy (TEM) in a Tecnai F20 (FEI company, OR, USA) microscope operating at 200 kV. TEM specimens were prepared by dispersing small amounts of catalysts onto Cu grid-supported holey carbon films. For the analysis of the microstructure, scanning transmission electron microscopy (STEM) images were acquired with a high annular angle dark field (HAADF) detector (E.A. Fischione Instruments, Inc., PA, USA) and an electron



probe of a 1 nm diameter. For the elemental distribution analysis, energy-dispersive X-ray spectroscopy (EDS) maps were collected using a TEAM EDS (EDAX, Inc., NJ, USA) spectrometer.

### **2.3.2 N<sub>2</sub> adsorption-desorption**

The N<sub>2</sub> adsorption-desorption assay was conducted with a Micromeritics Tristar (Norcross, GA, USA) instrument. The function of TriStar was verified with reference materials (Micromeritics). Prior to the measurement, the samples were pretreated with a Micromeritics FlowPrep with sample degasser (Norcross, GA, USA) at 160 °C for 2 h. The surface area,  $S_{\text{BET}}$ , was determined from N<sub>2</sub> isotherms using the Brunauer–Emmett–Teller equation (BET) at -196.15 °C (77 K) [174, 175]. The BET model assumes multilayer gas adsorption on the adsorbent's surface and obtains the sample surface area value by determining the monolayer volume of adsorbed gas from the isotherm data [176, 177]. BET surface area was calculated at relative pressures between 0.05 and 0.3. The pore volume and size were calculated from the N<sub>2</sub> desorption values based on the Barrett–Joyner–Halenda (BJH) model [178-180]. The BJH model determines the mesopore volume distribution, which accounts for the change in adsorbate layer thickness and the liquid condensed in the pores [181]. The pore volume was calculated as the uptake (cm<sup>3</sup>/g) at a relative pressure of 0.95.

### **2.3.3 Thermogravimetric analysis**

Thermogravimetric analysis (TGA) was performed on an SDT Q600 TA instrument (New Castle, DE, USA). The TGA profiles were used to characterize the thermal stability of MOFs. About 20 mg of sample was placed in a cylindrical alumina crucible and heated in static air from ambient temperature to 700 °C with a nominal heating rate of 10 °C/min. The change in weight of MOF samples was used to determine the moisture content, decomposition of the linkers, and formation of metal oxides.

### **2.3.4 Fourier transform infrared spectroscopy**

Infrared spectra of the synthesized catalysts were recorded on a JASCO Fourier transform infrared (FTIR) spectrometer (Easton, MD, USA), equipped with an attenuated total reflection stage (ATR).

Samples of about 5 mg were used in each analysis. The sample was scanned in the spectral range between 400 and 4000  $\text{cm}^{-1}$  at a 4  $\text{cm}^{-1}$  resolution. Spectra were collected using a deuterated triglycine sulfate (DTGS) detector averaging 256 scans.

### **2.3.5 Diffuse reflectance infrared Fourier transform spectroscopy**

Diffuse reflectance infrared Fourier transform spectroscopy (DRIFTS) with adsorbed pyridine was performed to characterize acid sites; measurements were made with a JASCO FTIR-4700 equipped with high temperature DiffuseIR™ cell (PIKE Technology, WI, USA). The protocol for the DRIFTS experiments with temperature programmed desorption is described elsewhere and used with a slight modification [182, 183]. In short, MOF samples (~5 mg) were placed in a cylindrical alumina crucible and treated in nitrogen gas (50 mL/min) at 150°C for 30 min unless otherwise noted. After the treatment, the DRIFT spectra of MOF catalysts were recorded as the background spectra. The MOF catalysts were then saturated with pyridine vapor in the low of N<sub>2</sub> gas (50 mL/min). The adsorbed pyridine was removed by flushing with N<sub>2</sub> gas (50 mL/min) at 50, 100, or 150°C for 30 min before recording the DRIFT spectra. All spectra were recorded with 256 scans between 4000–400  $\text{cm}^{-1}$  at a 4  $\text{cm}^{-1}$  resolution using a mercury cadmium telluride (MCT) detector cooled with liquid nitrogen. The ratio of Brønsted acid to Lewis acid sites (B/L) was calculated from the integrated area of the bands (after background subtraction) of adsorbed pyridine at 1067 and 1030  $\text{cm}^{-1}$  [184].

### **2.3.6 X-ray diffraction**

X-ray diffraction of MOFs was conducted with a Bruker AXS Model D8 Advance A28 diffractometer (Germany) using CuK<sub>α</sub> radiation in the 2θ range from 5° to 40° with 0.02 degree/step. Samples of about 200 mg were used in each analysis.

### **2.3.7 Inductively coupled plasma-optical emission spectroscopy**

Inductively coupled plasma-optical emission spectroscopy (ICP-OES) measurements were performed using a 100 mg sample dissolved in 10 mL of nitric acid. Heating was used to ensure

that the sample was completely dissolved. Once cooled, the sample was further diluted to 25 mL with double distilled water. Measurements were acquired on a Varian 720-ES spectrometer equipped with a seaspray nebulizer and cyclonic class spray chamber. Parameters included a sample intake of 1 mL/min, argon plasma flow rate of 15 L/min, and an auxiliary gas (Ar) flow rate of 1.5 L/min. The instrument was calibrated using a CRMS manufactured by VHG.

## 2.4 Dehydration of glucose

A 50 mg sample of glucose and 1 g [C<sub>4</sub>C<sub>1</sub>im]Cl were added to a 25 mL pressure tube. The catalyst was loaded with respect to the glucose at a glucose:Al molar ratio of 25:1 unless otherwise noted. The pressure tube was sealed, stirred at 700 RPM (to minimize mass transfer limitations) and kept in an oil bath at 120°C unless otherwise noted. The reaction was stopped by quenching in a cold-water bath, followed by adding water (~5 mL) to dissolve the remaining glucose and prevent the solidification of ionic liquid. The solution was centrifuged and the residual solids were removed. The liquid sample was withdrawn and analyzed for changes in glucose and the occurrence of dehydration products.

## 2.5 Product analysis and quantification

The reactants and products were analyzed by a High-Pressure Liquid Chromatography (HPLC, Agilent Technology, Santa Clara, CA, USA) equipped with a refractive index detector (RID) and diode array detector (DAD). An Aminex HPX-87H column (300 x 7.8 mm, Bio-Rad®, Hercules, CA, USA) was used for reactant and product separation at 60°C with 0.6 mL/min of 4 mM H<sub>2</sub>SO<sub>4</sub> as the mobile phase. The concentrations of sugars and other products were determined by the peak areas from the RID signals. The main HMF product was determined by the peak area from the DAD signals at 280 nm. Sugar and reaction products were calibrated against certified standards (Absolute Standards, Inc., Hamden, CT, USA). The glucose conversion, product yield, and product selectivity were calculated as follows:

$$\text{Glucose conversion (\%)} = \frac{\text{mole of glucose reacted}}{\text{initial mole of glucose}} \times 100$$

$$\text{Product yield (\%)} = \frac{\text{mole of product generated}}{\text{initial mole of glucose}} \times 100$$

$$\text{Product selectivity (\%)} = \frac{\text{Product yield}}{\text{Glucose conversion}} \times 100$$

To ensure that the determination of glucose conversion and HMF selectivity were accurate, control experiments using PTA<sub>c</sub>MIL-101(Al)-NH<sub>2</sub>, ionic liquid, and water were conducted at ambient temperature for 2h. The change in glucose and HMF concentrations in the presence of MOFs was negligible (see *Supplementary Information and Fig. 3.S1* for detail). Moreover, to confirm the formation of HMF, solvent extraction by ethyl acetate was used with the reaction solution. The extracted solution was analyzed by Agilent gas chromatography-mass spectrometry (GC-MS, model 7890A and 5977A, Agilent Technologies, Santa Clara, CA, USA) equipped with a DB-1701 column (Agilent Technologies, 30 m × 0.25 mm id, 0.25 μm) (see *Supplementary Information and Fig. 3.S2* for detail).

### 3. Results

Encapsulating phosphotungstic acid (PTA) in MIL-101(Al)-NH<sub>2</sub> (Al-MOF) formed encapsulated PTA<sub>c</sub>MIL-101(Al)-NH<sub>2</sub> (PTA<sub>c</sub>Al-MOF) catalysts. The effect of PTA loading on MOF physicochemical and acid properties was investigated. Subsequently, the efficiency of PTA<sub>c</sub>Al-MOF catalysis of glucose dehydration was measured by comparing the performance of encapsulated PTA catalysts with different PTA loading.

#### 3.1 Physicochemical properties of the PTA<sub>c</sub>MIL-101(Al)-NH<sub>2</sub> catalyst

To evaluate the physicochemical properties of the encapsulated PTA<sub>c</sub>Al-MOF catalysts, first, an N<sub>2</sub> adsorption-desorption was performed to measure the surface area and pore volume (**Fig. 3.S3A**). The bare Al-MOF exhibited a Type IV isotherm, which suggested that the MIL-101(Al)-NH<sub>2</sub> catalyst was mesoporous. On the basis of the isotherms, the MOF total surface area and pore volume were calculated and shown in **Table 3.1**. As a control, the surface area and pore volume of Al-MOF were 1487 m<sup>2</sup>/g and 0.92 cc/g, similar to reported values [185, 186]. As expected, an

increase in PTA loading decreased both total surface area and pore volume, which indicated that the encapsulated PTA occupied the pores of the Al-MOF. The average pore diameter of the synthesized catalysts was ~2.4-2.7 nm, in agreement with reported values of 1.6-2.9 nm [143, 187]. The critical diameter for D-glucose was ~0.84-0.85 nm [188], which is sufficiently small to enable access to the active sites within the MOF structure.

Next, X-ray diffraction (XRD) was conducted to determine the crystallinity of the encapsulated PTA<sub>c</sub>Al-MOF catalysts (**Fig. 3.S3B**). As a control, the X-ray diffractogram of the PTA exhibited unique peaks at 7.2° and 9.0°, similar to reported values.[189] The consistency between the diffractograms of the encapsulated PTA<sub>c</sub>Al-MOF catalysts and bare Al-MOF suggested that, during synthesis, the PTA<sub>c</sub>Al-MOF catalysts retained the structural integrity of the MIL-101 framework. These PTA peaks were not observed in the encapsulated PTA<sub>c</sub>Al-MOF catalysts, which suggested that PTA was well dispersed in the pores of Al-MOF [189] and/or the PTA clusters in the pentagonal and hexagonal windows of Al-MOF were indeed smaller than 1.6-1.2 nm [189-191]. Interestingly, the PTA<sub>c</sub>Al-MOF catalysts showed slightly broader XRD peaks and a shoulder (~11°). The peak broadening and occurrence of the shoulder was hypothesized to be due to the interaction of the encapsulated PTA clusters with the MIL-101 framework, which resulted in changes in the symmetry of the clusters in the MOF cages. Previous studies using POM-encapsulated MIL-101 MOFs showed similar XRD peak broadening [140, 141, 163, 166, 192, 193]. To measure PTA dispersion in the Al-MOF catalyst's pore structure, the encapsulated 14%PTA<sub>c</sub>Al-MOF catalyst was imaged by STEM-HAADF. As a control, the STEM-HAADF image and elemental mapping of the bare Al-MOF showed that it was highly porous with dispersed Al (**Fig. 3.1A and B**). The STEM-HAADF image and elemental composition mapping of aluminum (Al) and tungsten (W) of the 14%PTA<sub>c</sub>Al-MOF showed a highly porous and uniform distribution of W and Al clusters within the Al-MOF catalyst (**Fig. 3.1C-F**), which confirmed our XRD data which indicated that PTA was highly dispersed in the pores of the Al-MOF catalyst.

To determine the surface functionality of the synthesized catalysts, FTIR was performed on catalysts (**Fig. 3.S4**). The bare Al-MOF showed -NH<sub>2</sub> bands. The FTIR spectra of encapsulated PTA<sub>c</sub>Al-MOF catalysts contained bands from -NH<sub>2</sub> and W=O/W-O-W functionalities, which confirmed the encapsulation of PTA (see *Supplementary Information, Fig. 3.S4*).

**Table 3.1.** Physicochemical properties of MOFs with varying PTA content.

| Entry | PTA loading [g/30mL] <sup>a</sup> | Catalyst <sup>b</sup>                           | Al [wt.%] <sup>c</sup> | W [wt.%] <sup>c</sup> | PTA [wt.%] <sup>c</sup> | B/L <sup>d</sup> | S <sub>BET</sub> [m <sup>2</sup> /g] | Total pore volume [cm <sup>3</sup> /g] | Pore diameter (nm) |
|-------|-----------------------------------|---|------------------------|-----------------------|-------------------------|------------------|--------------------------------------|--|--------------------|
| 1     | 0.00                              | NH <sub>2</sub> -MIL-101(Al)                    | 11.56                  | -                     |                         | 0.37             | 1487                                 | 0.92                                   | 2.49               |
| 2     | 0.10                              | 8%PTA <sub>c</sub> MIL-101(Al)-NH <sub>2</sub>  | 9.33                   | 6.2                   | 8.1                     | 0.53             | 1375                                 | 0.82                                   | 2.39               |
| 3     | 0.25                              | 14%PTA <sub>c</sub> MIL-101(Al)-NH <sub>2</sub> | 9.53                   | 11.03                 | 14.3                    | 0.78             | 1276                                 | 0.78                                   | 2.46               |
| 4     | 0.50                              | 15%PTA <sub>c</sub> MIL-101(Al)-NH <sub>2</sub> | 9.19                   | 11.51                 | 15.0                    | 0.96             | 1061                                 | 0.72                                   | 2.72               |
| 5     | 1.00                              | 17%PTA <sub>c</sub> MIL-101(Al)-NH <sub>2</sub> | 9.64                   | 13.00                 | 16.9                    | 1.04             | 961                                  | 0.59                                   | 2.45               |
| 6     | 2.00                              | 18%PTA <sub>c</sub> MIL-101(Al)-NH <sub>2</sub> | 9.11                   | 13.52                 | 17.5                    | 1.14             | 854                                  | 0.57                                   | 2.69               |

<sup>a</sup>per 30 mL DMF, <sup>b</sup>number before catalyst name indicates the encapsulated PTA measured by ICP-OES, <sup>c</sup>composition measured by ICP-OES, <sup>d</sup>B/L indicates Brønsted acid/Lewis acid site ratio from the area integral by diffuse reflectance infrared Fourier transform spectroscopy (DRIFTS).

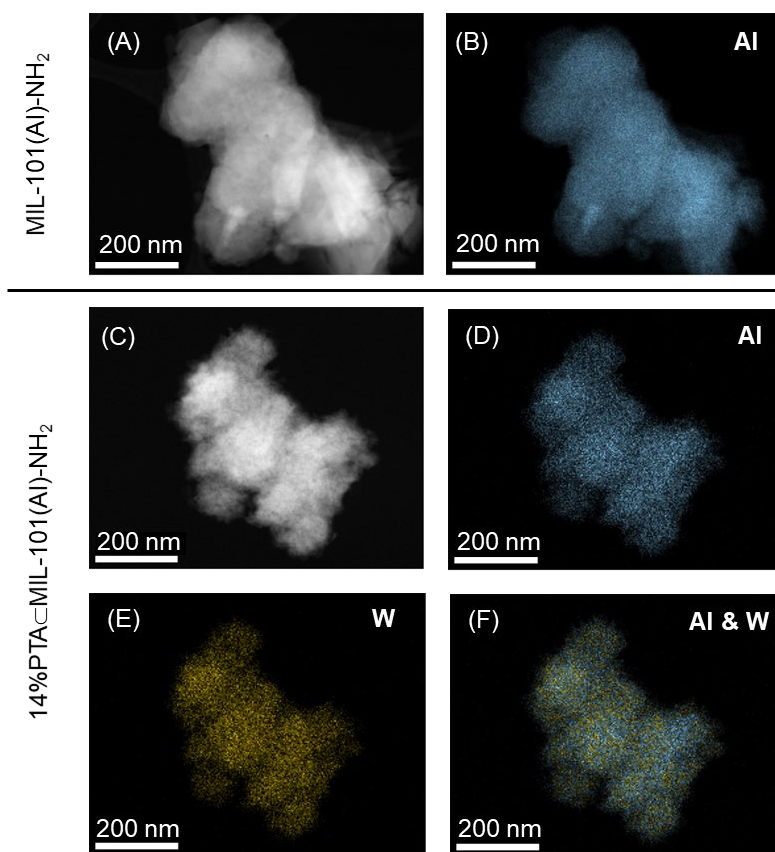


**Figure 3.1.** STEM-HAADF images and corresponding elemental mapping of (A-B) MIL-101(AI)-NH<sub>2</sub> and (C-F) 14%PTA@MIL-101(AI)-NH<sub>2</sub>.

During synthesis, the PTA loading was varied from 0.1 to 2.0 g in 30 mL of DMF. To quantify the actual amount of encapsulated PTA, ICP-OES was conducted on encapsulated PTA@Al-MOF catalysts. As a control, the bare Al-MOF catalyst contained 11.56 wt.% Al, similar to a reported value [141]. All the encapsulated PTA@Al-MOF catalysts had a W/P molar ratio of 12, which was the same as that in PTA (H<sub>3</sub>PW<sub>12</sub>O<sub>40</sub>) and which confirmed successful PTA encapsulation [194]. As expected, increases in PTA loading during synthesis progressively increased the W content and decreased the Al/W molar ratio. Interestingly, a PTA loading greater than 0.25 g/30 mL (entry 3) during synthesis did not result in a significant increase in encapsulated PTA. These results suggested that there was an optimal PTA loading that could occupy the MOF pores.

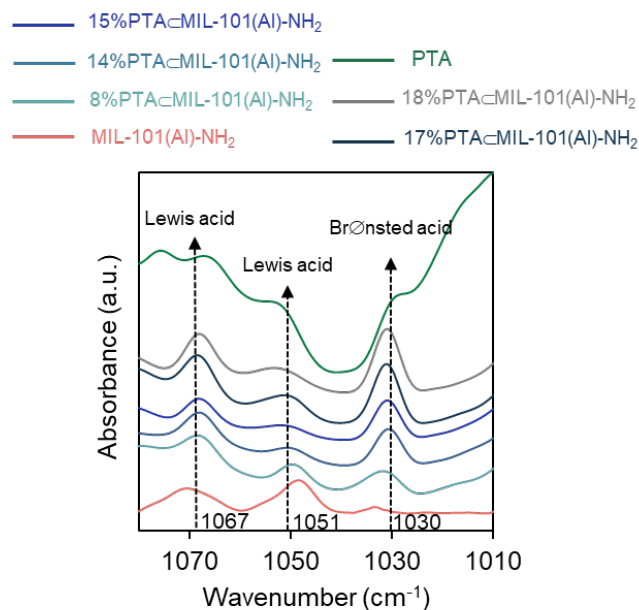


**Figure 3.2.** Acid properties of encapsulated PTA@Al-MOF catalysts measured by diffuse reflectance infrared Fourier transform spectroscopy (DRIFTS).

### 3.2 Acid properties of the catalysts by diffuse reflectance infrared Fourier transform spectroscopy

Selective glucose conversion to HMF requires a cooperative effect between Lewis and Brønsted acid catalysts for the cascade of glucose isomerization to fructose followed by fructose dehydration to HMF. Hence, it is important to distinguish and quantify the acid sites. To characterize the acid sites of the synthesized MOFs, DRIFTS was performed with adsorbed pyridine. Pyridine was chosen as an in-situ titrant for probing the acid site density of MOFs because of previous success in observation of Lewis acid and Brønsted acid sites in MOFs [195-197]. To avoid degradation of bare Al-MOF and encapsulated PTA@Al-MOF catalysts, DRIFTS was performed in a range of 30 - 150°C according to their thermal stability from the TGA result (**Fig. 3.S5**). After pyridine adsorption, the DRIFT spectra of these MOFs demonstrated characteristic bands at 1067, 1051, and 1030  $\text{cm}^{-1}$  (**Fig. 3.2**). The 1067 and 1051  $\text{cm}^{-1}$  bands corresponded to the interaction between pyridine and coordinated unsaturated metal sites (cus), i.e., Lewis acid sites [197, 198]. The band at 1030  $\text{cm}^{-1}$  corresponded to the interaction between pyridine and the Brønsted acid sites from encapsulated



PTA. Surprisingly, a weak band at  $1300\text{ cm}^{-1}$  in the MIL-101(Al)-NH<sub>2</sub> sample was observed, which suggested the presence of Brønsted acidity in MOFs. Similarly, studies by Herbst et al. [199], Halls et al. [25], Vimont et al. [200], and Volkringer et al. [197] showed that MIL-101(Cr), MIL-100(Cr), and MIL-100(Al) exhibited Brønsted acidity. The origin of Brønsted acidity in MOFs remains the topic of debate. However, its origin was hypothesized to come from the water molecules bound to metal sites [197]. Moreover, this water coordinated to the metal sites was not easily removed during activation of MOFs because a high temperature was required to remove the bound water. The high temperature can cause the structural damage to the MOFs and cause a loss in catalytic activity (see *Supplementary Information and Fig. 3.S6* for detail).

Next, the Brønsted acid to Lewis acid ratio (B/L) was determined using the area integral of these bands (**Table 3.1**). An increase in encapsulated PTA loading increased the intensity of the Brønsted acid band at  $1030\text{ cm}^{-1}$  and increased the B/L ratio of the catalysts. It should be noted that an increase in encapsulated PTA within MOFs was not proportional to an increase in B/L ratio. The acidic properties of encapsulated catalysts are difficult to be determined because the interaction between encapsulated species and the host support can modify their acidic properties. Juan-Alcañiz et al. showed the interaction between encapsulated PTA and the MIL-100(Cr) framework decreased Lewis acidity [201], which agrees with our finding of an increase in the B/L ratio after encapsulating more PTA because of an increase in Brønsted acid sites and a decrease in Lewis acid sites.

### **3.3 PTA<sub>enc</sub>MIL-101(Al)-NH<sub>2</sub>-catalyzed glucose dehydration to 5-hydroxymethylfurfural**

To determine the effect of PTA encapsulation on the catalytic performance, glucose dehydration was performed with encapsulated PTA<sub>enc</sub>MIL-101(Al)-NH<sub>2</sub> catalysts (**Fig. 3.3**). A glucose:Al molar ratio of 25:1 was used in all experiments to normalize the Al content in the catalysts and compare catalytic performance with different encapsulated PTA loadings. As a control, a blank (no added catalyst) did not show any HMF production, which suggested that (1) the reaction is not autocatalytic, and (2) [C<sub>2</sub>C<sub>1</sub>im]Cl could not catalyze glucose dehydration. All catalysts were active

for glucose dehydration in  $[\text{C}_2\text{C}_1\text{im}]\text{Cl}$  at  $120^\circ\text{C}$  (**Fig. 3.3A**). Another control of using PTA as a catalyst showed a low HMF selectivity of 13% at 43% glucose conversion. Fructose, levulinic acid, or formic acid were not observed as products. These results suggested the PTA catalyst was not selective to HMF as in previous studies [163]. The bare Al-MOF catalyst appeared to be an efficient catalyst for glucose dehydration; however, it was not the most selective for HMF. All encapsulated PTA $\subset$ Al-MOF catalysts were more selective for HMF than MIL-101(Al)-NH<sub>2</sub>, which indicated that the encapsulated PTA in the pores of the Al-MOF enhanced HMF selectivity (**Fig. 3.S7**). Moreover, HMF selectivity exhibited a volcano-shaped profile vs. the Brønsted to Lewis acid site ratio (B/L) (**Fig. 3.4**). The optimal B/L of 0.78 (14%PTA $\subset$ Al-MOF catalyst) maximized the HMF selectivity of 58% at 44% glucose conversion at  $120^\circ\text{C}$  after 2h (**Fig. 3.3B**). These results suggested that cooperativity between Brønsted acidic PTA and Lewis acid sites of Al-MOF catalyst enhanced HMF selectivity.

To determine the importance of encapsulating PTA, a glucose dehydration reaction was performed with a physical mix of PTA and bare Al-MOF catalyst at the same composition as 14%PTA $\subset$ Al-MOF catalyst. HMF selectivity by the physical mix catalyst was 33%, lower than that of encapsulated 14%PTA $\subset$ Al-MOF catalysts (58%). These results confirmed the importance of PTA encapsulation in maximizing HMF selectivity. Interestingly, the HMF selectivity of the physically mixed catalyst converged to that of PTA alone (**Fig. 3.3B**). Although the Brønsted acid such as PTA catalyzes fructose dehydration to HMF, the free PTA molecules in the physical mix can catalyze aldol addition and condensation reactions from HMF via 2,5-dioxo-6-hydroxyhexanal [202], which resulted in humin formation. Moreover, the free PTA in the physical mix has a strong interaction with the surface of MOF, partially blocking the channels of MOFs and inhibiting the reactant accessibility to active sites [203, 204]. This blocking effect is the reason why the HMF selectivity of the physical mix was lower than that of encapsulated PTA in MOFs [189]. Thus, the physical mix showed a high glucose conversion with a poor HMF selectivity, in agreement with the study by Zhang et al. [163].

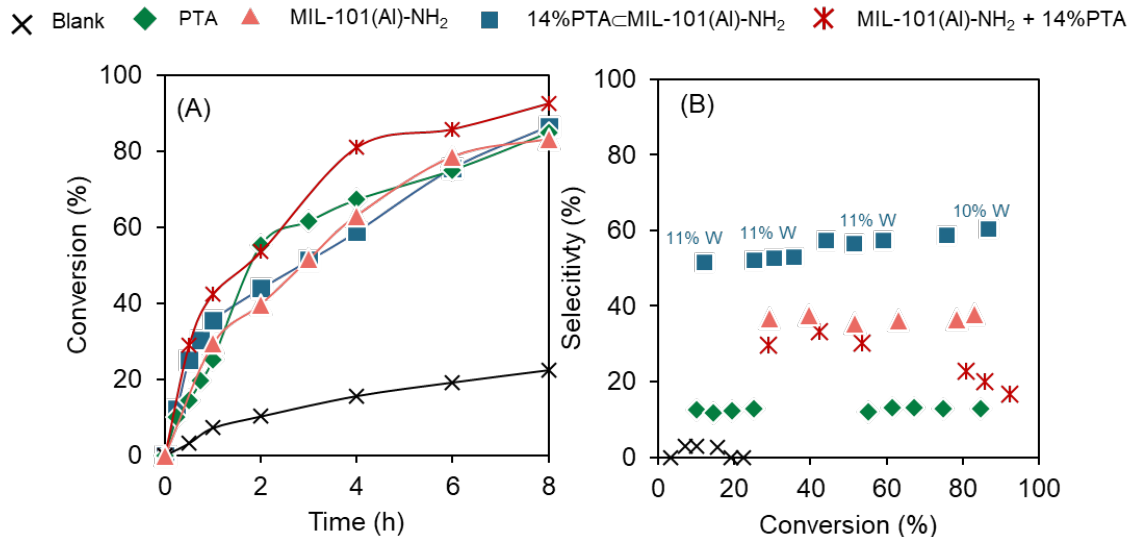


**Figure 3.3.** Catalytic performance of encapsulated PTA-MIL-101(AI)-NH<sub>2</sub> catalysts. (A) Catalyst activity for glucose dehydration as a function of time. (B) HMF selectivity with the W content of the spent catalysts assessed by ICP-OES. Reaction condition: glucose:Al molar ratio=25:1, 50 mg glucose, 1 g [C<sub>4</sub>C<sub>1</sub>im]Cl, 120°C. Phosphotungstic acid = 14 wt.% in PTA alone and physical mix between PTA + bare Al-MOF to match the PTA in 14%PTA-MIL-101(AI)-NH<sub>2</sub>. The percent of tungsten (%W) in **Figure 3.3B** indicates the W content in the used catalyst at the specific conversion.

To evaluate the stability of PTA in encapsulated PTA-MIL-101(AI)-NH<sub>2</sub> catalysts during the reaction, ICP-OES was performed on spent encapsulated 14%PTA-MIL-101(AI)-NH<sub>2</sub> catalyst (**Fig. 3.3B**). The W content of the encapsulated 14%PTA-MIL-101(AI)-NH<sub>2</sub> catalyst remained relatively constant (~11 wt.% W), which confirmed the stability of the PTA within the 14%PTA-MIL-101(AI)-NH<sub>2</sub> catalyst.

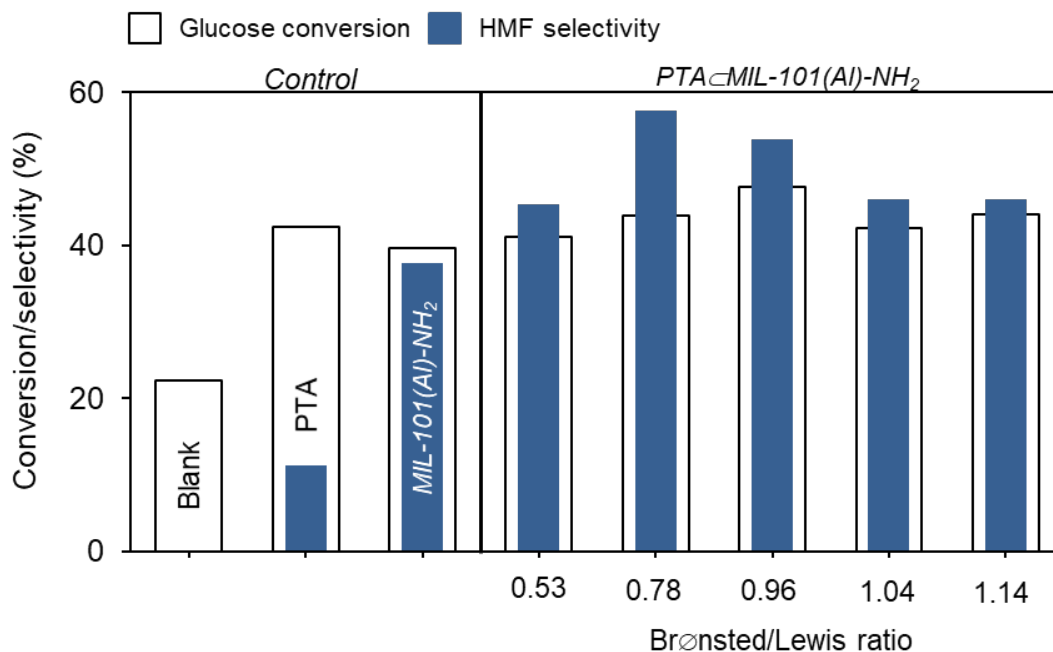


**Figure 3.4.** HMF selectivity of encapsulated PTA-MIL-101(AI)-NH<sub>2</sub> catalysts at similar glucose conversions. Reaction condition: glucose:Al molar ratio=25:1, 50 mg glucose, 1 g [C<sub>4</sub>C<sub>1</sub>im]Cl, 120°C, 2h.

### 3.4 Solvent effect on the glucose dehydration to 5-hydroxymethylfurfural

The solvent affects the rate of reaction, product selectivity, and product stability [205, 206]. A major consideration in catalytic biomass conversion is the stability of reactants, intermediates, and product in the reaction solvent. To investigate the effect of solvent on the stability of these molecules, glucose, fructose and HMF were used as reactants in various solvents. The 14%PTA-Al-MOF was chosen as catalyst because it had the greatest HMF selectivity. For glucose, [C<sub>4</sub>C<sub>1</sub>im]Cl was the best performing solvent as shown by the greatest HMF selectivity at similar conversion to other solvents (**Fig. 3.5**). However, there was no obvious correlation between the HMF selectivity and solvent properties, such as dielectric constant or donor number.

Next, fructose was used as a reactant in [C<sub>4</sub>C<sub>1</sub>im]Cl (**Fig. 3.6**). Three solvents, DMA, 2-butanol, and *p*-dioxane, were selected for comparison with [C<sub>4</sub>C<sub>1</sub>im]Cl. Without added catalyst (blank), HMF selectivity was 47% at 96% fructose conversion in [C<sub>4</sub>C<sub>1</sub>im]Cl. The other solvents did not yield HMF

and showed <20% fructose conversion. As expected, added 14%PTA<sub>⊂</sub>MIL-101(AI)-NH<sub>2</sub> catalyst improved the HMF selectivity in all solvents; more specifically, HMF selectivity in [C<sub>4</sub>C<sub>1</sub>im]Cl was 89% at 94% fructose conversion, two times greater HMF selectivity compared with a reaction without added catalyst. Although added 14%PTA<sub>⊂</sub>MIL-101(AI)-NH<sub>2</sub> catalyst improved the fructose conversion in DMA, 2-butanol, and *p*-dioxane from <20% to >60%, the HMF selectivity in these three solvents was low (<22%). These results suggested that [C<sub>4</sub>C<sub>1</sub>im]Cl can act as both acid catalyst [207, 208] and solvent in fructose dehydration reaction. Moreover, the 14%PTA<sub>⊂</sub>MIL-101(AI)-NH<sub>2</sub> enhanced HMF selectivity from fructose dehydration.

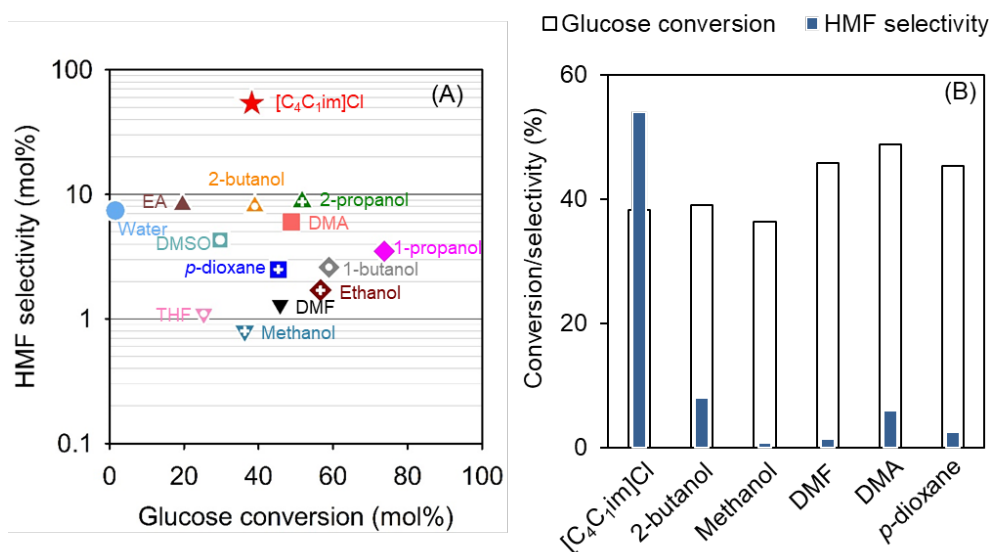


**Figure 3.5.** Solvent effect on glucose conversion and HMF selectivity (A) and comparison of conversion and selectivity in selected solvents(B) by using 14%PTA<sub>⊂</sub>MIL-101(AI)-NH<sub>2</sub> catalyst. Reaction condition: glucose:Al molar ratio=25:1, 50 mg glucose, 1 g solvent, 120°C, 2 h.

Next, HMF was used as a reactant in these four solvents to investigate the HMF stability (Fig. 3.7). Without any catalyst(blank), HMF conversion was 11% in [C<sub>4</sub>C<sub>1</sub>im]Cl, and conversion increased slightly in other solvents. There were no identifiable products which suggests the HMF was likely degraded into humin [209, 210]. The added 14%PTA<sub>⊂</sub>MIL-101(AI)-NH<sub>2</sub> catalyst enhanced HMF conversion to 15% in [C<sub>4</sub>C<sub>1</sub>im]Cl. The presence of 14%PTA<sub>⊂</sub>MIL-101(AI)-NH<sub>2</sub> catalyst in other

solvents improved the HMF conversion more than in  $[C_4C_{1im}]Cl$ . These results suggested that (1) HMF was not stable in these solvents and (2) although the 14%PTA $\subset$ MIL-101(Al)-NH<sub>2</sub> catalyst improved glucose/fructose dehydration to HMF, the catalyst facilitated HMF conversion to humin. Thus, to minimize HMF degradation and maintain the high HMF yield, a reactive HMF extraction process should be considered [211].

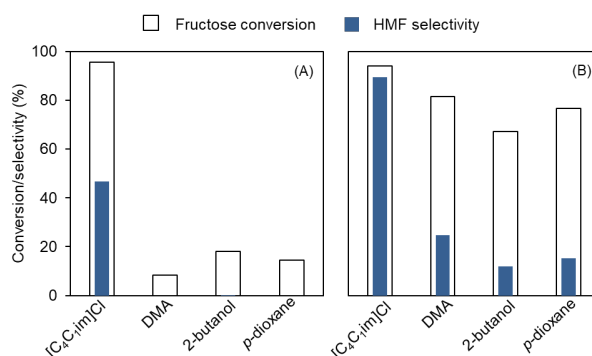


**Figure 3.6.** Solvent effect on fructose conversion to HMF (A) without added catalyst and (B) catalytic performance of encapsulated 14%PTA $\subset$ MIL-101(Al)-NH<sub>2</sub>. Reaction condition: fructose:Al molar ratio = 25:1, 50 mg fructose, 1 g solvent, 120°C, 2h.

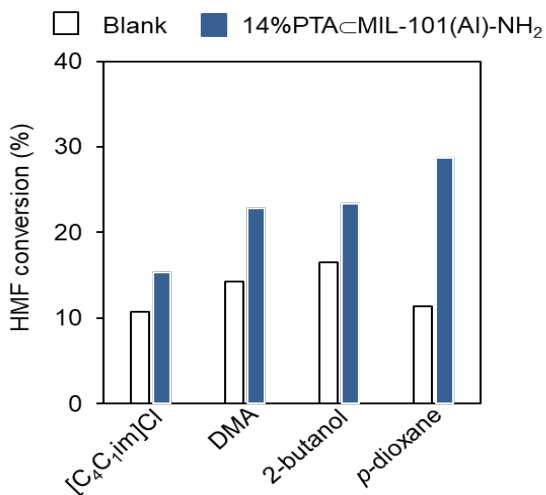


**Figure 3.7.** HMF conversion in different solvents with/without 14%PTA $\subset$ MIL-101(Al)-NH<sub>2</sub>. Reaction condition: HMF:Al molar ratio = 25:1, 50 mg HMF, 1 g solvent, 120°C, 2h.

### 3.5 Stability of HMF in the catalytic system and [C<sub>4</sub>C<sub>1</sub>im]Cl

To maintain the high HMF selectivity in the reaction, it was important to determine the stability of the HMF under the reaction condition. Thus, HMF was heated in the same experimental condition that was used for glucose dehydration (120°C) in [C<sub>4</sub>C<sub>1</sub>im]Cl solvent and catalysts. Without catalysts (blank), HMF degradation was ~11% after 6h (**Fig. 3.8**). Levulinic acid and formic acid were not observed. These results suggested that [C<sub>4</sub>C<sub>1</sub>im]Cl was not able to rehydrate HMF. With added encapsulated 8% and 14%PTA<sub>⊂</sub>Al-MOF catalysts, a slight increase in HMF conversion was observed, which reached ~18% after 6h. With PTA alone, the HMF conversion rate was 41%, greater than that of conversion in the presence of encapsulated 8% and 14%PTA<sub>⊂</sub>Al-MOF catalysts and reaching 19% and 21% after 6h, respectively.

Next, the physical mixture of PTA and 8%PTA<sub>⊂</sub>MIL-101(Al)-NH<sub>2</sub> catalyst was evaluated to check the HMF stability. The amount of PTA in the physical mixture of PTA and 8%PTA<sub>⊂</sub>Al-MOF catalyst was maintained at the same level as for the encapsulated 14%PTA<sub>⊂</sub>Al-MOF catalyst. As expected, the physical mixture increased HMF conversion by 34% at 6h reaction time compared with 21% HMF conversion by 14%PTA<sub>⊂</sub>Al-MOF catalyst. These results demonstrated that PTA in the bulk solution degraded the HMF and decreased the HMF selectivity, similar to a finding of Zhang et al. [163]. The encapsulation of PTA in the pores of Al-MOF catalyst minimized PTA leaching into the solvent and limited conversion of HMF, which, in turn, maintained the HMF selectivity.

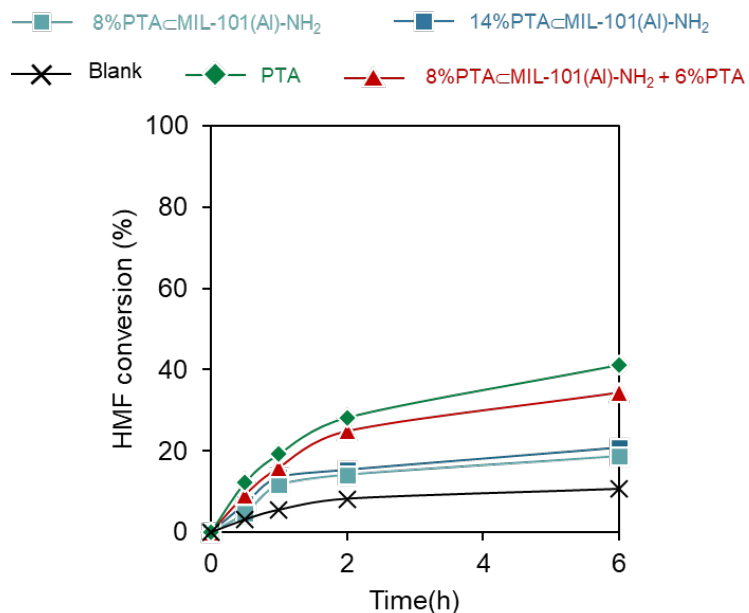


**Figure 3.8.** HMF conversion by encapsulated PTA⊂MIL-101(AI)-NH<sub>2</sub>. Reaction condition: 50 mg HMF, 30 mg catalyst, 1 g solvent, 120°C. Phosphotungstic acid = 14 wt.% in PTA alone and physical mix between 6%PTA + 8%Al-MOF to match the PTA in 14%PTA⊂Al-MOF.

### 3.6 Reuse of encapsulated PTA⊂MIL-101(AI)-NH<sub>2</sub> for glucose dehydration

To determine the ability to reuse the encapsulated PTA⊂Al-MOF catalyst, the used catalyst was recovered by centrifugation, washed with water, and dried in a vacuum oven at 130°C to remove moisture, residual products, intermediates, and unreacted glucose. Then, the catalyst was reused four times. The 14%PTA⊂Al-MOF was chosen because it had the greatest HMF selectivity. The 14%PTA⊂Al-MOF catalyst maintained its catalytic performance with HMF selectivity of ~ 55% at 40% glucose conversion after the 4<sup>th</sup> cycle, <10% decrease in both glucose conversion and HMF selectivity compared with fresh catalyst (**Fig. 3.9**). In all cycles, the selectivity to HMF was between 55-62%. Next, ICP-EOS was used to measure the Tungsten(W) content in the used catalysts. Only a slight W loss (<3 wt.%) in the used catalysts was observed after four recycles, which indicated that little to no PTA leached from the 14%PTA⊂Al-MOF catalyst.



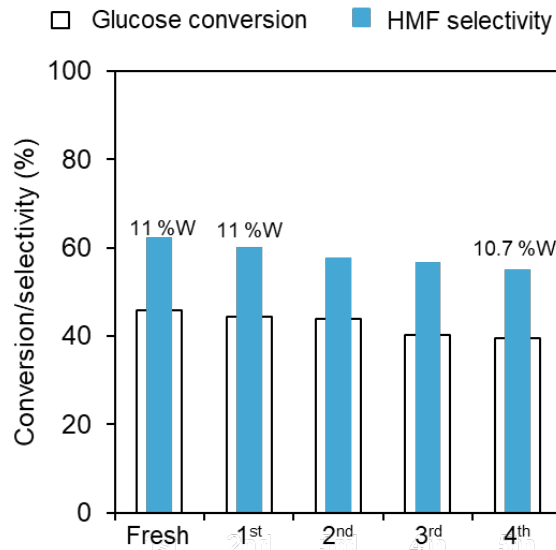


**Figure 3.9.** Reuse of 14%PTA-MIL-101(Al)-NH<sub>2</sub> for glucose dehydration. Reaction condition: glucose: Al molar ratio = 25:1, 1 g [C<sub>4</sub>C<sub>1</sub>im]Cl, 120°C, 2 h. Tungsten content (%W) indicates the W content in the used catalyst.

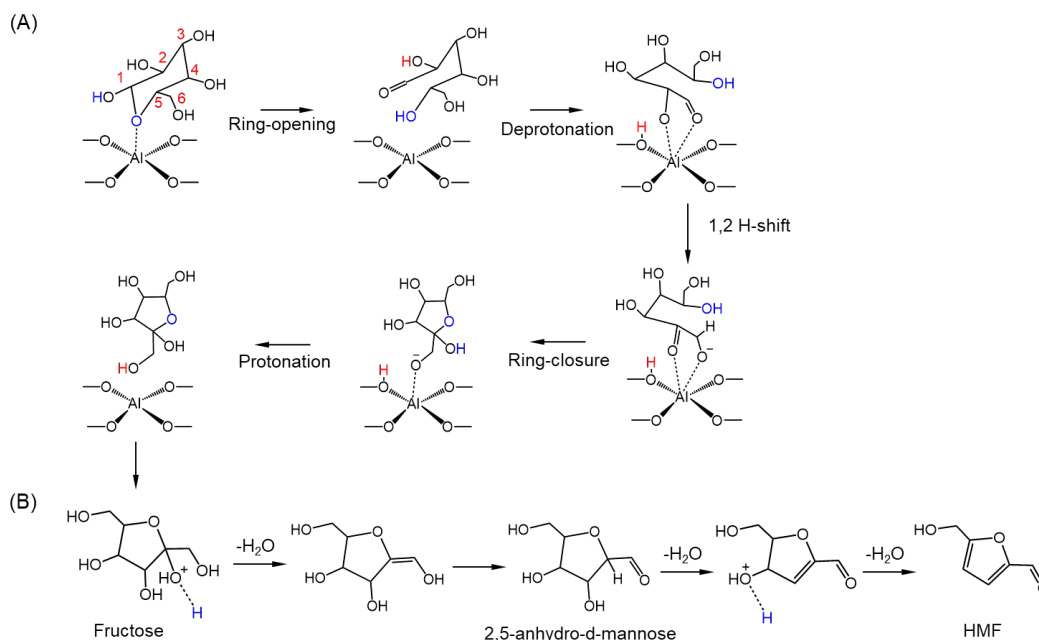
### 3.7 Proposed chemical pathway for glucose dehydration to HMF by PTA-MIL-101(Al)-NH<sub>2</sub>

On the basis of the foregoing findings, **Scheme 2** shows a proposed mechanism for glucose dehydration to HMF by PTA-MIL-101(Al)-NH<sub>2</sub> catalysts. The reaction proceeds by the synergy between Lewis-Brønsted acid sites: (1) glucose isomerization to fructose by the Lewis acid of MIL-101(Al)-NH<sub>2</sub>, and (2) dehydration of resulting fructose to HMF by the Brønsted acid of PTA and/or MIL-101(Al)-NH<sub>2</sub>.

The glucose isomerization to fructose by Lewis acid sites consists of a sequence of ring opening, deprotonation, isomerization, protonation, and ring closure processes as shown by Hensen et al. [212-214]. We postulated that glucose initially binds to the Al active site imbedded in the MIL-101 framework via its ring oxygen atom and followed by the ring opening process to form the acyclic glucose. Subsequently, the deprotonation of the hydroxyl group at C<sub>2</sub> occurred by the metal-oxo clusters. Next, the aldose-ketose isomerization induces the hydride shift from the C<sub>2</sub> to C<sub>1</sub> carbon

atom. The reaction undergoes a ring-closure reaction yielding anionic fructofuranose bound to Al site. Finally, the terminal oxygen anionic fructofuranose is protonated to generate fructose.

The fructose undergoes dehydration by Brønsted acid sites to produce HMF by dehydration and tautomerization. First, the hydroxyl group of the fructose at the alpha position is protonated by acidic protons of Brønsted acid catalysts, which resulted in the formation of water. Next, the cyclic enol intermediate is formed and subsequently tautomerized to 2,5-anhydro-d-mannose [215-217]. Then, the reaction proceeds by two sequential dehydrations to form HMF.



**Scheme 2.** Proposed reaction mechanism for glucose dehydration to HMF over PTA<sub>6</sub>MIL-101(Al)-NH<sub>2</sub>. The reaction proceeds by (A) glucose dehydration to fructose, followed by (B) fructose dehydration to HMF.

#### 4. Discussion

A major challenge in selective glucose conversion to HMF is the design of catalysts that possess Lewis and Brønsted acid sites that can act cooperatively [128, 218, 219]. Here, the effect of PTA encapsulation in PTA<sub>6</sub>MIL-101(Al)-NH<sub>2</sub> catalysts (PTA<sub>6</sub>Al-MOF) on glucose conversion to HMF

was investigated. The synergy between encapsulated PTA and Al-MOFs enabled the high HMF selectivity. Moreover, the results demonstrated that the encapsulation of PTA in MIL-101(Al)-NH<sub>2</sub> catalysts minimized PTA leaching into the bulk solution, thereby preventing degradation of the HMF product.

The most significant finding was that the HMF selectivity strongly depended on the location of the PTA. Encapsulation of PTA in MIL-101(Al)-NH<sub>2</sub> pores provided two benefits. First, the close proximity between the Lewis acid sites of the Al-MOF and the Brønsted acidic PTA promoted HMF formation. The fructose formed from glucose isomerization by Lewis acid (MIL-101(Al)-NH<sub>2</sub>) was dehydrated to HMF by the encapsulated PTA catalyst. Tangsermvit et al. showed that the proximity between Lewis and Brønsted acid sites was important in achieving a high HMF yield [220], a result that agrees with our findings. Second, encapsulated PTA catalysts minimized PTA leaching into the bulk solution and, consequently, prevented HMF degradation. Although Brønsted acids catalyze fructose dehydration to HMF, they also catalyze undesired HMF rehydration to levulinic acid [221] and/or degradation to humin [127]. The MIL-101 structure of the Al-MOF possesses both mesoporous windows (29-34 Å) and microporous windows, the latter corresponding to large hexagonal pores (15-16 Å), and somewhat smaller pentagonal pores (~12 Å) [222-224]. Keggin-type heteropolyacids, ~13-14 Å in size [164], are larger than the pentagonal pores in MIL-101, thereby the heteropolyacids are preventing from leaching out and causing side reactions (rehydration and/or humin formation). These results explained the retention of HMF selectivity and the ability to recycle the PTA@MIL-101(Al)-NH<sub>2</sub> catalyst. Hence, encapsulated Brønsted acidic PTA in the pores of MIL-101(Al)-NH<sub>2</sub> not only provided Brønsted acidity for fructose dehydration but also prevented PTA leaching into the bulk solution, that otherwise had the potential to degrade HMF.

Another significant finding was the discovery of the high selectivity of PTA@Al-MOF for glucose dehydration. Many investigators used solid Lewis acid catalysts (Sn-containing β-zeolites [133] and Nb<sub>2</sub>O<sub>5</sub> [131]) with homogeneous catalysts such as HCl to maximize HMF selectivity (**Table 3.S3**). Their results suggested that the cooperative effect between Lewis acid and Brønsted acid species

was critical in maximizing HMF selectivity in glucose dehydration. Qu et al. impregnated  $\text{SO}_4^{2-}$  on  $\text{ZrO}_2$  by  $\text{H}_2\text{SO}_4$  acid [225]. Although the  $\text{SO}_4^{2-}/\text{ZrO}_2$  in biphasic THF/ $\text{H}_2\text{O}$  system reached a high HMF selectivity of 67% at 93% glucose conversion, both HMF selectivity and glucose conversion dropped ~10% after the 4<sup>th</sup> catalyst recycling due to leaching of  $\text{SO}_4^{2-}$  [225]. The ability to create the solid bifunctional Lewis-Bronsted catalysts will enhance the commercial feasibility of HMF production. Zhang et al. encapsulated PTA in MIL-101(Cr) to produce the bifunctional acid catalysts with PTA as a Brønsted acid and MIL-101(Cr) as a Lewis acid [163]. The PTA<sub>⊂</sub>MIL-101(Cr) catalysts were selective toward HMF in fructose dehydration. However, they were not selective toward HMF in glucose dehydration and gave only 10% HMF selectivity at 21% glucose conversion at 100°C after 3h. Compared with MOF-derived catalysts for glucose dehydration, the PTA<sub>⊂</sub>Al-MOF catalysts described in this report were superior to other MOF-derived catalysts in terms of HMF selectivity (**Table 3.S3**).

These findings demonstrate that PTA<sub>⊂</sub>Al-MOF catalyst was a selective and recyclable catalyst for glucose dehydration to HMF. The PTA<sub>⊂</sub>MIL-101(Al)-NH<sub>2</sub> catalyst was easy to synthesize compared with other solid acid catalysts for selective glucose conversion to HMF, such as modified β-zeolites [226]. Moreover, the ability to control the ratio of numbers of Brønsted acid sites to Lewis acid sites in PTA<sub>⊂</sub>Al-MOF catalysts provides opportunities to use the catalysts in various organic reactions, such as esterification [227], alkylation [228], and benzylation [229].

Although PTA<sub>⊂</sub>Al-MOF catalyst is promising for selective glucose conversion to HMF, the interactions between the framework, metal nodes, and PTA (acidic protons) that affect the acid properties and catalytic performance has not been extensively investigated. Juan-Alcañiz et al. reported the partial W substitution by  $\text{Cr}^{3+}$  of MIL-101(Cr) at high temperatures [164]. The W-substituted heteropolyacids and/or the formation of W-Al complex metal nodes might be the active sites for this reaction. Additional studies should identify the interaction between W in PTA and Al in Al-MOF by <sup>27</sup>Al Magic Angle Spin (MAS) Nuclear Magnetic Resonance (NMR). The knowledge will help in designing selective catalysts and systems for glucose dehydration.

## 5. Conclusion

Phosphotungstic acid encapsulated MIL-101(Al)-NH<sub>2</sub> catalyst (PTA<sub>c</sub>MIL-101(Al)-NH<sub>2</sub>) was developed for selective glucose conversion to HMF. The encapsulation of Brønsted acidic phosphotungstic acid in the pores of MIL-101(Al)-NH<sub>2</sub> provided the proximity between Brønsted acid sites and Lewis acid sites of MIL-101(Al)-NH<sub>2</sub> for the efficient cascade of glucose isomerization and fructose dehydration. The synergistic effect of Brønsted and Lewis acid sites in the phosphotungstic acid encapsulated MIL-101(Al)-NH<sub>2</sub> catalyst is the key contributor to the high HMF selectivity and glucose conversion; this synergy cannot occur if the agents are introduced separately. Moreover, the encapsulated phosphotungstic acid was stable in the pores of MIL-101(Al)-NH<sub>2</sub>, which minimized leaching of PTA into the bulk solution and reaction with the HMF to generate undesired products. As a result, the encapsulated PTA<sub>c</sub>MIL-101(Al)-NH<sub>2</sub> catalyst maintained its catalytic performance after recycling four times. These results underscore the importance of phosphotungstic acid encapsulation to provide the cooperative effect between Brønsted and Lewis acidic sites for maximizing the HMF formation and minimizing subsequent HMF conversion/degradation. This encapsulated metal-organic framework catalyst should be applicable to other acid-catalyzed biomass transformations.

## Acknowledgment

A part of this material is based upon work supported by the National Science Foundation under Cooperative Agreement No. 1355438 and Internal Research Grant, Office of the Executive Vice President for Research, University of Louisville. This work was performed in part at the Conn Center for Renewable Energy Research at the University of Louisville, which belongs to the National Science Foundation NNCI KY Manufacturing and Nano Integration Node, supported by ECCS-1542174. The authors would like to thank Dr. Howard Fried for his valuable comments and suggestions on the manuscript.

## 6. Supplementary Information

### The adsorption of glucose and HMF on the PTA-MIL-101(Al)-NH<sub>2</sub> catalyst

MOFs act like a sponge that can adsorb organic compounds, including glucose [230, 231]. To ensure that our calculation of glucose conversion and HMF selectivity were accurate, we performed a control experiment by measuring the glucose and HMF concentrations in the presence of MOFs for 2h at ambient conditions. We observed <1.5% decrease in glucose and HMF concentrations after added MOFs for 2 h. These results suggested that, after the reaction, glucose and HMF were not adsorbed by MOFs.

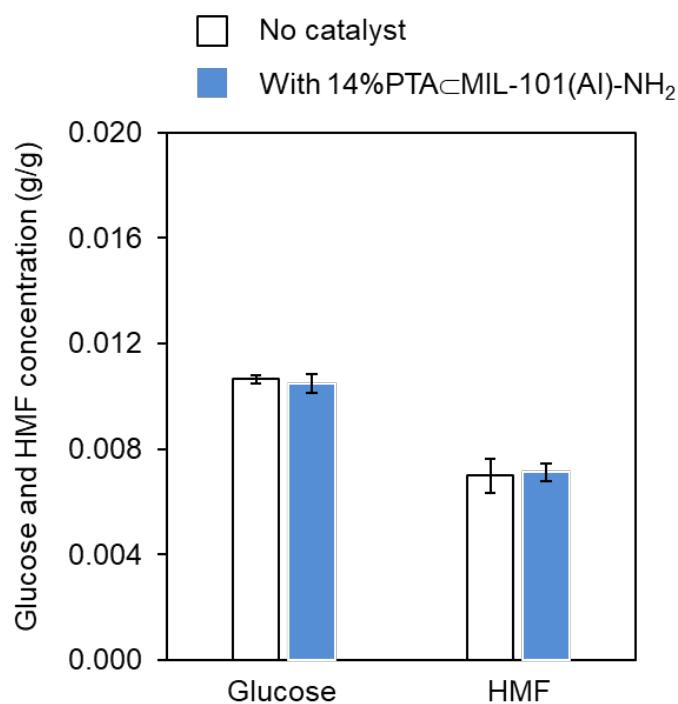


**Figure 3.S1.** Glucose and HMF concentrations with and without 14%PTA-MIL-101(Al)-NH<sub>2</sub> after stirring for 2h.

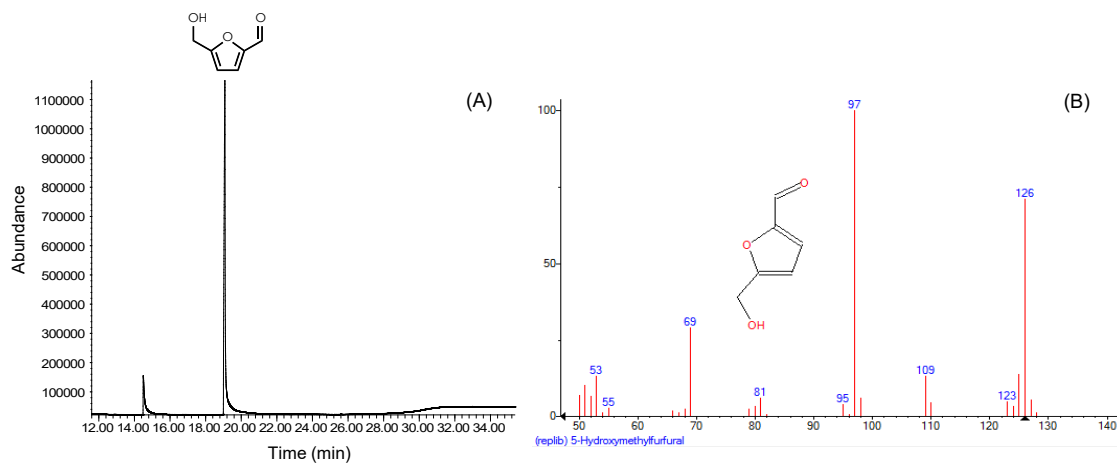


**Figure 3.S2.** Gas chromatography and mass spectrometry profiles of extracted HMF. (A) Elution profile of extracted HMF from the reaction solution, and (B) mass fingerprint of the extracted HMF. **Figure 3.S2** shows the elution profile and mass fingerprint of extracted HMF from the reaction solution. These results confirmed the formation of HMF in the reaction solution.

### Physicochemical properties of the Brønsted acidic phosphotungstic acid encapsulated MIL-101(AI)-NH<sub>2</sub> metal-organic framework (PTA<sub>c</sub>MIL-101(AI)-NH<sub>2</sub>) catalysts

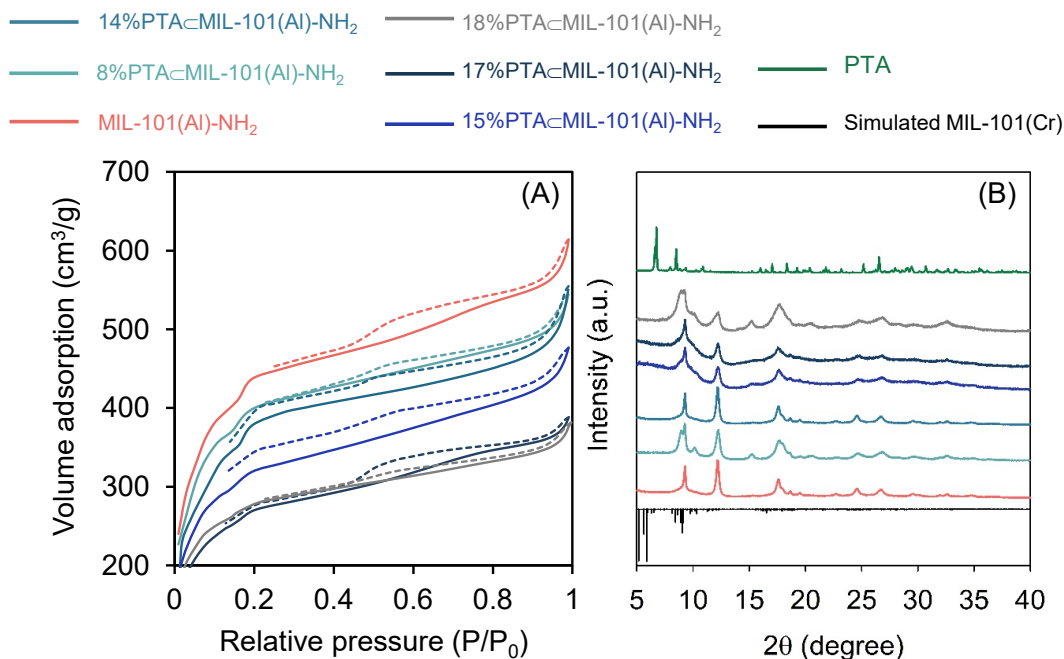


**Figure 3.S3.** Characterization of PTA<sub>c</sub>MIL-101(AI)-NH<sub>2</sub> by (A) N<sub>2</sub> adsorption-desorption and (B) X-ray diffraction (XRD).

The calculated BET surface area and BJH pore volume from these isotherms were slightly lower in the 8%PTAcMIL-101(AI)-NH<sub>2</sub> catalyst (1375 m<sup>2</sup>/g and 0.82 cm<sup>3</sup>/g) compared with those of MIL-101(AI)-NH<sub>2</sub> catalyst (1487 m<sup>2</sup>/g and 0.92 cm<sup>3</sup>/g) (**Table 3.1**), which suggested that PTA occupied the accessible surface area and pore space. The BET surface area and BJH pore volume progressively decreased with increasing PTA content and reached 854 m<sup>2</sup>/g surface area and 0.57 cm<sup>3</sup>/g pore volume of 18%PTAcMIL-101(AI)-NH<sub>2</sub>, consistent with the shape of isotherms.

To identify changes in the crystal structure of the MIL-101(AI)-NH<sub>2</sub> after encapsulation and impregnation, we performed XRD on these samples (**Fig. 3.S3B**). We did not observe any distinct differences between bare MIL-101(AI)-NH<sub>2</sub> and encapsulated catalysts below 0.25g PTA/30mL



DMF (**entry 3, Table 3.1**), which indicated the consistency in the MIL-101 framework structure of PTA<sub>c</sub>MIL-101(Al)-NH<sub>2</sub> catalysts. These results suggest that adding PTA during synthesis did not affect the formation of the MIL-101 framework. A further increase in PTA loading higher than 14% resulted in two peaks at 10° and 15°, which were hypothesized to be associated with the (110) and (200) planes of PTA.

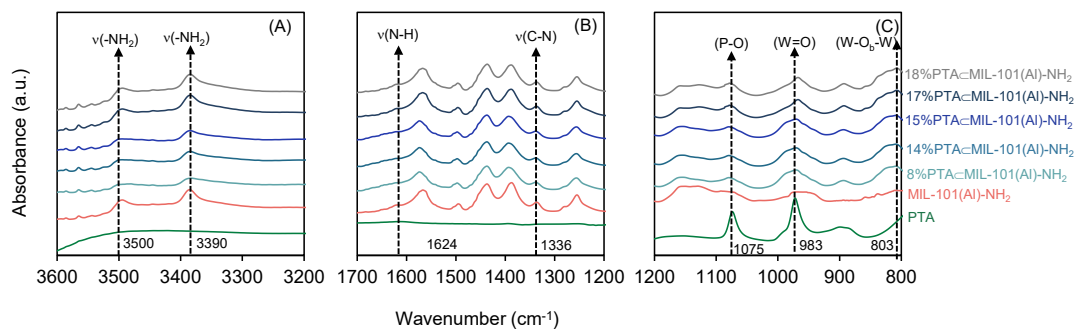


**Figure 3.S4.** FTIR spectra of PTA<sub>c</sub>MIL-101(Al)-NH<sub>2</sub> catalysts in the wavenumber range of (A) 3600-3200 cm<sup>-1</sup>, (B) 1700-1200 cm<sup>-1</sup> and (C) 1200-800 cm<sup>-1</sup>.

The FTIR spectra of MIL-101(Al)-NH<sub>2</sub> and PTA<sub>c</sub>MIL-101(Al)-NH<sub>2</sub> showed bands at 3390 and 3500 cm<sup>-1</sup> corresponding to the symmetric and asymmetric stretching of primary -NH<sub>2</sub> groups (**Fig. 3.S4A**). The shoulder at 1624 cm<sup>-1</sup> and 1336 cm<sup>-1</sup> corresponded to the N-H bending of the -NH<sub>2</sub> group and C-N stretching absorption of aromatic amines, respectively (**Fig. 3.S4B**) [143]. Together, these bands confirmed the presence of -NH<sub>2</sub> groups in the MIL-101(Al)-NH<sub>2</sub>. In addition, the PTA encapsulation did not affect the MIL-101(Al)-NH<sub>2</sub> framework. The incorporation of PTA was confirmed by FTIR spectroscopy. The characteristic peak at 1075 cm<sup>-1</sup> was assigned to the asymmetric vibrations of P-O stretching in the central PO<sub>4</sub> tetrahedron. A peak at 983 cm<sup>-1</sup> was assigned to terminal W=O<sub>d</sub> stretching (O<sub>d</sub> as terminal oxygen atom), whereas the peak at 803 cm<sup>-1</sup> was assigned to the W-O<sub>b</sub>-W vibration (O<sub>b</sub> as oxygen atom bridging between corner-sharing octahedra) (**Fig. 3.S4C**) [232].

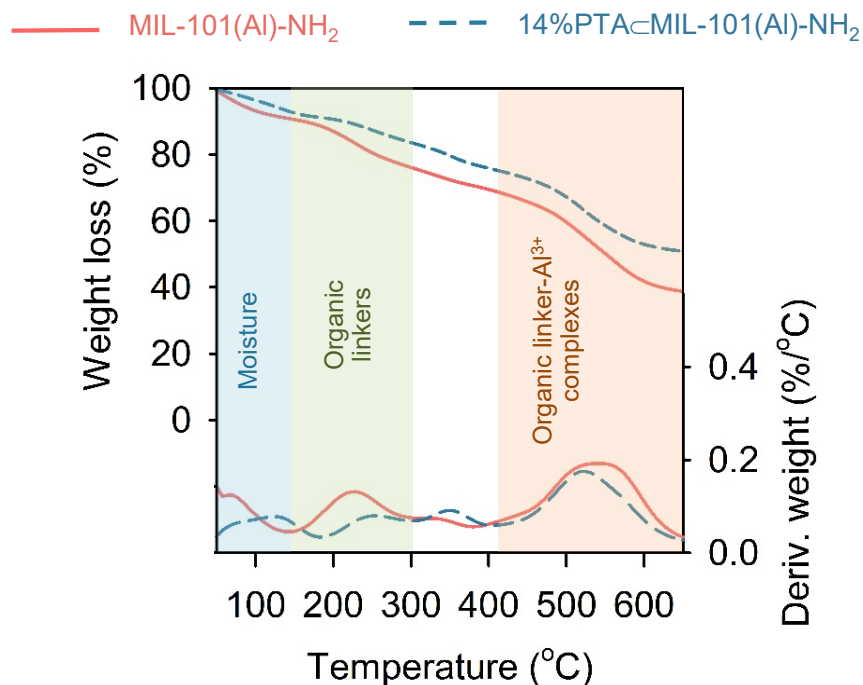


**Figure 3.S5.** Thermogravimetric analysis (TGA) and Differential Thermogravimetric analysis (DTG) of bare Al-MOF and 14%PTA-Al-MOF catalysts showing the change in weight of the catalysts as a function of temperature.

#### **Effect of temperature on MIL-101(AI)-NH<sub>2</sub> glucose dehydration activity**

We treated MIL-101(AI)-NH<sub>2</sub> at 80, 120, and 150°C in vacuo for 8h. Then we used the catalysts for glucose dehydration at 120°C for 2h (**Fig. 3.S6**). We did not observe any significant difference in glucose conversion by the heat-treated MOFs. However, HMF selectivity decreased as the treatment temperature increased. These results implied that heat treatment affected the acid properties and resulted in changes in HMF selectivity, in agreement with findings by Halls et al. [25]. We hypothesized that high temperature removed the bound water and decreased the Bronsted acid sites. For these reasons, the HMF selectivity decreased because Bronsted acid sites are needed to dehydrate the resulting fructose into HMF.

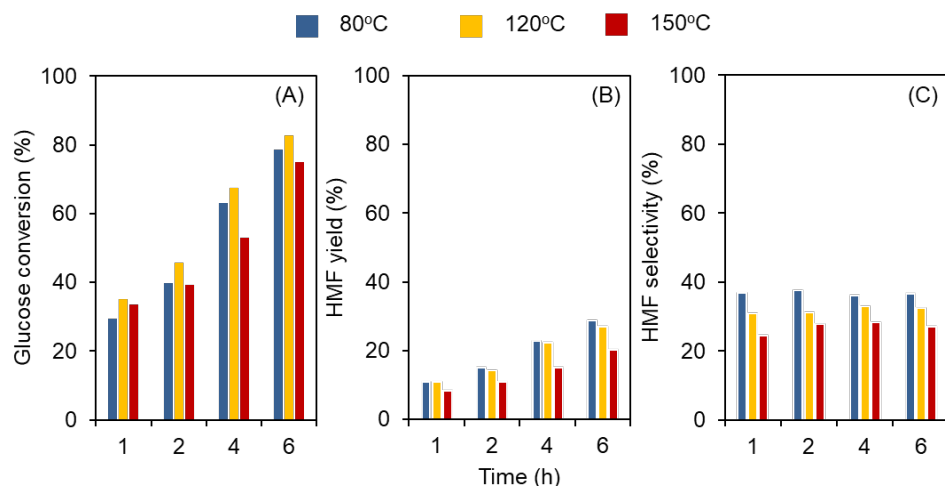


**Figure 3.S6.** Catalytic conversion of MIL-101(Al)-NH<sub>2</sub> treated at 80-150°C (A) glucose conversion (B) HMF yield and (C) HMF selectivity. Reaction condition: glucose: Al molar ratio = 25:1, 50 mg glucose, 1 g [C<sub>4</sub>C<sub>1</sub>im]Cl, 120°C, 2h.

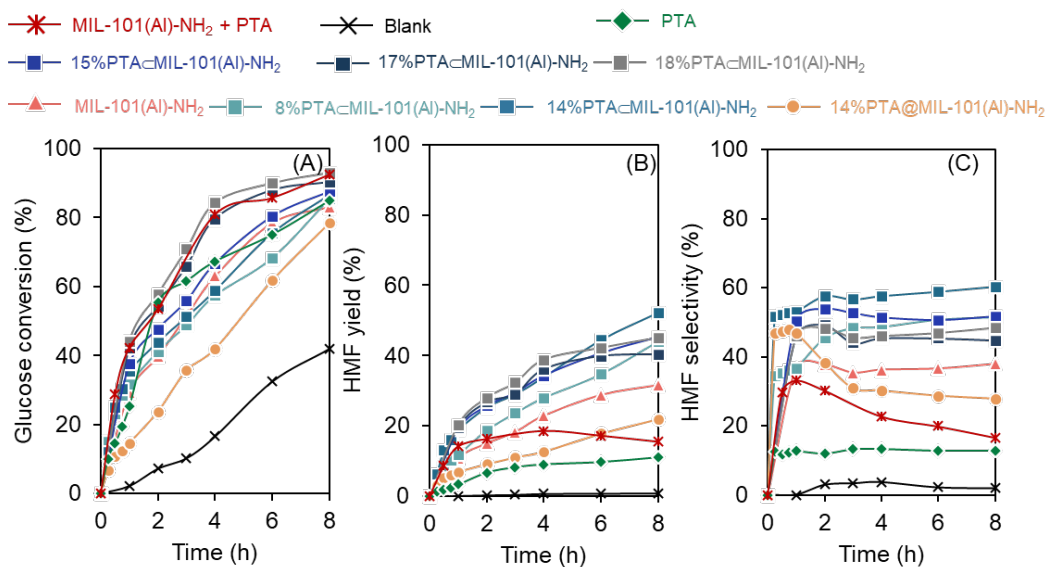


**Figure 3.S7.** Catalytic performance of encapsulated PTA@MIL-101(Al)-NH<sub>2</sub> catalysts and different PTA loading on HMF selectivity at time on steam (A) glucose conversion, (B) HMF yield and (C) HMF selectivity. Reaction condition: glucose: Al molar ratio = 25:1, 50 mg glucose, 1 g [C<sub>4</sub>C<sub>1</sub>im]Cl, 120°C.

**Table 3.S1.** List of chemicals/reagents used in this study

| <b>Chemical</b>                      | <b>Supplier</b>             | <b>Purity</b> | <b>CAS Number</b> |
|--------------------------------------|-----------------------------|---------------|-------------------|
| D-glucose monohydrate                | VWR International, USA      | 99%           | 50-99-7           |
| 1-butyl-3-methylimidazolium chloride | Alfa Aesar, USA             | 96%           | 79917-90-1        |
| 2-aminoterephthalic acid             | Acros Organics, USA         | 99%           | 10312-55-7        |
| Aluminum chloride hexahydrate        | Ward's Science, Canada      | 99%           | 7784-13-6         |
| Phosphotungstic acid                 | Strem Chemicals, USA        | 99%           | 12501-23-4        |
| Methanol                             | Sigma-Aldrich, USA          | 99.8%         | 67-56-1           |
| Ethanol                              | VWR, USA                    | 200 proof     | 64-17-5           |
| 1-propanol                           | TCI America, USA            | >99.5%        | 71-23-8           |
| 2-propanol                           | TCI America, USA            | >99.5%        | 67-63-0           |
| 1-butanol                            | Sigma-Aldrich, USA          | 99.5%         | 71-36-3           |
| 2-butanol                            | TCI America, USA            | >99.0%        | 75-65-0           |
| 1,4-dioxane                          | VWR, USA                    | >99.9%        | 123-91-1          |
| Ethyl acetate                        | VWR, USA                    | >99.5%        | 141-78-4          |
| <i>N,N</i> -dimethylformamide        | Chem-Impex Int'l. Inc., USA | 99.8%         | 68-12-2           |
| <i>N,N</i> -dimethylacetamide        | Sigma-Aldrich, USA          | 99.8%         | 127-19-5          |
| Dimethyl sulfoxide                   | Sigma-Aldrich, USA          | 99.9%         | 67-68-5           |
| Tetrahydrofuran                      | Sigma-Aldrich, USA          | 99%           | 109-99-9          |

**Table 3.S2.** Selected Bronsted acidic polyoxometalate-derived MOF catalysts prepared by impregnation, encapsulation, and mechanical synthesis.

| No | POM   | MOF                     | Method        | Reaction  | Ref   |
|----|---|-------------------------|---------------|---|-------|
| 1  | PTA   | MOF-808(Zr)             | impregnation  | biomass conversion (esterification, hydrogenation, and lactonization) | [233] |
| 2  | PTA   | MIL-101(Cr)             | encapsulation | hydroisomerization  | [234] |
| 3  | LaW <sub>10</sub> O <sub>36</sub>   | MIL-101(Cr)             | impregnation  | Oxidative desulfurization   | [235] |
| 4  | PW <sub>11</sub> Zn   | MIL-101(Cr)             | impregnation  | desulfurization   | [236] |
| 5  | PTA   | MIL-101(Cr)             | encapsulation | alcoholysis   | [237] |
| 6  | PTA   | UiO-66(Zr)              | encapsulation | oxidative desulfurization   | [238] |
| 7  | polyoxomolybdic acid and polyoxomolybdic cobalt   | UiO-bpy and UiO-67 (Zr) | encapsulation | olefin Epoxidation  | [239] |
| 8  | [Co <sup>II</sup> Co <sup>III</sup> W <sub>11</sub> O <sub>39</sub> (H <sub>2</sub> O)] <sup>7-</sup> and [Co <sub>4</sub> (PW <sub>9</sub> O <sub>34</sub> ) <sub>2</sub> (H <sub>2</sub> O) <sub>2</sub> ] <sup>10-</sup> | MIL-101(Fe)             | encapsulation | water oxidation   | [240] |
| 9  | PTA   | MIL-101(Cr)             | encapsulation | oxidative desulfurization   | [241] |

|    |   |             |                                  |  |       |
|----|---|-------------|----------------------------------|--|-------|
| 10 | PTA   | MIL-100(Fe) | encapsulation                    | esterification and acetalization         | [242] |
| 11 | PTA   | HKUST-1(Cu) | mechanochemical                  | phenol oxidation                         | [243] |
| 12 | $[PZnMo_2W_9O_{39}]^{5-}$                       | MIL-101(Cr) | impregnation                     | oxidation of alkenes                     | [244] |
| 13 | $H_{3+n}PMo_{12-n}V_nO_{40}$ (n = 1, 2, 3)      | MOF-1(Cu)   | encapsulation                    | oxidative desulfurization                | [245] |
| 14 | $[SO_3H-(CH_2)_3-HIM]_3PW_{12}O_{40}$           | MIL-100(Fe) | encapsulation                    | Esterification of oleic acid             | [246] |
| 15 | $H_5PV_2Mo_{10}O_{40}$                          | NU-1000(Zr) | impregnation                     | aerobic Oxidation                        | [247] |
| 16 | $P^V Mo^VI 11 Mn^{II} (H_2O) O_{39}]^{5-}$      | MIL-100(Fe) | encapsulation                    | reduction of p-nitrophenol               | [248] |
| 17 | $K_5[CoW_{12}O_{40}]$                           | MIL-101(Cr) | encapsulation                    | methanolysis of epoxides                 | [249] |
| 18 | PTA   | MIL-101(Cr) | encapsulation                    | Knoevenagel condensation of benzaldehyde | [164] |
| 19 | porous coordination polymer(Cr)-NH <sub>2</sub> |             | 190 °C, 480 min, water/THF (1:2) | glucose dehydration                      | [250] |

**Table 3.S3.** Selected metal-organic framework (MOF) catalysts and solid catalysts for glucose dehydration

| Entry | Catalyst                              | Solvent  | Temp (°C) | Time (h) | Conversion (wt.%) | HMF yield (mol%) | HMF selectivity (mol%) | Ref       |
|-------|---------------------------------------|--|-----------|----------|-------------------|------------------|------------------------|-----------|
| 1     | PTA-CMIL-101(Al)-NH <sub>2</sub>      | 1-butyl-3-methylimidazolium chloride               | 120       | 2        | 44                | 26               | 58                     | This work |
|       |                                       |  |           | 8        | 87                | 52               | 60                     |           |
| 2     | UiO-66-NH <sub>2</sub>                | water  | 140       | 3        | 16                |                  | 35                     | [251]     |
| 3     | UiO-66                                | DMSO-d <sub>6</sub> <sup>a</sup>                   | 160       | 0.5      | -                 | 28               | -                      | [252]     |
| 4     | UiO-66                                | 39:1 (v/v) DMSO-d <sub>6</sub> /water <sup>a</sup> | 160       | 0.5      | -                 | 37               | -                      | [252]     |
| 5     | MIL-101(Cr)-SO <sub>3</sub> H         | 9:1 (v/v) GVL/water <sup>b</sup>                   | 150       | 2        | 91                | 40               | 44                     | [253]     |
| 6     | PO <sub>4</sub> /NU(half)             | 9:1 (v/v) 2-propanol/water                         | 140       | 9        | >99               | 49               | <50                    | [254]     |
| 7     | PTA(3.0)/MIL-101                      | 1-ethyl-3-methylimidazolium chloride               | 100       | 3        | 21                | 2                | 10                     | [255]     |
| 8     | MIL-101(Cr)-SO <sub>3</sub> H (15.0%) | 1-butyl-3-methylimidazolium chloride               | 120       | 2        | -                 | 8                | -                      | [256]     |
| 9     | Hierarchical Sn-containing β-zeolite  | 1:2.3 (v/v) DMSO/THF <sup>c</sup>                  | 160       | 3.5      | 99                | 41               | 42                     | [257]     |
| 10    | pTSA-Ca/AC <sup>d</sup>               | 6:1 (v/v) MIBK/water <sup>e*</sup>                 | 180       | 24       | 93                | 57               | 61                     | [130]     |

|    |  |  |     |     |    |     |    |       |
|----|--|--|-----|-----|----|-----|----|-------|
| 11 | Nb <sub>2</sub> O <sub>5</sub> + HCl<br>(0.2 M)              | 4:1 (v/v)<br>THF/water <sup>c*</sup>       | 130 | 2   | 93 | 47  | 51 | [131] |
| 12 | SO <sub>4</sub> <sup>2-</sup> /ZrO <sub>2</sub> <sup>f</sup> | 2:1 (v/v)<br>NaCl-THF/water <sup>c*</sup>  | 160 | 2   | 93 | 62  | 67 | [225] |
| 13 | Nb <sub>3</sub> Zr <sub>7</sub> +<br>CaCl <sub>2</sub>       | 2.3:1 (v/v)<br>MIBK/water <sup>e*</sup>    | 175 | 1.5 | 99 | 44  | 44 | [258] |
| 14 | Sn-containing<br>β-zeolite +<br>HCl                          | water                                      | 160 | 1.5 | 45 | 2.7 | 6  | [259] |
|    |  | 3:1 (v/v) 1-<br>butanol/water <sup>*</sup> | 160 | 1.5 | 77 | 20  | 26 |       |
|    |  | 3:1 (v/v)<br>NaCl-THF/water <sup>c*</sup>  | 180 | 1.2 | 79 | 57  | 72 |       |

<sup>a</sup>DMSO-d<sub>6</sub> = Dimethyl sulfoxide-d<sub>6</sub>, <sup>b</sup>GVL=γ-valerolactone, <sup>c</sup>THF = tetrahydrofuran, <sup>d</sup>p-

toluenesulfonic acid-Ca/activated charcoal, <sup>e</sup>MIBK = methyl isobutyl ketone, <sup>f</sup>SO<sub>4</sub><sup>2-</sup>/ZrO<sub>2</sub> = ZrO<sub>2</sub> was

impregnated with 0.5 M sulfuric acid solution, <sup>\*</sup>biphasic system

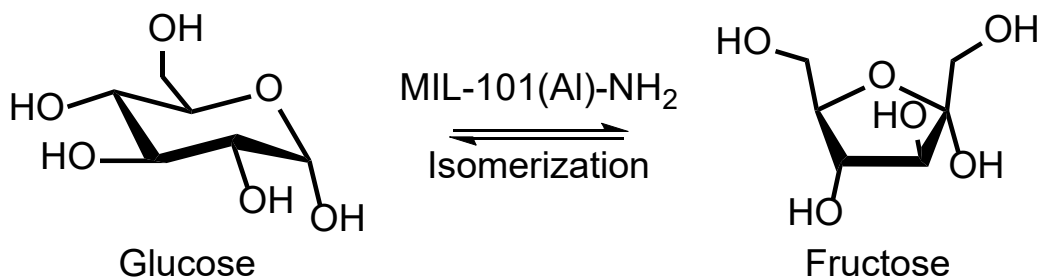


CHAPTER 4  
ALUMINUM-CONTAINING METAL ORGANIC FRAMEWORKS AS SELECTIVE AND  
REUSABLE CATALYSTS FOR GLUCOSE ISOMERIZATION TO FRUCTOSE

**1. Introduction**

Fructose is an essential precursor for food/beverages [260], such as fructose syrup and soft drinks, and for chemical feedstocks, such, 5-hydroxymethylfurfural, levulinic acid, and lactic acid [261, 262]. Currently, sugar mills produce fructose by enzymatic isomerization of glucose. This approach yields 33-55% fructose. Jin et al. performed the glucose isomerization by glucose isomerase (GI) enzyme and obtained 47% yield of D-fructose at 60 °C [263]. Lee et al. used GI enzyme along with citric buffer, and the fructose yield was 35% [264]. Jia et al. used a novel thermostable GI, and the maximum fructose yield was 52% [265]. Zhang et al. used a mimic GI and obtained 33% fructose yield [266]. Jin et al. immobilized the GI and obtained 55% fructose yield [267]. However, enzyme-based production has several drawbacks, particularly a requirement for narrow operating conditions (pH and temperature) [268, 269], a high cost of the enzymes [270], and enzyme inactivation [271]. Homogeneous catalysts, such as chromium and aluminum chloride salts, are effective glucose isomerization agents. However, homogeneous catalysts require an extra step of separating the catalyst from the product. Sn-containing  $\beta$  [271-273], MFI [274], and MCM-41 zeolites [275] are effective for glucose isomerization and showed >50% fructose selectivity. However, zeolite synthesis is complex and requires long crystallization times [271]. Moreover, the instability of these zeolites is a major challenge [276]. Thus, the industry needs efficient and stable heterogeneous catalysts for glucose isomerization.

Metal-organic frameworks (MOFs) have drawn attention as heterogeneous catalysts for biomass transformation reactions. MOFs are composed of metal clusters and organic linkers, connected by coordination networks [23, 24]. The interconnected pores and high surface area of MOFs provide a high density of active sites and a large contact area for reactants. These attributes make MOFs attractive catalysts [31] for many organic reactions, such as acetalization [25, 26], hydrogenation [27, 28], esterifications [29, 30], and isomerization [277, 278] [279]. MOFs' catalytic functions come from their unsaturated metal sites, providing Lewis acid sites for glucose isomerization reactions. The UiO-66 and its analog have been used for glucose isomerization in water [280] and alcohols [281]. Akiyama et al. show that MIL-101(Cr)-SO<sub>3</sub>H has a selectivity of 27% towards fructose in the water at 78% glucose conversion [282]. Yabushita et al. used NU-1000 for the glucose isomerization in water and observed 19% fructose yield at 60% glucose conversion at 140 °C after 5h [254]. Guo et al. used Cr(OH)<sub>3</sub>/MIL-101(Cr) composite catalyst and achieved 59.3% fructose yield at 76.5% glucose conversion at 100 °C after 24h [283]. Oozeerally et al. used ZIF-8 for the glucose isomerization in water and observed 17% fructose yield at 60% glucose conversion at 140 °C after 3h [284]. Most of these MOFs showed low fructose yield, which limited the application of MOFs for glucose isomerization. Although homogenous AlCl<sub>3</sub> salts have been used for glucose isomerization [285-287], the use of Al<sup>3+</sup> catalytic site in MOF materials for glucose-to-fructose transformation is still largely uncovered.



**Scheme 1.** Glucose isomerization to fructose by MIL-101(Al)-NH<sub>2</sub>

The objective of this work was to evaluate aluminum-containing MOF (Al-MOF) catalysts for glucose isomerization (**Scheme 1**). Among Al-MOFs, MIL-101(Al)-NH<sub>2</sub> gave a high fructose

selectivity of 64% at 82% glucose conversion. The presence of amino groups enhanced medium-to-strong Lewis acid strength, fructose selectivity, and glucose conversion. Moreover, MIL-101(Al)-NH<sub>2</sub> MOF was stable and reusable up to four times without losing catalytic performance.

## **2. Materials and Methods**

**2.1. Materials.** Table 4.S1 lists the manufacturers, CAS numbers, and purities of chemicals, reagents, and solvents used in this study.

### **2.2 Synthesis of metal-organic frameworks**

MIL-101(Al)-NH<sub>2</sub> and MIL-53(Al)-H/NH<sub>2</sub> were synthesized by solvothermal methods (see *Supplementary Information for detail*).

### **2.3 Characterization of the metal-organic framework**

The synthesized MOFs were characterized by X-ray diffraction (XRD), nitrogen adsorption-desorption, attenuated total reflectance-Fourier-transform infrared spectroscopy (ATR-FTIR), thermogravimetric analysis (TGA), high-resolution transmission electron microscopy (HRTEM), and inductively coupled plasma-optical emission spectroscopy (ICP-OES) (see *Supplementary Information for detail*).

### **2.4. Determination of acid sites by diffuse reflectance infrared Fourier transform spectroscopy.**

Diffuse reflectance infrared Fourier transform spectroscopy (DRIFTS) with adsorbed pyridine was performed to characterize the acid sites. The temperature-programmed desorption was conducted with the JASCO FTIR equipped with a high-temperature DiffuseIR™ cell (PIKE Technology, WI, USA). The sample treatment and DRIFTS experiments with temperature-programmed desorption were conducted with a slight modification as described [182]. In short, the MOF sample (~5 mg) was placed in a cylindrical alumina crucible and treated in N<sub>2</sub> gas (50 mL/min) at 130 °C for 60 min unless otherwise noted. After the pretreatment, the sample was cooled to 30 °C. The DRIFT

spectrum of fresh catalyst was recorded as the background spectrum. The samples were then saturated with pyridine vapor by the flow of N<sub>2</sub> gas (50 mL/min). Then the physisorbed pyridine was removed by flushing with N<sub>2</sub> gas (50 mL/min) at 50, 100, or 150 °C for 30 min before recording the DRIFT spectra. Because of the limited thermal stability of Al-MOF, a lower desorption temperature (maximum 150 °C) was used. All spectra were recorded with 256 scans between 4000–400 cm<sup>-1</sup> at a 4 cm<sup>-1</sup> resolution. The amount of Lewis acid sites at each desorption temperature was calculated from the integrated area of bands (after background subtraction) of adsorbed pyridine at 1067 cm<sup>-1</sup>. This Lewis acid determination was adapted from Yu et al [184]. A cascade increase in the desorption temperature from 30-150 °C allows for identification of weak and medium to strong Lewis acid sites of MOFs. The Lewis acid peaks at 150 °C implied the medium-to-strong Lewis acid sites because of a strong coordination between pyridine and Lewis acid sites at a high desorption temperature. The Lewis acid peaks at 30 °C indicated the combination of weak and medium-to-strong Lewis acid sites. To calculate the weak Lewis acid sites, Lewis acid peak area at 150 °C was subtracted from that at 30 °C.

**2.5. Isomerization of glucose.** To evaluate the catalysts, the glucose isomerization reaction was conducted with 25 mL pressure tubes in an oil bath. Typically, 5 wt. % glucose in solvent (1 mL) and catalyst (glucose:metal molar ratio of 25:1) were added to the tubes, which were sealed and stirred at 120 °C. Xylitol was added as an internal standard to the solution of reactants and products after completing the reaction. The reaction was stopped by quenching in a cold-water bath followed by adding water (5 mL) to dissolve the remaining glucose and solvents. The solution was centrifuged, and the solid catalyst was removed. The liquid sample was then analyzed using High-Pressure Liquid Chromatography (HPLC).

## **2.6. Product analysis and quantification**

The reactants and products were analyzed using an HPLC (Agilent Technology, Santa Clara, CA, USA) equipped with a refractive index detector (RID) and diode array detector (DAD). An Aminex HPX-87H column (300 x 7.8 mm, Bio-Rad®, Hercules, CA, USA) was used for reactant and product

separation at 60°C with 0.6 ml/min of 4 mM H<sub>2</sub>SO<sub>4</sub> as the mobile phase. The concentrations of sugars were determined by the peak area from the RID signals. The concentrations of HMF were determined by the peak area from the DAD signals at 280 nm wavelength. All reactants and products were calibrated against certified standards (Absolute Standards, Inc., Hamden, CT, USA). The glucose conversion, product yield, and product selectivity were calculated as follows:

$$\text{Glucose conversion (\%)} = \frac{\text{glucose reacted (mol)}}{\text{initial glucose (mol)}} \times 100$$

$$\text{Product yield (\%)} = \frac{\text{product formed (mol)}}{\text{initial glucose (mol)}} \times 100$$

$$\text{Product selectivity (\%)} = \frac{\text{Product yield (\%)}}{\text{Glucose conversion (\%)}} \times 100$$

Specific activity and productivity were used to express the rate per metal site at which glucose was consumed, and fructose was formed, respectively. They were calculated at low glucose conversion (< 15%) to ensure that there were no side reactions [288]; the following expressions were used.

$$\text{Specific activity (h}^{-1}\text{)} = \frac{\text{glucose reacted (mol)}}{\text{metal (mol)} \times \text{time (h)}}$$

$$\text{Productivity (h}^{-1}\text{)} = \frac{\text{fructose formed (mol)}}{\text{metal (mol)} \times \text{time (h)}}$$

## 2.7. Catalyst reusability

For the MOF recycling tests, the spent catalysts were collected by centrifugation of the reaction mixture, and the liquid portion was decanted for HPLC analysis. The solid catalyst was washed twice with 5 mL of ethanol and twice with 5 mL of water to remove residual reactants and products. The solid catalyst was then separated by centrifugation and dried in a vacuum oven at 120 °C overnight before reuse.

## 3. Results

We synthesized three aluminum-containing metal-organic frameworks (Al-MOFs), MIL-101(Al)-NH<sub>2</sub>, MIL-53(Al)-NH<sub>2</sub>, and MIL-53(Al). Then we evaluated their catalytic performance for glucose isomerization in ethanol. We chose ethanol as a solvent because ethanol shifted the isomerization

equilibrium to the fructose side [289-291], which enabled us to evaluate and compare isomerization ability of different Al-MOF catalysts.

### 3.1. Characterization of physicochemical and acidic properties of Al-MOFs

To characterize the physicochemical properties, we analyzed the synthesized Al-MOFs by ICP-OES, XRD, N<sub>2</sub> adsorption-desorption measurements, HRTEM, TGA, and FTIR (Fig. 4.1 and Fig. 4.S1).

The metal content was determined by ICP-OES (Table 4.S2).

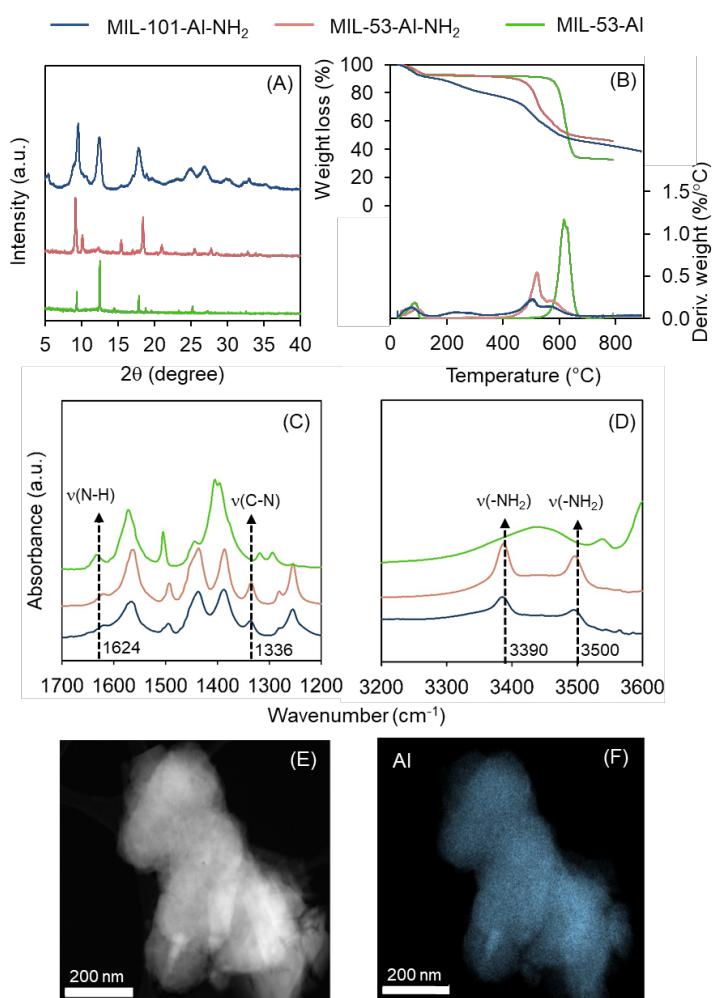


**Figure 4.1.** Physicochemical properties of MIL-101-Al-NH<sub>2</sub>, MIL-53-Al and MIL-53-Al-NH<sub>2</sub> by XRD (A), TGA (B), FTIR (C and D). HRTEM image of MIL-101(Al)-NH<sub>2</sub> (E), and aluminum mapping of MIL-101(Al)-NH<sub>2</sub> (F).

**Figure 4.1A** showed the XRD patterns of MIL-101(Al)-NH<sub>2</sub>, MIL-53(Al), and MIL-53(Al)-NH<sub>2</sub>. It can be seen that the XRD patterns for the prepared Al-MOFs are similar to that reported in literature [292-297]. The N<sub>2</sub> adsorption isotherm of the synthesized MIL-101(Al)-NH<sub>2</sub> showed a type IV isotherm (**Fig. 4.S1**) [141], which suggested that the MIL-101(Al)-NH<sub>2</sub> was a mesoporous material. The calculated surface area and pore volume were 1487 m<sup>2</sup>/g and 0.92 cc/g, respectively, similar to reported values [141-143, 145, 298, 299]. To determine the thermal stability of the Al-MOFs, we performed TGA (**Fig. 4.1B**). The TGA profile of MIL-101(Al)-NH<sub>2</sub> exhibited three mass loss zones, namely at 30–150 °C (~10 wt. %), 150–400 °C (14 wt. %) and 380–800 °C (35 wt. %). These zones corresponded to mass loss resulting from: (1) the evaporation of water molecules, (2) the degradation of organic linkers, and (3) the degradation of the organic 2-aminoterephthalic acid-Al<sup>3+</sup> complexes. The TGA profile of MIL-53-Al exhibited two mass loss zones, namely at 30–150 °C (~7.8 wt. %), and 550–700 °C (57 wt. %). The TGA profile of MIL-53(Al)-NH<sub>2</sub> exhibited two mass loss zones, namely at 30–150 °C (~7.2 wt. %), and 430–650 °C (41 wt. %). These two zones corresponded to mass loss resulting from: (1) the evaporation of water molecules, and (2) the degradation of organic linkers-Al<sup>3+</sup> complexes which matched with the literature [296].

To characterize the surface functional groups present, we analyzed Al-MOFs by ATR-FTIR (**Fig. 4.1C-D**). The shoulder at 1336 cm<sup>-1</sup> can be assigned to the C-N stretching absorption of aromatic amines. These bands confirmed the presence of –NH<sub>2</sub> groups in MIL-101(Al)-NH<sub>2</sub> and MIL-53-Al-NH<sub>2</sub> [143]. The ATR-FTIR spectrum showed bands that corresponded to the symmetric and asymmetric stretching of primary amines (3390 and 3500 cm<sup>-1</sup>) (**Fig. 4.1D**), which indicated the presence of –NH<sub>2</sub> functional groups that are uncoordinated. As control, MIL-53-Al was evaluated by FTIR and did not show any –NH<sub>2</sub> and C-N bands. HRTEM measurements with elemental mapping demonstrated that MIL-101-Al-NH<sub>2</sub> was porous with well-dispersed aluminum species (**Fig. 4.1E-F**). The Al content measured by ICP-OES was 11.6 wt.% (**Table 4.S2**). Overall, these characteristics matched reported values [141-143, 145, 298, 299] and confirmed the formation of the MIL-101(Al)-NH<sub>2</sub> structure [141, 299].

To probe the acid properties, we performed DRIFTS with adsorbed pyridine on three Al-MOF catalysts. We chose pyridine as an in-situ titrant for probing the Lewis acid site density of MOFs because of previous success in measuring Lewis acid sites in MOFs [25, 300, 301]. To avoid degradation of these three MOFs, we performed DRIFT in the range of 30-150 °C according to their thermal stability in TGA analysis. After pyridine adsorption, the DRIFT spectra of these MOFs had characteristic bands at 1067 and 1050  $\text{cm}^{-1}$  (**Fig. 4.2**), which corresponded to the coordination between pyridine and coordinated unsaturated sites (CUSs) [301, 302]. This coordination provided the vital Lewis acid sites (LAS) that interacted with pyridine. Determination of acid properties of MOFs can be difficult. Common acid titration techniques, such as  $\text{NH}_3$ -TPD [303], TGA-TPD [304, 305], and dynamic IR [306, 307] using various titrants (pyridine [184, 300], acetonitrile [301], 2,6-di-tert-butylpyridine [308]) typically require high desorption temperatures (>400 °C). However, MOFs decompose at such high temperature.

The numbers of MOF Lewis acid sites were calculated from the integrated area of the bands (after background subtraction) of adsorbed pyridine at 1067  $\text{cm}^{-1}$ . An increase in the desorption temperature from 30-150 °C enabled identification of weak and medium-to-strong LAS sites of MOFs. The intensity of this band decreased with increasing desorption temperature for all the MOFs. The 1067  $\text{cm}^{-1}$  band almost disappeared completely at 150°C for MIL-53(Al), which indicated that this MOFs had weak Lewis acid sites. Conversely, the amino-functionalized MOFs displayed a stronger 1067  $\text{cm}^{-1}$  band at 150 °C, which suggested that they had stronger Lewis acid sites compared with their amino-free isostructural counterparts [184, 309]. We calculated the Lewis acid site density of MOFs using the peak area of 1067  $\text{cm}^{-1}$ . The calculated total LAS density was in the order MIL-101(Al)- $\text{NH}_2$  (90 a.u./g) > MIL-53(Al)- $\text{NH}_2$  (52 a.u./g) > MIL-53(Al) (44 a.u./g). Interestingly, the presence of - $\text{NH}_2$  groups of MIL-53(Al)- $\text{NH}_2$  and MIL-101(Al)- $\text{NH}_2$  gave a high density of medium-to-strong LAS, compared with that of MIL-53(Al).



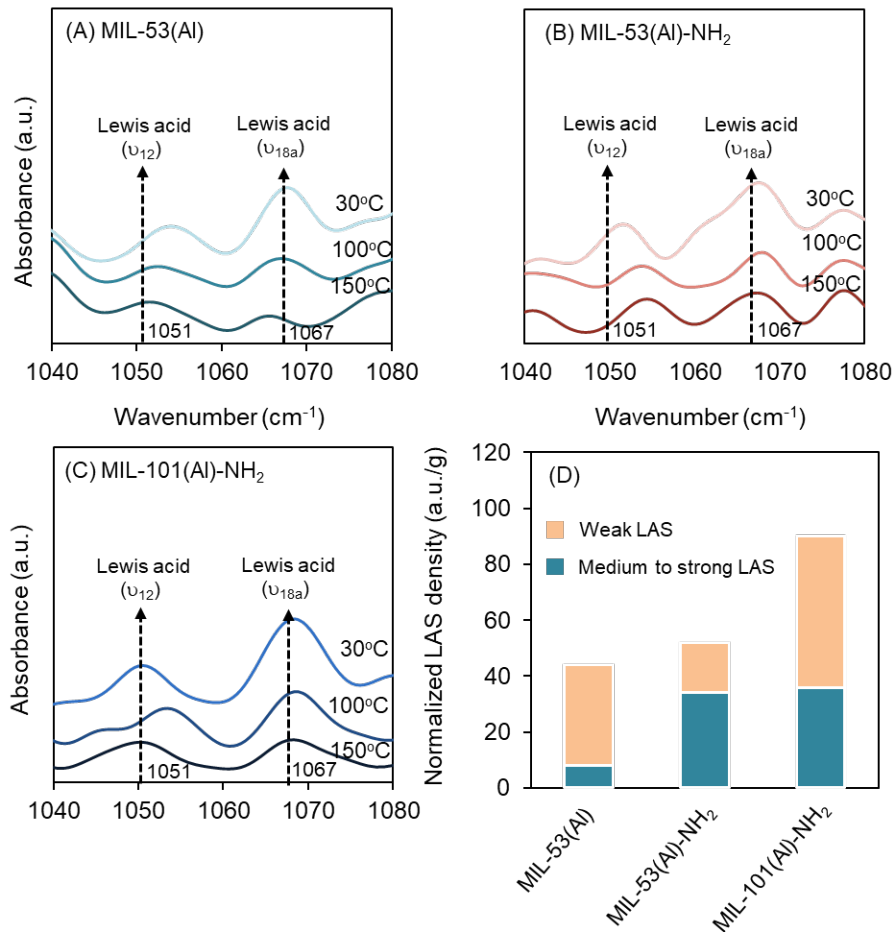


**Figure 4.2.** DRIFTS spectra with temperature programmed desorption of pyridine from MIL-53(Al) (A), MIL-53(Al)-NH<sub>2</sub> (B), MIL-101(Al)-NH<sub>2</sub> (C) and normalized LAS density (D).

### 3.2. Catalytic performance of amino-functionalized metal-organic frameworks

Because we expected that a high density of medium-to-strong Lewis acid sites improved the fructose selectivity, we conducted glucose isomerization using the synthesized Al-MOFs in ethanol at 120°C (**Table 4.1**). The catalyst loading was based on their aluminum content to understand the meaning of metal sites in catalytic performance. As a control, a blank experiment (no added catalyst) showed 8.1 wt.% glucose conversion. However, we did not observe fructose in the control reaction after 2 h, which suggested that glucose isomerization required a catalyst. The synthesized Al-MOFs were active for glucose conversion. Among all the MOFs tested, MIL-101(Al)-NH<sub>2</sub> demonstrated the highest specific activity and productivity of 36 h<sup>-1</sup> and 20 h<sup>-1</sup>, respectively.

Interestingly, we observed that amino groups (-NH<sub>2</sub>) in MIL-53(Al)-NH<sub>2</sub> increased both specific activity and productivity compared with the amino-free isostructural MOF (MIL-53-Al). The orders of specific activity and productivity were the same as the order of Lewis acid strengths (**Fig. 4.2**).

To evaluate the catalytic activity, we performed glucose isomerization for 4 h with the three Al-MOFs (**Fig. 4.3**). We observed glucose conversion and fructose selectivity with a trend similar to the trends for specific activity and productivity. MIL-101(Al)-NH<sub>2</sub> yielded 64% fructose selectivity at 82% glucose conversion after 4 h. To compare the quality of aluminum sites of these Al-MOF catalysts, we plotted the fructose selectivity vs. glucose conversion. MIL-101(Al)-NH<sub>2</sub> and MIL-53(Al)-NH<sub>2</sub> had the highest selectivity of fructose (50-64%) at ~25-82% glucose conversion. Whereas the MIL-53(Al) had lower selectivity to fructose compared with MIL-101(Al)-NH<sub>2</sub> and MIL-53(Al)-NH<sub>2</sub> at all conversions. These results suggested that (1) MIL-101(Al)-NH<sub>2</sub> and MIL-53(Al)-NH<sub>2</sub> had similar quality of aluminum active sites, and (2) amino groups improved glucose conversion and fructose selectivity. Overall, these results indicated that amino-functionalized MOFs enhanced the catalytic activity and fructose selectivity. Given that the MIL-101(Al)-NH<sub>2</sub> exhibited the highest selectivity to fructose and glucose conversion, we examined MIL-101(Al)-NH<sub>2</sub> further.

| <b>Table 4.1.</b> Catalyst screening for glucose isomerization |   |  |
|--|---|--|
| Catalyst   | Specific activity <sup>a</sup> (h <sup>-1</sup> ) | Productivity <sup>a</sup> (h <sup>-1</sup> ) |
| MIL-101(Al)-NH <sub>2</sub>                                    | 35.92   | 19.80  |
| MIL-53(Al)-NH <sub>2</sub>                                     | 5.16  | 1.89   |
| MIL-53(Al)   | 0.79  | 0.15   |
| Blank (no catalyst)  | 8.1 <sup>b</sup>                                  |  |

<sup>a</sup>calculated at conversion <15%, <sup>b</sup> blank yielded 8.1 wt.% glucose conversion after 2 h, 120 °C

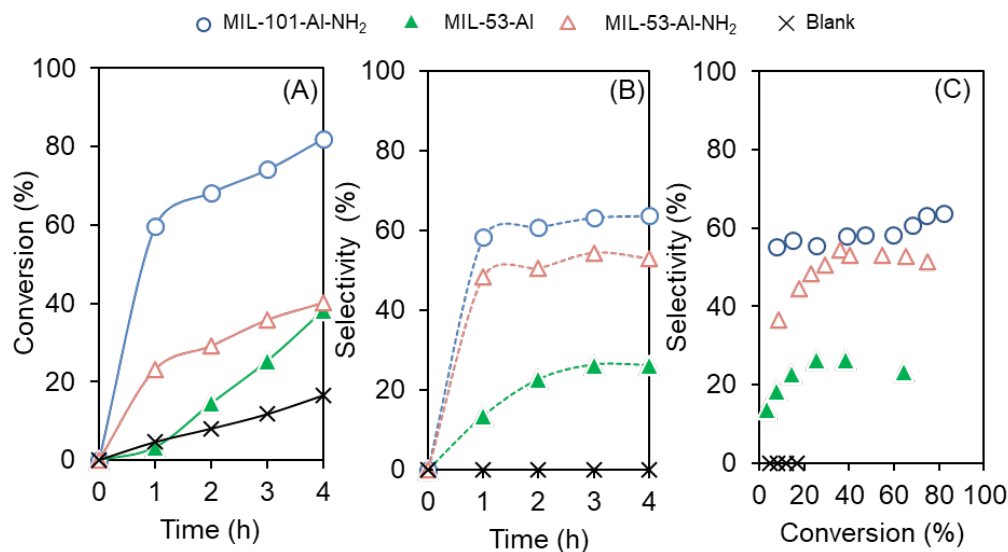


**Figure 4.3.** Glucose isomerization by selected Al-containing metal-organic frameworks. Glucose conversion (A), fructose selectivity (B), and relationship between fructose selectivity versus glucose conversion (C). Reaction condition: 5 wt. % glucose in ethanol (1 g), catalyst (glucose: metal molar ratio of 25:1), 120 °C.

### 3.3. Effects of Al-MOF precursors on glucose isomerization

To decouple the contribution of precursors of Al-MOF, we performed glucose isomerization with 2-aminoterephthalic acid (2-ATA, linker) and aluminum precursor (AlCl<sub>3</sub>) in the form of a physical mixture at 120°C for 2 h. As a control, we conducted the same glucose isomerization experiment using 1,4-benzenedicarboxylic acid, the amino-free version of 2-aminoterephthalic acid. We found that 1,4-benzenedicarboxylic acid yielded 6% glucose conversion, which indicated that free –COOH groups were not active for glucose isomerization (**Table 4.2**). Compared with 1,4-benzenedicarboxylic acid, 2-aminoterephthalic acid gave 79% glucose conversion. We observed a trace of fructose, 4.2% 5-hydroxymethylfurfural selectivity, and brown particles in the reaction mixture. These results suggested that the amino group made 2-aminoterephthalic acid more active and promoted side reactions, such as dehydration and degradation. The AlCl<sub>3</sub> catalyst showed 97% glucose conversion with 26% fructose selectivity. A physical mixture of AlCl<sub>3</sub> and 2-aminoterephthalic acid gave a moderate glucose conversion of 46% with a slight fructose formation

(3.5% fructose selectivity), whereas MIL-101(Al)-NH<sub>2</sub> exhibited 60.9% fructose selectivity at 68.2% glucose conversion. These results demonstrated the importance of coordinately unsaturated Al sites (CUS) in the amino-functional groups in MIL-101(Al)-NH<sub>2</sub> for good activity and selectivity in glucose isomerization.

| <b>Table 4.2.</b> Catalytic activity of linker and ligands for the glucose isomerization in ethanol |   |                    |                             |          |
|---|---|--------------------|-----------------------------|----------|
| Entry   | Catalyst  | Conversion (mol %) | Product selectivity (mol %) |          |
|   |   |                    | HMF                         | Fructose |
| 1   | AlCl <sub>3</sub> .6H <sub>2</sub> O <sup>a</sup> | 96.6               | 1.1                         | 26.0     |
| 2   | 2-ATA <sup>a</sup>                                | 78.5               | 4.2                         | 1.2      |
| 3   | BDC <sup>b</sup>                                  | 6.0                | 0                           | 0        |
| 4   | AlCl <sub>3</sub> +2-ATA <sup>c</sup>             | 46.0               | 2.5                         | 3.5      |
| 5   | MIL-101(Al)-NH <sub>2</sub>                       | 68.2               | 0                           | 60.9     |

<sup>a</sup>AlCl<sub>3</sub> and 2-ATA were loaded with a similar Al and 2-ATA content to MIL-101(Al)-NH<sub>2</sub>; <sup>b</sup>BCD

(benzenedicarboxylic acid) was loaded based on similar terephthalic acid equivalent to 2-ATA;

<sup>c</sup>AlCl<sub>3</sub> + 2-ATA were physically mixed with similar content to MIL-101(Al)-NH<sub>2</sub>. Reaction condition: glucose: metal (Al) molar ratio=25:1, 120 °C, 2 h, 5 wt.% glucose (0.05 g), 1 g ethanol.

### 3.4 Effects of solvents on the glucose isomerization by MIL-101(Al)-NH<sub>2</sub>

Water has been used as a common solvent for glucose isomerization. At first, we performed the glucose isomerization reaction by using three Al-MOFs in water (**Table 4.S3**). Interestingly, we obtained lower conversion (40.3%) and selectivity (35.4%) of fructose by using MIL-101-Al-NH<sub>2</sub>. The MIL-53-Al and MIL-53-Al-NH<sub>2</sub> also showed lower selectivity of fructose (**Table 4.S3**). Previous studies used MIL-101(Cr) [310], NU-1000 [254], ZIF-8 [284] for the glucose isomerization in water and they also obtained low selectivity (>32%) selectivity of fructose. Later, we investigated the effect of different solvents on the catalytic activity of glucose isomerization using MIL-101(Al)-NH<sub>2</sub>. We examined various solvents, including (1) polar protic solvent (1-propanol, 2-propanol, 1-

butanol, 2-butanol, methanol, ethanol), and (2) polar aprotic solvents (DMA, DMSO, and ethyl acetate). Ethyl acetate gave a low yield of fructose (5.9 %). DMA and DMSO have a low fructose selectivity than the primary alcohol (1-propanol, 1-Butanol) (**Fig. 4.S2**). 1-Propanol gave the selectivity of Fructose 54.8 %, whereas 2-Propanol gave the selectivity about 33.1. We observed a similar trend for another pair of primary and secondary alcohols where 1-Butanol gave the selectivity of 54.6%, but 2-Butanol gave the selectivity about 26.8%. Primary alcohol works better for the glucose isomerization reaction than secondary alcohol, and this might happen because the nucleophilic substitution on primary alcohol is higher than the secondary alcohol. Among all the solvents, ethanol has the highest selectivity of fructose (~61%). Previous studies found that ethanol changes the anomeric equilibrium of glucose, thus changing the apparent chemical equilibrium and facilitating the isomerization of glucose [311]. Visuri et al. reported that adding ethanol into water shifted the isomerization equilibrium and increased the fructose concentration in its equilibrium mixture with glucose [312]. The equilibrium change occurred due to the solvation effect because the solubility of fructose in ethanol is approximately 2.8-fold higher than the glucose at 293 K [313]. Yabushita et al. also reported a higher fructose yield (50%) by using ethanol as solvent and hydrotalcite as catalyst [314].

### **3.5. Stability and reusability of MIL-101(Al)-NH<sub>2</sub> in glucose isomerization**

The ability to reuse catalysts is important for their practical use. We recovered the MIL-101(Al)-NH<sub>2</sub> by centrifugation and washing with water to remove the residual products, intermediates, and unreacted glucose. The catalyst was then dried in a vacuum oven at 130 °C to remove moisture. We selected this temperature based on our TGA results to minimize the decomposition of MIL-101(Al)-NH<sub>2</sub>. The MIL-101(Al)-NH<sub>2</sub> catalyst maintained the catalytic performance with < 9% drop in glucose conversion, and the catalyst retained its fructose selectivity (61%) for four cycles (**Fig. 4.4A**). Further, after the 4<sup>th</sup> reuse cycle, we characterized the used MIL-101(Al)-NH<sub>2</sub> catalyst by ICP-OES, XRD, and FTIR (**Fig. 4.S3**). The aluminum content of the used catalyst, measured by ICP-OES, was 10.5 wt.%, similar to that of the fresh catalysts (11.6 wt.%); thus, minimal aluminum leaching occurred even after 4 cycles. The XRD and FTIR spectra of the used catalyst exhibited

chemical structure and functionality similar to fresh Al-MOF, which suggested minimal changes in chemical structure of the Al-MOF after reuse. Together, these filtration and characterization results demonstrated catalyst stability under the present experimental conditions. Overall, MIL-101(Al)-NH<sub>2</sub> maintained high selectivity to fructose for all the cycles and structural integrity after four recycles.

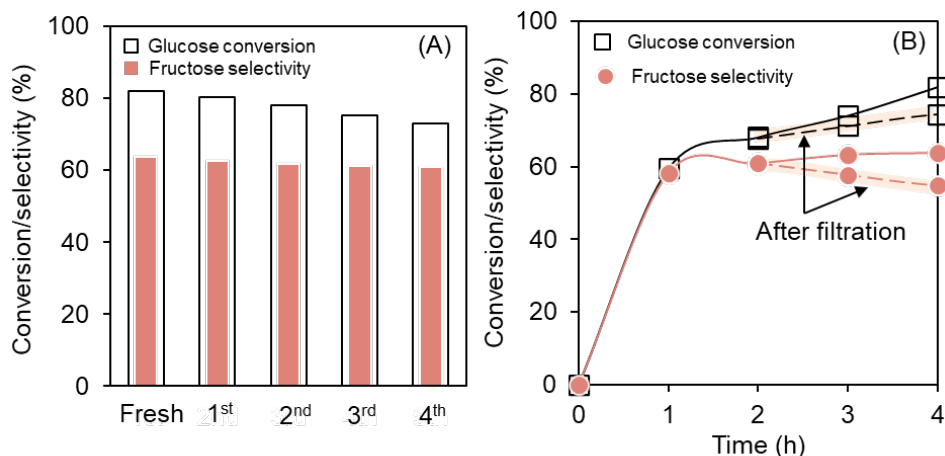


**Figure 4.4.** Reusability and stability of MIL-101(Al)-NH<sub>2</sub> for the glucose isomerization. Recycle test of MIL-101(Al)-NH<sub>2</sub> catalyst at 120 °C, 4 h (A), and filtration test after 1 h at 120 °C (B). A dashed line with orange highlight represents the reaction data after filtering the catalyst. An undashed line represents the reaction data without filtering the catalyst. Reaction condition: 5 wt. % glucose in ethanol (1 g), catalyst (glucose: metal molar ratio of 25:1), 120 °C.

To evaluate the catalyst stability under the reaction condition, we performed filtration experiments. Glucose isomerization was conducted for 1 h at 120 °C with MIL-101(Al)-NH<sub>2</sub>, followed by filtering the MIL-101(Al)-NH<sub>2</sub> catalyst from the reaction mixture, and heating the filtrate under the same reaction condition (120 °C) for 4 h (**Fig. 4.4B**). We sampled the reaction mixture three times during 4 h and monitored changes in glucose and fructose concentrations. The glucose conversion increased ~16%, in agreement with our blank experiment (no catalyst), which showed glucose conversion under the same experimental condition (**Table 4.1**). Whereas the fructose selectivity

slightly decreased. These results suggested that there was little to no Al species leaching from MIL-101(Al)-NH<sub>2</sub> into the reaction mixture.

#### 4. Discussion

We discovered the amino-based aluminum-containing metal-organic frameworks (Al-MOFs) as active and selective catalysts for glucose isomerization to fructose. The current commercial glucose isomerization process uses the enzyme glucose isomerase. However, as with any enzymic process, the reaction conditions (pH and temperature) must be strictly controlled to maintain enzyme activity; this requirement contributes to a high operating cost. We demonstrated that the MIL-101(Al)-NH<sub>2</sub> and MIL-53(Al)-NH<sub>2</sub> were selective for glucose isomerization and reached 64% fructose selectivity at 82% glucose conversion by MIL-101(Al)-NH<sub>2</sub> and 53% fructose selectivity at 75% glucose conversion by MIL-53(Al)-NH<sub>2</sub> at 120°C in ethanol.

The most significant finding was that the incorporation of the amino group enhanced fructose selectivity of MIL-101(Al)-NH<sub>2</sub>. The amino groups in the MOF structure enhanced medium-to-strong Lewis acid strength and promoted glucose conversion and fructose selectivity for glucose isomerization. MIL-101(Al)-NH<sub>2</sub> catalyst showed catalytic activity similar to that of Sn-containing  $\beta$ -zeolite in glucose isomerization (**Fig. 4.5**). In theory, the amino groups in the 2-aminoterephthalic acid linkers, electron-donating group, donate electron density to a conjugated  $\pi$  system by resonance or inductive effects, making the  $\pi$  system more nucleophilic. This increase in electron density of –COOH groups of 2-aminoterephthalic acid decreases the Lewis acid characters of coordinated unsaturated sites (CUSs) and catalytic activity of the reaction [315, 316]. Because Lewis acid sites are the active sites for glucose isomerization, we should have observed lower activity and selectivity in –NH<sub>2</sub> containing MOFs [315-317]. However, lower activity was not the case for MIL-53(Al)-NH<sub>2</sub>, which had a greater activity (glucose conversion) and fructose selectivity compared with its amino-free analog, MIL-53(Al).

Our results corroborated previous studies, which showed that amino groups of MOFs enhanced their catalytic activity for esterification [30, 318], condensation [319, 320], and photocatalysis reactions [321]. However, the origin of this enhancement by amino groups in MOFs has been debated. Caratelli et al. [318] and Hajek et al. [319] used quantum calculations to investigate the function of amino groups in UiO-66(Zr) and their contribution in esterification and aldol condensation reaction. They found that amino groups did not have a direct effect in the reaction mechanism. The location/orientation of the functional groups in the framework in different solvent environments affect the adsorption of reactants [318], hydrophobicity/hydrophilicity of the catalytic sites, porosity, and accessibility to the metal sites [317, 322]. These attributes contribute to the reactivity of MOFs in glucose isomerization. Future quantum calculation and molecular dynamic simulation studies will focus on decoupling the effect of Al sites and functional groups of Al-MOFs on glucose isomerization.

Defects in metal-organic frameworks (MOFs) have significant roles in catalytic performance. Introduction of  $\text{-NH}_2$  groups during MOF synthesis might create the defective MOFs with missing linkers. Lewis acid sites generated from the uncoordinated metal sites of missing linkers [323]. Previous studies tuned the MOFs' acid sites is by adding modulators (acetic acid, trifluoroacetic acid [324, 325], formic acid, and benzoic acid [326]) during synthesis and generated defective MOFs. Our future studies will be focused on the calculation of defect sites of MOFs, their effects on acid sites and performance in the catalytic reaction.

Our findings demonstrated that MIL-101(Al)- $\text{NH}_2$  was an active, selective, and stable catalyst for glucose isomerization in ethanol. In **Fig. 4.5**, we summarize the activity of selected catalysts for glucose isomerization to fructose. The MIL-101(Al)- $\text{NH}_2$  catalyst was superior to other MOFs because of high catalytic activity and fructose selectivity. The synthesis procedures of Al-MOFs are simple with catalytic performance for glucose isomerization comparable to the solid catalyst alternative, Sn-containing zeolites [271-275]. Our findings offer a new understanding of how amino groups increased the Lewis acid strength, and the findings could guide the development of reusable



selective catalysts for glucose isomerization. Moreover, this new understanding is expected to extend to other Lewis acid-catalyzed organic reactions [327], such as Diels-Alder [328], Meerwein–Ponndorf–Verley [329, 330], oxidation [317], Friedel-Crafts [331, 332], hydration [333], and production of 5-hydroxymethylfurfural from cellulose [273].

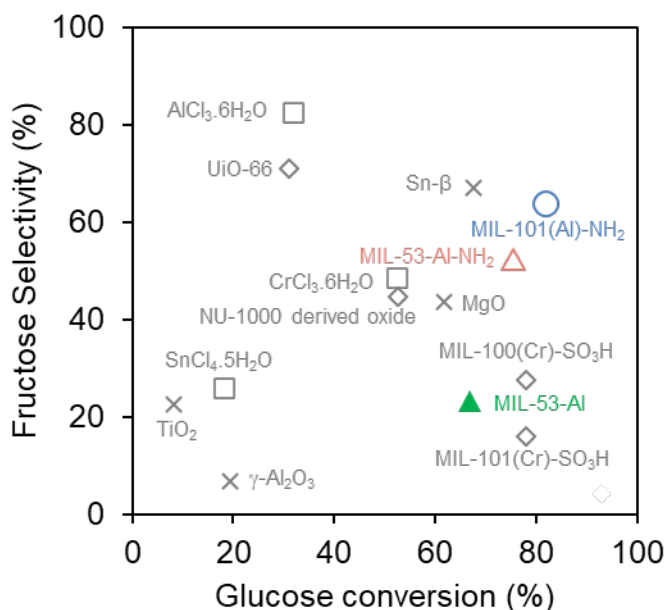


**Figure 4.5.** Selected catalysts for glucose isomerization reaction and their reactivity. These catalysts were used under different reaction conditions (glucose/catalyst loading, solvent, reaction temperature, and reaction time (see *Supplementary Information for detail, Table 4.S4*) [277, 310, 334-336].

## 5. Conclusion

We demonstrated the viability of aluminum-containing metal organic frameworks (Al-MOFs) for glucose isomerization to fructose in ethanol, and eliminated concerns about selectivity, stability, and reuse of the catalysts. MIL-101(Al)-NH<sub>2</sub> yielded 64% fructose selectivity at 82% glucose conversion at 120°C. The MIL-101(Al)-NH<sub>2</sub> retained its catalytic performance after reusing four times. These results provide a new perspective in the application of Al-MOFs for production of fructose from renewable glucose for biorefineries.

**Acknowledgements**

A part of this material is based upon work supported by the National Science Foundation under Cooperative Agreement No. 1355438 and Internal Research Grant, Office of the Executive Vice President for Research, University of Louisville. This work was performed in part at the Conn Center for Renewable Energy Research at the University of Louisville, which belongs to the National Science Foundation NNCI KY Manufacturing and Nano Integration Node, supported by ECCS-1542174. The authors would like to thank Dr. Howard Fried for his valuable comments and suggestions on the manuscript.

## 6. Supplementary Information

### 1. Materials and Methods

| <b>Table 4.S1.</b> List of chemicals/reagents used in this study |  |               |                   |
|--|--|---------------|-------------------|
| <b>Chemical</b>  | <b>Supplier</b>                            | <b>Purity</b> | <b>CAS Number</b> |
| d-glucose  | VWR International (PA, USA)                | 99%           | 50-99-7           |
| d-fructose   | Ward's science (NY, USA)                   | 100%          | 57-48-7           |
| Xylitol  | Acros Organics (NJ, USA)                   | 99+%          | 87-99-0           |
| 2-aminoterephthalic acid   | Acros Organics (NJ, USA)                   | 99%           | 10312-55-7        |
| 1,4-benzenedicarboxylic acid                                     | Acros Organics (NJ, USA)                   | >99%          | 100-21-0          |
| Aluminum chloride hexahydrate                                    | Ward's science (NY, USA)                   | 100%          | 7784-13-6         |
| Aluminum nitrate nonahydrate                                     | Ward's science (NY, USA)                   | 100%          | 7784-27-2         |
| 1,4-benzendicarboxylic acid                                      | Tokyo Chemical Industry (PA, USA)          | >99.0%        | 100-21-0          |
| Chromium nitrate nonahydrate                                     | BeanTown Chemical (NH, USA)                | 98.5%         | 7789-02-8         |
| N,N-dimethylformamide (DMF)                                      | Chem-Impex Int' l. Inc.                    | 100%          | 68-12-2           |
| Methanol   | Ward's science (NY, USA)                   | >99.8%        | 67-56-1           |
| Ethanol  | Decon Laboratories, Inc. (PA, USA)         | 200<br>Proof  | 64-17-5           |
| Acetone  | Electron Microscopy Sciences (PA ,<br>USA) | 99.8%         | 67-64-1           |
| Pyridine   | Chem-Impex Int'l. Inc. (IL,<br>USA)        | 99.97%        | 110-86-1          |

### 1.1. Synthesis of metal-organic frameworks

**Synthesis of MIL-101(Al)-NH<sub>2</sub>.** MIL-101(Al)-NH<sub>2</sub> was synthesized by the solvothermal method with a slight modification [141]. Typically, a mixture of aluminum chloride hexahydrate (0.51 g, 2 mmol) and 2-aminoterephthalic acid (0.56 g, 3 mmol) in DMF (30 mL) was kept without stirring at 130 °C for 72 h in a Teflon-lined autoclave reactor. The reactor was then cooled to ambient temperature. The remaining solids in the reaction were separated from the solution by centrifugation at 6000 RPM for 5 min. The solids were washed with DMF under sonication for 10 min, which was followed by washing with methanol at room temperature. The solid catalysts were then washed with hot (70 °C) methanol for 5 h and dried under vacuum at 80 °C overnight. Inductively coupled plasma-optical emission spectroscopy (ICP-OES) revealed the aluminum content was 11.6 wt.%.

**Synthesis of MIL-53(Al).** MIL-53(Al) was synthesized by the hydrothermal method [295]. Thirteen grams of aluminum nitrate (Al(NO<sub>3</sub>)<sub>3</sub> · 9H<sub>2</sub>O) and 2.88 g of 1,4-benzenedicarboxylic acid (BDC) were mixed in 50 mL water and kept in a Teflon-lined autoclave reactor without stirring at 220 °C for 72 h. Then, the solution was centrifuged and washed with water to a pH of 7 to remove the nitric acid that formed during the synthesis. The solid was purified by a solvent extraction method using N,N-dimethylformamide (DMF) to remove the unreacted BDC, and the solid was dried in a vacuum oven for 2 h. Then, the solid was washed with methanol to remove the DMF molecules trapped inside the MOF's pores. Finally, the solid was dried in an oven at 80 °C overnight. The as-synthesized MOF was activated by calcination[337]. A 1.5 g portion of MIL-53-Al MOF was calcined in a furnace at 330°C for 72h. Inductively coupled plasma-optical emission spectroscopy (ICP-OES) revealed an aluminum content of 12.0 wt.%.

**Synthesis of MIL-53(Al)-NH<sub>2</sub>.** MIL-53(Al)-NH<sub>2</sub> was synthesized by the solvothermal method [141]. A mixture of aluminum chloride hexahydrate (2.55 g, 10 mmol) and 2-aminoterephthalic acid (2.8 g, 15.5 mmol) in DMF (40 mL) was kept without stirring at 130 °C for 72 h in a Teflon-lined autoclave reactor. The reactor was then cooled at room temperature, and the solids were separated from the

solution by centrifugation (6000 RPM, 5 min). The solids were washed with DMF under sonication for 10 min and followed by washing with methanol at room temperature. The solid catalysts were then washed with hot (70 °C) methanol for 5 h and dried under vacuum at 80 °C overnight. The ICP-OES revealed an aluminum content of 12.1 wt.%.

### **Characterization of metal-organic frameworks**

The metal content and physiochemical properties of the synthesized catalysts were determined by X-ray diffraction (XRD), N<sub>2</sub> adsorption-desorption, Fourier-transform infrared spectroscopy (FTIR), thermogravimetric analysis (TGA), high-resolution transmission electron microscopy (HRTEM), and inductively coupled plasma-optical emission spectroscopy (ICP-OES).

#### **X-ray diffraction**

X-ray diffraction (XRD) analysis of MOF samples was performed on a Bruker D8 Discover diffractometer (Bellerica, MA, USA) using CuK<sub>α</sub> radiation in the 2θ range from 10° to 40° with 0.5 sec/step. Samples of 200 mg were used in each analysis.

#### **N<sub>2</sub> adsorption-desorption measurement**

The N<sub>2</sub> adsorption-desorption was measured by a Micromeritics Tristar (Norcross, GA, USA) instrument to calculate the surface area, pore size, and pore volume. The function of TriStar was verified with reference materials (Micromeritics). Before the measurement, the sample was pretreated at 150 °C for 3 h using a Micromeritics FlowPrep with sample degasser (Norcross, GA, USA). The surface area, S<sub>BET</sub>, was determined from N<sub>2</sub> isotherms by Brunauer–Emmett–Teller equation (BET) at -196.1 °C. BET surface area was calculated over the range of relative pressures between 0.05 and 0.3. The pore volume was estimated from the N<sub>2</sub> desorption values according to the Barrett–Joyner–Halenda (BJH) model. The pore volume was calculated as the uptake (cm<sup>3</sup>/g) at a relative pressure of 0.95. We measured the average pore size of the samples by the BJH model.

### **Fourier transform infrared spectroscopy**

Infrared spectra of the samples were recorded on a JASCO Fourier transform infrared (FTIR) spectrometer (Easton, MD, USA), equipped with an attenuated total reflection stage (ATR). The samples of ~5 mg were used in each analysis. The sample was scanned in the spectral range between 400 and 4000  $\text{cm}^{-1}$  at a 4  $\text{cm}^{-1}$  resolution. Spectra were collected using deuterated triglycine sulfate (DTGS) detector averaging 256 scans.

### **Thermogravimetric analysis**

The moisture and organic compounds on the catalysts were measured by thermogravimetric analysis (TGA) using an SDT Q600 TA instrument (New Castle, DE, USA). In short, ~20 mg of sample was placed in a cylindrical alumina crucible and heated in the air from room temperature to 700 °C with a heating rate of 10 °C/min under  $\text{N}_2$  flow (100 ml/min). The moisture content of the catalyst was calculated from the weight loss below 150 °C.

### **Transmission electron microscopy and energy-dispersive X-ray spectroscopy analysis**

To determine the microstructure and elemental distribution of the catalysts, high-resolution transmission electron microscopy (HRTEM) was performed using a Tecnai F20 (FEI company, OR, USA) microscope operating at 200 kV. The HRTEM specimens were prepared by dispersing small amounts of catalysts onto Cu grid-supported holey carbon films. For the analysis of the microstructure, scanning transmission electron microscopy (STEM) images were acquired using a high annular angle dark field (HAADF) detector (E.A. Fischione Instruments, Inc., PA, USA) and an electron probe of a 1 nm diameter. In addition, energy-dispersive X-ray spectroscopy (EDS) maps for the elemental distribution analysis were collected using a TEAM EDS (EDAX, Inc., NJ, USA) spectrometer.

### **Inductively coupled plasma-optical emission spectroscopy**

The metal content of the catalysts was determined by inductively coupled plasma-optical emission spectroscopy (ICP-OES). ICP-OES measurements were performed using a 100 mg sample

dissolved in 10 mL of nitric acid. Heating was used to ensure that the sample was completely dissolved. Once cooled, the sample was further diluted to 25 mL with double distilled water. Measurements were acquired on a Varian 720-ES spectrometer equipped with a seaspray nebulizer and cyclonic class spray chamber. Parameters included a sample intake of 1 mL/min, argon plasma flow rate of 15 L/min, and an auxiliary gas (Ar) flow rate of 1.5 L/min. The instrument was calibrated using certified reference materials manufactured by VHGTM Instrument (LGC Standards USA, NH, USA).

## 2. Results

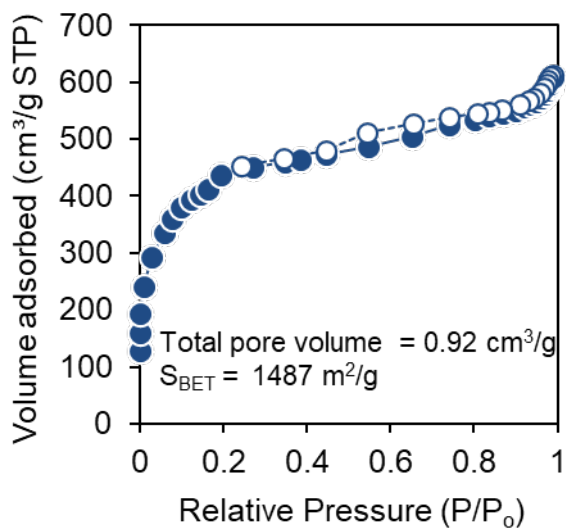


**Figure 4.S1.** Characterization of MIL-101(Al)-NH<sub>2</sub> by N<sub>2</sub> adsorption-desorption of at 77 K

| <b>Table 4.S2.</b> Calculated surface area, pore volume, average pore diameter and metal content of Al-MOFs |                     |                      |                       |                      |
|---|---------------------|----------------------|-----------------------|----------------------|
| MOFs  | Surface area        | Total pore volume    | average pore diameter | Metal content by ICP |
|   | [m <sup>2</sup> /g] | [cm <sup>3</sup> /g] | (nm)                  | (wt.%)               |
| Fresh MIL-101(Al)-NH <sub>2</sub>   | 1487                | 0.92                 | 2.73                  | 11.6                 |
| Spent MIL-101(Al)-NH <sub>2</sub>   | 871                 | 0.57                 | 2.68                  | 10.5                 |

| <b>Table 4.S3.</b> Catalytic activity of Al-MOFs for the glucose isomerization in water |                            |                    |                             |          |
|---|----------------------------|--------------------|-----------------------------|----------|
| Entry   | Catalyst                   | Conversion (mol %) | Product selectivity (mol %) |          |
|   |                            |                    | HMF                         | Fructose |
| 1   | MIL-53-Al                  | 25.2               | 0                           | 5.2      |
| 2   | MIL-53-Al-NH <sub>2</sub>  | 32.2               | 0                           | 16.9     |
| 3   | MIL-101-Al-NH <sub>2</sub> | 40.3               | 0.3                         | 35.4     |

Reaction condition: Glucose: Al molar ratio = 25:1, 5 wt.% glucose (0.05 g glucose in 1 g water),

120 °C, 2 h



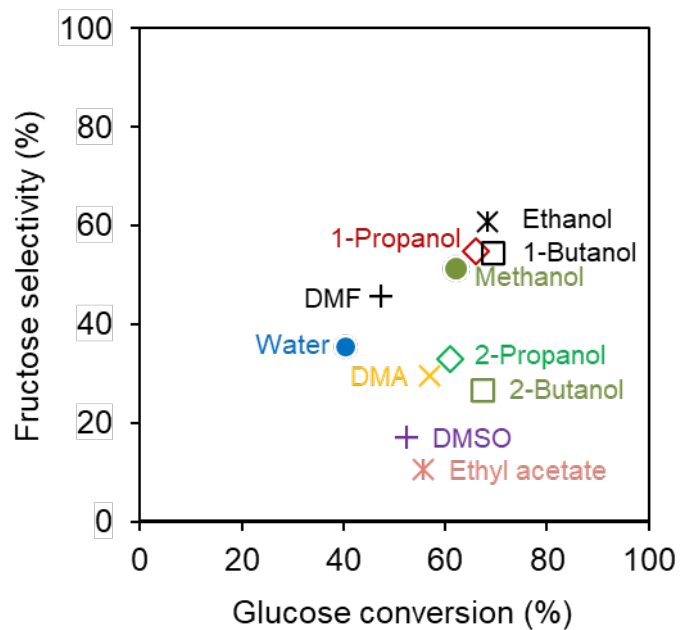


**Figure 4.S2.** Effect of solvent for glucose isomerization by MIL-101-Al-NH<sub>2</sub>. Reaction condition: 5 wt. % glucose in solvent (1 g), catalyst (glucose: metal molar ratio of 25:1), 120 °C, 2 h.

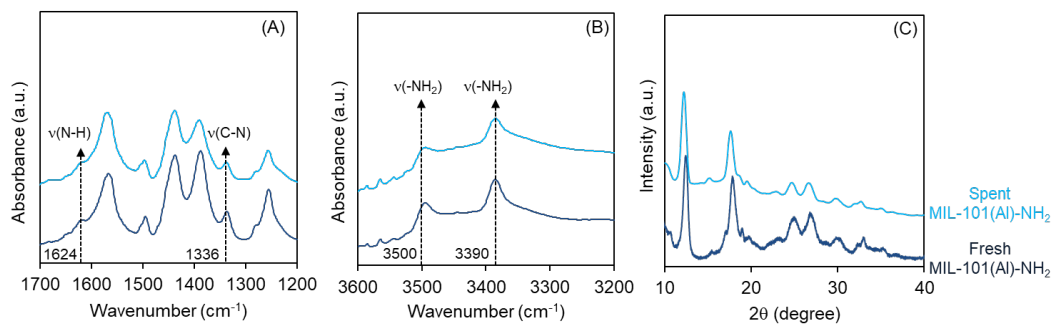


**Figure 4.S3.** Characterization of the used MIL-101(AI)-NH<sub>2</sub> after 4 reuse cycles by FTIR (A & B) and XRD (C).

### 3. Discussion

| Table 4.S4: Catalytic performance of selected homogeneous and heterogeneous catalysts |       |  |                        |                    |                          |           |
|---|-------|--|------------------------|--------------------|--------------------------|-----------|
| Type of catalysts   | Entry | Catalyst   | Glucose conversion (%) | Fructose yield (%) | Fructose selectivity (%) | Ref.      |
| Homogenous  | 1     | $\text{AlCl}_3 \cdot 6\text{H}_2\text{O}^{\text{a}}$ | 31.8                   | 26.3               | 82.7                     | [334]     |
|   | 2     | $\text{CrCl}_3 \cdot 6\text{H}_2\text{O}^{\text{a}}$ | 52.3                   | 25.4               | 48.6                     |           |
|   | 3     | $\text{SnCl}_4 \cdot 5\text{H}_2\text{O}^{\text{a}}$ | 18.2                   | 4.7                | 26.0                     |           |
| Heterogenous  | 4     | Sn $\beta$ -zeolites <sup>b</sup>                    | 67.5                   | 45.3               | 67.1                     | [335]     |
|   | 5     | $\text{MgO}^{\text{c}}$                              | 61.8                   | 27.0               | 43.6                     |           |
|   | 6     | $\gamma\text{-Al}_2\text{O}_3^{\text{c}}$            | 8.2                    | 1.9                | 22.7                     |           |
|   | 7     | $\text{TiO}_2^{\text{c}}$                            | 19.4                   | 1.32               | 6.8                      |           |
| MOFs  | 8     | MIL-101(Cr) <sup>d</sup>                             | 78.0                   | 12.6               | 16.1                     | [310]     |
|   | 9     | MIL-100(Cr)- $\text{SO}_3\text{H}^{\text{d}}$        | 78.0                   | 21.6               | 27.7                     |           |
|   | 10    | NU-1000 <sup>e</sup>                                 | 60                     | 19                 | 31.7                     | [254]     |
|   | 11    | UiO-66 <sup>f</sup>                                  | 31.0                   | 22.0               | 71.0                     | [277]     |
|   | 12    | ZIF-8 <sup>g</sup>                                   | 72.6                   | 17.0               | 23.4                     | [284]     |
|   | 13    | MIL-101(Al)- $\text{NH}_2$                           | 82                     | 52.3               | 63.8                     | This work |

<sup>a</sup> Condition: 1.0 mL  $\text{H}_2\text{O}$ , 0.25 M glucose, 25.0 mM catalyst, 120 °C, 180 min

<sup>b</sup> Condition: 1.0 mL  $\text{H}_2\text{O}$ , 0.25 M glucose, glucose:Sn = 200 : 1 by mol, 120 °C, 180 min

<sup>c</sup> Condition: 4 wt. % glucose, 2 wt. % catalyst, 100 °C, 60 min

<sup>d</sup> Condition: 0.2 g catalyst, 25 mg glucose, 2.0 g water, 100 °C, 24h.

<sup>e</sup> Condition: 100 mM glucose aqueous solution (1 mL), 10 mg catalyst, 140 °C, 5h

<sup>f</sup> Condition: 10 wt. % glucose in deionized water (4 mL), 10 mg catalyst, 140 °C, 3h

<sup>g</sup> Condition: 10 wt. % glucose in deionized water (3 mL), 40 mg catalyst, 140 °C, 3h

## CHAPTER 5

### ALUMINUM BASED METAL-ORGANIC FRAMEWORK AS WATER-TOLERANT LEWIS ACID CATALYST FOR SELECTIVE DIHYDROXYACETONE ISOMERIZATION TO LACTIC ACID<sup>3</sup>

#### 1. Introduction

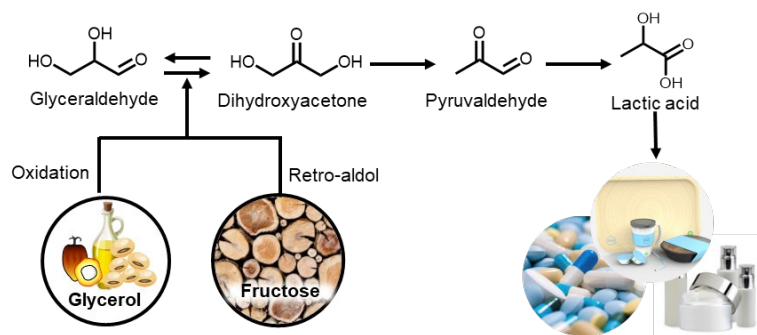
Lactic acid is an important platform chemical for biodegradable polylactic acid, propylene glycol, and acrylic acid [338]. Lactic acid can be produced by acid-catalyzed isomerization of dihydroxyacetone, obtained from biomass-derived glycerol, xylose [339-343], or fructose [344]. This acid-catalyzed isomerization reaction proceeds by a cascade of dihydroxyacetone dehydration to pyruvaldehyde and subsequent pyruvaldehyde rehydration to lactic acid (**Scheme 1**) [345, 346]. The challenge in lactic acid production is the development of effective and selective water-tolerant acid catalysts [347].

Jolimaitre et al. [348] and Rasrendra et al. [346] showed that Al<sup>3+</sup> Lewis acid salts were active and selective for dihydroxyacetone conversion to lactic acid. For example, Rasrendra et al. reported a high lactic acid yield of 90% at 100% dihydroxyacetone conversion by AlCl<sub>3</sub> [346]. However, the reaction with Lewis acid salts presents a classic problem of catalyst separation and product purification that contributes to the production cost of lactic acid. Sun et al. used Sn-containing  $\beta$ -zeolites, unique solid Lewis acid catalysts, and achieved an attractive lactic acid yield of 86% from dihydroxyacetone [349]. The Lewis acid sites in Sn-  $\beta$  zeolites are hypothesized to be responsible for the high lactic acid selectivity. Although Sn-containing zeolites are active for dihydroxyacetone conversion, they deactivated after three cycles due to the formation of coke and humins that prevent diffusion of substrates [350].

---

<sup>3</sup> This chapter has been published in *ChemCatChem* (Rahaman et al., 2022, *ChemCatChem*, 14, e202101756). The copyright clearance from the publisher has been included in the "APPENDIX" section.

Alternatively, Dapsens et al. described the desilication of commercial ZSM-5 zeolites and achieved >90% lactic acid selectivity at 91% conversion at 140 °C for 6 h [351]. However, desilication weakens the zeolite's mechanical strength and severely damages the microporous framework [352, 353]. Thus, the industry needs efficient heterogeneous catalysts with recyclability for dihydroxyacetone isomerization to lactic acid.



**Scheme 1.** Chemical pathway for lactic acid production and its use.

Inspired by the high activity and selectivity of Al Lewis acid salts for dihydroxyacetone isomerization to lactic acid [346, 348], we set out to develop an efficient Al-derived solid Lewis acid catalyst. To do so, we investigated the catalytic activity of Al-based metal-organic frameworks (MOFs). Metal-organic frameworks are porous crystalline materials composed of metal clusters (nodes) connected by organic ligands that form coordination networks [23, 24, 135]. Metal-organic frameworks are attractive materials because of the ability to tailor metal centers, pore size, and functional groups along with an ease in synthesis compared with zeolitic materials. As a result, metal-organic frameworks have been used in many applications, such as energy storage [354, 355], gas adsorption [356], drug delivery [357], and solid catalysts [23, 24]. Importantly for our goal, the exposed metal nodes endow MOFs with Lewis acid sites, and the tunability of their linker can enhance MOF catalytic ability. These attributes make MOFs attractive as solid Lewis acid catalysts. Yet, although MOFs are promising catalysts for the chemical industry, they adsorb water quickly, which blocks the active sites and compromises MOF catalytic activity [358-363].

In this work, we showed that the MIL-101(Al)-NH<sub>2</sub> (Al-MOF) was a water-tolerant and active solid Lewis acid catalyst for selective dihydroxyacetone isomerization to lactic acid. The Al-MOF gave a high lactic acid yield of 88% at 120 °C after 24 h. Furthermore, we reused Al-MOF four times without loss of catalytic performance.

## **2. Experimental Section**

### **2.1 Materials**

All chemicals were used as received unless otherwise noted. **Table 5.S1** lists their CAS numbers, purity, and manufacturers.

### **2.2 Synthesis of metal-organic framework**

The MIL-101(Al)-NH<sub>2</sub> metal-organic frameworks (MOFs) were synthesized with a slight modification of the solvothermal method [141]. Typically, a mixture of aluminum chloride hexahydrate (0.51 g, 2 mmol) and 2-aminoterephthalic acid (0.56 g, 3 mmol) in 30 mL dimethylformamide (DMF) was kept without stirring in a Teflon-lined autoclave reactor at 130 °C for 72 h. Then the reactor was cooled to ambient temperature, and the solids were separated from the solution by centrifugation (6000 RPM, 5 min). Next, the solids were washed with DMF under sonication for 10 min and followed by washing with methanol at ambient temperature. Then the solid catalysts were kept in hot (70 °C) methanol for 5 h and dried under vacuum at 80 °C for overnight.

### **2.3 Characterization of the catalysts**

The metal content and physiochemical properties of the synthesized catalysts were determined by X-ray diffraction (XRD), N<sub>2</sub> adsorption-desorption, thermogravimetric analysis (TGA), high-resolution transmission electron microscopy (HRTEM), inductively coupled plasma-optical emission spectroscopy (ICP-OES), Fourier-transform infrared spectroscopy (FTIR), and diffuse reflectance infrared Fourier transform spectroscopy (DRIFTS).

### **X-ray diffraction**

X-ray diffraction (XRD) analysis of samples was conducted on a Bruker AXS Model D8 Advance A28 diffractometer (Germany) using CuK $\alpha$  radiation in the  $2\theta$  range from 5° to 40° with 0.02 degree/step. Samples of 200 mg were used in each analysis.

### **N<sub>2</sub> adsorption-desorption measurement**

The surface area, pore size, and pore volume of the catalysts were calculated from N<sub>2</sub> adsorption-desorption measured by a Micromeritics Tristar (Norcross, GA, USA) instrument. The TriStar was calibrated with reference materials (Micromeritics, Norcross, GA, USA). Prior to the measurement, the sample was pretreated at 130 °C for 4 h using a Micromeritics FlowPrep with sample degasser (Norcross, GA, USA). The surface area,  $S_{\text{BET}}$ , was determined from N<sub>2</sub> isotherms by Brunauer–Emmett–Teller equation (BET) at -196.15 °C [174, 175]. The BET surface area was calculated in the range of relative pressures between 0.05 and 0.3. The pore volume was estimated from the N<sub>2</sub> desorption values according to the Barrett–Joyner–Halenda (BJH) model [178]. The pore volume was calculated as the uptake (cm<sup>3</sup>/g) at a relative pressure of 0.95. The average pore size of the samples was measured by the BJH model [179, 180].

### **Thermogravimetric analysis**

To determine the thermal stability of catalysts, thermogravimetric analysis (TGA) was performed with an SDT Q600 TA instrument (New Castle, DE, USA). In short, ~20 mg of the sample was placed in a cylindrical alumina crucible and heated in the air from ambient temperature to 700 °C with a heating rate of 10 °C/min under N<sub>2</sub> flow (100 ml/min). The change in weight of samples was used to determine the moisture content, decomposition of the linkers, and formation of metal oxides.

### **Transmission electron microscopy and energy-dispersive X-ray spectroscopy analysis**

To determine the microstructure and elemental distribution of the catalysts, high-resolution transmission electron microscopy (HRTEM) was performed using a Tecnai F20 (FEI company, OR,

USA) microscope operating at 200 kV. The HRTEM specimens were prepared by dispersing small amounts of catalysts onto Cu grid-supported holey carbon films. For the analysis of the microstructure, scanning transmission electron microscopy (STEM) images were acquired using a high annular angle dark field (HAADF) detector (E.A. Fischione Instruments, Inc., PA, USA) and an electron probe of a 1 nm diameter. In addition, energy-dispersive X-ray spectroscopy (EDS) maps for the elemental distribution analysis were collected using a TEAM EDS (EDAX, Inc., NJ, USA) spectrometer.

#### **Inductively coupled plasma-optical emission spectroscopy**

The metal content of the catalysts was determined by inductively coupled plasma-optical emission spectroscopy (ICP-OES). ICP-OES measurements were performed using a 100 mg sample dissolved in 10 mL of nitric acid. Heating was used to ensure that the sample was completely dissolved. Once cooled, the sample was further diluted to 25 mL with double distilled water. Measurements were acquired on a Varian 720-ES spectrometer equipped with a seaspray nebulizer and cyclonic class spray chamber. Parameters included a sample intake of 1 mL/min, argon plasma flow rate of 15 L/min, and an auxiliary gas (Ar) flow rate of 1.5 L/min. The instrument was calibrated using certified reference materials manufactured by VHG<sup>TM</sup> Instrument (LGC Standards USA, NH, USA).

#### **Fourier transform infrared spectroscopy**

Infrared spectra of samples were recorded on a JASCO Fourier transform infrared (FTIR) spectrometer (Easton, MD, USA), equipped with an attenuated total reflection stage (ATR). Samples of 5 mg were used in each analysis. The samples were scanned between 400 and 4000  $\text{cm}^{-1}$  at a 4  $\text{cm}^{-1}$  resolution. Spectra were collected using a deuterated triglycine sulfate (DTGS) detector averaging 256 scans.

### **Diffuse reflectance infrared Fourier transform spectroscopy**

Diffuse reflectance infrared Fourier transform spectroscopy (DRIFTS) with adsorbed pyridine was performed to characterize the acid sites. The temperature-programmed desorption was conducted with the JASCO FTIR equipped with a high-temperature DiffuseIR™ cell (PIKE Technology, WI, USA). The sample treatment and DRIFTS experiments with temperature-programmed desorption were conducted with a slight modification as described [182]. In short, the MOF sample (~5 mg) was placed in a cylindrical alumina crucible and treated in N<sub>2</sub> gas (50 mL/min) at 130°C for 60 min unless otherwise noted. After the pretreatment, the sample was cooled to 30 °C. The DRIFT spectrum of fresh catalyst was recorded as the background spectrum. The samples were then saturated with pyridine vapor by the flow of N<sub>2</sub> gas (50 mL/min). Then the physisorbed pyridine was removed by flushing with N<sub>2</sub> gas (50 mL/min) at 50, 100, or 150°C for 30 min before recording the DRIFT spectra. All spectra were recorded with 256 scans between 4000–400 cm<sup>-1</sup> at a 4 cm<sup>-1</sup> resolution. The amount of Lewis acid sites at each desorption temperature was calculated from the integrated area of bands (after background subtraction) of adsorbed pyridine at 1067 cm<sup>-1</sup> and 1445 cm<sup>-1</sup> [184]. Because of the limited thermal stability of Al-MOF, a lower desorption temperature (maximum 150°C) was used.

### **2.4 Isomerization of dihydroxyacetone**

Approximately 10 mg dihydroxyacetone and 2 g water were added to a 25 mL pressure tube in an oil bath. The catalyst was loaded using a dihydroxyacetone:Al molar ratio of 14:1, unless otherwise noted. The pressure tube was sealed and stirred at 600 rpm (to minimize mass transfer limitations), unless otherwise noted. The reaction was stopped by quenching in a cold water bath, then water (~5 mL) was added to dissolve the remaining dihydroxyacetone and products. The solution was centrifuged, and the residual solids were removed. The liquid sample was analyzed by HPLC to measure the concentration of dihydroxyacetone and isomerization products.



## 2.5 Product analysis and quantification

The reactants and products were analyzed by High-Pressure Liquid Chromatography (HPLC, Agilent Technology, Santa Clara, CA, USA) equipped with a refractive index detector (RID) and diode array detector. An Aminex HPX-87H (300 x 7.8 mm, Bio-Rad<sup>®</sup>, Hercules, CA, USA) was used for reactants and product separation at 60°C with 0.6 mL/min 4 mM H<sub>2</sub>SO<sub>4</sub> as a mobile phase. The concentration of reactants and products was determined by the peak area from the RID signals. Reactants and reaction products were calibrated against certified standards (Absolute Standards, Inc., Hamden, CT, USA). The dihydroxyacetone conversion, product yield, and product selectivity were calculated as follows:

$$\text{Dihydroxyacetone conversion (\%)} = \frac{\text{dihydroxyacetone reacted (mol)}}{\text{initial dihydroxyacetone (mol)}} \times 100$$

$$\text{Product yield (\%)} = \frac{\text{product generated (mol)}}{\text{initial dihydroxyacetone (mol)}} \times 100$$

$$\text{Product selectivity (\%)} = \frac{\text{product yield}}{\text{dihydroxyacetone conversion}} \times 100$$

$$\text{TOF (h}^{-1}\text{)} = \frac{\text{dihydroxyacetone reacted (mol)}}{\text{metal (mol)} \times \text{time (h)}}$$

$$\text{TON} = \frac{\text{dihydroxyacetone reacted (mol)}}{\text{metal (mole)}}$$

$$\text{Productivity (h}^{-1}\text{)} = \frac{\text{Lactic acid formed (mole)}}{\text{metal (mole)} \times \text{time (h)}} \times 100$$

## 3. Results

### 3.1 Physicochemical properties of the catalysts

To assess our catalyst's physical and chemical properties, we characterized MIL-101(Al)-NH<sub>2</sub> (Al-MOF) by XRD, N<sub>2</sub> adsorption-desorption, TGA, FTIR, ICP-OES, and HRTEM (**Fig. 5.S1**). The N<sub>2</sub> adsorption-desorption assay of the MIL-101(Al)-NH<sub>2</sub> showed a type IV isotherm, which suggested the mesoporous characteristic of Al-MOF [141]. The calculated surface area and pore volume were 1487 m<sup>2</sup>/g and 0.92 cc/g (**Table 5.S2**), respectively, similar to reported values [141-143, 145, 298,

299]. As a control, the surface area and pore volume of  $\gamma\text{-Al}_2\text{O}_3$  was 191 m<sup>2</sup>/g and 0.5 cc/g, respectively, in agreement with a report by Samad et al. [364]. The XRD pattern of MIL-101(Al)-NH<sub>2</sub> coincided with the simulated MIL-101 framework, which confirmed the formation of the MIL-101 structure [141, 299]. The STEM-HAADF images and elemental phase mapping of aluminum of MIL-101(Al)-NH<sub>2</sub> showed that this material was porous, and aluminum was highly dispersed (**Fig. 5.S1C-D**). The inductively coupled plasma-optical emission spectroscopy (ICP-OES) showed that MIL-101(Al)-NH<sub>2</sub> had an aluminum content of 11.6 wt.%.

To confirm the presence of functional groups and the thermal stability of our MIL-101(Al)-NH<sub>2</sub>, we performed FTIR and TGA (**Fig. 5.S1E-G**). The FTIR spectrum of MIL-101(Al)-NH<sub>2</sub> showed bands corresponding to the symmetric and asymmetric stretching of primary amines (3390 and 3500 cm<sup>-1</sup>) (**Fig. 5.S1F**). The presence of these amine bands suggested that the amino groups (-NH<sub>2</sub> groups) were free without coordination. Furthermore, the shoulder at 1624 cm<sup>-1</sup> corresponded to the N-H scissoring vibration. The band at 1336 cm<sup>-1</sup> corresponded to the C-N stretching absorption of aromatic amines, which confirmed the presence of -NH<sub>2</sub> groups in the MOF [143]. Thermal stability is an essential property of catalysts to ensure continuous operation without losing their structural integrity and catalytic performance. The TGA profile of MIL-101(Al)-NH<sub>2</sub> exhibited three mass loss zones between 30–150 °C (~10 wt. %), 150–380 °C (~20 wt. %), and 380–680 °C (~33 wt. %). These mass reductions corresponded, respectively, to (1) the evaporation of the water molecules, (2) the degradation of organic linkers, and (3) the degradation of the organic 2-aminoterephthalic acid-Al<sup>3+</sup> complexes.

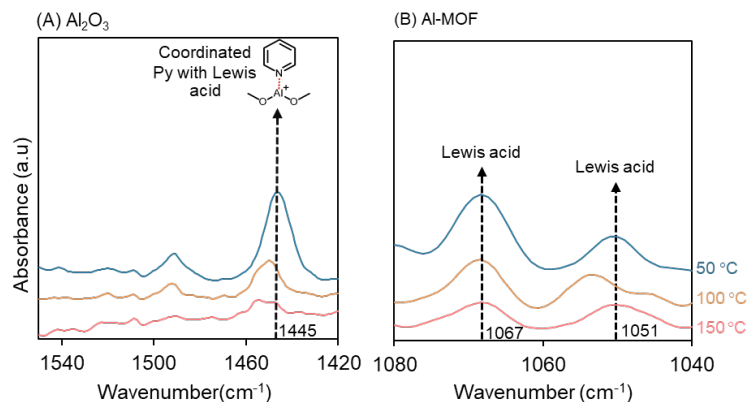


**Figure 5.1.** Diffuse reflectance infrared Fourier transform (DRIFT) spectra of adsorbed pyridine with  $\gamma$ - $\text{Al}_2\text{O}_3$  (A) and MIL-101(Al)- $\text{NH}_2$  (B).

### 3.2 Acid properties of the catalysts

Selective dihydroxyacetone isomerization to lactic acid requires acid catalysts for the cascade of dihydroxyacetone dehydration to pyruvaldehyde, followed by pyruvaldehyde rehydration to lactic acid. Hence, it is essential to distinguish and quantify the acid sites of catalysts. To characterize the acid sites, we performed temperature-programmed desorption using DRIFTS with adsorbed pyridine on  $\gamma$ - $\text{Al}_2\text{O}_3$  and MIL-101(Al)- $\text{NH}_2$  (**Fig. 5.1**). Currently, there are no ideal techniques for acid site identification and determination for MOFs [365]. We chose pyridine as an in-situ titrant for probing the acid site density of MOFs because of previous observations of Lewis acid and Brønsted acid sites in MOFs [195-197]. The DRIFT spectrum of MIL-101(Al)- $\text{NH}_2$  MOF had characteristic bands at 1067 and 1051  $\text{cm}^{-1}$ , corresponding to the coordination between pyridine and Lewis acid sites from the  $\text{Al}^{3+}$  metal center [301, 302]. The intensity of the bands for both catalysts decreased with increasing desorption temperature from 50 to 150°C. The band for  $\gamma$ - $\text{Al}_2\text{O}_3$  at 1445  $\text{cm}^{-1}$  almost disappeared at 150°C. Conversely, the Al-MOF displayed a comparatively stronger band at 1067 and 1051  $\text{cm}^{-1}$  at 150°C, which suggested that it had stronger Lewis acid sites compared with the  $\gamma$ - $\text{Al}_2\text{O}_3$ . The DRIFT spectra of adsorbed pyridine enabled determination of Lewis acid site density (**Table 5.S2**). DRIFT results suggested that MIL-101(Al)- $\text{NH}_2$  had a greater Lewis acid strength and site density compared with  $\gamma$ - $\text{Al}_2\text{O}_3$ .

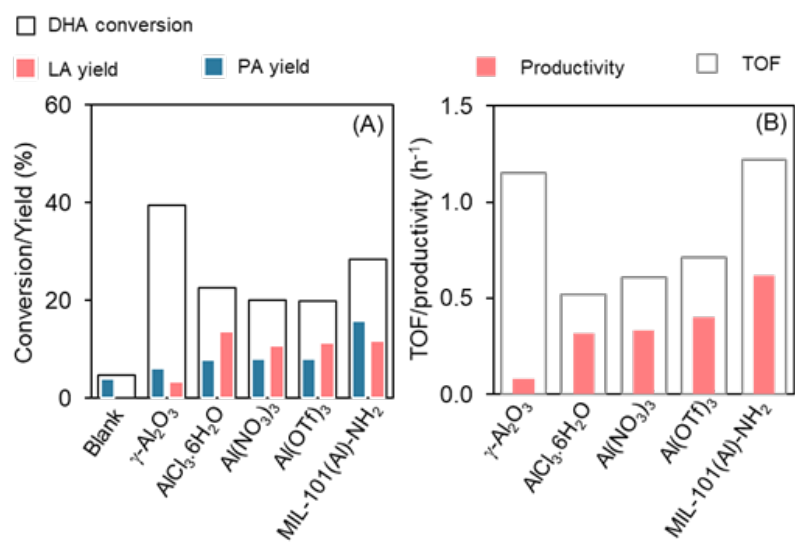


**Figure 5.2.** Catalytic activity of MIL-101(Al)-NH<sub>2</sub> and aluminum-containing homogenous and heterogeneous catalysts, conversion/yield (A), and TOF/productivity (B). Reaction condition. dihydroxyacetone: Al molar ratio = 14:1, 90 °C, 4 h, 10 mg dihydroxyacetone in 2 g water. DHA, PA, and LA indicate dihydroxyacetone, pyruvaldehyde, and lactic acid, respectively.

### 3.3 Screening of aluminum-containing catalysts for dihydroxyacetone conversion

We measured the efficiency of the dihydroxyacetone isomerization to lactic acid by evaluating the catalytic performance of selected aluminum-containing catalysts in water at 90°C for 4h and a dihydroxyacetone:Al molar ratio of 14:1 (**Fig. 5.2**). Pyruvaldehyde and lactic acid were the primary reaction products. Our blank (without catalyst) experiment showed <5% dihydroxyacetone conversion. These results indicated that catalysts were needed to facilitate this reaction. The  $\gamma$ -Al<sub>2</sub>O<sub>3</sub> was the most active with 42.7% dihydroxyacetone conversion. However, these catalysts differed in lactic acid productivity, with MIL-101(Al)-NH<sub>2</sub> having the greatest productivity of 0.62 h<sup>-1</sup>. All Al-containing homogeneous catalysts showed higher productivity compared with  $\gamma$ -Al<sub>2</sub>O<sub>3</sub> (**Table 5.S3**). For comparison, we calculated the productivity on the basis of total gram of catalyst (see Supplementary Information for details). We also compared the catalytic activity of dihydroxyacetone isomerization to lactic acid by MIL-101(Al)-NH<sub>2</sub> and AlCl<sub>3</sub>·6H<sub>2</sub>O at 90 °C for 24 h

(Fig. 5.S2). With the high catalytic activity and product selectivity, we chose MIL-101(Al)-NH<sub>2</sub> for further studies as a water-tolerant solid Lewis acid catalyst.

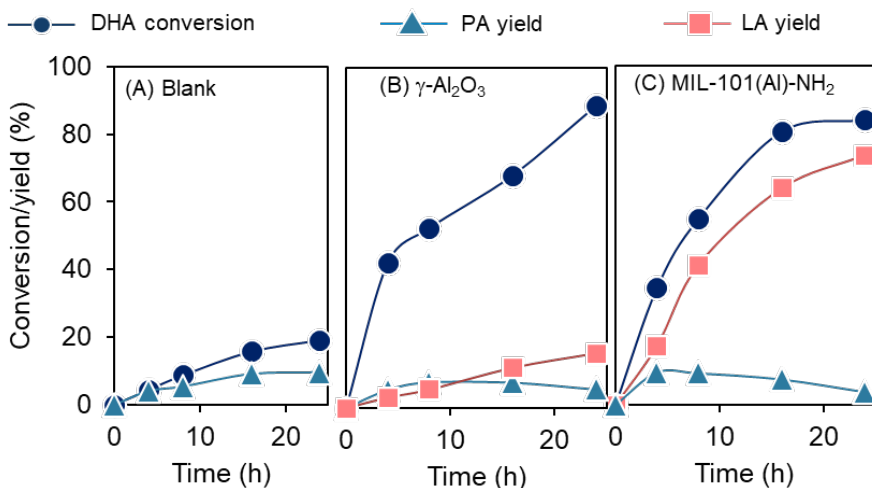


**Figure 5.3.** Catalytic activity of blank (A),  $\gamma$ -Al<sub>2</sub>O<sub>3</sub> (B), and MIL-101(Al)-NH<sub>2</sub> (C). Reaction condition. dihydroxyacetone: Al molar ratio = 14:1, 90 °C, 10 mg dihydroxyacetone in 2 g water. DHA, PA, and LA indicate dihydroxyacetone, pyruvaldehyde, and lactic acid, respectively.

### 3.4 Effect of Lewis acid sites of MIL-101(Al)-NH<sub>2</sub> MOF on dihydroxyacetone conversion

Next, we examined the product evolution of MIL-101(Al)-NH<sub>2</sub> by comparing with blank (no catalyst) and  $\gamma$ -Al<sub>2</sub>O<sub>3</sub> as our controls at 90 °C (Fig. 5.3). We chose  $\gamma$ -Al<sub>2</sub>O<sub>3</sub> as a proxy for solid Lewis acid catalyst [366-368]. The blank gave 9.6% pyruvaldehyde yield at 19.1% dihydroxyacetone conversion at 90 °C after 24h. We did not observe any lactic acid. For  $\gamma$ -Al<sub>2</sub>O<sub>3</sub>, dihydroxyacetone conversion progressively increased and reached 90% after 24 h. However, we observed a low yield of lactic acid (16%) by 24 h. We also observed a low yield of pyruvaldehyde (< 10%). We observed a brown substance on the  $\gamma$ -Al<sub>2</sub>O<sub>3</sub> surface and in the reaction mixture, which indicated formation of unwanted humin. Our observation of humin was in agreement with previous studies using zeolites [304] and Al<sub>2</sub>O<sub>3</sub> [369] as catalysts for dihydroxyacetone conversion. The Al-MOF demonstrated a progressive increase in lactic acid yield and reached 74% at 84% dihydroxyacetone conversion.

An increase in lactic acid yield and conversion of dihydroxyacetone with time suggested that Al-MOF was active and selective to lactic acid.

To elucidate the effect of the Lewis acid sites of MIL-101(Al)-NH<sub>2</sub> and  $\gamma$ -Al<sub>2</sub>O<sub>3</sub> catalysts on the dihydroxyacetone dehydration and pyruvaldehyde rehydration, we plotted lactic acid and pyruvaldehyde selectivity versus dihydroxyacetone conversion (**Fig. 5.4**). MIL-101(Al)-NH<sub>2</sub> showed high lactic acid selectivity (88%) compared with  $\gamma$ -Al<sub>2</sub>O<sub>3</sub> at similar DHA conversion, which corroborated a greater Lewis acid strength and site density of MIL-101(Al)-NH<sub>2</sub> compared with  $\gamma$ -Al<sub>2</sub>O<sub>3</sub> (**Fig. 5.1 & Table 5.S2**). Thus, the results suggested that Lewis acid sites were important in selective dihydroxyacetone isomerization to lactic acid.

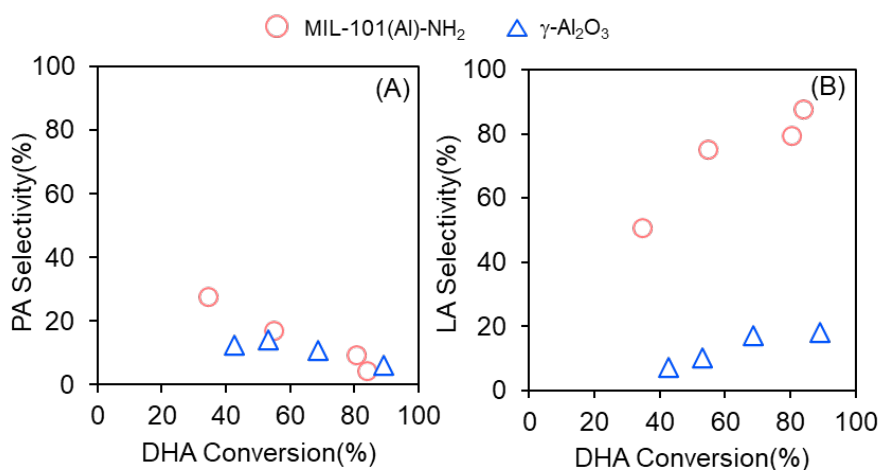


**Figure 5.4.** Comparison of catalytic activity of dihydroxyacetone isomerization to lactic acid at 90 °C by MIL-101(Al)-NH<sub>2</sub> and  $\gamma$ -Al<sub>2</sub>O<sub>3</sub>. Relationships between pyruvaldehyde selectivity vs dihydroxyacetone conversion (A) and lactic acid selectivity vs dihydroxyacetone conversion (B). Reaction condition. dihydroxyacetone: Al molar ratio = 14:1, 90 °C, 10 mg dihydroxyacetone in 2 g water over 4-24 h. DHA, PA, and LA indicate dihydroxyacetone, pyruvaldehyde, and lactic acid, respectively.

We observed pyruvaldehyde as our reaction product in our blank experiment (**Fig. 5.3A**). Hence, we could not rule out temperature-mediated dihydroxyacetone dehydration to pyruvaldehyde. To test this possibility, we used dihydroxyacetone as a reactant in water without catalysts. We heated the reaction to 90, 105, and 120 °C (**Fig. 5.S3**). Dihydroxyacetone conversion increased with increasing temperature. Pyruvaldehyde was the main reaction product. We did not observe lactic acid, which suggested that dihydroxyacetone isomerization required acid catalysts. Pyruvaldehyde yield increased and reached a maximum of 24% after 24 h at 105°C. A further increase in reaction temperature to 120°C decreased the pyruvaldehyde yield.

Next, we placed pyruvaldehyde in water without any catalyst and heated the solution at 90, 105, and 120 °C for 6 h (**Fig. 5.S4**). We found only a negligible amount of lactic acid produced (<1%). This result suggested that Lewis acid sites were needed to convert pyruvaldehyde to lactic acid. Hossain et al. also reported the formation of pyruvaldehyde from heating a dilute solution of dihydroxyacetone at 140°C [304], in agreement with our findings. Although our results suggested that dihydroxyacetone dehydration was non-catalytic and reaction temperature mediated the dihydroxyacetone dehydration, we could not rule out a mediating activity of Lewis acid sites in MIL-101(Al)-NH<sub>2</sub>.

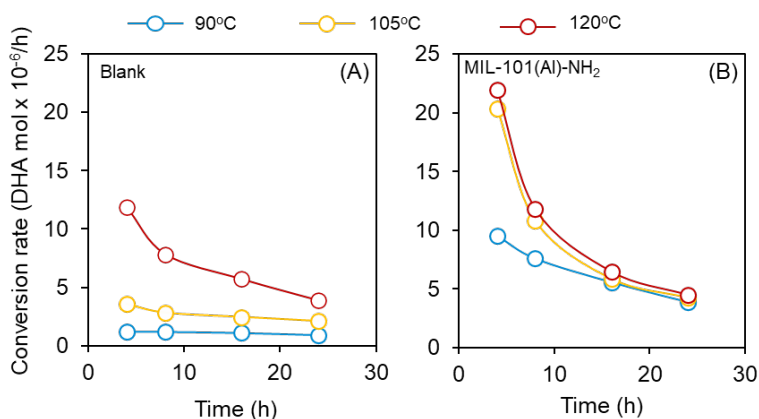


**Figure 5.5.** Effect of MIL-101(Al)-NH<sub>2</sub> catalysts and reaction temperature on dihydroxyacetone conversion rate. Reaction condition. dihydroxyacetone: Al molar ratio = 14:1 and 10 mg dihydroxyacetone in 2 g water.

Further, we compared the conversion rate of dihydroxyacetone dehydration with blank and MIL-101(AI)-NH<sub>2</sub> for 24 h (**Fig. 5.5**). The dihydroxyacetone conversion rate decreased as a function of time because the dihydroxyacetone concentration became progressively depleted. The blank experiment (without catalyst) showed a low conversion rate of dihydroxyacetone at 90 and 105 °C (1.0-3.6 μmol/h). The dihydroxyacetone conversion rate increased to 11.8 μmol/h at 120 °C after 4h. By adding MIL-101-AI-NH<sub>2</sub> as catalyst, the dihydroxyacetone conversion rate increased significantly to 22.0 μmol/h at 120 °C after 4h. These results suggested that (1) reaction temperature facilitated the dihydroxyacetone dehydration at temperature > 105 °C, and (2) at lower temperature (90 °C), the Lewis acid sites in MIL-101(AI)-NH<sub>2</sub> were needed for the dihydroxyacetone dehydration step.

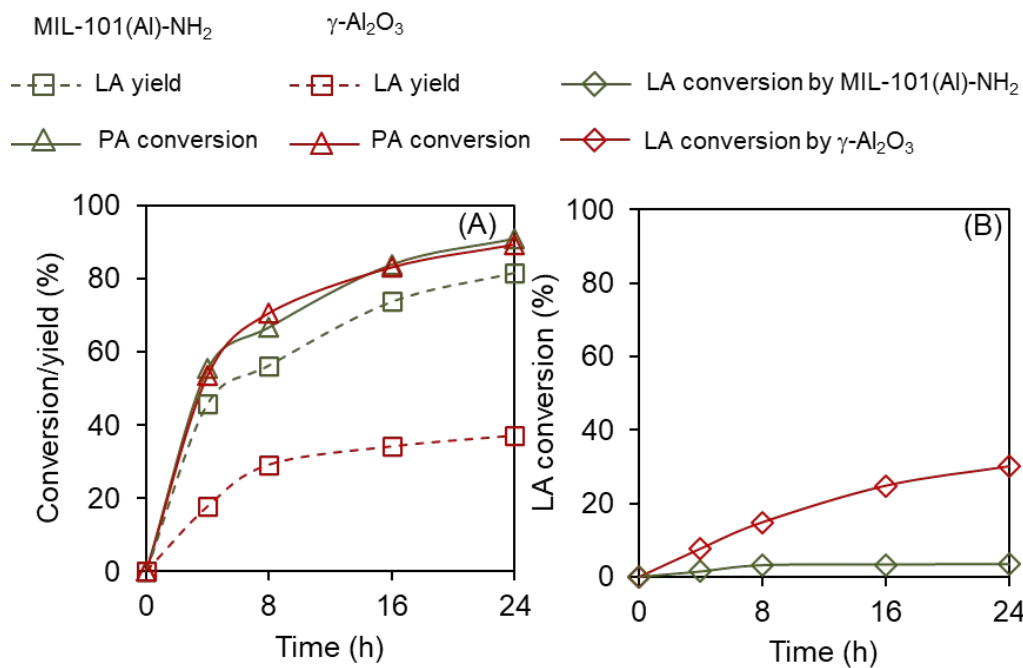


**Figure 5.6.** Catalytic activity of MIL-101(AI)-NH<sub>2</sub> and  $\gamma$ -Al<sub>2</sub>O<sub>3</sub> using pyruvaldehyde (A) and lactic acid (B) as a feed. Reaction condition. pyruvaldehyde or lactic acid: Al molar ratio = 14:1, 90 °C, 8 mg pyruvaldehyde or 10 mg lactic acid in 2 g water. PA and LA indicate pyruvaldehyde and lactic acid, respectively.



### 3.5 Effect of Lewis acid sites on pyruvaldehyde conversion and lactic acid stability

To decouple the activities of the MIL-101(Al)-NH<sub>2</sub> in pyruvaldehyde rehydration, we performed the same experiment with pyruvaldehyde as a reactant at 90°C (**Fig. 5.6A**). The Al-MOF increased lactic acid yield with time, and the yield reached 82% at 91% pyruvaldehyde conversion after 24 h. Interestingly, the lactic acid yield profiles with pyruvaldehyde as a reactant were similar to the yield with dihydroxyacetone as a reactant (**Fig. 5.3C**). Next, we used lactic acid as a reactant with the Al-MOF catalyst (**Fig. 5.6B**). We found that lactic acid was stable in Al-MOF at 90°C with only 3.5% of conversion of lactic acid after 24 h. For  $\gamma$ -Al<sub>2</sub>O<sub>3</sub>, we ran the same experiment with pyruvaldehyde and lactic acid as reactants at 90°C. We observed similar pyruvaldehyde conversion as Al-MOF but lower lactic acid yield (37% after 24 h) when using pyruvaldehyde as a reactant with  $\gamma$ -Al<sub>2</sub>O<sub>3</sub> (**Fig. 5.6A**). With lactic acid alone, we observed a higher conversion of lactic acid (30%) with  $\gamma$ -Al<sub>2</sub>O<sub>3</sub> than with Al-MOF (**Fig. 5.6B**). These results suggested that Al-MOF did not catalyze side reactions or degradation of lactic acid. Together, these results suggested that Al-MOF was selective to lactic acid and stable in the presence of lactic acid.

### 3.6 Effect of reaction temperature on the dihydroxyacetone isomerization by MIL-101(Al)-NH<sub>2</sub>

To determine the effect of reaction temperature on the catalytic performance of MIL-101(Al)-NH<sub>2</sub>, we ran the dihydroxyacetone isomerization reaction in water using MIL-101(Al)-NH<sub>2</sub> at 90, 105, and 120 °C (**Fig. 5.S5**). As a control, we used  $\gamma$ -Al<sub>2</sub>O<sub>3</sub> as the solid Lewis acid catalyst and ran the dihydroxyacetone isomerization reaction in water at 90, 105, and 120 °C as well (**Fig. 5.S6**). Pyruvaldehyde and lactic acid were major reaction products. The evolution of pyruvaldehyde yield had a volcano shape, which suggested that pyruvaldehyde was an intermediate. Using  $\gamma$ -Al<sub>2</sub>O<sub>3</sub>, we found that the dihydroxyacetone conversion and lactic acid yield increased with time and reaction temperature. For  $\gamma$ -Al<sub>2</sub>O<sub>3</sub>, dihydroxyacetone conversion and yield of pyruvaldehyde and lactic acid showed similar behaviors at 105 and 120°C. We found a high dihydroxyacetone conversion of 95%

and a 44% lactic acid yield at 120 °C after 24h (**Fig. 5.S6**). These results suggested that 105°C was the optimal reaction temperature for  $\gamma$ -Al<sub>2</sub>O<sub>3</sub>. For MIL-101(Al)-NH<sub>2</sub>, increased reaction time and temperature progressively increased the dihydroxyacetone conversion and lactic acid yield. We obtained the highest yield of lactic acid (~89%) at 97% dihydroxyacetone conversion at 120 °C after 24h (**Fig. 5.S5**). These results suggested that Lewis acid sites were required for the formation of lactic acid in water regardless of reaction temperature (90-120 °C), which corroborated our blank experiments (**Fig. 5.S3**).

### **3.7 Stability and reusability of MIL-101(Al)-NH<sub>2</sub> in dihydroxyacetone conversion**

To evaluate the catalyst stability under the reaction condition, we performed the filtration experiments by conducting the DHA isomerization using Al-MOF over 8 h at 90 °C, filtering the Al-MOF catalyst from the reaction mixture, and heating the filtrate under the same reaction condition (90 °C) for 16 h (**Fig. 5.7A**). We sampled the reaction mixture 3 times during 16 h and measured dihydroxyacetone conversion and lactic acid yield. The dihydroxyacetone conversion and pyruvaldehyde yield increased slightly during the prolonged 16 h, in line with our dihydroxyacetone conversion with blank (**Fig. 5.S3A**). Whereas the yield of lactic acid remained constant. These results suggested that (1) there was a minimal Al species leaching from Al-MOF into the reaction mixture, (2) lactic acid was stable at 90 °C over 16 h, (3) pyruvaldehyde rehydration to lactic acid required catalysts.

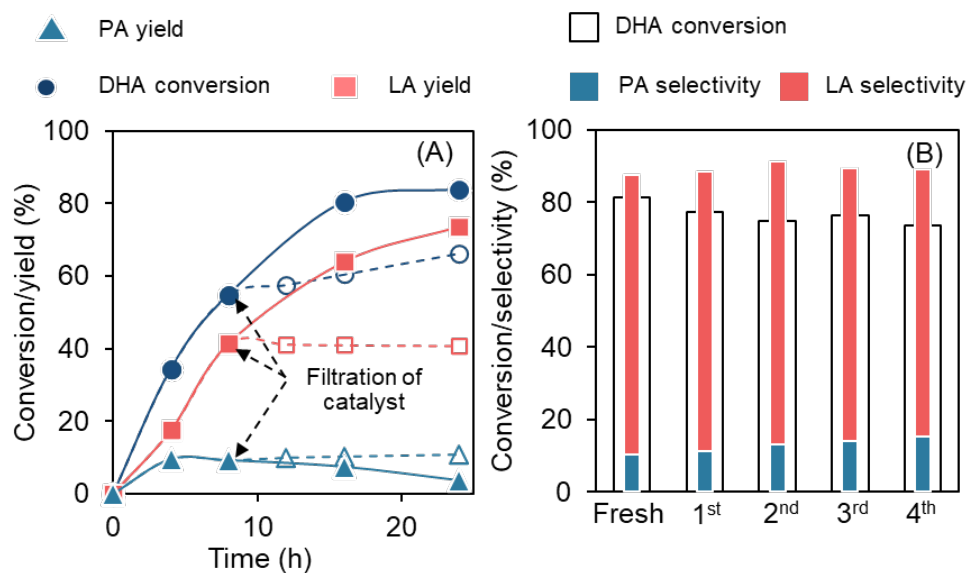


**Figure 5.7.** Stability and reusability of Al-MOFs for the dihydroxyacetone isomerization by filtration test at 90 °C (A) and recycle of MIL-101(Al)-NH<sub>2</sub> catalyst at 120 °C, 4h (B). Reaction condition. dihydroxyacetone: Al molar ratio = 14:1. DHA, PA, and LA indicate dihydroxyacetone, pyruvaldehyde, and lactic acid, respectively.

The ability to recycle catalysts is important for their practical use. We recycled the MIL-101(Al)-NH<sub>2</sub> by centrifugation and washing with water to remove the residual products, intermediates, and unreacted dihydroxyacetone. The catalyst was then dried in a vacuum oven at 130°C to remove moisture. We selected this temperature based on our TGA results to minimize the decomposition of Al-MOFs. The Al-MOF catalyst maintained the catalytic performance with a <7% drop in dihydroxyacetone conversion and retained its lactic acid selectivity (73%) for four cycles (**Fig. 5.7B**). We also observed the pyruvaldehyde selectivity increased slightly over time. This slight increase in pyruvaldehyde selectivity was hypothesized because of a slight loss of Lewis acid sites and blockage of active sites. Further, we characterized the spent Al-MOF catalyst after 4th reuse cycle by ICP-OES, XRD, FTIR, and DRIFTS (**Fig. 5.S1 and 5.S7**). The aluminum content of the spent catalyst, measured by ICP-OES, was 11.0 wt.%, similar to that of the fresh catalysts (11.6 wt.%), which suggested minimal aluminum leaching even after 4 recycles. The XRD, FTIR, and DRIFT spectra of the spent catalyst exhibited similar chemical structure, functionality, and acid

properties to those of fresh Al-MOF, which suggested minimal changes in chemical structure and acid properties of the Al-MOF after reuse. Together, these filtration and characterization results suggested catalyst stability under the present experimental conditions. Overall, MIL-101(Al)-NH<sub>2</sub> maintained high lactic acid selectivity for all the cycles and structural integrity after four recycles.

#### 4. Discussion

We investigated the catalytic performance of MIL-101(Al)-NH<sub>2</sub> for dihydroxyacetone isomerization in water. The challenge in dihydroxyacetone isomerization to lactic acid is the development of active and selective solid acid catalysts. The dihydroxyacetone isomerization reaction is a cascade in which (1) dihydroxyacetone is dehydrated to pyruvaldehyde, followed by (2) pyruvaldehyde rehydrated to lactic acid. We found that the dihydroxyacetone dehydration to pyruvaldehyde is a non-catalytic reaction and can be accelerated in the presence of Lewis acids, whereas pyruvaldehyde rehydration to lactic acid requires the Lewis acid sites (**Fig. 5.S4**). Moreover, we found that Al-MOFs are active and selective toward pyruvaldehyde rehydration to lactic acid.

The most significant finding was that Al-MOF was a water-tolerant solid Lewis acid catalyst that selectively catalyzed the conversion of dihydroxyacetone to lactic acid. In **Table 5.S4**, we summarized the activity of selected catalysts for dihydroxyacetone isomerization into lactic acid. Homogeneous Al salts showed high selectivity to lactic acid (90%) (entry 16) [346]. However, homogeneous catalysts need to be separated from the products, which complicates the conversion process. Zeolites have high catalytic activity for the dihydroxyacetone isomerization and high lactic acid yield (entries 2-8) [304, 351, 370]. Sn-containing solid catalysts showed high lactic acid selectivity (>90%) with complete dihydroxyacetone conversion (entries 3, 9) [371, 372]. However, the synthesis of Sn-containing solid catalysts is complex and requires long crystallization times [271]. Most solid Lewis acid catalysts react with water and decompose or deactivate over time [373, 374]. For example, Lewis acidic H-USY-6 zeolite is effective for the isomerization of triose sugars to lactic acid. Still, coke formation and irreversible framework damage occur when lactic acid is produced under aqueous conditions [370]. Takagaki et al. used boehmite  $\gamma$ -AlO(OH) as a solid

Lewis acid catalyst for the dihydroxyacetone isomerization in water and observed 32% lactic acid selectivity at complete dihydroxyacetone conversion. Christensen et al. used Sn-Beta for the isomerization of dihydroxyacetone in water. They observed severe catalyst deactivation due to the formation of large carbonaceous deposits, which decreased the formation of lactic acid [375]. MOFs have sponge-like crystal structures, which are ideal for water capture [376, 377]. However, water could either displace the bound ligand, collapse the MOF structure, or block the active sites (metal nodes) and prevent the accessibility of reactants to the metal nodes [378]. In addition, MOFs are unstable in aqueous media [379-381]. Many MOFs, including Mg-MOFs [382], MOF-5 [383, 384], IRMOF-1 [385], deactivate rapidly in water. Our results demonstrated that MIL-101(Al)-NH<sub>2</sub> was water-tolerant and possessed Lewis acidity for selective dihydroxyacetone isomerization to lactic acid.

Another significant finding was that Lewis acid sites enhanced dihydroxyacetone dehydration to pyruvaldehyde. The activity of acid sites for dihydroxyacetone dehydration is controversial [386, 387]. Liu et al. [388] and Kim et al. [389] used Sn-MFI and Sn-MCM-41 catalysts for the conversion of dihydroxyacetone. They found that both Brønsted and Lewis acid sites were important for the selective production of lactic acid. Brønsted acids catalyzed dihydroxyacetone dehydration to pyruvaldehyde, and Lewis acids catalyzed pyruvaldehyde rehydration to lactic acid. In contrast, Santos et al. [390] reported that the water-tolerant Lewis acid Nb<sub>2</sub>O<sub>5</sub> had high catalytic activity (75% selectivity at 160 °C) to transform glyceraldehyde into lactic acid. However, they did not assess the reusability of Nb<sub>2</sub>O<sub>5</sub>. Surprisingly, our findings revealed that common solid Lewis acid catalysts, such as  $\gamma$ -Al<sub>2</sub>O<sub>3</sub>, were active but not selective to dihydroxyacetone isomerization to lactic acid. One possible reason is because lactic acid acted as a Brønsted acid catalyst and competed with the Lewis acidic sites of  $\gamma$ -Al<sub>2</sub>O<sub>3</sub>; this competition promoted side reactions and product degradation [387], which corroborated our findings of the instability of lactic acid in the presence of  $\gamma$ -Al<sub>2</sub>O<sub>3</sub>. In this current work, we further extended our previous study [304] by demonstrating that, although the reaction temperature facilitated the dihydroxyacetone dehydration, the added solid Lewis acidic Al-MOF catalysts enhanced the dihydroxyacetone conversion and pyruvaldehyde selectivity.

When starting with dihydroxyacetone, we observed pyruvaldehyde and lactic acid as reaction products, in line with the cascade reaction pathway and pyruvaldehyde as an intermediate. On the basis of the foregoing findings, **Figure 5.8** shows a proposed mechanism for dihydroxyacetone dehydration on MIL-101(Al)-NH<sub>2</sub> catalyst. The reaction proceeds by (1) keto-enol tautomerization of dihydroxyacetone to enediol derivative, (2) dehydration of enediol derivative to pyruvaldehyde, and (3) pyruvaldehyde rehydration on MIL-101(Al)-NH<sub>2</sub> to form lactic acid.

First, dihydroxyacetone interacts with Lewis acidic Al sites of MIL-101(Al)-NH<sub>2</sub> through its carbonyl and hydroxyl groups and then undergoes a keto-enol tautomerization to enediol derivative, compound **A**. The presence of Lewis acidic MIL-101(Al)-NH<sub>2</sub> accelerates the keto-enol tautomerization and subsequent dehydration by activating carbonyl and hydroxyl groups of dihydroxyacetones. Second, dehydration of enediol results in the enol form of pyruvaldehyde, which is subsequently tautomerized into pyruvaldehyde [391, 392]. Third, the pyruvaldehyde undergoes rehydration into lactic acid by MIL-101(Al)-NH<sub>2</sub>. In this step, the Lewis acidic sites of MIL-101(Al)-NH<sub>2</sub> generate protons by dissociation of H<sub>2</sub>O molecules and activate the carbon of the carbonyl group into a specific intermediate, compound **B**. Subsequently, a 1,2-hydride shift of compound **B** on Lewis acidic Al sites of MIL-101(Al)-NH<sub>2</sub> occurs by shifting proton from methine carbon to carbonyl carbon. Simultaneously abstraction of proton generated from H<sub>2</sub>O dissociation by the carbonyl oxygen enables the formation of lactic acid product. The Lewis acidic MIL-101(Al)-NH<sub>2</sub> was responsible for the selective pyruvaldehyde rehydration to lactic acid.

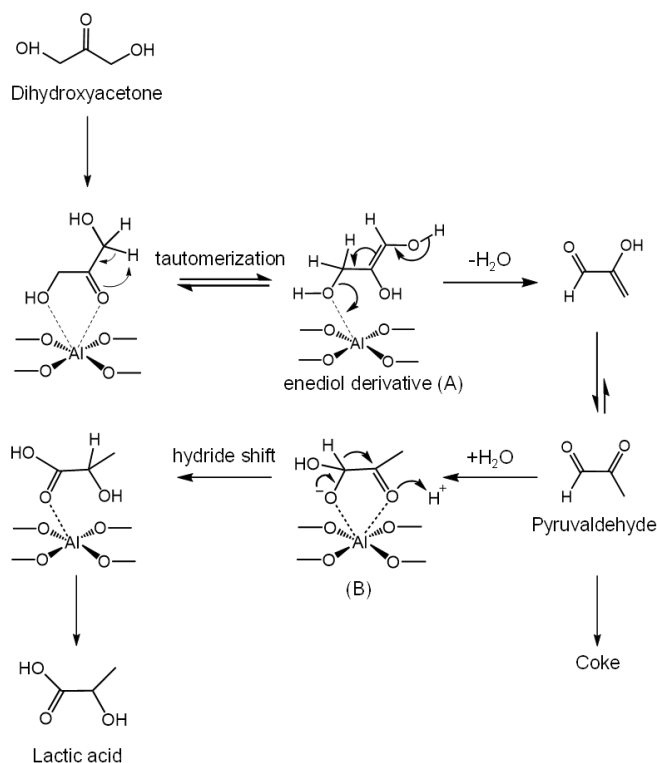


**Figure 5.8.** Proposed chemical pathway for the DHA conversion to lactic acid by MIL-101(Al)-NH<sub>2</sub>.

Our findings provide a new understanding of the water-tolerant Lewis acidic MIL-101(Al)-NH<sub>2</sub> for selective dihydroxyacetone isomerization to lactic acid. The development of water-tolerant and recyclable solid Lewis acid catalysts remains a challenge in lactic acid production. The understanding gained from this work can guide the design of selective solid catalysts and control reaction temperature to maximize the lactic acid yield. Moreover, the use of water-tolerant Lewis acidic MIL-101(Al)-NH<sub>2</sub> could be extended to other aqueous acid-catalyzed biomass conversion reactions, such as isomerization [393], Meerwein–Ponndorf–Verley reduction [394], acetalization [395], hydrolysis [396], esterification [397], condensation [398], and dehydration.

## **5. Conclusion**

We present a new catalytic strategy for dihydroxyacetone isomerization to lactic acid by Lewis acidic MIL-101(Al)-NH<sub>2</sub> metal-organic framework (MOF). We found that the Lewis acidic MIL-101(Al)-NH<sub>2</sub> MOF facilitated the dehydration of dihydroxyacetone to pyruvaldehyde. The Lewis acidic MIL-101(Al)-NH<sub>2</sub> MOF enhanced the subsequent pyruvaldehyde rehydration to lactic acid. These findings underscore the importance of MIL-101(Al)-NH<sub>2</sub> as a promising water-tolerant Lewis acid catalyst for lactic acid production. Further research may extend this work by investigating the cooperative effect of temperature and Lewis acidic MIL-101(Al)-NH<sub>2</sub> MOF, elucidating the function of amino groups in the linker, and developing of the techno-economic analysis model for the feasibility of using Al-MOF as catalyst.

## **Acknowledgements**

A part of this material is based upon work supported by the National Science Foundation under Cooperative Agreement No. 1355438 and Internal Research Grant, Office of the Executive Vice President for Research, University of Louisville. This work was performed in part at the Conn Center for Renewable Energy Research at the University of Louisville, which belongs to the National Science Foundation NNCI KY Manufacturing and Nano Integration Node, supported by ECCS-1542174. The authors would like to thank Dr. Howard Fried for his valuable comments and suggestions on the manuscript.



## 6. Supplementary Information

### 1. Experimental Section

**Table 5.S1.** List of chemicals/reagents used in this study

| Chemical                           | Supplier                                    | Purity | CAS Number |
|------------------------------------|---|--------|------------|
| Dihydroxyacetone                   | Oakwood Chemical (Estil, SC, USA)           | 95%    | 96-26-4    |
| Pyruvaldehyde                      | VWR International (Radnor, PA, USA)         | 40%    | 78-98-8    |
| Lactic acid                        | VWR International (Radnor, PA, USA)         | 88%    | 79-33-4    |
| $\gamma$ -alumina                  | Sasol (Sandton, South Africa)               | -      | 1344-28-1  |
| 2-aminoterephthalic acid (2-ATA)   | Acros Organics (Fair Lawn, NJ, USA)         | 99%    | 10312-55-7 |
| 1,4-benzenedicarboxylic acid (BDC) | Acros Organics (Fair Lawn, NJ, USA)         | >99%   | 100-21-0   |
| Aluminum chloride hexahydrate      | Ward's science (West Henrietta, NY, USA)    | 100%   | 7784-13-6  |
| N,N-dimethylformamide (DMF)        | Chem-Impex Int'l. Inc.                      | 100%   | 68-12-2    |
| Methanol                           | Ward's science (West Henrietta, NY, USA)    | >99.8% | 67-56-1    |
| Pyridine                           | Chem-Impex Int'l. Inc. (Wood Dale, IL, USA) | 99.97% | 110-86-1   |

## 2. Results

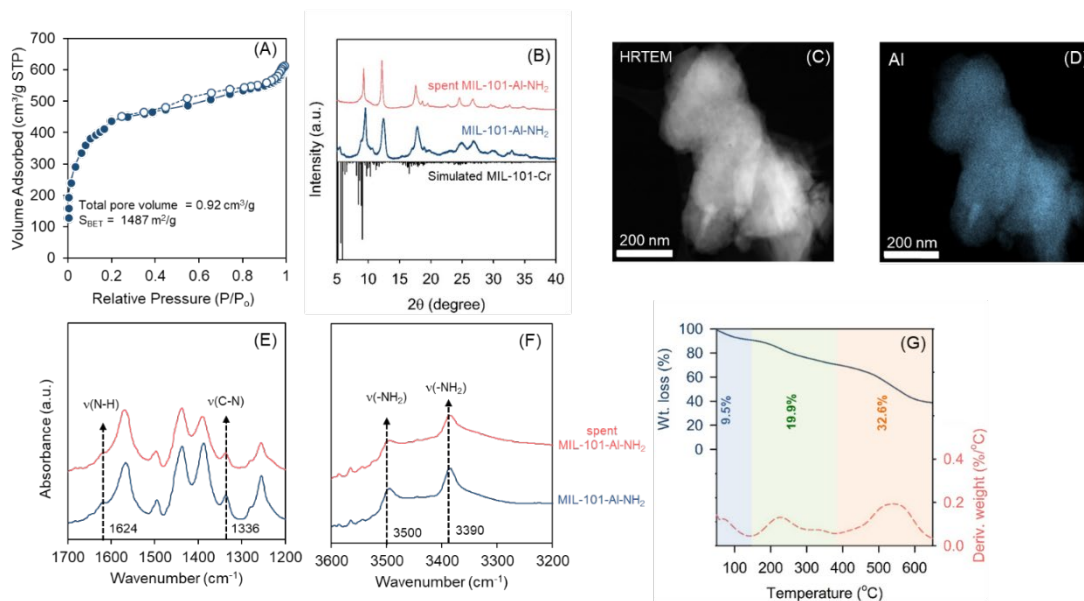


**Figure 5.S1.** N<sub>2</sub> adsorption-desorption isotherm of MIL-101(AI)-NH<sub>2</sub> at -196.15°C (A), x-ray diffractogram of MIL-101(AI)-NH<sub>2</sub>, spent MIL-101(AI)-NH<sub>2</sub> and its simulated 101 framework (B), high-resolution transmission electron microscopy (HRTEM) images (C), Al mapping (D), FTIR of MIL-101(AI)-NH<sub>2</sub> and spent MIL-101(AI)-NH<sub>2</sub> (E-F), and TGA profile of MIL-101(AI)-NH<sub>2</sub> (G).

**Table 5.S2.** Physical properties of catalysts used in this study

| Catalyst                         | Physicochemical properties          |   |                    |                           |
|----------------------------------|-------------------------------------|---|--------------------|---------------------------|
|                                  | V <sup>a</sup> (cm <sup>3</sup> /g) | S <sub>BET</sub> <sup>b</sup> (m <sup>2</sup> /g) | Pore diameter (nm) | LAS <sup>c</sup> (a.u./g) |
| MIL-101(Al)-NH <sub>2</sub>      | 0.92                                | 1487  | 2.49               | 90.6 (83.5) <sup>d</sup>  |
| γ-Al <sub>2</sub> O <sub>3</sub> | 0.50                                | 191   | 10.5               | 65.4 (58.4) <sup>e</sup>  |

Note. (a) Total pore volume. (b) BET surface area (c) area integral (a.u.)/g catalyst by diffuse reflectance infrared Fourier transform spectroscopy (DRIFTS) at 150 °C. <sup>d,e</sup> values in parenthesis indicate the calculated Lewis acid site density of spent catalysts

**Table 5.S3.** Turnover frequency (TOF) and productivity of selected aluminum-containing catalysts toward dihydroxyacetone isomerization

| Entry | Catalyst                             | DHA conv. (%) | TOF <sup>a</sup> (h <sup>-1</sup> ) | TON <sup>b</sup> | Productivity <sup>c</sup> (h <sup>-1</sup> ) | Productivity <sup>d</sup> (h <sup>-1</sup> ) | Yield (%) |      |
|-------|--------------------------------------|---------------|-------------------------------------|------------------|--|--|-----------|------|
|       |                                      |               |                                     |                  |  |  | PA        | LA   |
| 1     | γ-Al <sub>2</sub> O <sub>3</sub>     | 42.70         | 1.15                                | 4.60             | 0.08   | 0.04   | 5.3       | 3.1  |
| 2     | AlCl <sub>3</sub> .6H <sub>2</sub> O | 22.50         | 0.52                                | 2.08             | 0.32   | 0.12   | 7.8       | 13.7 |
| 3     | Al(NO <sub>3</sub> ) <sub>3</sub>    | 20.00         | 0.61                                | 2.45             | 0.33   | 0.08   | 8.0       | 10.8 |
| 4     | Al(OTf) <sub>3</sub>                 | 19.90         | 0.71                                | 2.83             | 0.40   | 0.08   | 8.1       | 11.3 |
| 5     | MIL-101(Al)-NH <sub>2</sub>          | 34.40         | 1.22                                | 4.89             | 0.62   | 0.02   | 9.6       | 17.5 |
| 6     | No catalyst                          | 4.40          | -                                   | -                | -  | -  | 4.1       | 0.0  |

Reaction condition. dihydroxyacetone (DHA):Al molar ratio = 14:1, 90 °C, 4h, 10 mg DHA in 2 g water, PA = pyruvaldehyde, LA = lactic acid. <sup>b</sup>TOF = mol of DHA reacted/mol of metal/h, <sup>b</sup>TON = mol of DHA reacted/mol of metal, <sup>c</sup>Productivity = mol of LA generated/mol of metal/h, <sup>d</sup>Productivity = g of LA generated/g of catalyst/h. TON was calculated at the DHA conversion < 20% [399, 400].

### Catalyst screening and determination of productivity

We can calculate productivity using the basis of total catalysts mass or just active sites. These resulting values affect our evaluation of the catalyst performance. For comparison, we calculated the productivity on the basis of mass of lactic acid and catalyst (**Table 5.S3**). The productivity based on mass was in the order of  $\text{AlCl}_3 > \gamma\text{-Al}_2\text{O}_3 > \text{Al-MOF}$ . Compared with Al-MOF,  $\text{AlCl}_3$  yielded similar selectivity to pyruvaldehyde and lactic acid (**Fig. 5.S2D and 5.S2E**), which suggested that (1)  $\text{AlCl}_3$  catalyst was selective to lactic acid production, in agreement with previous studies by Rasrendra et al. [346] and (2)  $\text{AlCl}_3$  and Al-MOF had similar quality of Al active sites. Although  $\text{AlCl}_3$  catalyzed the highest productivity on the mass basis, it is a homogenous catalyst and presents a classic problem of separation from reaction products and catalyst reuse [401, 402]. The common solid Lewis acidic catalyst, such as  $\gamma\text{-Al}_2\text{O}_3$ , had a higher productivity on the basis of mass than Al-MOF. However,  $\gamma\text{-Al}_2\text{O}_3$  catalyst was not selective to lactic acid. With the high catalytic activity, product selectivity, and potential reuse, we chose MIL-101(Al)- $\text{NH}_2$  for further studies *as a water-tolerant* solid Lewis acid catalyst.

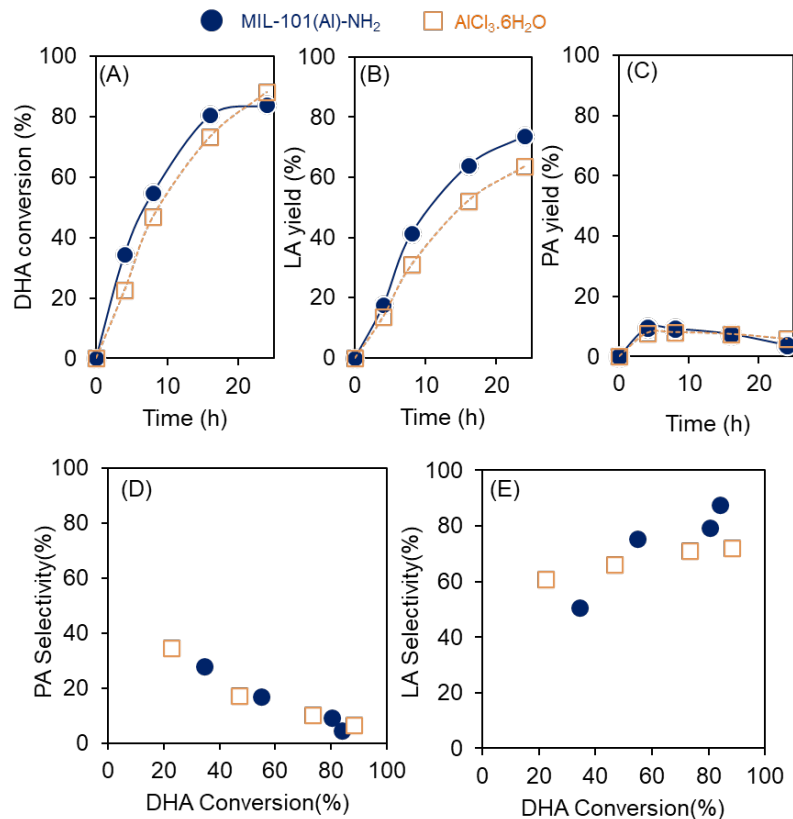


**Figure 5.S2.** Comparison of catalytic activity of dihydroxyacetone isomerization to lactic acid by MIL-101(Al)-NH<sub>2</sub> and AlCl<sub>3</sub>·6H<sub>2</sub>O. DHA conversion (A), LA yield (B), PA yield (C), PA selectivity vs DHA conversion (D), and LA selectivity vs DHA conversion (E). Reaction condition. dihydroxyacetone: Al molar ratio = 14:1, 90 °C, 10 mg dihydroxyacetone in 2 g water. DHA, PA, and LA indicates dihydroxyacetone, pyruvaldehyde, and lactic acid, respectively.

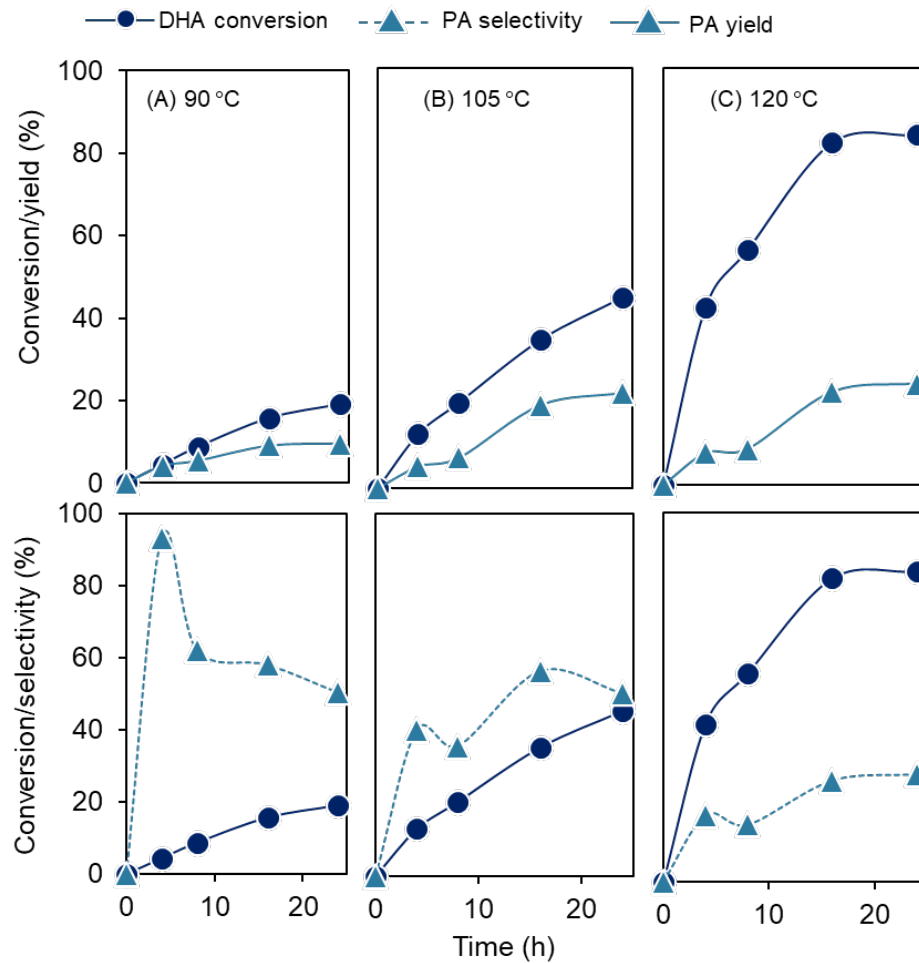


**Figure 5.S3.** Conversion of dihydroxyacetone (DHA) without added catalysts at 90 °C (A), 105 °C (B), and 120 °C (C). Reaction condition. 10 mg dihydroxyacetone in 2 g water. PA indicates pyruvaldehyde.

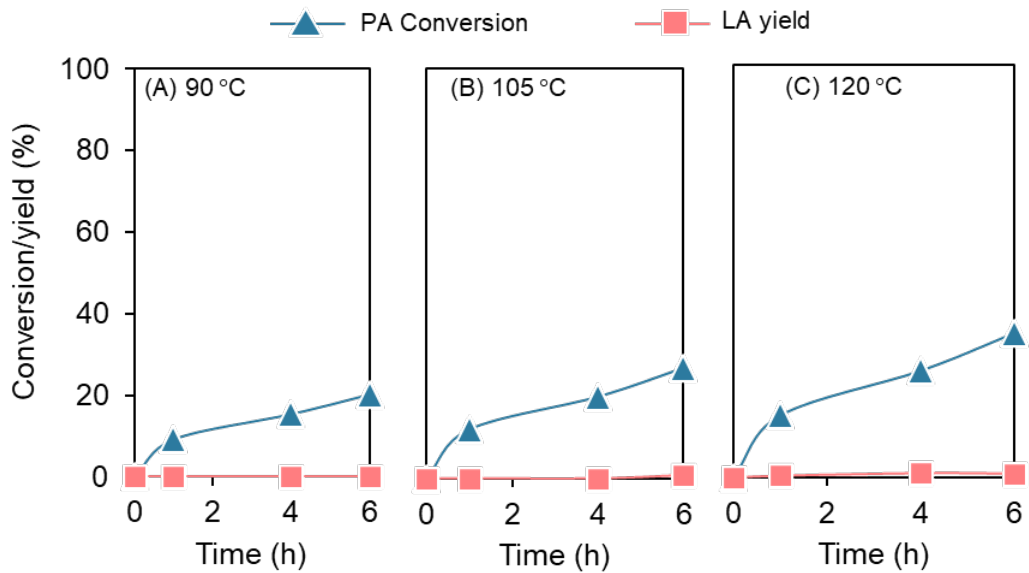


**Figure 5.S4.** Conversion of pyruvaldehyde (PA) without added catalysts at 90 °C (A), 105 °C (B), and 120 °C (C). Reaction condition. 8 mg pyruvaldehyde in 2 g water. LA indicates lactic acid.

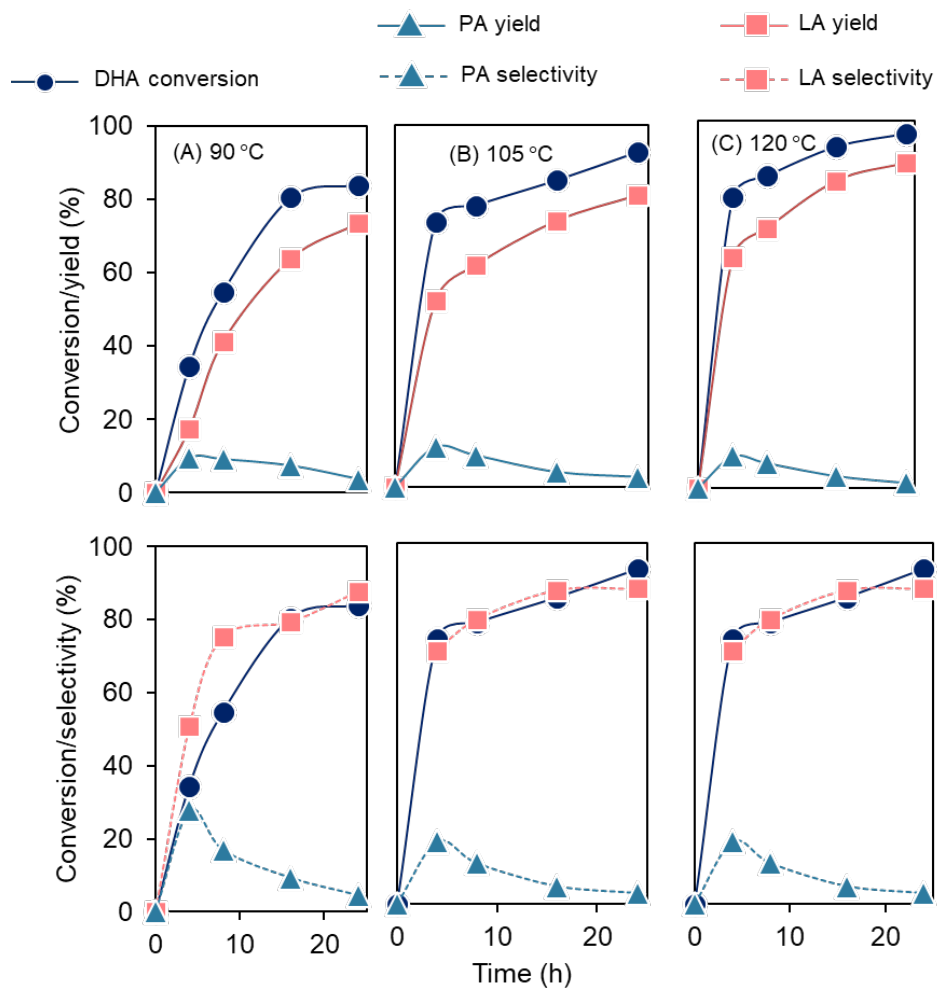


**Figure 5.S5.** Catalytic activity at different temperature of MIL-101-Al-NH<sub>2</sub> (A) 90 °C (B) 105 °C and (C) 120 °C, Reaction condition. dihydroxyacetone (DHA): Al molar ratio=14:1, 10 mg DHA in 2 g water. PA and LA indicate pyruvaldehyde and lactic acid, respectively.



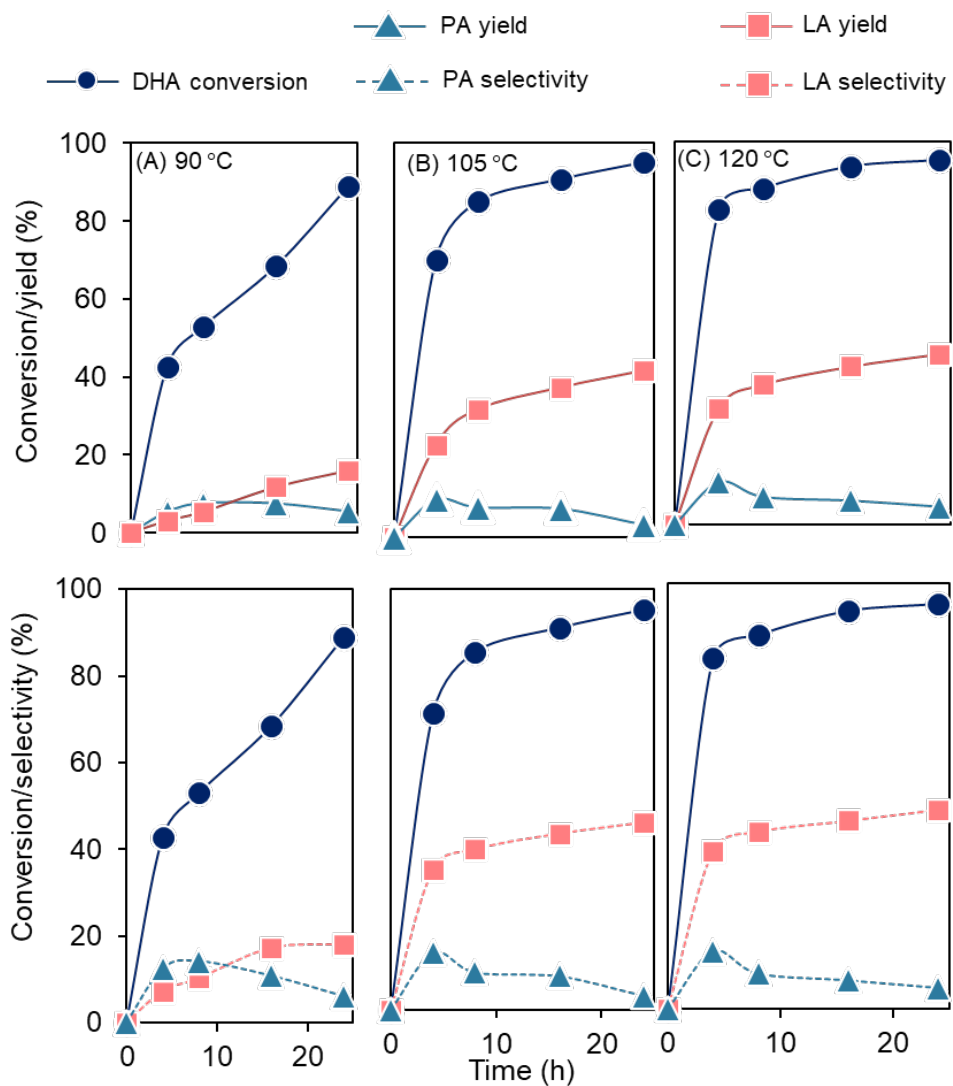


**Figure 5.S6.** Catalytic activity at different temperature of  $\gamma\text{-Al}_2\text{O}_3$  (A) 90 °C (B) 105 °C and (C) 120 °C, Reaction condition. dihydroxyacetone (DHA): Al molar ratio=14:1, 10 mg DHA in 2 g water. PA and LA indicate pyruvaldehyde and lactic acid, respectively.

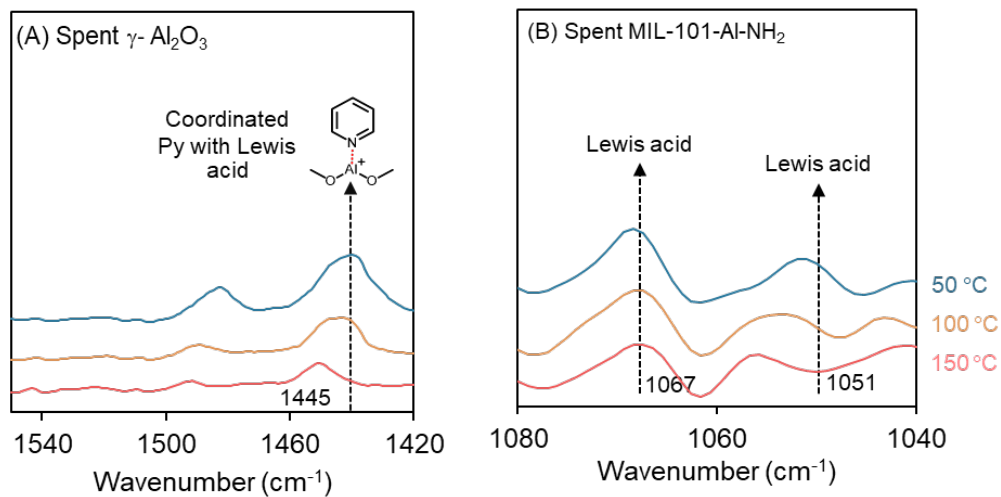


**Figure 5.S7.** Acid properties of spent  $\gamma$ -Al<sub>2</sub>O<sub>3</sub> (A) and spent MIL-101-Al-NH<sub>2</sub> (B) measured by diffuse reflectance infrared Fourier transform spectroscopy (DRIFTS) with adsorbed pyridine.

### 3. Discussion

**Table 5.S4.** Catalytic performance of selected catalysts used for dihydroxyacetone isomerization to lactic acid

| Catalyst type | Entry | Catalyst                           | Condition                         | Conversion (mol %) | Lactic acid yield (mol %) | Selectivity (mol %) | Ref.       |
|---------------|-------|------------------------------------|-----------------------------------|--------------------|---------------------------|---------------------|------------|
| MOF           | 1     | MIL-101(Al)-NH <sub>2</sub>        | 120 °C, 24 h, in H <sub>2</sub> O | 96                 | 89                        | 92                  | This study |
| Zeolites      | 2     | Pb-Sn-containing $\beta$ -zeolites | 190 °C, 2 h, in H <sub>2</sub> O  | 99                 | 52                        | 52                  | [347]      |
|               | 3     | Sn-containing Y-zeolites           | 80 °C, 5 h, in H <sub>2</sub> O   | 99                 | 89                        | 90                  | [371]      |
|               | 4     | H-USY-6 (Si/Al = 6)                | 125 °C, 24 h, in H <sub>2</sub> O | 99                 | 71                        | 72                  | [370]      |
|               | 5     | H-Beta (Si/Al = 12.5)              |                                   | 99                 | 63                        | 64                  |            |
|               | 6     | H-USY-30 (Si/Al = 30)              |                                   | 99                 | 47                        | 47                  |            |
|               | 7     | Modified ZSM-5                     | 140 °C, 6 h, in H <sub>2</sub> O  | 96                 | 50                        | 52                  | [304]      |
|               | 8     | Desilicated MFI-type               | 140 °C, 6 h, in H <sub>2</sub> O  | 91                 | 73                        | 80                  | [351]      |

|                      |    |   |                                       |     |    |    |       |
|----------------------|----|---|---------------------------------------|-----|----|----|-------|
|                      |    | (ZSM-5)<br>zeolites                               |                                       |     |    |    |       |
| Metal<br>phosphate   | 9  | Silica<br>modified<br>tin(iv)<br>phosphates       | 140 °C, 5 h,<br>in H <sub>2</sub> O   | 100 | 94 | 94 | [372] |
|                      | 10 | NbPO <sup>a</sup>                                 | 150 °C, 6 h in<br>H <sub>2</sub> O    | 90  | 42 | 47 | [403] |
| Metal<br>oxide/resin | 11 | Al resin  | 100 °C, 5 h,<br>in H <sub>2</sub> O   | 100 | 42 | 42 | [346] |
|                      | 12 | Nb <sub>2</sub> O <sub>5</sub> .nH <sub>2</sub> O | 140 °C, 3 h,<br>in H <sub>2</sub> O   | >99 | 72 | 72 | [369] |
|                      | 13 | Cr-Ti<br>oxides/SiO <sub>2</sub>                  | 130 °C, 5 h,<br>in H <sub>2</sub> O   | 100 | 80 | 80 | [404] |
| Metal<br>hydroxide   | 14 | AlO(OH)   | 140 °C, 3 h,<br>in H <sub>2</sub> O   | >99 | 32 | 32 | [369] |
|                      | 15 | Ca(OH) <sub>2</sub>                               | 55 °C, 6 h, in<br>H <sub>2</sub> O    | 100 | 59 | 59 | [405] |
| Metal<br>chloride    | 16 | AlCl <sub>3</sub> .6H <sub>2</sub> O              | 140 °C, 1.5<br>h, in H <sub>2</sub> O | 100 | 90 | 90 | [346] |

<sup>a</sup> Continuous process

CHAPTER 6  
COOPERATIVE EFFECT OF LEWIS AND BRØNSTED ACIDITY IN UIO-66(ZR)  
METAL-ORGANIC FRAMEWORKS FOR ESTERIFICATION OF LEVULINIC ACID WITH  
METHANOL

**1. Introduction**

Fossil fuels are common feedstocks for current chemical productions. However, fossil fuels are non-renewable; processing fossil fuels generated a large amount of greenhouse gases, contributing to global warming. Sustainable chemical production from renewable lignocellulose can mitigate the global warming. Alkyl levulinates are versatile chemicals from lignocellulose with potential applications as solvents [406], plasticizers [407], resin precursors [408], bio-lubricants [409], fuel additives [410], and precursors to synthesize various chemicals, such as  $\gamma$ -valerolactone, pyrrolidone, 2-methyltetrahydrofuran, valeric acid [411, 412]. Production of alkyl levulinate proceeds by the esterification of cellulose-derived levulinic acid with alcohols by acid catalysts. Although various homogeneous Brønsted acid catalysts (sulfuric, phosphoric, and hydrochloric acids) catalyze this reaction [411], they pose numerous disadvantages in (1) corrosion of reactors; (2) environmental problems from disposal of chemicals; and (3) product separation and catalysts recycle. For these reasons, heterogeneous catalysts are attractive alternatives [411].

Metal-organic frameworks (MOFs) are porous solid catalysts [23, 24, 135]. Their pore-sizes and pore functionality can be tailored by varying metals and organic linkers in the framework [31]. Introducing defects during MOF synthesis enables changes in their acid sites [323]. One potential strategy to tune MOFs' acid sites is by adding modulators (acetic acid, trifluoroacetic acid [324, 325], formic acid, and benzoic acid)[326] during synthesis to outcompete the metal coordination

with linkers. Therefore, the resulting modulated MOFs contained uncoordinated metal sites, which serve as Lewis acid sites for catalytic reactions [413, 414]. For example, Vermoortele et al. used trifluoroacetic acid as a modulator to synthesize UiO-66(Zr) MOF [17]. They found that addition of modulator creates extra Lewis acid sites in MOFs, and they are highly active catalyst for several Lewis acid catalyzed reactions such as MPV of 4-tert-butylcyclohexanone (TCH) with isopropanol, cyclization of citronellal to isopulegol) etc. Atzori et al. [415] used Benzoic Acid and Morris et al. [416] used a series of carboxylic acid as modulators to synthesize defected UiO-66(Zr) MOFs. However, the nature of these defects, the cooperative effect of both Brønsted and Lewis acidity of MOFs, and their role in catalytic activity are not thoroughly investigated.

In this work, we used various amounts of acetic acid as modulators to synthesize UiO-66 MOFs, create surface defects in the framework, and evaluate the catalytic performance of these defected MOFs for the levulinic acid esterification in methanol. We found Lewis acid sites generated from the uncoordinated metal sites ( $Zr^{4+}$ ) of missing linkers and the Brønsted acidity induced from the surface hydroxyl group. The cooperative Brønsted-Lewis acid sites are responsible for the superior catalytic performance of defective UiO-66 MOFs. The UiO-66-A130 with the highest modulator concentration showed high methyl levulinate selectivity (93%) and was reusable up to 4 times without losing significant catalytic performance.

## **2. Materials and Methods**

### **2.1 Materials.**

All chemicals were used as received unless otherwise noted. **Table 6.S1** lists their CAS numbers, purity, and manufacturers.

### **2.2 Synthesis of UiO-66 with Modulators**

UiO-66 MOFs were synthesized by the previously described solvothermal method in a 45 mL Teflon-lined autoclave reactor [413]. The UiO-66 MOF without any modulator (acetic acid) referred as UiO-66-A0. The five defective UiO-66 samples (named UiO-66-A10, UiO-66-A35, UiO-66-A70,

UiO-66-A100, UiO-66-A130) were synthesized by the same method, with different amounts of acetic acid as a modulator (see **Table 6.1**).

**Table 6.1.** molar composition of the reagents during the synthesis of UiO-66 MOFs

| Sample name* | ZrCl <sub>4</sub> , mol | Terephthalate, mol | Acetic acid, mol | DMF, mol |
|--------------|-------------------------|--------------------|------------------|----------|
| UiO-66-A0    | 1                       | 1                  | 0                | 750      |
| UiO-66-A10   | 1                       | 1                  | 10               | 750      |
| UiO-66-A35   | 1                       | 1                  | 35               | 750      |
| UiO-66-A70   | 1                       | 1                  | 70               | 750      |
| UiO-66-A100  | 1                       | 1                  | 100              | 750      |
| UiO-66-A130  | 1                       | 1                  | 130              | 750      |

Here "A" indicates the acetic acid as a modulator, and the number after "A" indicates the amount (mol) of added acetic acid during the synthesis.

Briefly, a mixture of ZrCl<sub>4</sub> (1 mol) and acetic acid (quantities given in **Table 6.1**) was dissolved in N, N'-dimethylformamide (DMF, 750 mol) by using sonication for about 10 min. An equimolar ratio of the linker, terephthalate (1,4-benzenedicarboxylic acid), was added to the solution and dispersed by sonication for about 10 min. The tightly sealed autoclave was kept in an oven without stirring at 120 °C for 24 h. Then the reactor was cooled at room temperature, and the solids were separated from the solution by centrifugation (6000 RPM, 10 min). Next, the solids were suspended in DMF (10 mL) three times a day for 4h and centrifuged to remove the suspension. After then the particles were washed with ethanol (10 mL) four times for two days to remove DMF and finally dried under vacuum at 80 °C for overnight.

### 2.3 Characterization of metal-organic frameworks

The metal content and physicochemical properties of the synthesized catalysts were determined by X-ray diffraction (XRD), N<sub>2</sub> adsorption-desorption, thermogravimetric analysis (TGA), inductively

coupled plasma-optical emission spectroscopy (ICP-OES), Fourier-transform infrared spectroscopy (FTIR), and diffuse reflectance infrared Fourier transform spectroscopy (DRIFTS).

### **X-ray diffraction**

X-ray diffraction (XRD) analysis of samples was conducted on a Bruker AXS Model D8 Advance A28 diffractometer (Germany) using  $\text{CuK}\alpha$  radiation in the  $2\theta$  range from  $10^\circ$  to  $40^\circ$  with 0.02 degree/step. Samples of 200 mg were used in each analysis.

### **$\text{N}_2$ adsorption-desorption measurement**

The catalysts' surface area, pore size, and pore volume were calculated from  $\text{N}_2$  adsorption-desorption measured by a Micromeritics Tristar (Norcross, GA, USA) instrument. The TriStar was calibrated with reference materials (Micromeritics, Norcross, GA, USA). Prior to the measurement, the sample was pretreated at  $130^\circ\text{C}$  for 4 h using a Micromeritics FlowPrep with sample degasser (Norcross, GA, USA). The surface area,  $S_{\text{BET}}$ , was determined from  $\text{N}_2$  isotherms by Brunauer–Emmett–Teller equation (BET) at  $-196.15^\circ\text{C}$  [174, 175]. The BET surface area was calculated in the range of relative pressures between 0.05 and 0.3. The pore volume was estimated from the  $\text{N}_2$  desorption values according to the Barrett–Joyner–Halenda (BJH) model [178]. The pore volume was calculated as the uptake ( $\text{cm}^3/\text{g}$ ) at a relative pressure of 0.95. The average pore size of the samples was measured by the BJH model [179, 180].

### **Thermogravimetric analysis**

To determine the thermal stability of catalysts, thermogravimetric analysis (TGA) was performed with an SDT Q600 TA instrument (New Castle, DE, USA). In short,  $\sim 20$  mg of the sample was placed in a cylindrical alumina crucible and heated in the air from ambient temperature to  $700^\circ\text{C}$  with a heating rate of  $10^\circ\text{C}/\text{min}$  under  $\text{N}_2$  flow ( $100\text{ ml}/\text{min}$ ). The change in weight of samples was used to determine the moisture content, decomposition of the linkers, and formation of metal oxides.



### **Fourier transform infrared spectroscopy**

Infrared spectra of samples were recorded on a JASCO Fourier transform infrared (FTIR) spectrometer (Easton, MD, USA), equipped with an attenuated total reflection stage (ATR). Samples of 5 mg were used in each analysis. The samples were scanned between 400 and 4000  $\text{cm}^{-1}$  at a 4  $\text{cm}^{-1}$  resolution. Spectra were collected using a deuterated triglycine sulfate (DTGS) detector averaging 256 scans.

### **Inductively coupled plasma-optical emission spectroscopy**

The metal content of the catalysts was determined by inductively coupled plasma-optical emission spectroscopy (ICP-OES). ICP-OES measurements were performed using a 100 mg sample dissolved in 10 mL of nitric acid. Heating was used to ensure that the sample was completely dissolved. Once cooled, the sample was further diluted to 25 mL with double distilled water. Measurements were acquired on a Varian 720-ES spectrometer equipped with a seaspray nebulizer and cyclonic class spray chamber. Parameters included a sample intake of 1 mL/min, argon plasma flow rate of 15 L/min, and an auxiliary gas (Ar) flow rate of 1.5 L/min. The instrument was calibrated using certified reference materials manufactured by VHG<sup>TM</sup> Instrument (LGC Standards USA, NH, USA).

### **Diffuse reflectance infrared Fourier transform spectroscopy**

Diffuse reflectance infrared Fourier transform spectroscopy (DRIFTS) with adsorbed pyridine was performed to characterize the acid sites. Pyridine-DRIFT analysis is a common technique to identify and quantify the acid sites of catalysts, such as zeolites [304]. Although semi-quantitative, this technique has been applied on various MOFs, such as Fe-MOF [417], Al-MOF [418], Zr-MOF [419], and Cr-MOF [420], to investigate the surface acidic properties. We chose pyridine as an in-situ titrant for probing the Lewis acid site density of MOFs because of the success in observing Lewis acid sites in MOFs from the previous studies [25, 300, 301]. Briefly, the temperature-programmed desorption was conducted with the JASCO FTIR equipped with a high-temperature DiffuseIR<sup>TM</sup> cell (PIKE Technology, WI, USA). The sample treatment and DRIFTS experiments with temperature-

programmed desorption were conducted with a slight modification as described [182]. In short, the MOF sample (~5 mg) was placed in a cylindrical alumina crucible and treated in N<sub>2</sub> gas (50 mL/min) at 130 °C for 60 min unless otherwise noted. After the pretreatment, the sample was cooled to 30 °C. The DRIFT spectrum of fresh catalyst was recorded as the background spectrum. The samples were then saturated with pyridine vapor by the flow of N<sub>2</sub> gas (50 mL/min). Then the physisorbed pyridine was removed by flushing with N<sub>2</sub> gas (50 mL/min) at 50, 100, or 150 °C for 30 min before recording the DRIFT spectra. Because of the limited thermal stability of MOFs, a lower desorption temperature (maximum 150 °C) was used. All spectra were recorded with 256 scans between 4000–400 cm<sup>-1</sup> at a 4 cm<sup>-1</sup> resolution. The Lewis acid sites were calculated from the integrated area of bands (after background subtraction) of adsorbed pyridine at 1018 and 1067 cm<sup>-1</sup> [184].

#### **2.4 Measurement of acid properties by pH change in methanol**

The Brønsted acid properties of synthesized catalysts were determined by measuring the pH change of methanol upon suspending catalysts inside, as described by previous studies [199, 421, 422]. In short, 6 mg catalysts were suspended in 24 mL methanol and kept stirring at ambient temperature before pH measurement. This amount was selected because previous experiments, which varied the amount of catalysts, revealed that it was high enough, so the measured pH was independent of the solid amount. The pH was measured with a gel-filled, double junction electrode (Milwaukee Instruments, Inc., Rocky Mount, NC, USA). The electrode was calibrated with the pH 4, 7, and 9 buffers. All measurements were conducted in triplicate.

#### **2.5 Esterification of levulinic acid and alcohol**

The reactions were carried out using 25 mL pressure tubes in an oil bath. Typically, levulinic acid, methanol, and catalysts were added into 25 mL pressure tube, sealed, and stirred at 65 °C unless otherwise noted. The molar ratio of levulinic acid/methanol was kept at 1:25 (25 mg levulinic acid: 172.4 mg methanol) with 10.75 mg catalyst unless otherwise noted. Xylitol was used as an internal standard. The reaction was stopped by quenching in the cold water bath, followed by adding water (~10 mL) to dissolve the remaining levulinic acid and methanol. The solution was centrifuged, and

the solid catalysts were removed. The liquid sample was then plugged into HPLC for the analysis of the product distribution.

## 2.6 Product analysis and quantification

The reactants and products were analyzed by High-Pressure Liquid Chromatography (HPLC, Agilent Technology, Santa Clara, CA, USA) equipped with a refractive index detector (RID) and diode array detector (DAD). The Aminex HPX-87H (300 x 7.8 mm, Bio-Rad®, Hercules, CA, USA) was used for reactants and products separation at 60°C with 0.6 ml/min of 4mM H<sub>2</sub>SO<sub>4</sub> as a mobile phase. The concentration of the product was determined by the peak area from the RID signals. Reaction products were calibrated against certified standards (Absolute Standards, Inc., Hamden, CT, USA). The levulinic acid conversion, product yield, and product selectivity were calculated as follows:

$$\text{Levulinic acid conversion (\%)} = \frac{\text{levulinic acid reacted (mol)}}{\text{initial levulinic acid (mol)}} \times 100$$

$$\text{Product yield (\%)} = \frac{\text{product generated (mol)}}{\text{initial levulinic acid (mol)}} \times 100$$

$$\text{Product selectivity (\%)} = \frac{\text{Product yield}}{\text{LA conversion}} \times 100$$

## 3. Results

We synthesized the UiO-66(Zr) MOFs with and without any modulator. Then we characterized these MOFs by XRD, N<sub>2</sub> adsorption-desorption, TGA, FTIR, ICP-OES, DRIFT, and methanol titration to assess the effect of modulators on their physical and chemical properties. We evaluated their catalytic activity in esterification of levulinic acid with methanol.

### 3.1 Physicochemical properties of synthesized UiO-66 catalysts

To identify changes in physical and chemical characteristics of synthesized UiO-66 catalysts due to added modulators, we characterized them by X-ray diffraction and N<sub>2</sub> adsorption-desorption. X-ray diffractograms of UiO-66 showed characteristic peaks at 12.0, 14.7, 17.0, 18.5, 19.1, 25.6, and

30.6° (**Fig. 6.1A**), corresponding to (022), (222), (004), (133), (024), (006) and (117) [423, 424]. An increase in modulator content exhibited an increase in signal intensity at 17.0, 24.2, 25.7, and 30.6°, which indicated an increase in the crystallite size of UiO-66 MOFs [415, 425]. An increase in acetic acid concentration resulted in the in-situ formation of Zr<sup>4+</sup>-acetic acid complexes between acetic acid and Zr-ions. It slowed down the crystal nucleation rate, leading to a larger crystal size [425, 426]. From the ICP-OES, we found that the Zr content (wt.%) for UiO-66 MOFs was between 24 to 33 %, which is in agreement with the previous reports [427].

The FTIR spectra for all UiO-66 MOFs showed a band at 556 cm<sup>-1</sup> (**Fig. 6.S1**), corresponding to the Zr-oxygen stretching of the UiO-66(Zr) structure [428, 429]. The bands at 478 cm<sup>-1</sup> and 672 cm<sup>-1</sup> for UiO-66(Zr) were attributed to in-plane and out-of-plane bending vibrations of COO<sup>-</sup>. The band at 1395 cm<sup>-1</sup> in UiO-66(Zr) corresponded to the stretching vibration of the coordinated C-O group. The bands at ~1508 and ~1584 cm<sup>-1</sup> were assigned to the stretching vibration of C=C in the benzene ring of the organic ligand H<sub>2</sub>bdc [430-432].

The N<sub>2</sub> adsorption-desorption isotherms of the UiO-66 with different modulator concentrations were a combination of types I and IV isotherms (**Fig. 6.1B**), which indicated these MOFs had both micropores and mesopores. As a control, the UiO-66 had a BET surface area of 891 m<sup>2</sup>/g, and pore volume of 0.49 cm<sup>3</sup>/g, which agrees well with the previously reported value [413]. The modulated UiO-66 yielded ~40% increase in surface area and 37% increase in pore volume, compared with the control of bare UiO-66 (**Table 6.S2**). One reason for increased surface area and pore volume was because the presence of acetic acid competed with the organic linker to connect with the secondary building units (SBUs) and created vacancies in the structure [425]. These vacancies increased the surface area and pore volume [433].

To confirm the increase in open metal sites, we performed DRIFTS with adsorbed pyridine as a chemical probe. After pyridine adsorption, the DRIFT spectra of these MOFs had characteristic bands at 1067 and 1018 cm<sup>-1</sup> (**Fig. 6.1C**), which corresponded to the coordination between pyridine

and open metal sites [301, 302]; this coordination provided the vital Lewis acid sites (LAS) that interacted with pyridine. We calculated the Lewis acid site density (a.u./g catalyst) of MOFs using the LAS peak area (**Table 6.S2**). We used the bare UiO-66 as a benchmark and calculated the changes in the LAS density for modulated UiO-66 MOFs. We found that an increase in acetic acid concentration increased the relative LAS density in the order: UiO-66 < UiO-66-A-35 < UiO-66-A-70 < UiO-66-A-100 < UiO-66-A-130.

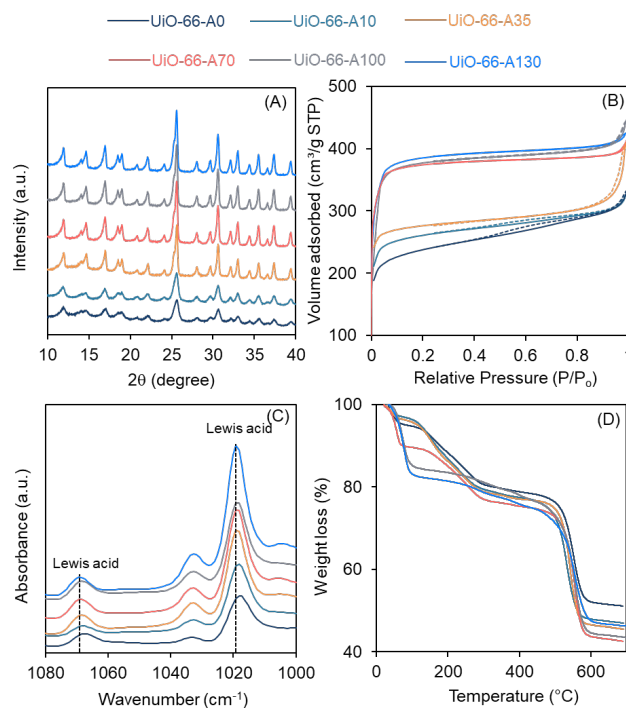


**Figure 6.1.** Physicochemical structure of synthesized UiO-66 with modulators by XRD (A), N<sub>2</sub>-adsorption-desorption (B), DRIFTS (C), and TGA (D).

Thermal stability is an essential property of catalysts to ensure continuous operation without losing their structural integrity and catalytic performance. The weight loss of under 150 °C is attributed to the desorption of water molecules and residual solvent adsorbed at the surface of MOFs (**Fig. 6.1D**). The weight loss (~15 %) in the range of 150–350 °C occurred due to the evaporation of DMF in the channel and the dehydroxylation process. The hydroxyl groups bound to the metal ion center were detached in water molecules during this process, changing the Zr center's coordination

environment. When the temperature was higher than 450 °C, the organic ligand gradually decomposed to 700 °C. These results suggested that UiO-66 MOFs had excellent thermal stability and could maintain structural integrity below 450 °C [434, 435]. The amount of defect sites in UiO-66 associated with missing linkers was determined by TGA profiles and calculated as previously described (**Table 6.S3**) [436].

### 3.2. Brønsted acid properties of Zr MOFs

To determine the Brønsted acid strength of UiO-66 MOFs, we adopted the method by Llabres i Xamena and co-workers [421, 422] by measuring pH change of methanol (**Table 6.2**). We measured the polarizing power of the MOFs on the methanol molecules [422]. As a control, blank (bare methanol) showed a pH of 6.0, which was in agreement with previous reports [421, 422]. The suspension of dehydrated UiO-66-A0 in methanol produced a decrease in pH from 6.0 to 4.2, which indicated the Brønsted acidity of UiO-66. Interestingly, the suspension of hydrated UiO-66-A0 in methanol showed a decrease in pH to 3.4, which suggested that hydration induced Brønsted acid sites in MOFs. The pH change of methanol with hydrated UiO-66-A0, UiO-66-A70, and UiO-66-A130 was 3.4, 2.5, and 2.2, respectively.

**Table 6.2.** pH values of hydrated and dehydrated MOFs suspended in methanol

| Catalyst         | pH                      |            |                       |
|------------------|-------------------------|------------|-----------------------|
|                  | Dehydrated <sup>a</sup> |            | Hydrated <sup>b</sup> |
|                  | With solid              | With solid | Filtrate only         |
| UiO-66-A0        | 4.2                     | 3.4        | 5.9                   |
| UiO-66-A70       | 4.0                     | 2.5        | 5.9                   |
| UiO-66-A130      | 3.5                     | 2.2        | 6.0                   |
| Amberlyst-36     | -                       | 3.7        | 6.0                   |
| Methanol (blank) | -                       | 6.0        | -                     |

<sup>a</sup>MOFs were dried at 150 °C for 12 h under vacuum before suspension in methanol. <sup>b</sup>pH of a stirred suspension of 6 mg of MOF in 24 mL of methanol at 25 °C.

These results suggested that the strength of the Brønsted acid was in the following order: UiO-66-A130 > UiO-66-A70 > UiO-66-A0. This increase in Brønsted acidity of hydrated UiO-66 MOFs stemmed from strongly polarized bound water on the CUS of UiO-66 [421]. A large pH change of methanol with UiO-66-A130 compared with blank indicated the high polarizing power of UiO-66-A130 on the methanol molecules and the high strength of Brønsted acid [422]. Moreover, after removing hydrated solids, the pH of methanol was ~5.9-6.0, which suggested that the Brønsted acidic proton was on the surface of hydrated solids.

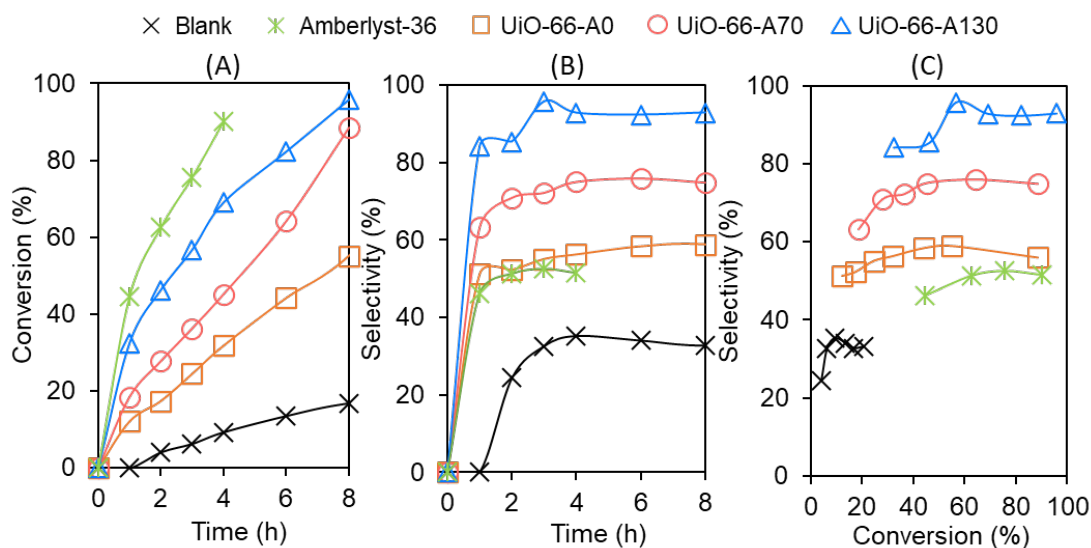


**Figure 6.2.** Catalytic activity of selected Zr-MOFs; time on stream of Levulinic acid conversion (A), methyl levulinate selectivity (B), and conversion over selectivity (C). Reaction condition. Levulinic acid: methanol =1:25 (molar ratio), 10.75 mg catalyst (43 wt% based on levulinic acid, 65°C, 0.5-8.0 h.

### 3.3. Esterification of levulinic acid with alcohol by UiO-66

To evaluate the catalytic activity of modulated UiO-66 MOFs, we performed esterification of levulinic acid and methanol over 8 h (Fig. 6.2). All catalysts were active for the esterification of levulinic acid. As a control, a blank (no added catalyst) experiment showed a low conversion of levulinic acid of 20% after 12 h. We used Amberlyst-36, a commercial solid Brønsted acid catalyst,

as an additional control. Amberlyst-36 catalyzed a progressive increase in conversion of levulinic acid and reached 51% selectivity to methyl levulinate at 63% conversion of levulinic acid after 2 h. Although a prolonged reaction time of 4 h increased the conversion of levulinate to 90%, the selectivity to methyl levulinate remained constant at 51%. We postulated that the constant selectivity of methyl levulinate with the increasing conversion of levulinic acid was due to the formation of by-product water [437, 438], which poisoned the Amberlyst-36.

Modulators effectively introduce defects by creating the uncoordinated metal sites which serve as active Lewis acid sites for catalytic reactions [413, 414]. Moreover, defective UiO-66 MOFs have a higher degree of hydrophilicity which induced the Brønsted acid sites and improved the catalytic activity. When we used UiO-66 MOFs of varying modulator concentrations, all catalysts showed a progressive increase in conversion of levulinic acid. An increase in modulator concentration increased the levulinic acid conversion and ester formation rates. UiO-66, UiO-66-A70, and UiO-66-A130 reached 55, 88, and 96% conversion of levulinic acid after 8 h, respectively. The modulated UiO-66 catalyst with the highest LAS density, UiO-66-A130, had the highest catalytic activity and showed 93% selectivity of methyl levulinate after 8 h. To evaluate the quality of the Lewis acid sites, we plotted the selectivity to methyl levulinate as a function of conversion using UiO-66, UiO-66-A70, and UiO-66-A130 MOFs. The selectivity to methyl levulinate at a similar conversion was in the order of UiO-66-A130 > UiO-66-A70 > UiO-66-A0 > Amberlyst-36. This order of selectivity to methyl levulinate was the same order as Lewis acid sites measured by pyridine-DRIFTS (**Table 6.S2**).



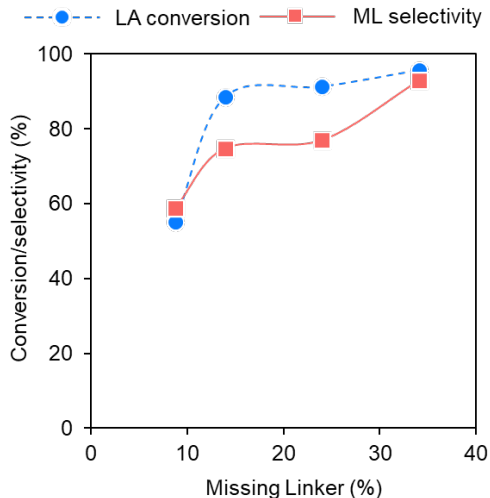


**Figure 6.3:** Levulinic acid conversion Vs the number of linker defects in UiO-66 MOFs

### 3.4. Effect of missing linkers on levulinic acid conversion

Next, we calculated the missing linkers of UiO-66 MOFs based on TGA results (**Table 6.S2**). An increase in modulator concentration increased the amount of missing linkers. We found that missing linkers were in the order of UiO-66-A130 (34%) > UiO-66-A70 (13.9%) > UiO-66 (8.8%). MOFs with a high amount of missing linkers had unsaturated metal sites ( $Zr^{4+}$ ), which served as catalytic centers and increasing the Lewis acid sites and corroborated our pyridine-DRIFTS results (**Table 6.S2**). To evaluate the effect of missing linkers, we plotted the conversion of levulinic acid and selectivity to methyl levulinate as a function of missing linkers (**Fig. 6.3**). We found that conversion of levulinic acid and selectivity to methyl levulinate increased with increasing missing linkers.

The FTIR spectra of modulated UiO-66 MOFs had a distinct band at  $3674\text{ cm}^{-1}$ , which was assigned to  $\mu_3\text{-OH}$  on hydroxylated  $Zr_6O_8$  node [439] and acted as Brønsted acid sites (**Fig. 6.4**). Furthermore, the FTIR band intensity increased with the modulator concentration. This increase was in the same order as Brønsted acid strength of modulated MOFs determined by pH measurement in methanol (**Table 6.2**). Overall, these results suggested that UiO-66 MOFs with a high modulator concentration significantly increased the catalytic activity. Moreover, the

cooperative effects between the Lewis acid sites created by missing linkers and Brønsted acid sites induced by  $\mu$ 3-OH improved levulinic acid conversion and selectivity to methyl levulinate.

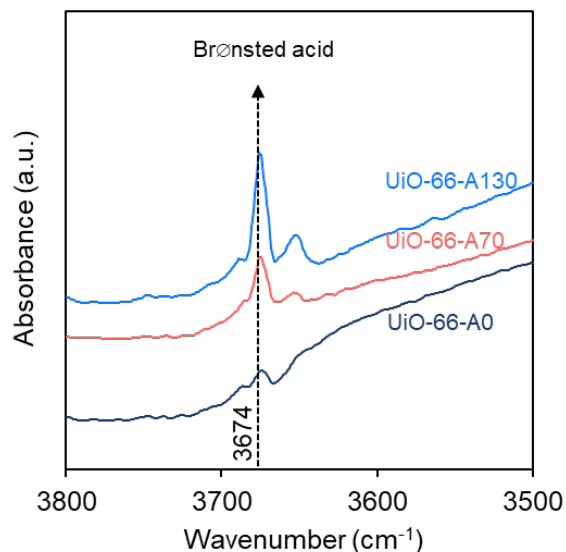


**Figure 6.4.** FTIR spectra of the hydroxyl-group region for modulated UiO-66 MOFs

### 3.5. Stability and reusability of UiO-66-A130

The ability to recycle the catalysts is essential for their practical use. To determine the recyclability of catalysts, we reused UiO-66-A130 four times by centrifugation and washing with water to remove residual products and unreacted levulinic acid. The washed MOF was then dried in a vacuum oven at 130 °C to remove moisture and residual solvent. The UiO-66-A130 maintained catalytic performance with a <10% drop in levulinic acid, and the catalyst retained its high selectivity to methyl levulinate (>90%) for four cycles (**Fig. 6.5A**).

To evaluate the catalyst stability under the reaction condition, we performed filtration experiments by conducting the levulinic acid esterification using UiO-66-A130 for 2 h at 65 °C, filtering the UiO-66-A130 catalyst from the reaction mixture, and heating the filtrate under the same reaction condition (65 °C) for 4 h (**Fig. 6.5B**). We sampled the reaction mixture two times during the 2 h and measured levulinic acid conversion and methyl levulinate selectivity. The conversion increased

slightly, and selectivity to methyl levulinate decreased slightly due to their thermal degradation; these results agreed with our blank experiments of levulinic acid esterification (**Fig. 6.2**). To rule out the catalytic conversion of levulinic acid and methyl levulinate by Zr species leached into the filtrate, we analyzed the filtrate by ICP-OES. We did not observe Zr (< 0.05 ppm based on the detection limit). These results indicated that (1) no visible Zr species leached from UiO-66-A130 into the reaction mixture, and (2) UiO-66-A130 was stable at 65 °C.

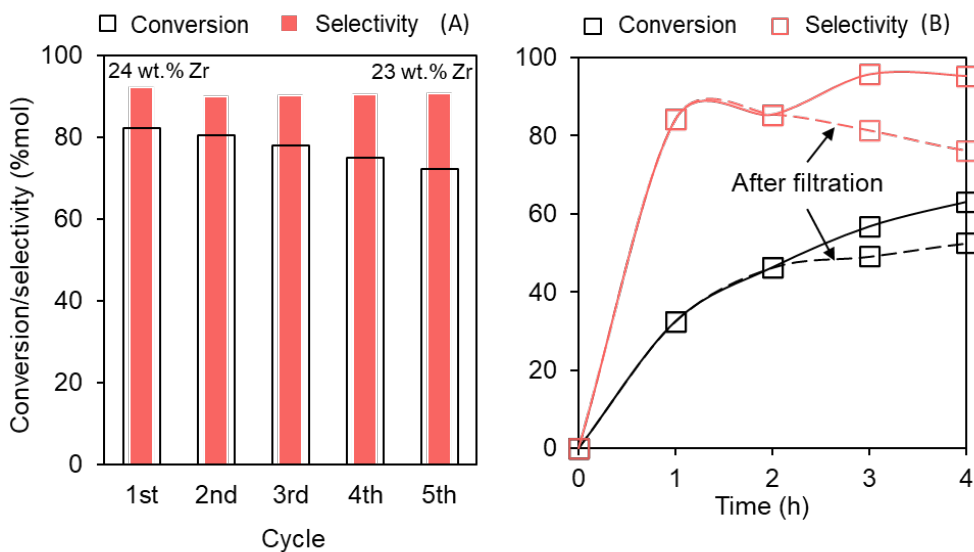


**Figure 6.5.** Reusability and stability of UiO-66-A130 catalysts for esterification of levulinic acid (LA) with methanol (MeOH) by recycle of UiO-66-A130 catalyst at 65 °C, 2 h (A) and filtration test at 65 °C (B). Reaction condition: LA: MeOH=1:25 (molar ratio), catalyst loading: 43 wt% based on based on LA, 65 °C.

Further, we used ICP-OES, XRD, and FTIR to characterize the spent UiO-66-A130 catalyst after the 4<sup>th</sup> reuse cycle (**Fig. 6.S2**). The zirconium content of the spent catalyst, measured by ICP-OES, was 23 wt.%, similar to the 24 wt.% of fresh catalysts; thus, there was minimal zirconium leaching even after four reuses. Similarly, the XRD and FTIR spectra of the reused catalyst exhibited chemical structure and functionality similar to fresh UiO-66-A130. These filtration and characterization results suggested catalyst stability under the present experimental conditions.

Overall, UiO-66-A130 maintained high selectivity to methyl levulinate for all the cycles and structural integrity after (at least) four recycles.

#### 4. Discussion

Here, we determined the effect of the modulator on the catalytic activity of modulated UiO-66 MOFs for the esterification of levulinic acid. An increase in modulator concentration created defects on the framework and increased the density of Lewis acid sites. Defected UiO-66 MOFs had a higher degree of hydrophilicity and induced the Brønsted acidity in the hydrated form. This increase in both Lewis and Brønsted acid sites enhanced the levulinic acid conversion and methyl levulinate selectivity. Our results explained the effects of the modulator concentration on creating defect-induced Lewis and Brønsted acidity and improving the reaction rate for esterification of levulinic acid.

Our most significant finding was the creation of both Lewis and Brønsted acid sites in defective UiO-66 MOFs which enables the high catalytic activity for esterification reaction. Esterification of levulinic acid is a Brønsted catalyzed reaction [440] and the combined effects of both Lewis and Brønsted acid sites improved the selectivity towards the alkyl levulinates. During the esterification reaction, the coordinated unsaturated Zr metals (Lewis acid site) favors the adsorption of levulinic acid atom whereas the presence of  $\mu_3$ -OH functions as Brønsted acidic sites, thus favoring the esterification of levulinic acid and methanol. Modulator-free, UiO-66-A0 MOF showed only 55% conversion of levulinic acid with 58% selectivity to methyl levulinate. On the other hand, we observed 96% conversion of levulinic acid with 93% selectivity to methyl levulinate by UiO-66-A130. The defects generated from the missing linkers of modulated MOFs activate the water molecules and worked as Brønsted acid catalysts [441]. The IR band at  $3674\text{ cm}^{-1}$  represents the  $\mu_3$ -OH hydroxyl group in MOFs, and UiO-66-A130 has a higher band intensity compared to other MOFs. Klet et al. [442] measured the Brønsted acidity in Zr- and Hf-based MOFs using potentiometric acid-base titration and found that the  $\mu_3$ -OH hydroxyl group has a higher Brønsted acidic strength. Overall, these results suggested that modulated UiO-66-A130 has higher Brønsted

acid sites induced from the hydration of defected MOFs and showed superior catalytic activity compared to modulator-free UiO-66-A0 MOF.

Our findings demonstrated the strategy of inducing Lewis and Brønsted acid sites in UiO-66 MOFs by incorporating a modulator during synthesis. Defective UiO-66 MOFs are the active, selective, and stable catalysts for the esterification of levulinic acid. Although our results show the defective UiO-66 MOFs catalysts were promising for levulinate esterification, the effect of functional group in organic ligand and the chain length of the modulators/alcohol have not been extensively investigated. The knowledge gained from this work will enable tuning the acid strength and balance Lewis/Brønsted acid ratio for various organic reactions, such as dehydration [443], isomerization [333], and acetalization [444], and cascade reactions that require both Lewis and Brønsted acidities, such as cellulose conversion to 5-hydroxymethylfurfural [443], lactic acid [333, 445], and levulinic acid [446].

## 5. Conclusion

This study described a strategy to create defects in UiO-66(Zr) MOFs by adding acetic acid as modulators during the synthesis. An increase in the modulator concentration increased the defect sites in UiO-66 MOFs. Defective UiO-66 MOFs have the unsaturated Lewis acid sites ( $Zr^{4+}$ ) created by missing linkers, and Brønsted acid sites originated from the surface hydroxyl groups ( $\mu_3$ -OH). The cooperative Brønsted-Lewis acid in defective MOFs improved the catalytic performance, and UiO-66-A130 was the most active catalyst for esterification of levulinic acid with 93% selectivity to methyl levulinate. Future work will investigate the stability of the defective UiO-66 MOFs in various solvents and reaction temperatures.

## Acknowledgment

A part of this material is based upon work supported by the National Science Foundation under Cooperative Agreement No. 1355438. This work was performed in part at the Conn Center for Renewable Energy Research at the University of Louisville, which belongs to the National Science Foundation NNCI KY Manufacturing and Nano Integration Node, supported by ECCS-1542174. The authors would like to thank Dr. Howard Fried for his valuable comments and suggestions on the manuscript.

## 6. Supporting Information

| <b>Table 6.S1.</b> List of chemicals/reagents used in this study |   |                              |                   |
|--|---|------------------------------|-------------------|
| <b>Material/Chemical</b>   | <b>Supplier</b>                               | <b>Purity</b>                | <b>CAS Number</b> |
| Levulinic acid   | Sigma-Aldrich, St. Louis, MO, USA             | 98%                          | 123-76-2          |
| Methyl levulinate  | Sigma-Aldrich, St. Louis, MO, USA             | >98%                         | 624-45-3          |
| Xylitol  | Acros Organics                                | 99+%                         | 87-99-0           |
| Zirconium<br>chloride  | (IV) Alfa Aesar(Ward Hill, MA)                | 99.5+%                       | 10026-11-6        |
| Terephthalic acid  | Tokyo Chemical Industry (Tokyo, Japan)        | >99.0%                       | 100-21-0          |
| Acetic Acid  | Alfa Aesar(Ward Hill, MA)                     | 99+%                         | 64-19-7           |
| Methanol   | Ward's science                                | Lab grade                    | 67-56-1           |
| Ethanol  | Decon Laboratories, Inc.                      | 200 Proof                    | 64-17-5           |
| N,N-<br>dimethylformamide  | Chem-Impex Int'l. Inc.                        | 100%                         | 68-12-2           |
| Pyridine   | Chem-Impex International (Wood Dale, IL, USA) | 99.97%                       | 110-86-1          |
| N <sub>2</sub> gas   | Welder supplies (Louisville, KY, USA)         | industrial grade:<br>99.999% |                   |

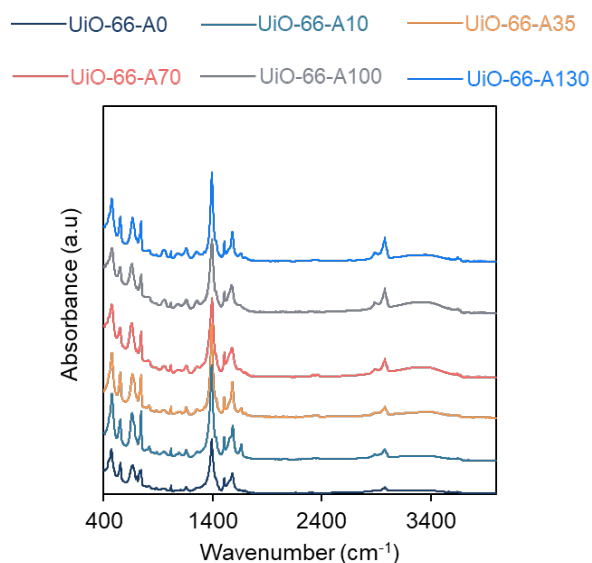


**Figure 6.S1:** FTIR spectrum of synthesized UiO-66 MOFs

**Table 6.S2.** Physical properties of catalysts used in this study

| Sample | $S_{\text{BET}}$<br>( $\text{m}^2/\text{g}$ ) | pore<br>volume<br>( $\text{cm}^3/\text{g}$ ) | Pore<br>size Dis.<br>(nm) | ICP-OES<br>Zr (wt %) | LAS<br>(a.u./g) | Missing<br>linker (wt.%) | Coordination<br>number |
|--------|---|--|---------------------------|----------------------|-----------------|--------------------------|------------------------|
| A0     | 891   | 0.49   | 2.20                      | 31.64                | 148             | 8.79                     | 10.95                  |
| A10    | 1023  | 0.51   | 1.99                      | 32.81                | 206             | 8.97                     | 10.92                  |
| A35    | 1143  | 0.58   | 2.03                      | 33.02                | 266             | 9.34                     | 10.88                  |
| A70    | 1207  | 0.62   | 2.05                      | 30.17                | 343             | 13.92                    | 10.33                  |
| A100   | 1220  | 0.65   | 2.13                      | 27.88                | 400             | 23.99                    | 9.12                   |
| A130   | 1246  | 0.67   | 2.15                      | 23.94                | 445             | 34.07                    | 7.91                   |

**Table 6.S3.** Amount of defect sites and coordination number of Zr and Hf clusters in UiO-66

|  | UiO-66-A0                                      | UiO-66-A10 | UiO-66-A35 | UiO-66-A70 | UiO-66-A100 | UiO-66-A130 |
|--|--|------------|------------|------------|-------------|-------------|
| Chemical formula                         | $C_{48}H_{28}O_{32}Zr_6$                       |            |            |            |             |             |
| Linker                                   | BDC = 1,4-benzenedicarboxylate ( $C_8H_6O_4$ ) |            |            |            |             |             |
| Dehydroxylated formular                  | $Zr_6O_6(BDC)_6$                               |            |            |            |             |             |
| Formula weight of dehydroxylated (g/mol) | 1628.03  |            |            |            |             |             |
| MO <sub>2</sub>                          | 123.22<br>(739.34)                             |            |            |            |             |             |
| Weight loss <sub>theoretical</sub>       | 54.6 %   |            |            |            |             |             |
| Weight loss <sub>actual</sub>            | 49.8 %   | 49.7 %     | 49.5       | 47.0 %     | 41.5 %      | 36.0 %      |
| Defect sites (%)                         | 8.8  | 8.9        | 9.3        | 13.9       | 24.0        | 34.1        |
| CN                                       | 10.9   | 10.9       | 10.8       | 10.3       | 9.1         | 7.9         |



### Determination of missing linkers in UiO-66(Zr) MOFs

The missing linkers reflects the amount of defect sites in UiO-66. The missing linkers were determined by TGA profiles as described in previous study [436]. In short, we assumed that only  $ZrO_2$  was formed at high temperatures (above 500-550 °C). The formula of dehydroxylated UiO-66(Zr) (300-500 °C in TGA profiles) was  $ZrO(CO_2)_2(C_6H_4)$ . Thus, the weight loss in the TGA profiles, which corresponds to the organic linkers (wt.% linker<sub>actual</sub>), was compared with the theoretical amount of organic linker (wt.% linker<sub>theoretical</sub>) from the ideal structure of UiO-66 (defect-free). Therefore, defects sites and the coordination number (CN) of the  $Zr_6$  clusters was calculated as follows:

$$\text{Defect sites (\%)} = \left( 1 - \frac{\text{wt.\% linker}_{\text{actual}}}{\text{wt.\% linker}_{\text{theoretical}}} \right) \times 100$$

$$\text{CN} = 12 \times \left( 1 - \frac{\text{defect sites (\%)}}{100} \right)$$

where defect sites (%) indicate the amount of missing linkers (BDC) of UiO-66, wt.% linker<sub>actual</sub> indicates the weight loss of UiO-66 associated to BDC linkers determined from TGA profile, wt.% linker<sub>theoretical</sub> indicates the amount of BDC linkers calculated from the defect-free structure of UiO-66 (i.e., 54.6 wt.%), and CN represents the coordination number of zirconium clusters. The ideal structure of UiO-66(Zr) has the coordination number of 12.

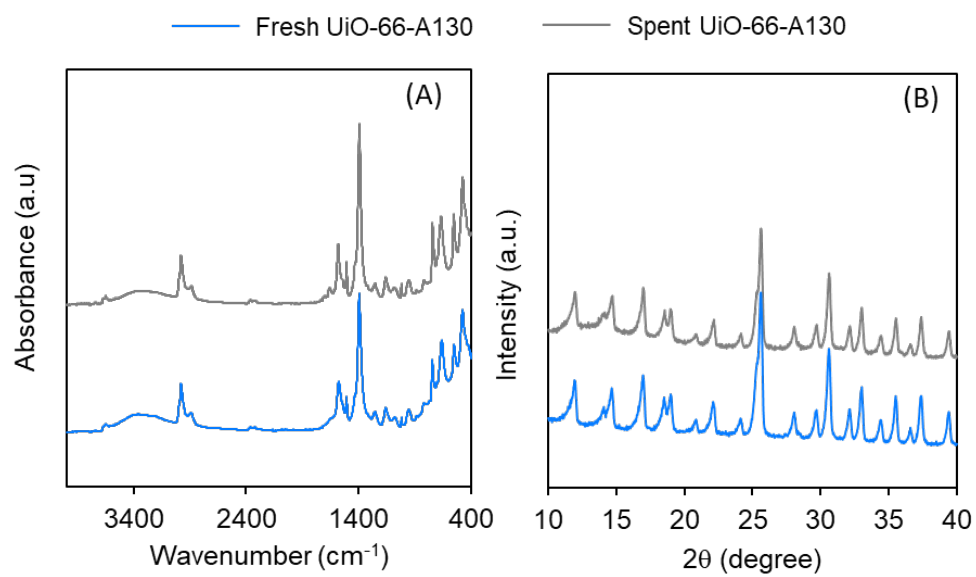


**Figure 6.S2.** Characterization of spent UiO-66-A130 by FTIR (A), and XRD (B).

CHAPTER 7  
MECHANISM OF TRANSFER HYDROGENATION OF CARBONYL COMPOUNDS BY  
ZIRCONIUM AND HAFNIUM-CONTAINING METAL-ORGANIC FRAMEWORKS<sup>4</sup>

### 1. Introduction

Production of fuels and chemicals from renewable biomass reduces reliance on fossil fuels [447] and mitigates global warming by reducing CO<sub>2</sub> emissions [448]. Biomass-derived compounds such as furfural, 5-hydroxymethylfurfural, and benzaldehyde contain oxygens in carbonyl groups and unsaturated C=C bonds. Catalytic hydrogenation is important to convert biomass-derived carbonyl compounds into high-value chemicals, such as g-valerolactone [449], di-hydroxy-methyl-tetrahydrofuran [450], tetrahydrofurfuryl alcohol [451], and hexitol [452]. Classic hydrogenation is based on metal catalysts, such as Pd/C [453], Pt/C [450], Rh/C [454, 455], Ni–Pd/SiO<sub>2</sub> [456], Au/Al<sub>2</sub>O<sub>3</sub> [457], Ni/Al<sub>2</sub>O<sub>3</sub> [458], Cu/Al<sub>2</sub>O<sub>3</sub> [459], Pt/Al<sub>2</sub>O<sub>3</sub> [460], PtSn/Al<sub>2</sub>O<sub>3</sub> [461], Ir/TiO<sub>2</sub> [462], and molecular H<sub>2</sub>. However, hydrogenation using molecular H<sub>2</sub> poses cost and safety concerns [463]. In addition, selective hydrogenation of the carbonyl group (C=O) is problematic because hydrogenation of C=C bonds is thermodynamically favorable compared with C=O bonds, and C=C bond hydrogenation produces undesired products [464, 465]. Therefore, many investigators have investigated catalytic transfer hydrogenation to overcome these challenges.

Catalytic transfer hydrogenation that uses hydrogen-donor solvents instead of molecular H<sub>2</sub> is an alternative approach to converting carbonyl compounds into corresponding alcohols [466]. Transfer hydrogenation can occur by: (1) direct hydrogen transfer from alcohol to the carbonyl group at the

---

<sup>4</sup> This chapter has been published in *Molecular Catalysis* (Rahaman et al., 2022, *Molecular Catalysis*, 522, 112247.). The copyright clearance from the publisher has been included in the "APPENDIX" section.

active metal site of a catalyst, and (2) a cascade of metal hydride formation and carbonyl reduction by Meerwein–Ponndorf–Verley (MPV) by Lewis acid catalysts. MPV reduction is promising for hydrogenation of biomass-derived carbonyls because of its high chemoselectivity, mild reaction conditions, and scalability [467, 468]. Lewis acidic Hf-, Zr-, and Sn-containing zeolites catalyzed MPV reduction [330, 469-475]. However, synthesis of these zeolites entails complex [276], and time-consuming [476] procedures and the use of hazardous reagents (e.g., HF) [477].

Recently, Hf- and Zr-containing metal-organic frameworks (MOFs), especially MOF-808 and UiO-66 frameworks [27, 28, 329, 421, 478, 479], have been shown to catalyze transfer hydrogenation of biomass-derived carbonyl compounds, such levulinic acid [480], furfural [28, 394, 431, 481], ethyl levulinate [482, 483], cinnamaldehyde [484]. For example, Mautschke et al. [478] showed that MOF-808(Zr) had a better catalytic performance for MPV of carbonyl compounds compared with UiO-66(Zr). Rojas-Buzo et al. [28] proposed that MOF-808(Hf) catalyzed transfer hydrogenation by a direct hydrogen transfer pathway. In contrast, Lin et al. [329] suggested that MOF-808(Hf) catalyzed MPV reduction. Although they proposed the MPV mechanism by MOF-808(Hf), the effect of linkers and dispersion interactions on the proposed mechanism remained unknown. Thus, still to be determined are the mechanism of transfer hydrogenation by MOF-808 and UiO-66 and the effect of Zr and Hf metal clusters.

Here, we evaluated the catalytic performance of Zr- and Hf-containing MOF-808 and UiO-66 catalyst for transfer hydrogenation of benzaldehyde in 2-propanol at 100 °C. Next, we combined experimental results and density functional theory to elucidate the mechanism by which Hf- and Zr-containing MOFs activate carbonyl compounds during transfer hydrogenation. Our results demonstrated that MOF-808 activated carbonyl groups by MPV, whereas UiO-66 activated carbonyls by direct transfer hydrogenation. Moreover, the Lewis acidic MOF-808(Hf) was the most active and selective to transfer hydrogenation (MPV) of benzaldehyde to benzyl alcohol. In addition, MOF-808(Hf) reduced other biomass-derived carbonyl compounds to corresponding alcohols with >89% selectivity with minimal side reactions. Furthermore, creating defect sites through adding a

modulator (formic acid) during MOF-808(Hf) synthesis enhanced its selectivity to alcohol. This study provided an insight into the development of active and selective Lewis acidic MOF catalysts for the transfer hydrogenation of biomass-derived carbonyl compounds.

## 2. Materials and Methods

**2.1. Materials.** All chemicals were used as received unless otherwise noted. **Table 7.S1** lists their CAS numbers, purity, and manufacturers (*Supplementary Information*).

**2.2. Synthesis of metal-organic frameworks.** UiO-66(Zr) [485], UiO-66(Hf) [486], MOF-808(Zr) [28], and MOF-808(Hf) [28] were synthesized using a solvothermal method with a slight modification. The detailed synthesis procedures are described in *the Supplementary Information*.

**2.3. Characterization of the catalyst.** The physiochemical properties of the MOFs were determined by X-ray diffraction (XRD), N<sub>2</sub> adsorption-desorption, Diffuse reflectance infrared Fourier transform spectroscopy (DRIFTS), Fourier-transform infrared spectroscopy (FTIR), and thermogravimetric analysis (TGA). The metal content was determined by inductively coupled plasma-optical emission spectroscopy (ICP-OES).

**2.3.1. X-ray diffraction.** X-ray diffraction (XRD) analysis of samples was conducted on a Bruker D8 Discover diffractometer (Billerica, MA, USA) using CuK $\alpha$  radiation in the 2 $\theta$  range from 10° to 40° with 0.5 seconds/step. Samples of 200 mg were used in each analysis.

**2.3.2. N<sub>2</sub> adsorption-desorption.** The N<sub>2</sub> adsorption-desorption was measured by a Micromeritics Tristar (Norcross, GA, USA) instrument to calculate the surface area, pore size, and pore volume. The function of TriStar was verified with reference materials (Micromeritics). Before the measurement, the sample was pretreated at 150 °C for 3 h using a Micromeritics FlowPrep with sample degasser (Norcross, GA, USA). The surface area, S<sub>BET</sub>, was determined from N<sub>2</sub> isotherms by Brunauer–Emmett–Teller equation (BET) at -196.1 °C [24, 25]. The BET surface area was

calculated for the range of relative pressures between 0.05 and 0.3. The pore volume was estimated from the N<sub>2</sub> desorption values according to the Barrett–Joyner–Halenda (BJH) model [26]. The pore volume was calculated as the uptake (cm<sup>3</sup>/g) at a relative pressure of 0.95. We measured the average pore size of the samples by the BJH model [27, 28].

**2.3.3. Thermogravimetric analysis.** To determine the thermal stability of synthesized MOFs, thermogravimetric analysis (TGA) was performed on an SDT Q600 TA instrument (New Castle, DE, USA). In short, ~20 mg of the sample was placed in a cylindrical alumina crucible and heated in the air from ambient temperature to 700 °C with a heating rate of 10 °C/min under N<sub>2</sub> flow (100 mL/min). The change in weight of MOF samples was used to determine the moisture content, decomposition of the linkers, and formation of metal oxides.

**2.3.4. Inductively coupled plasma-optical emission spectroscopy.** The metal content of the samples was determined by inductively coupled plasma-optical emission spectroscopy (ICP-OES). Measurements were performed using a 100 mg sample dissolved in 10 mL of nitric acid. Heating was used to ensure that the sample was completely dissolved. Once cooled, the sample was further diluted to 25 mL with double distilled water. Measurements were acquired on a Varian 720-ES spectrometer equipped with a seaspray nebulizer and cyclonic class spray chamber. Parameters included a sample intake of 1 mL/min, argon plasma flow rate of 15 L/min, and an auxiliary gas (Ar) flow rate of 1.5 L/min. The instrument was calibrated with certified reference materials (CRMs) by VHG (LGC Standards Ltd., Teddington, UK).

**2.3.5. Fourier-transform infrared spectroscopy.** Infrared spectra of samples were recorded on a JASCO Fourier transform infrared (FTIR) spectrometer (Easton, MD, USA), equipped with an attenuated total reflection stage (ATR). Samples of ~5 mg were used in each analysis. The samples were scanned between 400 and 4000 cm<sup>-1</sup> at a 4 cm<sup>-1</sup> resolution. Spectra were collected using deuterated triglycine sulfate (DTGS) detector averaging 256 scans.

**2.3.6. Diffuse reflectance infrared Fourier transform spectroscopy.** Diffuse reflectance infrared Fourier transform spectroscopy (DRIFTS) with adsorbed pyridine was performed to characterize the acid sites. The temperature-programmed desorption was conducted using the JASCO FTIR equipped with a high-temperature DiffuseIR™ cell (PIKE Technology, WI, USA). The sample treatment and DRIFTS experiments with temperature-programmed desorption were described elsewhere with a slight modification [182]. Briefly, the MOF sample (~5 mg) was placed in a cylindrical alumina crucible and treated in N<sub>2</sub> gas (50 mL/min) at 150 °C for 60 min unless otherwise noted. After the pretreatment, the sample was cooled to 30 °C, and the IR spectrum of fresh catalyst was recorded as the background spectrum. The samples were then saturated with pyridine vapor in a low concentration of N<sub>2</sub> gas (50 mL/min). Then the physisorbed pyridine was removed by flushing with N<sub>2</sub> gas (50 mL/min) at 150 °C for 30 min before recording the DRIFT spectra. All spectra were recorded with 256 scans in the range between 4000–400 cm<sup>-1</sup> at a 4 cm<sup>-1</sup> resolution. The amount of Lewis acid sites at each desorption temperature was calculated from the integrated area of bands (after background subtraction) of adsorbed pyridine at 1012, 1043, and 1070 cm<sup>-1</sup> [184].

The Brønsted acid properties of MOFs were determined by measuring the pH change of methanol in which MOFs were suspended, as described [199, 421, 422]. Briefly, 8 mg MOFs were suspended in 24 mL methanol with constant stirring at ambient temperature before pH measurement. The selected sample amount of 8 mg was based on previous experiments in which the amount of MOFs was varied; we found that 8 mg MOF was sufficient such that the measured pH was independent of the amount of solid. The pH was measured with a gel-filled, double junction electrode (Milwaukee Instruments, Inc., Rocky Mount, NC, USA). The electrode was calibrated with the pH 4, 7, and 9 buffers. All measurements were conducted in triplicate.

**2.4. Transfer hydrogenation of benzaldehyde.** Reactions were performed in 15 mL glass pressure vials in an oil bath. Typically, benzaldehyde, 2-propanol, and catalysts were added to the pressure vial, sealed, and stirred at the desired temperature. The reactor vessel contained three

mol% of the desired catalyst, 1% weight of benzaldehyde dissolved in 2-propanol, and 0.25% weight of hexadecane added as an internal standard. The benzaldehyde conversion and product yield were calculated based on the internal standard. The reaction was stopped by quenching in a cold-water bath, then adding ethyl acetate (5 mL) to dissolve the remaining benzaldehyde and products. The solution was centrifuged, and the solid catalyst was removed. The liquid sample was then diluted with ethyl acetate before analysis.

**2.5. Product analysis and quantification.** The reactants and products were analyzed by a gas chromatograph (7890B GC) (Agilent Technologies, Santa Clara, CA, USA) equipped with a mass spectrometer and flame ionization detector (FID) for product identification and quantification, respectively. A DB-1701 column (30m x 0.25mm x 0.25  $\mu$ m, Agilent Technologies, Santa Clara, CA, USA) was used for product separation with the following parameters: injection temperature 275  $^{\circ}$ C and FID detector temperature 300  $^{\circ}$ C; split ratio 1:50. The temperature program started at 50  $^{\circ}$ C with a heating rate of 8  $^{\circ}$ C/min to 200  $^{\circ}$ C. The conversion of benzaldehyde, product yield, and product selectivity were calculated using the following equations:

$$\text{Conversion (\%)} = \frac{\text{mole of benzaldehyde reacted}}{\text{initial mole of benzaldehyde}} \times 100$$

$$\text{Product yield (\%)} = \frac{\text{mole of product generated}}{\text{initial mole of benzaldehyde}} \times 100$$

$$\text{Product selectivity (\%)} = \frac{\text{Product yield}}{\text{Conversion}} \times 100$$

**2.6. Computational details.** Fig. 7.S1 depicts the cluster models used to represent the MOF-808(Zr/Hf) and UiO-66(Zr/Hf). These cluster models were constructed from their optimized periodic structures. The cluster model of MOF-808 consisted of one zirconium or hafnium oxide node with six benzene-1,3,5-tricarboxylate (BTC) coordinating linkers. In addition, an open Lewis acidic site of MOF-808 formed by removing an external water molecule was considered in the present work [487]. For UiO-66, the cluster involved one hafnium oxide node connected to twelve BTC linkers.



All structure optimizations were calculated from density functional theory (DFT) using the M06-L [488] density function as implemented in the code Gaussian 16 Revision B.01 [489]. The 6-31G(d,p) basis set was employed for the O, C, and H atoms, whereas the Zr and Hf atoms were described by the double-z of the Stuttgart-Dresden pseudopotential (SDD). During geometry optimizations, the entire cluster model except for the para-C atoms of benzoate linkers was allowed to relax. Vibrational frequency calculations were performed to identify the nature of all the stationary states along the reaction coordinate. The natural bond orbit method [490] was used to determine orbital overlapping, partial charges, and population analysis.

The difference in charge transfer (DCT) from the catalytic sites to the adsorbed benzaldehyde molecule between the adsorption and transition state complexes was calculated as follows:

$$\Delta CT = q(TS_{benzaldehyde}) - q(TS_{co-adsorbed\ benzaldehyde})$$

where  $q(TS_{benzaldehyde})$  and  $q(co-adsorbed\ benzaldehyde)$  represented net charges of the benzaldehyde molecule in the transition state and benzaldehyde in the co-adsorption state (co-adsorption of benzaldehyde and 2-propanol molecules), respectively.

### 3. Results

Initially, we screened 14 metal triflates to identify active metal species for the transfer hydrogenation of benzaldehyde. On the basis of this initial screening of metal triflates, we heterogenized Zr and Hf in UiO-66 and MOF-808 frameworks. We characterized their physicochemical characteristics, determined their MPV activities, and performed density functional theory to explain the reaction pathways.

### 3.1. Evaluation of the catalytic activity of catalysts for transfer hydrogenation of benzaldehyde

To identify the active metal species for MPV reaction, we screened 14 metal triflates with benzaldehyde as a reactant in 2-propanol at 100 °C for 3 h (**Fig. 7.S2**). We chose benzaldehyde because it represented lignin-derived aldehyde [491, 492]. We found Hf(OTf)<sub>4</sub> had the highest benzyl alcohol selectivity of 56% at 90% benzaldehyde conversion after 3 h; whereas Zr(OTf)<sub>4</sub> exhibited 24% benzyl alcohol selectivity at 76% conversion.

### 3.2. Synthesis and Characterization of Zr- and Hf-containing MOFs

Because Hf(OTf)<sub>4</sub> and Zr(OTf)<sub>4</sub> showed high selectivity to benzyl alcohol at high conversion, we heterogenized Hf and Zr species into UiO-66 and MOF-808 frameworks. To assess their physical and chemical properties, we characterized the synthesized MOFs by N<sub>2</sub> adsorption-desorption measurement, FTIR, TGA, XRD, DRIFTS, ICP-OES (**Fig. 7.S3, Fig. 7.S4, Table 7.S2, Table 7.S3**). The XRD and N<sub>2</sub>-adsorption/desorption of synthesized MOFs confirmed the formation of UiO-66 and MOF-808 structures. The ICP-OES results suggested that these MOFs had 26.3-31.6 wt.% Zr and 40.6-42.4 wt.% Hf. Together, the characteristics of these MOFs agreed well with previous reports (*see Supporting Information for detail*). The TGA profiles of these MOFs showed the typical three mass loss zones from physisorbed water, bound solvents, and degradation of frameworks. Moreover, the TGA results suggested that these Zr- and Hf-MOFs were stable up to 250 °C.

An ideal UiO-66 contains four Brønsted acidic sites ( $\mu_3$ -OH) per cluster and no Lewis acidic sites [493, 494]. To determine the Brønsted acidity of UiO-66, we measured the pH of the filtrate after suspending MOFs in methanol (**Table 7.1**). The pH after suspension with hydrated and dehydrated MOF-808(Zr) and MOF-808(Hf) did not change compared with the blank, which suggested that MOF-808(Zr) and MOF-808(Hf) possessed only Lewis acidity. These results agreed with previous observations [421]. Interestingly, suspension of dehydrated UiO-66 in methanol produced a decrease in pH from 6.0 to 4.2-4.3, which indicated the Brønsted acidity of UiO-66. Furthermore, the suspension of hydrated UiO-66 in methanol caused a further decrease in pH to 2.7-2.9, which

indicated that bound water increased Brønsted acid strength of UiO-66. This increase in Brønsted acidity of hydrated UiO-66 stemmed from strongly polarized bound water on the coordinatively unsaturated sites (CUS) of UiO-66 [421]. Moreover, after removing hydrated solids, the pH of methanol was ~5.8-6.0, which suggested that the Brønsted acidic proton was on the surface of hydrated solids.

**Table 7.1.** pH values of hydrated and dehydrated MOFs suspended in methanol

| Catalyst\pH      | Hydrated <sup>a</sup> | Dehydrated <sup>b</sup> |
|------------------|-----------------------|-------------------------|
| UiO-66(Zr)       | 2.7                   | 4.2                     |
| UiO-66(Hf)       | 2.9                   | 4.3                     |
| MOF-808(Zr)      | 5.8                   | 6.0                     |
| MOF-808(Hf)      | 5.9                   | 6.0                     |
| Methanol (blank) | 6.1                   | -                       |

<sup>a</sup>pH of a stirred suspension of 8 mg of MOF particles in 24 mL of methanol at 25 °C. <sup>b</sup>MOFs were dried at 150 °C for 12 h under vacuum before suspension in methanol.

Next, we performed DRIFTS to measure the acid properties of MOFs. DRIFT spectra of MOF-808(Hf) and MOF-808(Zr) confirmed their Lewis acidic properties (**Fig. 7.S4**). The UiO-66 MOF showed a weak band at 1070 cm<sup>-1</sup>, which suggested that UiO-66 had little Lewis acidity. We postulated that the weak band at 1070 cm<sup>-1</sup> came from defect formation during the MOF synthesis. To determine the amount of defects in synthesized UiO-66, we performed TGA on the MOFs and compared the results with the theoretical amount of linkers in ideal UiO-66 (**Fig. 7.S5, Table 7.S4, see Supporting Information for detail**). The defect sites of synthesized UiO-66(Zr) constituted 8.8%, in agreement with the reported value of 9.5% [421]. The calculated defect site of synthesized UiO-66(Hf) was 21.5%, in agreement with the reported TGA profile [495]. The defect sites of UiO-66(Zr) corroborated the occurrence of a weak Lewis acid peak at 1070 cm<sup>-1</sup> (**Fig. 7.S4**). These results agreed with findings by Cirujano et al. [422] and Guarinos et al. [421], which showed that bound water molecules on the defective Zr<sup>4+</sup> sites of UiO-66 induced Brønsted acidity from strongly

polarized bound H<sub>2</sub>O molecules and corroborated the large decrease in pH induced by hydrated UiO-66. Overall, our results suggested that the MOF-808 had only Lewis acid sites, whereas UiO-66 had a mixture of Brønsted and Lewis acid sites. Moreover, the Lewis acid sites of UiO-66 were not stable because they could turn into Brønsted acid sites in the presence of moisture. Thus, to precisely control the content of Brønsted and Lewis acid sites in UiO-66 catalysts, it is important to handle them in a controlled environment (i.e., glove box).

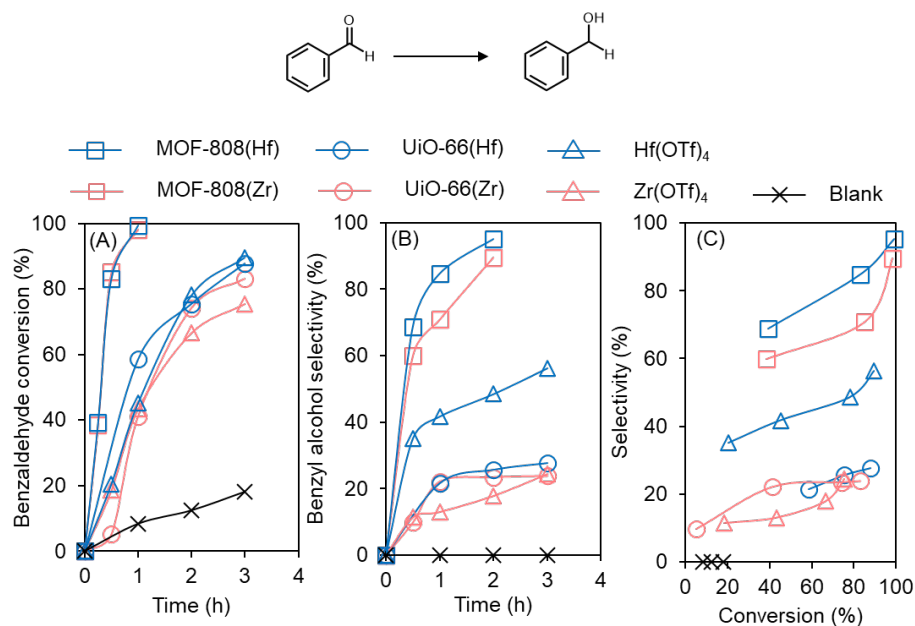


**Figure 7.1.** Catalytic activity of selected Zr- and Hf-containing catalysts; time on stream of benzaldehyde conversion (A), benzyl alcohol selectivity (B), and conversion over selectivity (C). Reaction condition: 1 wt.% benzaldehyde in 2-propanol, catalyst loading = 3 mol.% metal, 100 °C, 0.5-3.0 h.

### 3.3. Catalytic activity of Zr- and Hf-containing MOFs for benzaldehyde conversion

To evaluate their catalytic activity, we tested the Zr- and Hf-containing MOFs for benzaldehyde conversion through transfer hydrogenation during 3 h at the same metal loading. The control (no added catalyst) showed <20% benzaldehyde conversion without any benzyl alcohol formed. We used Zr(OTf)<sub>4</sub> and Hf(OTf)<sub>4</sub> as controls for Lewis acid catalyst. All catalysts showed a progressive

increase in benzaldehyde conversion and benzyl alcohol selectivity during 3 h (**Fig. 7.1A and 7.1B**). Catalyst Hf(OTf)<sub>4</sub> had 56% selectivity to benzyl alcohol at 90% conversion after 3 h, greater than the 24 % selectivity at 76% conversion for Zr(OTf)<sub>4</sub>. Interestingly, UiO-66(Zr) and UiO-66(Hf) showed similar catalytic behavior to catalysis by Zr(OTf)<sub>4</sub> and Hf(OTf)<sub>4</sub>. MOF-808(Zr) and MOF-808(Hf) outperformed UiO-66(Zr) and UiO-66(Hf). Moreover, Zr- and Hf-containing MOF-808 reached 90-95% selectivity to benzyl alcohol at 98-99% conversion after 2 h. The higher benzaldehyde conversion and selectivity to benzyl alcohol of MOF-808 suggested that Zr and Hf metal sites in the MOF-808 framework were more active and selective than triflate salts and UiO-66. These metal sites were not active for hydrogenation using molecular H<sub>2</sub> (see *Supplementary Materials for detail, Fig. 7.S6*).

To evaluate the quality of active sites, we plotted benzaldehyde conversion versus benzyl alcohol selectivity (**Fig. 7.1C**). As expected, the selectivity to benzyl alcohol was in the order of MOF-808(Hf) > MOF-808(Zr) > UiO-66(Hf) @ Hf(OTf)<sub>4</sub> > UiO-66(Zr) @ Zr(OTf)<sub>4</sub>. At similar benzaldehyde conversion, MOF-808(Hf) showed higher selectivity to benzyl alcohol compared with MOF-808(Zr). These results suggested that (1) Brønsted and Lewis acid sites were active for benzaldehyde conversion, and (2) Lewis acidic MOF-808 catalysts were more selective to benzyl alcohol than were triflate salts and UiO-66 catalysts.

Because our synthesized UiO-66 catalysts had both Brønsted and Lewis acidities, we used Brønsted acidic H<sub>2</sub>SO<sub>4</sub> as a control to decouple the activities of Brønsted and Lewis acidity for transfer hydrogenation (**Fig. 7.S7**). With benzaldehyde as a reactant, we did not observe benzyl alcohol as a reaction product. The H<sub>2</sub>SO<sub>4</sub> catalyst was active for benzaldehyde conversion. However, it was not selective to benzyl alcohol. Instead, we observed acetal as a product. Moreover, brown substances appeared in the reaction solution; we postulated that the brown substances were degradation products (coke). Next, we used benzyl alcohol as a reactant (**Fig. 7.S8**). The control, (no added catalyst) showed <20% conversion of benzyl alcohol without any products. Adding H<sub>2</sub>SO<sub>4</sub> catalyst yielded 2-benzyloxypropane as a major reaction product, which

suggested that H<sub>2</sub>SO<sub>4</sub> catalyzed etherification of benzyl alcohol with 2-propanol over Brønsted acidic H<sub>2</sub>SO<sub>4</sub>. Also, we again observed brown substances suggestive of degradation products (coke). Overall, our results indicated that Brønsted acids promoted undesired side reactions (forming acetals and degradation of reactants, intermediates, and reaction products).

Although ideal UiO-66 catalysts have only Brønsted acid sites, defect formation is unavoidable during UiO-66 synthesis. Our synthesized UiO-66(Zr) contained ~8.8% missing linkers, which acted like Lewis acids. Similarly, the synthesized UiO-66(Hf) catalyst contained ~3.1% defect sites. Although these defect sites catalyzed the transfer hydrogenation of benzaldehyde to benzyl alcohol, the selectivity to benzyl alcohol was low (27%) at 88% conversion. The low selectivity stemmed from (1) a low number of Lewis acidic sites and (2) the transformation of Lewis acid sites into Brønsted acid sites, which promoted unwanted side reactions.

To further substantiate the foregoing claim, we synthesized UiO-66(Hf) with added formic acid as a modulator and formed modulated UiO-66(Hf). The added formic acid during MOF synthesis created defect sites in the form of missing linkers. As expected, our calculation from TGA profile demonstrated that modulated UiO-66(Hf) had 21.5% defect sites (**Table 7.S4**). In addition, the modulated UiO-66(Hf) had 47% selectivity to benzyl alcohol after 3 h compared with 27% from unmodulated UiO-66(Hf) (**Fig. 7.S9**). These results suggested that adding Lewis acidic sites to UiO-66(Hf) enhanced the selectivity to benzyl alcohol.

#### **3.4. Density functional theory proposed mechanism of transfer hydrogenation of benzaldehyde by MOF-808 and UiO-66**

To explain the high catalytic activity of Zr- and Hf-containing MOF-808 for transfer hydrogenation of benzaldehyde with 2-propanol, we performed density functional theory (DFT) calculations [496]. Our calculations revealed that transfer hydrogenation of benzaldehyde by Zr- and Hf-containing MOFs followed the Meerwein–Ponndorf–Verley (MPV) two simultaneous elementary steps (**Fig. 7.2**): (1) hydrogen transfer from 2-propanol (alcohol) to benzaldehyde (reactant) to form

intermediate (co-Ads to Int) and (2) formation of benzyl alcohol as a reaction product (Int to Prod). Initially, the 2-propanol and benzaldehyde molecules interacted on each open site of the  $M^{4+}-O^{2-}$  of the metal clusters in MOF-808(M= Zr or Hf) (co-Ads). In the transition state (TS1), the oxygen (O) of the surface hydroxide group of MOFs severed the O-H bond of 2-propanol and simultaneously enabled the hydrogen transfer (H1) from the C2 of 2-propanol to the carbonyl C1 of benzaldehyde. After the TS1, the reaction proceeded with the formation of benzyl alkoxide intermediate, acetone, and water molecules (Int). Finally, benzyl alcohol (product) is formed by the hydrogenation of benzyl alkoxide in the transition state (TS2). The TS2 involved the concerted O-H2 bond breaking and the formation of the O1-H2 bond. In contrast to our findings, Rojas-Buzo et al.[28] found that MOF-808(Hf) catalyzed direct transfer hydrogenation.

**Figure 7.2** shows the optimized structures for the MPV reaction, and the relative free energies calculated for Zr- and Hf-containing MOF-808. The co-adsorption free energies of benzaldehyde and 2-propanol were  $-11.7$  and  $-10.9$  kcal/mol for MOF-808(Zr) and MOF-808(Hf), respectively (co-Ads, **Fig. 7.2**). The binding energy of MOF-808(Zr) was greater than that of MOF-808(Hf) because charge transfer from molecules to the active site of MOF-808(Zr) was  $0.191e$ , greater than the  $0.188e$  charge transfer of MOF-808(Hf). The activation energy of step 1 ( $E_{a1}$ ) was  $20.1$  and  $17.8$  kcal/mol for of Zr- and Hf-containing MOF-808, greater than the activation energy of step 2 (no barriers with  $E_{a2} = -1.3$  and  $-2.0$  kcal/mol for MOF-808(Zr) and MOF-808(Hf), respectively). These results suggested that the hydrogen transfer (step 1) was the rate-determining step. To explain the difference between MPV activity of Zr- and Hf-containing MOF-808, we further calculated the different amount of charge transfer (DCT) from the catalytic sites to the adsorbed benzaldehyde molecule between the adsorption and transition state complexes. The DCTs of MOF-808(Zr) and MOF-808(Hf) were  $0.462$  and  $0.471e$ , respectively. The higher DCT value of MOF-808(Hf) resulted in a lower activation energy barrier compared with MOF-808(Zr) ( $E_{a1}$  of MOF-808(Hf)  $< E_{a1}$  of MOF-808(Zr)), which corroborated the activation barriers shown in **Fig. 7.2**. With a low activation energy barrier, MOF-808(Hf) weakened the C=O carbonyl bond of benzaldehyde during the charge transfer process. It enhanced the ability of the C1 carbon atom to accept the H1

hydrogen (transferred) from 2-propanol. Overall, these results suggested that (1) Lewis acidic MOF-808 catalyzed transfer hydrogenation by MPV, and (2) MOF-808(Hf) was more active at MPV of benzaldehyde than MOF-808(Zr).

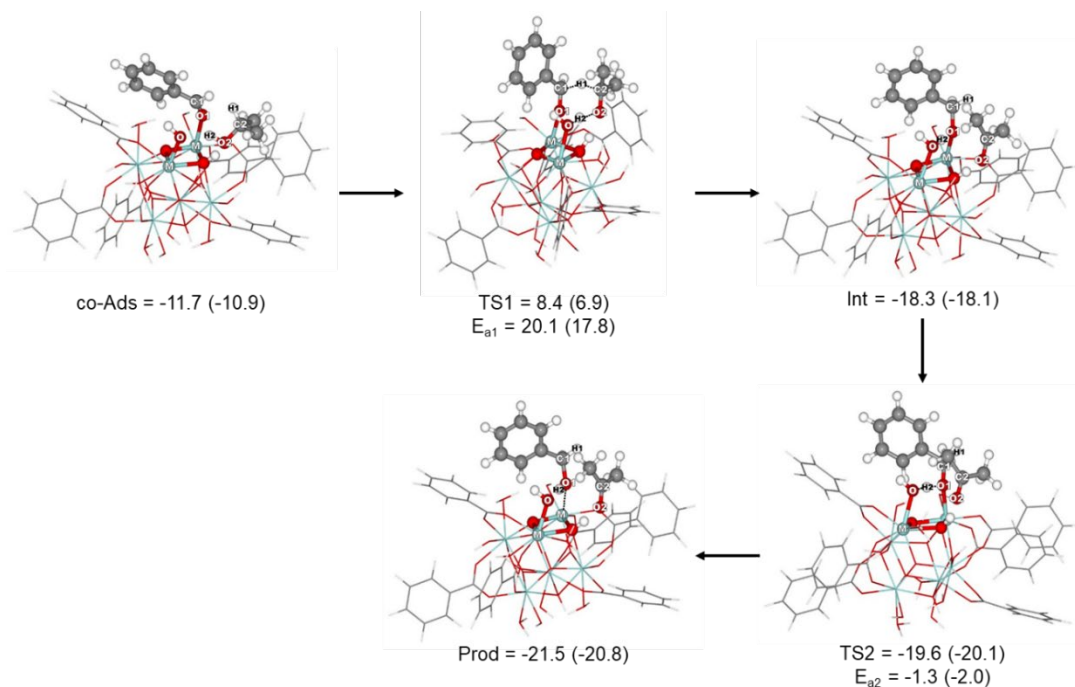


**Figure 7.2.** Proposed mechanism of MPV reduction of benzaldehyde with 2-propanol to produce benzyl alcohol by Zr- and Hf-containing MOF-808. Values in parentheses are the free energies of MOF-808(Hf) in kcal/mol. Co-Ads = co-adsorption of benzaldehyde and 2-propanol molecules, TS1 and TS2 = transition state of step 1 and 2, Int = intermediate, Prod = product, and  $E_{a1}$  and  $E_{a2}$  = activation energies of step 1 and 2.

Unlike MOF-808, UiO-66 did not have Lewis acidic sites to activate the carbonyl group of benzaldehyde for the MPV [28]. Therefore, we postulated that the Brønsted acid sites of UiO-66(Hf) participated in the benzaldehyde conversion. To test this hypothesis, we investigated the co-adsorption of benzaldehyde and 2-propanol on Hf (co\_Ads\_a) and Brønsted sites (co\_Ads\_b) on UiO-66(Hf) (**Fig. 7.S10**). The calculated energy of the co-adsorption on Hf was 3.8 kcal/mol (endothermic), whereas the co-adsorption of benzaldehyde and 2-propanol on the Brønsted site



was  $-4.7$  kcal/mol (exothermic); these energies suggested that Brønsted sites were the preferred sites for the co-adsorption, and the reaction proceeded without intermediates. **Figure 7.3** shows a proposed benzaldehyde conversion by UiO-66(Hf). The reaction proceeded by the co-adsorption of benzaldehyde and 2-propanol over the Brønsted site of UiO-66(Hf) (co-Ads). At the transition state (TS), the benzaldehyde was simultaneously hydrogenated at C1 and O1 atoms via the hydrogen transfer from 2-propanol to form the benzyl alcohol product (Prod). The activation energy barrier was  $28.4$  kcal/mol, significantly greater than the  $17.8$  kcal/mol (**Fig. 7.2**) activation energy for MOF-808(Hf). These results suggested that (1) Brønsted sites of UiO-66(Hf) were active for transfer hydrogenation, which corroborated our experimental results that showed high benzaldehyde conversion (**Fig. 7.1**), and (2) the UiO-66(Hf) Brønsted sites catalyzed the direct transfer hydrogenation.

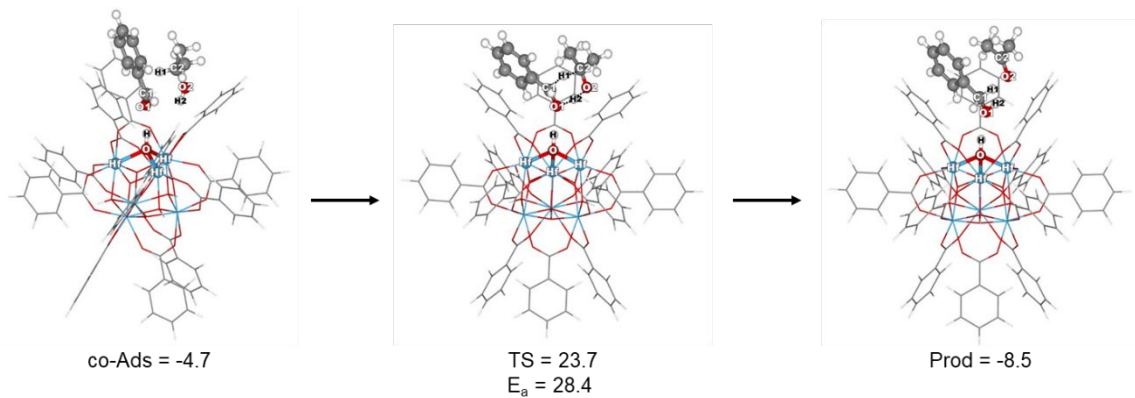


**Figure 7.3.** Proposed mechanism of benzaldehyde reaction with 2-propanol over Brønsted acid sites in UiO-66(Hf) and free energies (kcal/mol). Co-Ads = co-adsorption of benzaldehyde and 2-propanol molecules, TS = transition state, Prod = product, and E<sub>a</sub> = activation energy.

### 3.5. Proposed chemical pathway for Meerwein–Ponndorf–Verley reduction of benzaldehyde by MOF-808(Hf)

On the basis of our experimental results, we proposed a chemical pathway for the MOF-808(Hf)-catalyzed MPV reduction of benzaldehyde to benzyl alcohol (**Fig. 7.4**). First, 2-propanol and benzaldehyde molecules are co-absorbed on MOF-808(Hf) and interact with the Hf<sup>4+</sup>-O<sup>2-</sup> of the Hf

clusters. Next, acidic  $\text{Hf}^{4+}$  species activate the carbonyl groups in benzaldehyde. Then the reaction proceeds by a hydrogen transfer and 2-propanol O-H bond-breaking steps and forms the benzyl alkoxide intermediate, acetone, and water molecules. Finally, the benzyl alkoxide intermediate coordinated with the Hf metal center is transformed into benzyl alcohol.

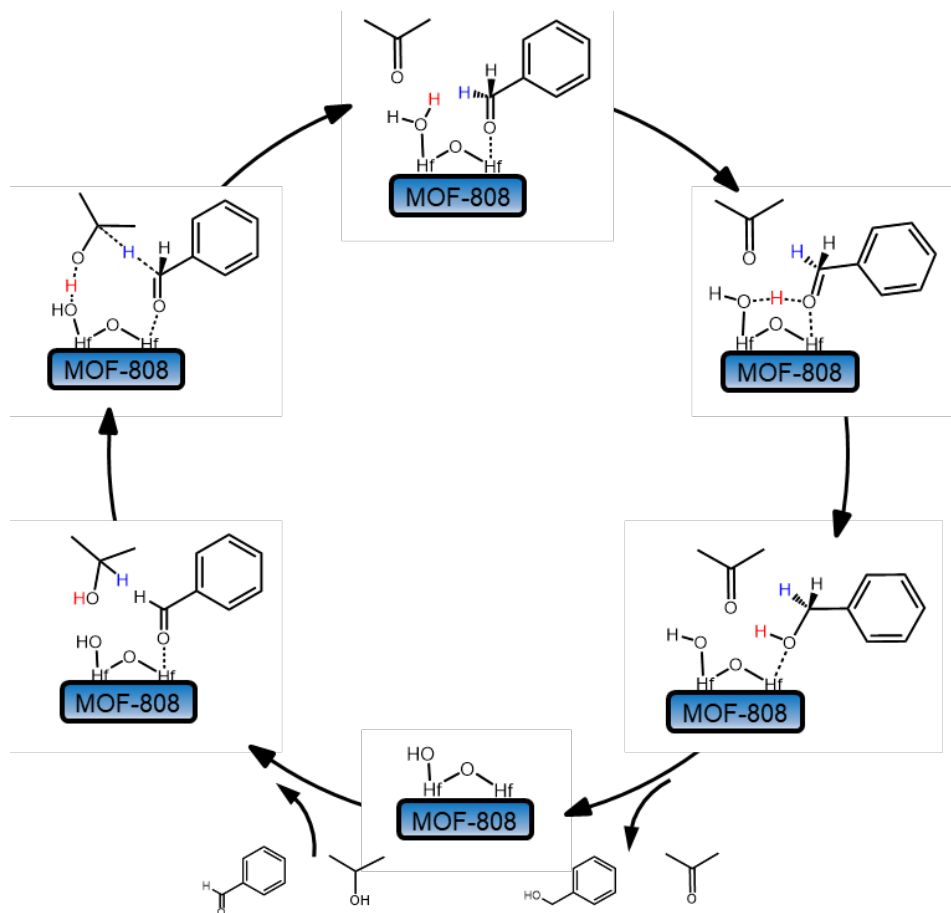


**Figure 7.4.** Proposed chemical pathway for Meerwein–Ponndorf–Verley reduction of benzaldehyde with 2-propanol to benzyl alcohol by MOF-808(Hf).

### 3.6. Transfer hydrogenation of selected carbonyl compounds with MOF-808(Hf)

Because Lewis acidic MOF-808(Hf) was active and selective for transfer hydrogenation of benzaldehyde, we used MOF-808(Hf) with six carbonyl compounds with aromatic, furan, and aliphatic structure, namely, furfural (a), 5-methyl furfural (b), 5-(hydroxymethyl) furfural (c), cyclohexanone (d), acetophenone (e), and 2-hexanone (f) (**Fig. 7.5**). MOF-808(Hf) reduced these carbonyls to corresponding alcohols with >89% selectivity with minimal side reactions (e.g., coke

formation) [497-500]. Interestingly, we obtained a low conversion (45.1%) of 5-methyl furfural (b). The low activity of MOF-808(Hf) on 5-methyl furfural (b) was due to steric hindrance and the presence of methyl group. The electron-donating nature of the methyl group in compound b increased electron density on the carbon atom of the carbonyl group. As a result, the attack of hydride ions on the carbonyl carbon was not favorable [501]. Although one would expect a low conversion of 5-(hydroxymethyl) furfural (compound c) due to structural similarity to compound b, our results showed 86.1% conversion of compound c. We postulated that the OH group of compound c formed a hydrogen bond with the oxygen atom in the furan ring and decreased electron density on the carbon atom of the carbonyl group. Therefore, the activity of the carbonyl group for proton subtraction is enhanced. Together, these results suggested high selectivity of MOF-808(Hf) for transfer hydrogenation of carbonyl compounds.

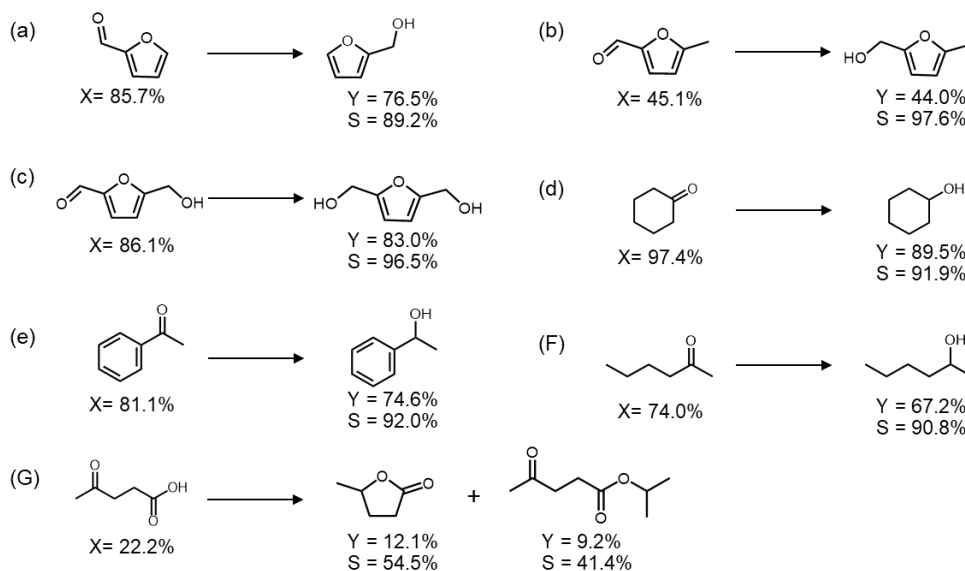


**Figure 7.5.** Transfer hydrogenation of selected carbonyls by MOF-808(Hf). X, Y, and S indicate the conversion of aldehydes, yield of their corresponding alcohols, and selectivity, respectively. Reaction condition. 1 wt.% carbonyl compound in 2-propanol, catalyst loading = 3 mol.% Hf, 100 °C, 1 h.

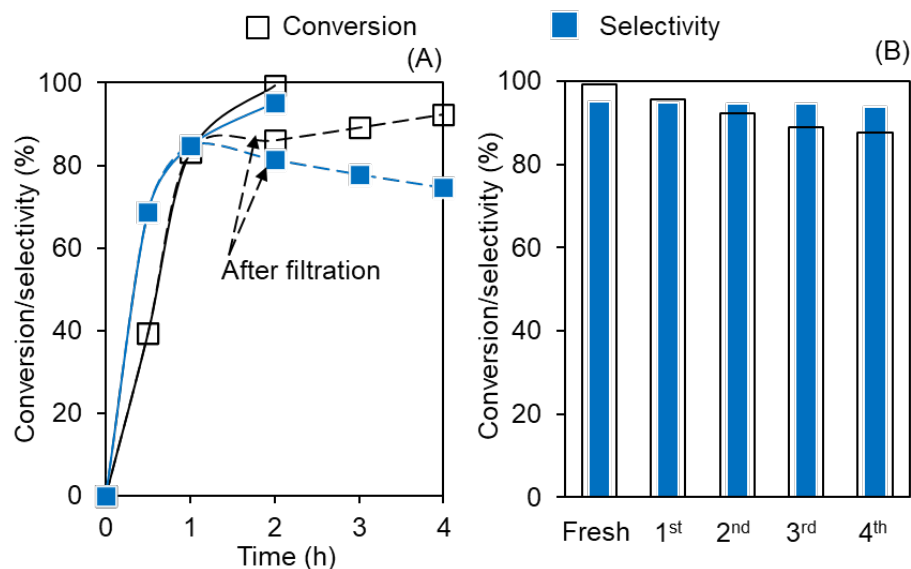


**Figure 7.6.** Stability and reusability of MOF-808(Hf) for the MPV reduction of benzaldehyde to benzyl alcohol by filtration test at 100 °C (A) and recycle of MOF-808(Hf) catalyst at 100 °C, 2 h (B). Reaction condition. 1 wt.% benzaldehyde in 2-propanol, catalyst loading = 3 mol.% metal (Hf).

### 3.7. Stability and reusability of MOF-808 in transfer hydrogenation of benzaldehyde

To evaluate the catalyst stability under the reaction condition, we performed filtration experiments by conducting the transfer hydrogenation using MOF-808(Hf) for 1 h at 100 °C, filtering the MOF-808(Hf) catalyst from the reaction mixture, and heating the filtrate under the same reaction condition (100 °C) for 4 h (**Fig. 7.6A**). We sampled the reaction mixture three times during the 3 h and measured benzaldehyde conversion and benzyl alcohol selectivity. The conversion of benzaldehyde slightly increased, whereas the selectivity to benzyl alcohol slightly decreased. One reason was that benzaldehyde and benzyl alcohol degraded at 100 °C, which corroborated our blank experiments of benzaldehyde (**Fig. 7.1**) and benzyl alcohol (**Fig. 7.S8**).

The ability to recycle catalysts is important for their practical use. We recycled the MOF-808(Hf) by centrifugation and washing with ethyl acetate to remove the residual products, intermediates, and unreacted benzaldehyde. The catalyst was then dried in a vacuum oven at 130 °C to remove moisture and residual solvent. We selected this temperature based on our TGA results to minimize

the decomposition of MOF-808. The MOF-808(Hf) catalyst maintained a high selectivity to benzyl alcohol (94%) with a slight decrease in benzaldehyde conversion (11%) over four cycles (**Fig. 7.6B**). Further, we used ICP-OES, XRD, and FTIR to characterize the spent MOF-808(Hf) catalyst after the 4<sup>th</sup> reuse cycle (**Fig. 7.S11**). The hafnium content of the spent catalyst, measured by ICP-OES, was 37.3 wt.%, ~8% lower than that of fresh catalysts (40.6 wt.%). This decrease in hafnium content after 4<sup>th</sup> reuse cycle was proportional to the drop in conversion of benzaldehyde, which suggested that metal leaching was the deactivation mechanism of MOF-808(Hf). However, this metal leaching was not significant as evidenced by a high selectivity to benzyl alcohol (94%) at 88% benzaldehyde conversion after 4 cycles. In a like manner, the XRD and FTIR spectra of the reused catalyst exhibited chemical structure and functionality similar to fresh MOF-808(Hf) (**Fig. 7.S11**). These filtration and characterization results suggested catalyst stability under the present experimental conditions. Overall, MOF-808(Hf) maintained high selectivity to benzyl alcohol for all the cycles and structural integrity after (at least) four recycles.

#### 4. Discussion

The challenge in catalytic transfer hydrogenation is developing active, selective, and reusable catalysts [464, 465]. We investigated the catalytic performance of Zr- and Hf-containing MOF-808 and UiO-66 catalysts for the transfer hydrogenation of carbonyl compounds to their corresponding alcohols. The Lewis acidic MOF-808(Hf) was the most active for transfer hydrogenation of benzaldehyde and the most selective to corresponding alcohols, with 95% selectivity to benzyl alcohol at 99% conversion of benzaldehyde. Our combined experimental and computational results explained the effects of the metal and acid sites on the chemical pathway of transfer hydrogenation of carbonyl compounds and the stability of products.

Our most significant finding was the detailed mechanism of MOF-808-catalyzed MPV and UiO-66-catalyzed direct transfer hydrogenation. Lewis acidic MOF-808 underwent the MPV pathway of carbonyl compounds, which was active and selective to corresponding alcohols, whereas UiO-66 could not catalyze transfer hydrogenation selectively. Although our calculations showed that

Brønsted acid sites of UiO-66 catalyzed direct transfer hydrogenation of carbonyl compounds, the high activation energy barrier made catalysis difficult. Moreover, Brønsted acids promoted the unwanted formation of acetals and degradation products. Thus, the selective transfer hydrogenation of carbonyl compounds by UiO-66 relied on the presence of Lewis acids from the generation of defects during MOF synthesis. For example, our synthesized UiO-66 contained ~8.8% missing linkers, which indicated that each missing linker molecule (terephthalic acid) created two coordinatively unsaturated  $Zr^{4+}$  that acted like Lewis acids. Our calculation of missing linkers implied that only ~18% of the total zirconium ions in UiO-66(Zr) participated in the MPV reaction. The rest of the zirconium ions initiated the direct transfer hydrogenation and unwanted side reactions (formation of hemiacetals and degradation products). Thus, we observed a low selectivity of benzyl alcohol products at a high benzaldehyde conversion. Conversely, all  $Zr^{4+}$  ions in MOF-808 participated in MPV of carbonyl compounds. As a result, MOF-808 provided a high selectivity of corresponding alcohols at a high conversion, which agreed with the high activity and selectivity of MOF-808 for the reduction of carbonyl compounds [28, 394, 502, 503].

Another significant finding was a lower activation energy of the transfer hydrogenation by MOF-808(Hf) compared with MOF-808(Zr). Our quantum calculations revealed that the charge transfer from Hf active sites to the benzaldehyde molecule was higher than that of Zr sites and resulted in lower activation energy. These findings implied that the charge transfer process was crucial in activating the C=O bond, and the charge transfer facilitated the transferred hydrogen from the -OH group of 2-propanol (H1). We postulated that this high charge transfer of MOF-808(Hf), compared with MOF-808(Zr), resulted in a greater Lewis acidity of Hf sites compared with Zr sites. As a result, MOF-808(Hf) had a high activity for transfer hydrogenation relative to MOF-808(Zr). These results agreed with findings by Koehle et al. [504] and Sittiwong et al. [505]. They observed that Hf active sites in Lewis acidic  $\beta$ -zeolites and UiO-66 MOFs provided a lower activation barrier than did Zr sites in catalytic transfer hydrogenation of furfural to furfuryl alcohol.

Our findings advance understanding of the function of Lewis and Brønsted acid sites of Hf- and Zr-containing MOF-808 and UiO-66 MOFs and reaction pathways for transfer hydrogenation. Moreover, the MOF synthesis procedures are simple, environmentally friendly, and scalable compared with the preparation of conventional selective catalysts for transfer hydrogenation, such as Hf-, Zr-, and Sn-containing zeolites [276, 476, 477]. Although defective UiO-66(Hf) was not selective to transfer hydrogenation, the knowledge gained from the defects-induced Brønsted acidity of UiO-66 will enable tuning the Brønsted acid strength and balance Lewis/Brønsted acid ratio for various organic reactions, such as dehydration [443], isomerization [333], condensation [398, 506-508], and acetalization [444] and cascade reactions that require both Lewis and Brønsted acidities, such as cellulose conversion to 5-hydroxymethylfurfural [443], lactic acid [333, 445], and levulinic acid [446].

## 5. Conclusion

Catalytic transfer hydrogenation is a promising approach for upgrading biomass-derived molecules to high-value chemicals. This study described the mechanism of transfer hydrogenation of benzaldehyde by Hf- and Zr-containing MOF-808 and UiO-66 metal-organic frameworks (MOFs). Although these MOFs have demonstrated their transfer hydrogenation ability, the effect of metal sites and acid sites on the chemical pathway was unknown. Our results demonstrated that Hf- and Zr-containing MOF-808 catalysts enabled selective MPV reduction of carbonyl compounds to corresponding alcohols. Moreover, MOF-808(Hf) was more active and selective to transfer hydrogenation because Hf active sites had a lower activation energy barrier compared with Zr sites. Although creating (Lewis acidic) defects in UiO-66 enhanced its selective transfer hydrogenation, the defects induced Brønsted acidity in the presence of water, which decreased the selectivity because of side reactions. Thus, caution must be exercised in creating and handling defective UiO-66 catalysts so as to control the type of acid sites. Future studies will focus on tuning the Brønsted and Lewis acidity of these MOFs, reversibility of the defects-induced Brønsted acidity, and long-term stability.

## Acknowledgment

A part of this material is based upon work supported by the National Science Foundation under Cooperative Agreement No. 1355438 and Internal Research Grant, Office of the Executive Vice President for Research, University of Louisville. This work was performed in part at the Conn Center for Renewable Energy Research at the University of Louisville, which belongs to the National Science Foundation NNCI KY Manufacturing and Nano Integration Node, supported by ECCS-1542174. T.M. acknowledges support from the Office of the Permanent Secretary, Ministry of Higher Education, Science, Research and Innovation, Thailand (Grant No. RGNS 63-038). The authors would like to thank Ashten Molley, Kyle Mills, Sandesh Uttarwar, and Francois Nkurunziza from University of Louisville for their help in performing selected MPV experiments. The authors would like to thank Dr. Howard Fried for his valuable comments and suggestions on the manuscript.

## 6. Supplementary Information

### 1. Materials and Methods

| <b>Table 7.S1.</b> List of chemicals/reagents used in this study |   |               |                   |
|--|---|---------------|-------------------|
| <b>Material/Chemical</b>   | <b>Supplier</b>                               | <b>Purity</b> | <b>CAS Number</b> |
| Benzaldehyde   | Alfa Aesar(Ward Hill, MA)                     | 99%           | 100-52-7          |
| Benzyl Alcohol   | Alfa Aesar(Ward Hill, MA)                     | 99%           | 100-51-6          |
| Cyclohexanone  | Beantown Chemical Corporation<br>(Hudson, NH) | 99%           | 108-94-1          |
| Ethyl Levulinate   | Alfa Aesar(Ward Hill, MA)                     | 98%           | 539-88-8          |
| 2-Furaldehyde  | Alfa Aesar(Ward Hill, MA)                     | 98%           | 98-01-1           |
| 5-Hydroxymethylfurfural  | Ark Pharm(Libertyville, IL)                   | 98%           | 67-47-0           |
| 4-Hydroxybenzaldehyde  | Oxchem, Irwindale CA                          | 95+%          | 123-08-0          |
| n-Hexadecane   | Alfa Aesar(Ward Hill, MA)                     | 99%           | 544-76-3          |
| 2-Propanol   | Sigma-Aldrich(St.Louis, MO)                   | 99.5%         | 67-63-0           |



|                                 |  |                     |             |
|---------------------------------|--|---------------------|-------------|
| Zirconium (IV) chloride         | Alfa Aesar(Ward Hill, MA)                        | 99.5+%              | 10026-11-6  |
| Hafnium (IV) chloride           | Alfa Aesar(Ward Hill, MA)                        | 99.9%               | 13499-05-03 |
| 1,3,5-benzenetricarboxylic acid | Beantown Chemical Corporation<br>(Hudson, NH)    | 98%                 | 554-95-0    |
| Terephthalic acid               | Tokyo Chemical Industry (Tokyo, Japan)           | >99.0%              | 100-21-0    |
| N, N-dimethylformamide          | Chem-Impex Int'l. Inc.                           | 100%                | 68-12-2     |
| Formic Acid                     | Beantown Chemical Corporation<br>(Hudson, NH)    | 97%                 | 64-18-6     |
| Hf(Otf) <sub>4</sub>            | Alfa Aesar(Ward Hill, MA)                        | 98%                 | 161337-67-3 |
| Zr(Otf) <sub>4</sub>            | Sigma-Aldrich(St.Louis, MO)                      | 97%                 | 89672-77-5  |
| Methanol                        | Ward's science                                   | Lab<br>grade        | 67-56-1     |
| Ethanol                         | Decon Laboratories, Inc.                         | 200<br>Proof        | 64-17-5     |
| Acetone                         | (Aqua Solutions, Inc., Deer Park, TX)            | Technic<br>al grade | 67-64-1     |
| Ethyl Acetate                   | Alfa Aesar(Ward Hill, MA)                        | 99%                 | 141-78-6    |
| Pyridine                        | Chem-Impex International (Wood Dale,<br>IL, USA) | 99.97%              | 110-86-1    |

## **1.1. Synthesis of metal-organic frameworks**

### **Synthesis of UiO-66(Zr)**

UiO-66(Zr) MOF was synthesized using the previously described solvothermal method in a 45 mL Teflon-lined autoclave reactor [485]. Typically, a mixture of  $ZrCl_4$  (0.53 g), terephthalic acid (0.37 g) was dissolved in DMF (30 mL) and kept in a sonicator for about 20 minutes. First, the tightly sealed autoclave was kept in an oven without stirring at 120 °C for 24 h. Then the reactor was cooled at room temperature, and the solids were separated from the solution by centrifugation (6000 RPM, 5 min). Next, the solids were washed by DMF (20 mL) three times and centrifuged to remove the suspension. After that, the particles were soaked in methanol for 3 h, washed with (20 mL) three times to remove DMF, and finally dried under vacuum at 80 °C for overnight.

### **Synthesis of UiO-66(Hf)**

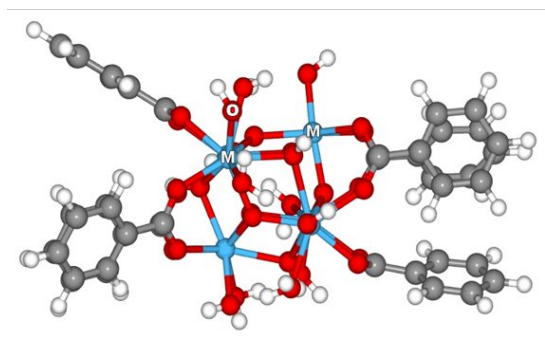
UiO-66(Hf) MOF was synthesized by the solvothermal method [486] with a slight modification. First,  $HfCl_4$  (384 mg) and terephthalic acid (200 mg) were dissolved in 16 mL of DMF. Next, the mixture was added to a 45 mL Teflon-lined autoclave reactor and placed in the oven at 120 °C for 48 h. The resulting product was cooled, centrifuged, and washed 3 times with DMF and acetone. Finally, the product was dried and activated in a vacuum oven at 100 °C for 12 hours.

### **Synthesis of modulated UiO-66(Hf)**

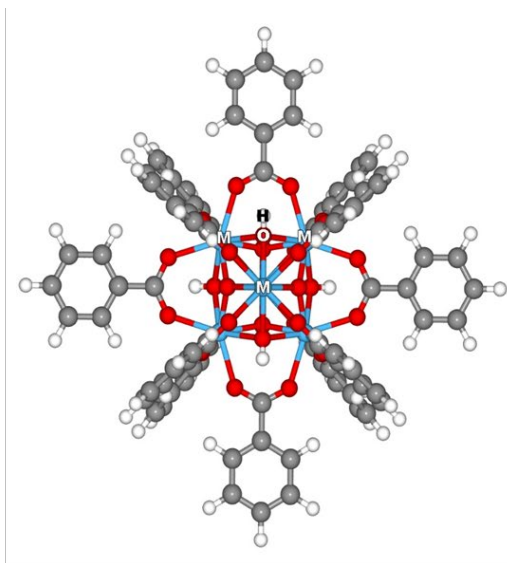
Modulated UiO-66(Hf) MOF was synthesized by the solvothermal method [486] with a slight modification. First,  $HfCl_4$  (384 mg) and terephthalic acid (200 mg) were dissolved in 16 mL of DMF and 4 mL of formic acid as a modulator. Next, the mixture was added to a 45 mL Teflon-lined autoclave reactor and placed in the oven at 120 °C for 48 h. The resulting product was cooled, centrifuged, and washed 3 times with DMF and acetone. Finally, the product was dried and activated in a vacuum oven at 100 °C for 12 hours.

### Synthesis of MOF-808 (Zr/Hf)

MOF-808 (Zr/Hf) MOFs were synthesized by the previously described solvothermal method with a slight modification [28]. The salt  $ZrCl_4$  (115 mg, 0.5 mmol) or  $HfCl_4$  (160 mg, 0.5 mmol) and the organic ligand 1,3,5-benzenetricarboxylic acid (110 mg or 0.5 mmol) were dissolved in a mixture of N-dimethylformamide (20 mL) and formic acid (20 mL) and sonicated for 30 min to ensure complete dissolution and mixing. The mixture was transferred in a 100 mL Teflon-lined autoclave reactor and placed in an oven at 100 °C for 72 hours. The resulting solid was cooled, centrifuged, and washed with DMF 3 times, followed by 2 times wash with acetone. The final product was dried and activated in a vacuum oven at 120 °C for 12 hours.



(a) MOF-808



(b) UiO-66

**Figure 7.S1.** Cluster model of MOF-808 (a) and UiO-66 (b) used in this work

## 2. Results

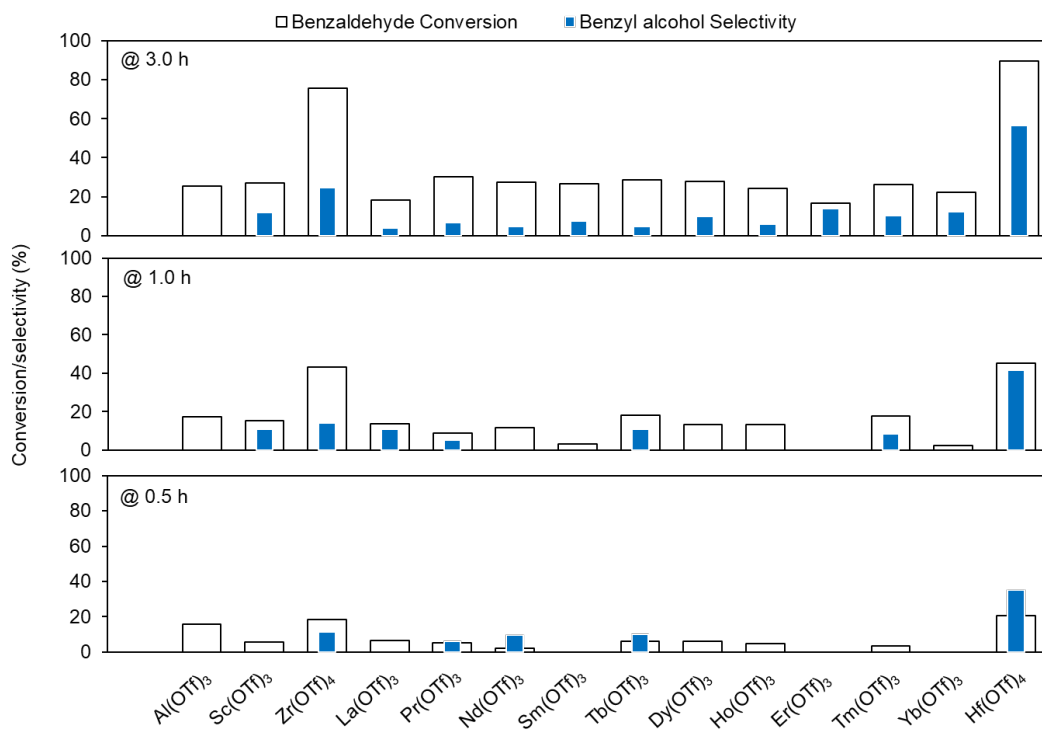


**Figure 7.S2.** Evolution profiles of benzaldehyde conversion and selectivity to benzyl alcohol for MPV reduction of benzaldehyde with 2-propanol by metal triflates. Reaction condition: 1 wt.% benzaldehyde in 2-propanol, 3 mol% triflate salts as catalyst, 100 °C, 0.5-3.0 h.

### 2.1. Physicochemical characteristics of synthesized Zr- and Hf-containing metal-organic frameworks (MOFs)

#### 2.1.1. N<sub>2</sub> adsorption-desorption isotherms of synthesized Zr- and Hf-containing MOFs

Their N<sub>2</sub> adsorption-desorption isotherms of these MOFs exhibited the type IV isotherm, which was the characteristic of mesoporous materials [28, 503]. We calculated the surface area, pore-volume, and average pore diameter of the synthesized MOFs (**Table 7.S2**) based on the N<sub>2</sub> adsorption-desorption isotherm (**Fig. 7.S3A**). UiO-66(Zr) and UiO-66(Hf) had surface area ~900-1100 m<sup>2</sup>/g, which was consistent with previously reported values of 800-1200 m<sup>2</sup>/g [394, 431, 509]. MOF-

808(Hf) and MOF-808(Zr) had a surface area of ~1050-1500 m<sup>2</sup>/g, which was consistent with previously reported values of 800-1450 m<sup>2</sup>/g [394, 431, 482].

| <b>Table 7.S2.</b> Calculated surface area, pore-volume, and average pore diameter of Zr- & Hf-containing MOFs |                     |                      |                       |
|--|---------------------|----------------------|-----------------------|
| MOFs   | Surface area        | Total pore volume    | average pore diameter |
|  | [m <sup>2</sup> /g] | [cm <sup>3</sup> /g] | (nm)                  |
| UiO-66(Zr)   | 905.7 [431]         | 0.51                 | 2.25                  |
| UiO-66(Hf)   | 1042.8 [510]        | 0.53                 | 2.02                  |
| MOF-808(Zr)  | 1421.2 [394]        | 0.83                 | 2.33                  |
| MOF-808(Hf)  | 1075.1 [503]        | 0.60                 | 2.23                  |

### 2.1.2. Functionality and metal content of synthesized Zr- and Hf-containing MOFs by FTIR and ICP-OES

The FTIR spectrum for all the Zr- and Hf-containing MOFs showed in **Fig. 7.S3B**. The band appears at 558 cm<sup>-1</sup>, corresponding to the Zr or Hf-oxygen stretching of the UiO-66(Zr) and UiO-66(Hf) structure [428, 429]. The band at 1398 cm<sup>-1</sup> in UiO-66(Zr) and UiO-66(Hf) corresponded to the stretching vibration of the coordinated C-O group. The bands at 489 cm<sup>-1</sup> and 672 cm<sup>-1</sup> for UiO-66(Zr) were attributed to in-plane and out-of-plane bending vibrations of COO<sup>-</sup>. For UiO-66(Zr) and UiO-66(Hf), the bands at ~1509 and ~1592-1598 cm<sup>-1</sup> were assigned to the stretching vibration of C=C in the benzene ring of the organic ligand H<sub>2</sub>bdc [430-432].

MOF-808(Zr) had a characteristic band at ~666 cm<sup>-1</sup>, which was assigned to Zr–O's vibration from the coordination between the carboxyl groups of BTC and the zirconium ions [511]. On the other hand, the band at 674 cm<sup>-1</sup> assigned to the vibration of Hf-O in the MOF-808(Hf) framework building blocks. For MOF-808, the bands at the 1450 cm<sup>-1</sup> and 1380 cm<sup>-1</sup> regions are assigned to the C =

C bond and O–H stretching mode in the organic linker’s aromatic compound [512]. For both MOFs, the band at 1611 cm<sup>-1</sup> was assigned to the stretching mode of the carboxylate group (COO<sup>-</sup>).

Using the ICP-OES, we got the Zr and Hf content (wt%) of the synthesized MOFs (**Table 7.S3**). The percentage of Zr content was 26 to 32% for Zr-MOFs, and Hf content was 40 to 42% for Hf-MOFs, which matched with the previously reported values from the literature [28, 394].

| <b>Table 7.S3.</b> Metal analysis of Zr- & Hf-containing MOFs by ICP-OES |                |           |                |           |
|--|----------------|-----------|----------------|-----------|
| Framework  | UiO-66         |           | MOF-808        |           |
| Metal node   | Zr             | Hf        | Zr             | Hf        |
| Metal content by ICP (wt.%)  | 31.6 [28, 394] | 42.4 [28] | 26.3 [28, 394] | 40.6 [28] |
| Metal content by TGA (wt.%)  | 37.8           | 40.7      | 35.5           | 51.6      |

### 2.1.3. Thermogravimetric profiles and thermal stability of synthesized Zr- and Hf-containing MOFs

Thermogravimetric analysis (TGA) of the synthesized MOFs was performed under a flow of air and a heating ramp of 10 °C/min from 25-700 °C. TGA and derivative curves (DTG) are presented in **Fig. 7.S3C**.

TGA profiles of synthesized Zr-/Hf-MOFs demonstrate that Zr- and Hf-containing MOF catalysts were sufficiently stable to carry out the transfer hydrogenation at 100 °C. For the UiO-66(Zr), the weight loss from room temperature to 150 °C happened due to the evaporation of physisorbed water in the pores. The weight loss (~15 %) in the range of 150–320 °C occurred due to the evaporation of DMF in the channel and the dehydroxylation process. The hydroxyl groups bound to the metal ion center were detached in water molecules during this process, changing the Zr center’s coordination environment. When the temperature was higher than 450 °C, the organic ligand gradually decomposed to 600 °C. These results suggested that UiO-66(Zr) had superior

thermal stability and could maintain structural integrity below 450 °C. Qiu et al. also observed the similar thermal properties of UiO-66(Zr) [431].

For the UiO-66(Hf), the weight loss from room temperature to 150 °C happened due to the evaporation of physisorbed water in the pores. The weight loss (~8 %) in the range of 150–350 °C occurred due to the evaporation of DMF in the channel and the dehydroxylation process. During this process, the hydroxyl groups bound to the center of the metal ion were detached in the form of water molecules, which changed the Hf center's coordination environment. When the temperature was higher than 450 °C, the organic ligand gradually decomposed till 650 °C. These results suggested that UiO-66(Hf) had superior thermal stability and could maintain structural integrity below 450 °C. Rojas et al. also observed similar thermal properties for UiO-66(Hf) [28].

The TGA profile of MOF-808(Zr) exhibited three mass loss zones in the 30–150 °C, 150–450 °C (18 wt. %), and 450–650 °C (11 wt. %). These zones correspond to the mass loss from (1) the evaporation of the physisorbed water molecules, (2) degradation of remnant formate,  $\mu_3$ -OH, and evaporation of physisorbed dimethylformamide (DMF), and (3) the degradation of the framework benzenetricarboxylate (BTC) ligand. Valekar et al. [394] also observed a similar TGA profile for MOF-808(Zr).

The TGA profile of MOF-808(Hf) exhibited three mass loss zones in the 30–150 °C (~6 wt. %), 150–450 °C (19 wt. %), and 450–650 °C (16 wt. %). These zones correspond to the mass loss from (1) the evaporation of the physisorbed water molecules, (2) degradation of remnant formate,  $\mu_3$ -OH, and evaporation of physisorbed dimethylformamide (DMF), and (3) the degradation of the framework benzenetricarboxylate (BTC) ligand. Rojas-Buzo et al. also observed a similar TGA curve for MOF-808(Hf) [28].

### 2.1.4. X-ray diffraction patterns of synthesized Zr- and Hf-containing MOFs

The XRD patterns of the UiO-66(Zr) and UiO-66(Hf) showed diffraction peaks at  $2\theta$  of  $12.06^\circ$ ,  $14.8^\circ$ ,  $17.1^\circ$ , and  $25.85^\circ$ , which corresponded to the following crystal planes, (022), (222), (004) and (006) and (244), respectively [28, 503, 513, 514]. XRD patterns MOF-808(Hf) and MOF-808(Zr) showed crystalline structure with similar diffraction peaks as previous reports [28, 394] (**Fig. 7.S3D**).

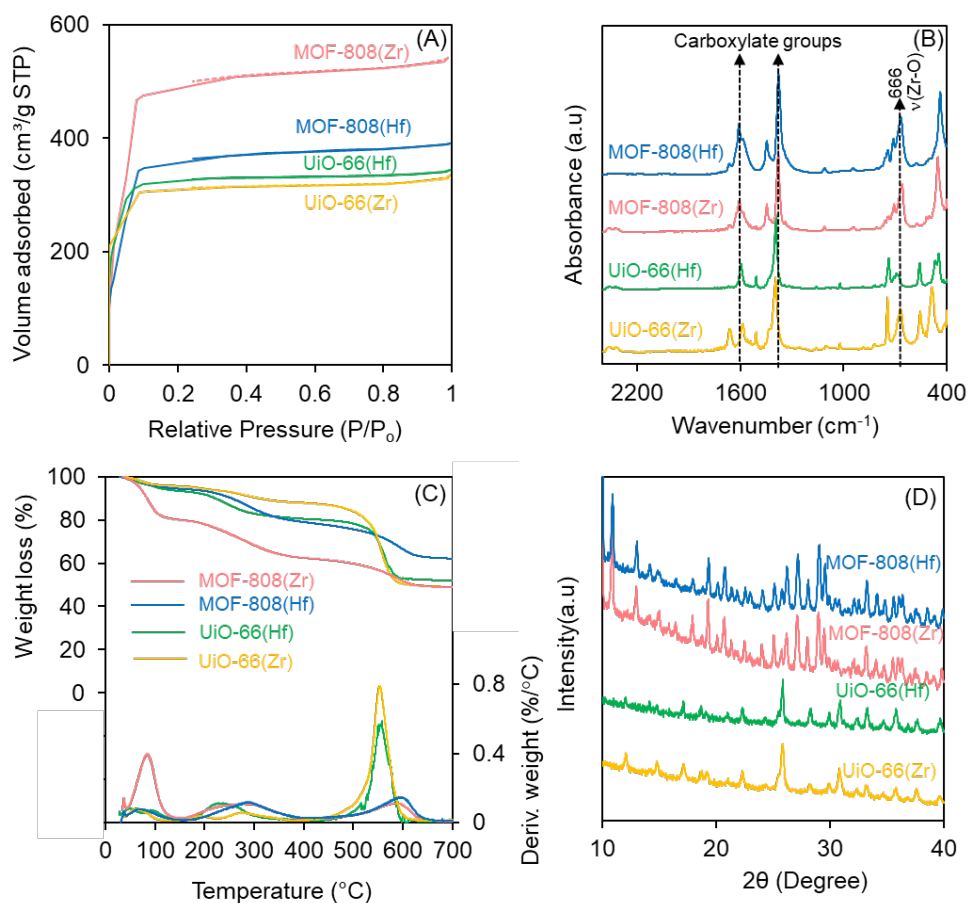


**Figure 7.S3.** Characterization data for Zr- and Hf-containing MOF catalysts by (A) N<sub>2</sub> adsorption-desorption, (B) FTIR, (C) TGA, and (D) XRD.



### 2.1.5. Acid properties of selected MOFs

To verify the presence of Lewis acids of MOFs, we performed the temperature-programmed desorption using DRIFTS with adsorbed pyridine on MOF-808(Zr) and MOF-808(Hf) (**Fig. 7.S4**). Pyridine-DRIFT analysis is a common technique to identify and quantify the acid sites of catalysts, such as zeolites [304]. Although semi-quantitative, this technique has been applied on various MOFs, such as Fe-MOF [417], Al-MOF [418], Zr-MOF [419], and Cr-MOF [420], to investigate the surface acidic properties. We chose pyridine as an in-situ titrant to probe the acid site density of MOFs because of previous success in observing Lewis acid sites in MOFs [195-197]. After pyridine adsorption, the DRIFT spectra of the MOF-808(Zr) and MOF-808(Hf) had three characteristic bands at 1012, 1043, and 1070  $\text{cm}^{-1}$  which are assignable to the  $\nu_1$ ,  $\nu_{12}$ , and  $\nu_{18}$  modes of pyridine coordination to open metal sites, respectively [301, 302, 417]. This coordination provided proof of the vital Lewis acid sites (LAS) that interacted with pyridine. We calculated the Lewis acid site density of MOFs using the LAS peak area. The density of Lewis acid sites of MOF-808(Hf) was 172 a.u./g, greater than that of MOF-808(Zr) (98 a.u./g), in line with previous studies by Rojas-Buzo et al. using FTIR with adsorbed acetonitrile- $\text{d}_3$  as a probe molecule [28].

In theory, metal sites of the ideal UiO-66 are fully coordinated with ligands. Thus, the reaction by UiO-66 should occur on the Brønsted acid sites. In UiO-66(Zr) spectrum, we observed a weak band at 1070  $\text{cm}^{-1}$ , which suggested that a small amount of defects (e.g., missing linkers) were formed during synthesis, in line with previous observations [421].

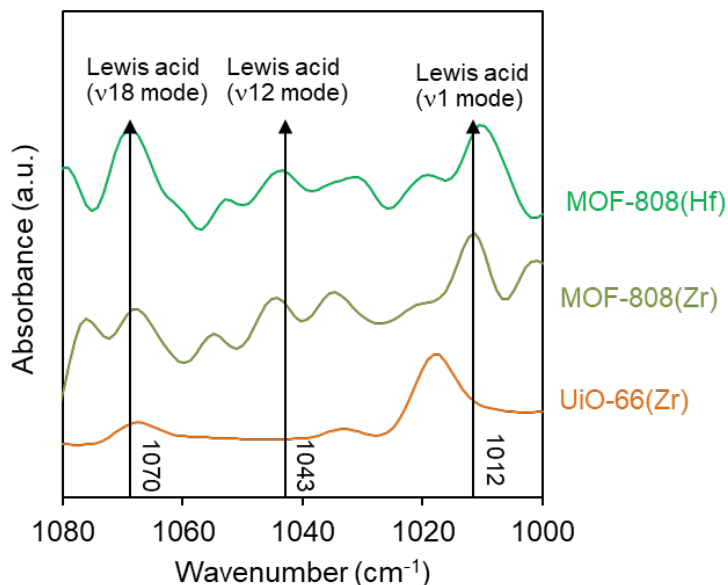


**Figure 7.S4.** Acid properties of MOF-808(Hf), MOF-808(Zr) and UiO-66(Zr) measured by diffuse reflectance infrared Fourier transform spectroscopy (DRIFTS).

### 2.1.6. Determination of missing linkers in UiO-66

The amount of defect sites in UiO-66 associated with missing linkers was determined by TGA profiles and calculated as previously described [436]. In short, we assumed that only  $ZrO_2$  and  $HfO_2$  were formed at high temperatures (above 500-550 °C). The formula of dehydroxylated UiO-66(Zr) and UiO-66(Hf), in the range 300-500 °C in TGA profiles, were  $ZrO(CO_2)_2(C_6H_4)$  and  $HfO(CO_2)_2(C_6H_4)$ . Thus, the weight loss in the TGA profiles, which corresponds to the organic linkers (wt.% linker<sub>actual</sub>), was compared with the theoretical amount of organic linker (wt.% linker<sub>theoretical</sub>) from the ideal structure of UiO-66 (defect-free). Therefore, defects sites and the coordination number (CN) of the  $Zr_6$  and  $Hf_6$  clusters were calculated as follows:

$$\text{Defect sites (\%)} = \left( 1 - \frac{\text{wt.\% linker}_{\text{actual}}}{\text{wt.\% linker}_{\text{theoretical}}} \right) \times 100$$

$$\text{CN} = 12 \times \left( 1 - \frac{\text{defect sites (\%)}}{100} \right)$$

where defect sites (%) indicate the amount of missing linkers (BDC) of UiO-66, wt.% linker<sub>actual</sub> indicates the weight loss of UiO-66 associated to BDC linkers determined from TGA profile, wt.% linker<sub>theoretical</sub> indicates the amount of BDC linkers calculated from the defect-free structure of UiO-66 (i.e., 54.6 wt.%), and CN represents the coordination number of zirconium or hafnium clusters. The ideal structure of UiO-66(Zr) and UiO-66(Hf) has the coordination number of 12.

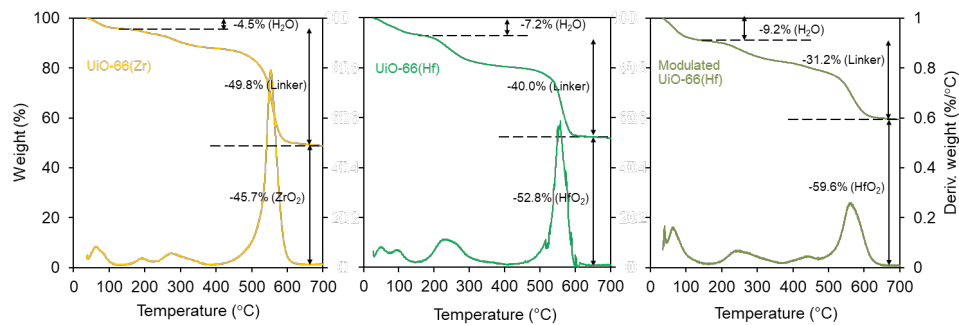


**Figure 7.S5.** Thermogravimetric analysis profiles of UiO-66(Zr), UiO-66(Hf), and modulated UiO-66(Hf)

**Table 7.S4.** Amount of defect sites and coordination number of Zr and Hf clusters in UiO-66

|  | UiO-66(Zr)                                     | UiO-66(Hf)               | UiO-66(Hf)-M             |
|--|--|--------------------------|--------------------------|
| Chemical formula                         | $C_{48}H_{28}O_{32}Zr_6$                       | $C_{48}H_{28}O_{32}Hf_6$ | $C_{48}H_{28}O_{32}Hf_6$ |
| Linker                                   | BDC = 1,4-benzenedicarboxylate ( $C_8H_6O_4$ ) |                          |                          |
| Dehydroxylated formula                   | $Zr_6O_6(BDC)_6$                               | $Hf_6O_6(BDC)_6$         | $Hf_6O_6(BDC)_6$         |
| Formula weight of dehydroxylated (g/mol) | 1628.03  | 2151.63                  | 2151.63                  |
| MO <sub>2</sub>                          | 123.22<br>(739.34)                             | 1262.93                  | 1262.93                  |
| Weight loss <sub>theoretical</sub>       | 54.6 %   | 41.3 %                   | 41.3 %                   |
| Weight loss <sub>actual</sub>            | 49.8 %   | 40.0 %                   | 31.2 %                   |
| Defect sites (%)                         | 8.8  | 3.1                      | 21.5                     |
| CN                                       | 10.9   | 11.6                     | 9.4                      |

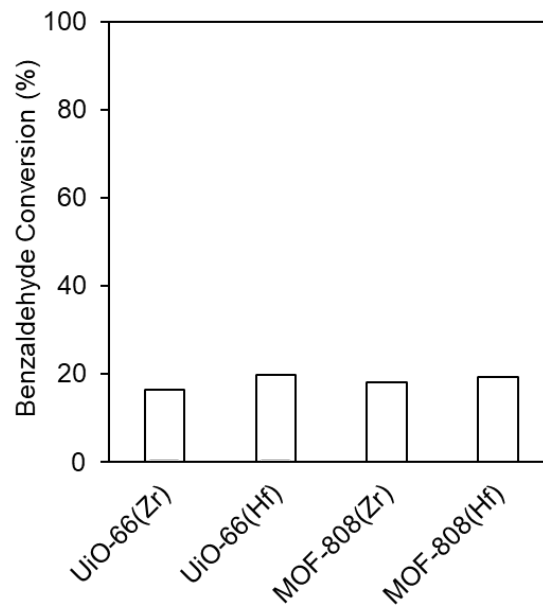


**Figure 7.S6.** Hydrogenation of benzaldehyde by Zr- and Hf-containing MOF-808 and UiO-66 catalysts. Reaction condition: 1 wt% benzaldehyde in ethyl acetate, 40 bar H<sub>2</sub>, 3 mol% catalyst, 100 °C, 4h

We evaluated Zr- and Hf-containing MOF-808 and UiO-66 catalysts for the hydrogenation of benzaldehyde using molecular H<sub>2</sub> (**Fig. 7.S6**). We observed a low conversion of benzaldehyde (< 20%) at 100 °C after 4h. However, we did not observe benzyl alcohol as a reaction product. One reason was that hydrogenation reaction by molecular hydrogen requires metal catalysts to split molecular hydrogen into atomic hydrogen [515, 516]. However, metal nodes of Zr- and Hf-containing MOFs could not catalyze hydrogenation using molecular hydrogen.

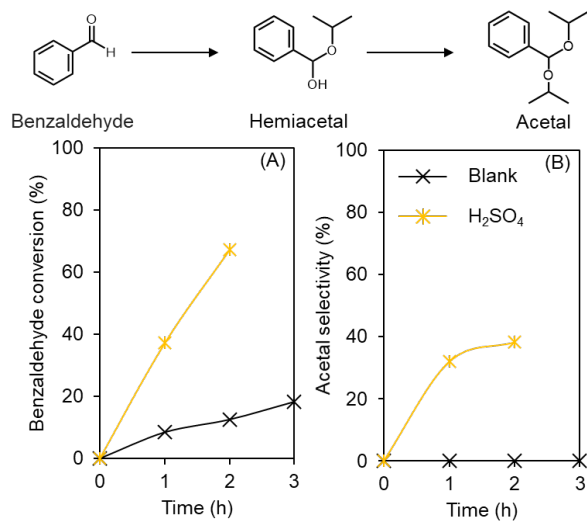


**Figure 7.S7.** Conversion of benzaldehyde by H<sub>2</sub>SO<sub>4</sub>. Evolution of benzaldehyde conversion (A) and product selectivity (B). Reaction condition: 1 wt.% benzaldehyde in 2-propanol, catalyst loading = 3 mol.%, 100 °C, 1.0-3.0 h.

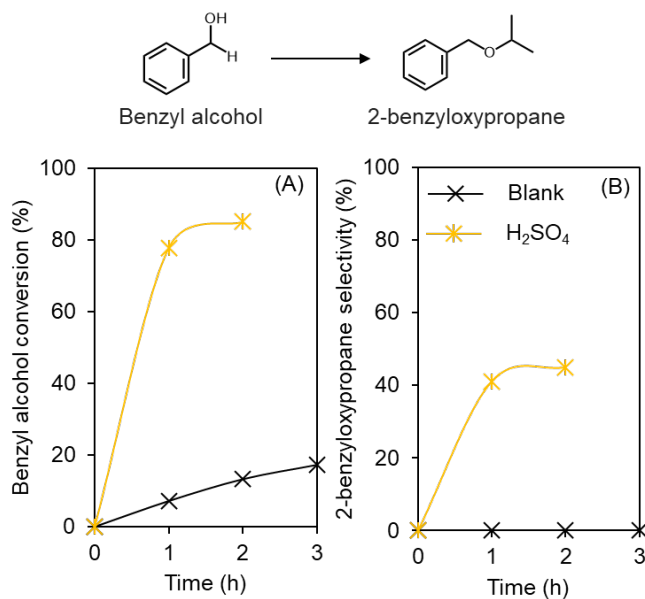


**Figure 7.S8.** Conversion of benzyl alcohol by H<sub>2</sub>SO<sub>4</sub>. Evolution of benzyl alcohol conversion (A) and product selectivity (B). Reaction condition: 1 wt.% benzyl alcohol in 2-propanol, catalyst loading = 3 mol.%, 100 °C, 1.0-3.0 h.

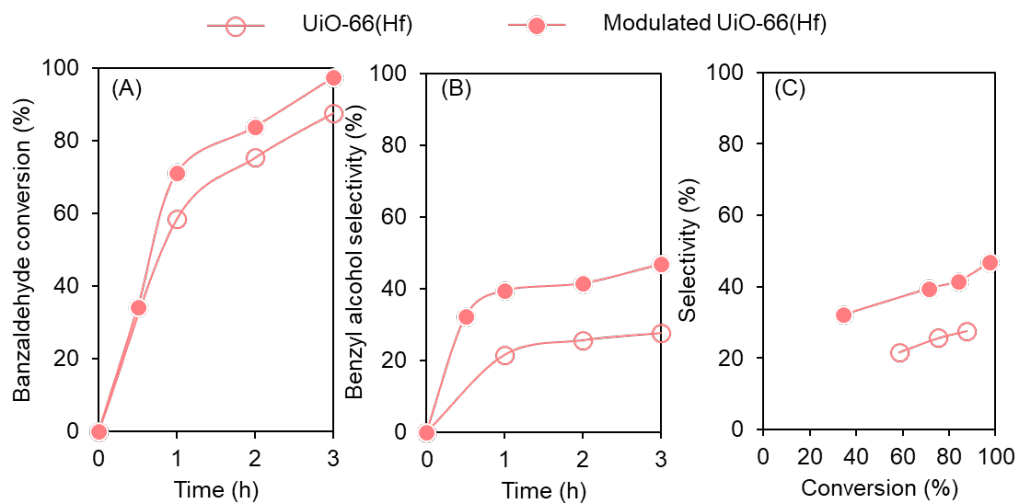


**Figure 7.S9.** Effect of the modulator on the transfer hydrogenation of benzaldehyde by UiO-66(Hf). Reaction condition: 1 wt.% benzaldehyde in 2-propanol, catalyst loading = 3 mol.%, 100 °C, 0.5-3.0 h.

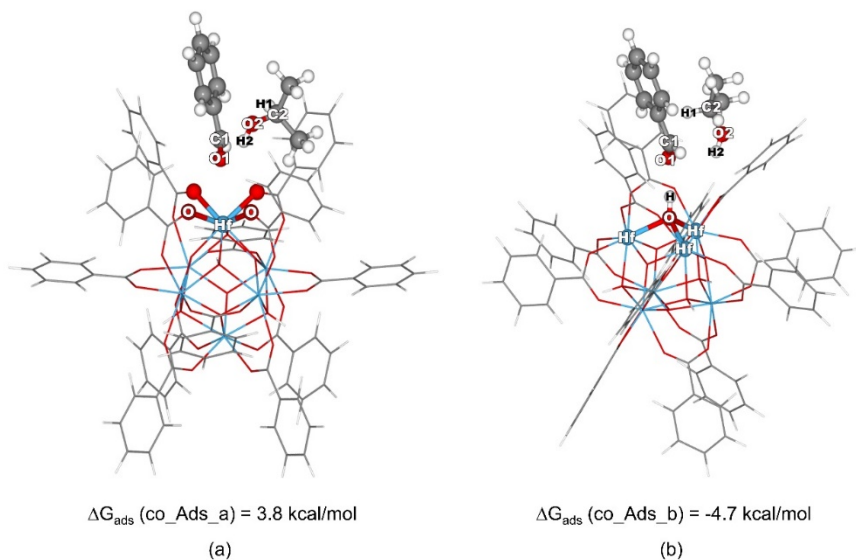


**Figure 7.S10.** Optimized structures of the benzaldehyde and 2-propanol co-adsorption complexes on Hf (a) and Brønsted sites (b) of UiO-66(Hf).

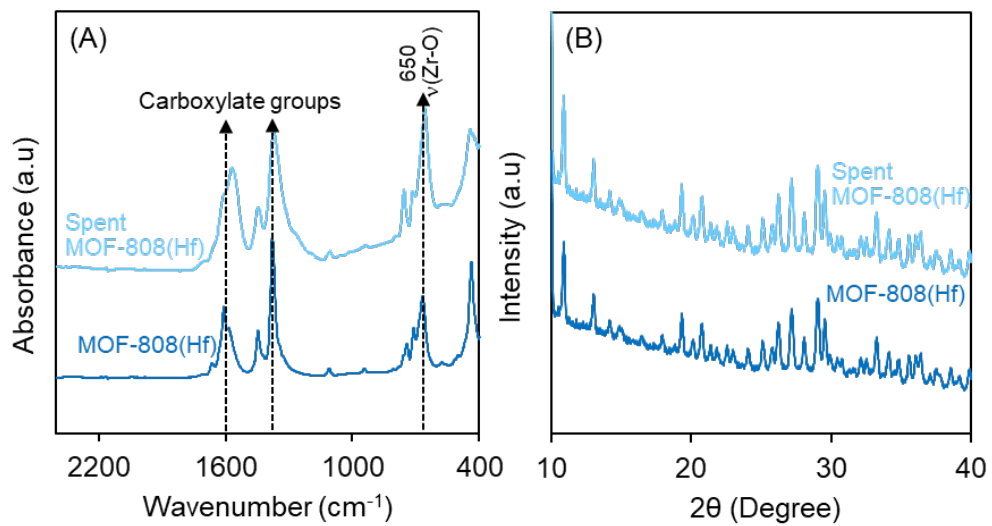


**Figure 7.S11.** Characterization of spent MOF-808(Hf) by FTIR (A), and XRD (B).



## CHAPTER 8

### CREATION OF BRØNSTED ACID SITES ON PLASTIC FOR ESTERIFICATION OF LEVULINIC ACID: A PLASTIC-TO-BIOREFINERY CIRCULAR ECONOMY

#### 1. Introduction

Alkyl levulinates are esters with applications in food [517], solvents, plasticizers [518], and fuel additives (diesel) [519, 520]. Levulinic acid is biomass-derived platform chemical produced by acid-catalyzed cascade reactions of dehydration and hydrolysis of glucose. The esterification of levulinic acid with alcohols in the presence of Brønsted acid catalysts yields alkyl levulinates [521]. Homogeneous Brønsted acidic catalysts, such as H<sub>2</sub>SO<sub>4</sub> [519, 522-524], HCl [525, 526], and ionic liquids [527-530], were used for esterification reactions. Xiong et al.[527] used a Brønsted acidic ionic liquid, [C<sub>6</sub>(C<sub>1</sub>im)<sub>2</sub>]HSO<sub>4</sub>, for esterification of acetic acid and obtained 100% selectivity to an ester at 98% conversion. Lucena et al.[524] used dilute H<sub>2</sub>SO<sub>4</sub> (0.5-1.0 w/w) catalyst for esterification of oleic acid. They obtained 99.9% ester at 100% conversion. Although effective, homogeneous Brønsted acidic catalysts are corrosive and difficult to separate and reuse; these negative properties contribute to production, equipment maintenance, and waste management costs [531]. Thus, we need to develop active, selective, and reusable solid Brønsted acid catalysts to bypass these limitations.

Commercial solid Brønsted acid catalysts, such as zeolites, have been used for esterification reactions [532-537]. They are non-corrosive and reusable compared with homogenous Brønsted acids [538]. However, existing solid Brønsted acid catalysts have had a disappointing performance. For example, Fernandes et al.[539] used zeolites (HMOR, HZSM-5, HY, and H-β) and obtained a low conversion of levulinic acid, in agreement with findings by Chaffey et al.[540], who did not find

esters as reaction products. Rodponthukwaji et al.[536] and Pavlogic et al.[537] used ZSM-5 and clinoptilolite zeolites for esterification of acetate and levulinate, respectively. They found that the microporous structure of zeolites limited the transport of reactants, intermediates, and products and led to coke formation. Conversely, ion-exchange resins with sulfonate groups, such as Amberlyst, are nonporous with acidic properties and active for esterification. For example, Tejero et al.[541] used Amberlyst-36 and obtained 78% selectivity of ester at 60% conversion. Trombettoni et al.[542] used Amberlyst-15 and obtained ~60% ester at 68% conversion. The conversion and selectivity for the esterification by these ion-exchange resins need to be improved to make the process economical.

Here, we describe solid Brønsted acidic catalysts created by sulfonating polypropylene (PP-SO<sub>3</sub>H) for esterification of levulinic acid with methanol. We varied the content of the sulfonate group and determined the relationship between the sulfonate group, acid strength, and catalytic performance for the esterification of levulinic acid. The PP-SO<sub>3</sub>H with the highest S/C ratio had the highest Brønsted acid strength and 96% selectivity for methyl levulinate at 94% conversion at 65 °C after 1h.

## **2. Materials and Methods**

**2.1. Materials.** All chemicals were used as received unless otherwise noted. Their CAS numbers, purity, and manufacturers are listed in **Table 8.S1** (Supplementary Information).

### **2.2. Synthesis of SO<sub>3</sub>H-functionalized polypropylene (PP-SO<sub>3</sub>H)**

PP-SO<sub>3</sub>H was synthesized as described with a slight modification [543, 544]. First, the PP powder (1.00 g) was dissolved in 25 mL of 1,1,2,2-tetrachloroethane with stirring (300 rpm) under reflux at 65 °C for 30 min. Next, different vol. % (10 - 33%) of chlorosulfonic acid was mixed with dichloromethane, keeping the total volume at 15 mL. Finally, the dichloromethane and the chlorosulfonic acid mixture were added to the polypropylene solution dropwise over 30 min. The resulting mixture was kept for an additional 2 h, and the solvents were removed by distillation. A

black precipitate was obtained by centrifugation and washed with deionized water until the supernatant became colorless, and the solids were dried overnight in a vacuum oven at 120 °C.

### **2.3. Physiochemical and acidic characterization of modified polypropylene catalysts**

The structural characteristics and morphologies of the catalysts were determined by X-ray diffraction, N<sub>2</sub> adsorption-desorption, scanning electron microscopy with energy dispersive X-ray spectrometry, Fourier-transform infrared spectroscopy, and measurement of pH change.

#### **2.3.1. X-ray diffraction**

X-ray diffraction (XRD) analysis of samples was performed on a Bruker AXS Model D8 Advance A28 diffractometer (Germany) with CuK $\alpha$  radiation in the 2 $\theta$  range from 10° to 40° and 0.02 degree/step. Samples of 200 mg were used in each analysis.

#### **2.3.2. N<sub>2</sub> adsorption-desorption**

The N<sub>2</sub> adsorption-desorption was measured by a Micromeritics Tristar (Norcross, GA, USA) instrument to calculate the surface area, pore size, and pore volume. The function of TriStar was verified with reference materials (Micromeritics). Prior to the measurement, the sample was pretreated at 120 °C for 4 h using a Micromeritics FlowPrep with sample degasser (Norcross, GA, USA). The surface area, S<sub>BET</sub>, was determined from N<sub>2</sub> isotherms by the Brunauer–Emmett–Teller equation (BET) at -196.1°C [174, 175]. The BET surface area was calculated over the range of relative pressures between 0.05 and 0.3. The pore volume was estimated from the N<sub>2</sub> desorption values according to the Barrett–Joyner–Halenda (BJH) model [178]. The pore volume was calculated as the uptake (cm<sup>3</sup>/g) at a relative pressure of 0.95. We measured the average pore size of the samples by the BJH model [179, 180].

### **2.3.3. Scanning electron microscopy**

To determine the microstructure and elemental distribution of the samples, scanning electron microscopy (SEM) was performed using a Tescan Vega V3 SEM microscope with energy dispersive X-ray spectrometry (EDS).

### **2.3.4. Fourier-transform infrared spectroscopy**

Infrared spectra of samples were recorded on a JASCO Fourier transform infrared (FTIR) spectrometer (Easton, MD, USA), equipped with an attenuated total reflection stage (ATR). 5 mg of sample was used in each analysis. The samples were scanned between 400 and 4000  $\text{cm}^{-1}$  at a 4  $\text{cm}^{-1}$  resolution. Spectra were collected using a deuterated triglycine sulfate (DTGS) detector averaging 256 scans.

### **2.3.5. Measurement of acid properties by pH change in methanol**

The Brønsted acid properties of synthesized catalysts were determined by measuring the pH change of methanol in which the catalyst was suspended, as described [199, 422]. In short, 8 mg catalyst was suspended in 24 mL methanol with constant stirring at ambient temperature before pH measurement. This amount of 8 mg was selected because previous experiments in which the amount of catalyst was varied revealed that it was high enough such that the measured pH was independent of the solid amount [545]. The pH was measured with a gel-filled, double junction electrode (Milwaukee Instruments, Inc., Rocky Mount, NC, USA). The electrode was calibrated with the pH 4, 7, and 9 buffers. All measurements were conducted in triplicate.

## **2.4. Esterification of levulinic acid and alcohol**

The reactions were conducted in 15 mL pressure tubes in an oil bath. Typically, levulinic acid, methanol, and catalysts were added, and the tube was sealed and stirred at 65 °C unless otherwise noted. The molar ratio of levulinic acid and methanol was kept at 1:25 (100 mg levulinic acid: 700 mg methanol) with 10 mg catalyst unless otherwise noted. Dodecane was used as an internal standard. The reaction was stopped by quenching in a cold water bath, followed by adding ethyl

acetate (~5 mL) to dissolve the remaining levulinic acid and methanol. The solution was centrifuged, and the solid catalysts were removed. The liquid sample was then analyzed by GC-MS to determine product distribution.

## 2.5. Product analysis and quantification

The reactants and products were analyzed by using a gas chromatograph (7890B GC) (Agilent Technologies, Santa Clara, CA, USA) equipped with a mass spectrometer and flame ionization detector (FID) for product identification and quantification, respectively. A DB-1701 column (30m x 0.25mm x 0.25  $\mu$ m, Agilent Technologies, Santa Clara, CA, USA) was used for product separation with the following parameters: injection temperature 275 °C and FID detector temperature 300 °C; split ratio 1:50. The temperature program started at 50 °C with a heating rate of 8 °C/min to 200 °C. The levulinic acid conversion, product yield, and product selectivity were calculated as follows:

$$\text{Reactant conversion (\%)} = \frac{\text{reactant reacted (mol)}}{\text{initial reactant (mol)}} \times 100$$

$$\text{Product yield (\%)} = \frac{\text{product generated (mol)}}{\text{initial reactant (mol)}} \times 100$$

$$\text{Product selectivity (\%)} = \frac{\text{product yield}}{\text{reactant conversion}} \times 100$$

## 3. Results

We modified polypropylene (PP) with a chemical donating agent to graft sulfonate groups onto the polymer surface to form sulfonated polypropylene (PP-SO<sub>3</sub>H). During synthesis, we used 10-33 vol.% of the chemical donating agent to vary the concentration of the sulfonate group on the PP-SO<sub>3</sub>H catalysts. We found that 10, 25, and 33 vol.% chemical donating agent generated PP-SO<sub>3</sub>H with S/C ratio (w/w) of 0.08, 0.18, and 0.23, respectively (**Table 8.1**). Based on the S/C ratio, we referred to these catalysts as PP-SO<sub>3</sub>H-0.08, PP-SO<sub>3</sub>H-0.18, and PP-SO<sub>3</sub>H-0.23. Then, we investigated the effect of sulfonate concentration on catalyst physicochemical properties. Because we expected that PP-SO<sub>3</sub>H materials would exhibit Brønsted acidity, we evaluated the catalytic performance of PP-SO<sub>3</sub>H catalysts in the esterification of levulinic acid.

### 3.1. Physicochemical properties of sulfonated polypropylene at different sulfonate loading

To evaluate the physicochemical properties of PP-SO<sub>3</sub>H catalysts, we characterized the catalysts by X-ray diffraction, Fourier-transform infrared spectroscopy (FTIR), N<sub>2</sub> adsorption-desorption, scanning electron microscope (SEM), contact angle analysis, and acidity. First, N<sub>2</sub> adsorption-desorption was examined to measure surface area, pore volume, and pore size (**Table 1**). The calculated surface area of unmodified PP was 0.65 m<sup>2</sup>/g with 0.0011 cc/g. An increase in sulfonate loading slightly increased the surface area from 0.65 to 1.14 m<sup>2</sup>/g, the pore volume from 0.0011 to 0.0027 cm<sup>3</sup>/g, and pore size from 6.49 to 9.47 nm. Unmodified PP had 0.92 g/mL density, which agreed with previous studies [546]. The surface modification increased the density of the polypropylene to greater than 1 g/mL. The surface area, pore size, and pore volume of modified polypropylene remained relatively constant after modification.

**Table 8.1.** Surface area, density, total pore volume, average pore size, carbon to sulfur ratio and pH in methanol of the PP-SO<sub>3</sub>H

| Polymer                       | Yield<br>(wt.%) | S/C<br>ratio<br>(w/w) | S <sub>BET</sub><br>(m <sup>2</sup> /g) | V <sub>p</sub><br>(cm <sup>3</sup> /g) | d <sub>p</sub><br>(nm) | Density <sup>a</sup><br>(g/mL) | pH in methanol <sup>b</sup> |          |
|-------------------------------|-----------------|-----------------------|---|--|------------------------|--------------------------------|-----------------------------|----------|
|                               |                 |                       |   |  |                        |                                | Suspension                  | Filtrate |
| PP                            | -               | -                     | 0.65                                    | 0.0011                                 | 6.49                   | 0.92                           | 6.0                         | 6.0      |
| PP-SO <sub>3</sub> H-<br>0.08 | 112             | 0.08                  | 0.76                                    | 0.0014                                 | 7.11                   | 1.01                           | 2.4                         | 6.0      |
| PP-SO <sub>3</sub> H-<br>0.18 | 128             | 0.18                  | 0.88                                    | 0.0018                                 | 8.16                   | 1.09                           | 2.1                         | 5.9      |
| PP-SO <sub>3</sub> H-<br>0.23 | 140             | 0.23                  | 1.14                                    | 0.0027                                 | 9.47                   | 1.14                           | 1.9                         | 5.9      |
| Amberlyst-36                  | -               | -                     | -                                       | -                                      | -                      | -                              | 3.6                         | 6.0      |

---

Note.  $S_{\text{BET}}$  = surface area determined by BET,  $V_p$  = pore volume determined by from the  $\text{N}_2$  desorption values according to the Barrett–Joyner–Halenda (BJH) model,  $d_p$  = average pore diameter determined by the BJH model, <sup>a</sup>Density calculated by the water displacement method through a graduated cylinder. <sup>b</sup> pH of a stirred suspension of 8 mg of catalysts in 24 mL of methanol at 25 °C. Methanol pH (blank) was 6.0.

### 3.2. Brønsted acid properties and chemical structure of modified polypropylene

The strength of Brønsted acidity is a good indicator for catalyst performance for esterification reactions [547]. Currently, there are no consistent measurements for determining the acid strength of the solid catalysts with sulfonate groups on the solid surface [548]. Thus, to determine the Brønsted acid strength of PP-SO<sub>3</sub>H catalysts, we used the method by Llabres i Xamena and co-workers [421, 422], who determined the strength of Brønsted acid by measuring pH change of methanol (**Table 8.1**). In the presence of solid catalysts, we measured the polarizing power of the solid catalyst on the methanol molecules [422]. As a control, blank (bare methanol) had a pH of 6.0, which agreed with previous reports [421, 422]. The pH of the solution with PP suspension was similar to that of the blank, which suggested that PP had no Brønsted acidity. Amberlyst-36 produced a pH of 3.6, which indicated that Amberlyst-36 was Brønsted acidic. Interestingly, the suspension of PP-SO<sub>3</sub>H in methanol showed a decrease in pH from 6.0 to 1.9-2.4, which suggested Brønsted acidity of PP-SO<sub>3</sub>H samples. The pH change of methanol with PP-SO<sub>3</sub>H samples was 2.4, 2.1, and 1.9 for PP-SO<sub>3</sub>H-0.08, PP-SO<sub>3</sub>H-0.18, and PP-SO<sub>3</sub>H-0.23, respectively. Thus, the Brønsted acid was in the following order: PP-SO<sub>3</sub>H-0.23 > PP-SO<sub>3</sub>H-0.18 > PP-SO<sub>3</sub>H-0.08 > Amberlyst-36. A large pH change of methanol with PP-SO<sub>3</sub>H-0.23 compared with blank indicated the high polarizing power of PP-SO<sub>3</sub>H-0.23 on the methanol molecules and the high strength of Brønsted acid [422]. Thus, the high sulfonate content of PP-SO<sub>3</sub>H samples produced high Brønsted acid strength. Upon removing all solids, the pH of methanol became ~5.9-6.0, close to the blank. Restoration of the pH suggested that the Brønsted acidic proton was on the surface of Amberlyst-36 and the PP-SO<sub>3</sub>H catalysts.

To determine the chemical properties of PP-SO<sub>3</sub>H, we characterized PP-SO<sub>3</sub>H by X-ray diffraction and FTIR (**Fig. 8.1**). As a control, unmodified PP showed the characteristic FTIR peaks of CH<sub>2</sub> bending and CH<sub>3</sub> stretching 1455 and 1375 cm<sup>-1</sup>, respectively. These two peaks were derived from polypropylene backbone, which agreed with previous studies [549-551]. Furthermore, the PP-SO<sub>3</sub>H catalysts showed sulfonate bending at 1128 and 1038 cm<sup>-1</sup>, respectively, which confirmed the presence of sulfonate groups on the polypropylene backbone [543, 552, 553]. Interestingly, we observed C=C bending at 1644 cm<sup>-1</sup>. Moreover, an increase in SO<sub>3</sub>H concentration (an increase in S/C ratio) showed the greater intensity of this band. These results suggested that introducing the sulfonate group triggered the formation of C=C bonds in the polypropylene backbone [554].

X-ray diffraction of pristine polypropylene showed the characteristic peaks of (110), (040), (130), (111), and (041) at 14.0, 16.9, 18.5, 21.7, and 21.9 °, respectively, which suggested the monoclinic  $\alpha$ -crystalline phase of PP [555, 556]. An increase in sulfonate concentration lowered the peak intensity, which suggested that sulfonate groups on polypropylene reduced the degree of crystallinity. In fact, the PP-SO<sub>3</sub>H materials with an S/C ratio greater than 0.08 became an amorphous-like structure.

We used SEM and contact angle measurement to characterize the PP-SO<sub>3</sub>H catalysts for wettability, water suspension, and morphology (**Fig. 8.2**). As a control, PP was hydrophobic with an estimated contact angle of 131°, in agreement with that of PP membrane (~139-149°) [557, 558]. The PP sample floated on water and was nonporous. PP-SO<sub>3</sub>H-0.08 had a contact angle of 53°. Most PP-SO<sub>3</sub>H-0.08 particles were at the bottom of the water. A higher SO<sub>3</sub>H concentration made PP-SO<sub>3</sub>H-0.18 and PP-SO<sub>3</sub>H-0.23 hydrophilic and suspended in water. Surprisingly, we observed that PP-SO<sub>3</sub>H-0.23 was porous. Increased hydrophilicity and density of PP-SO<sub>3</sub>H catalysts enhanced their dispersion in liquid phases, thereby increasing the mass transfer between catalysts in the soluble reactants.



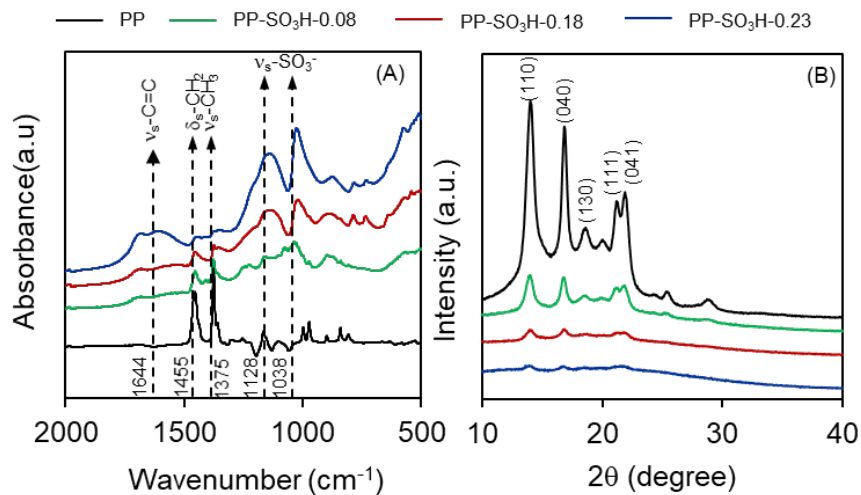


**Figure 8.1.** ATR-FTIR spectra (A) and X-ray diffraction patterns (B) of modified polypropylene with different sulfonate loading.

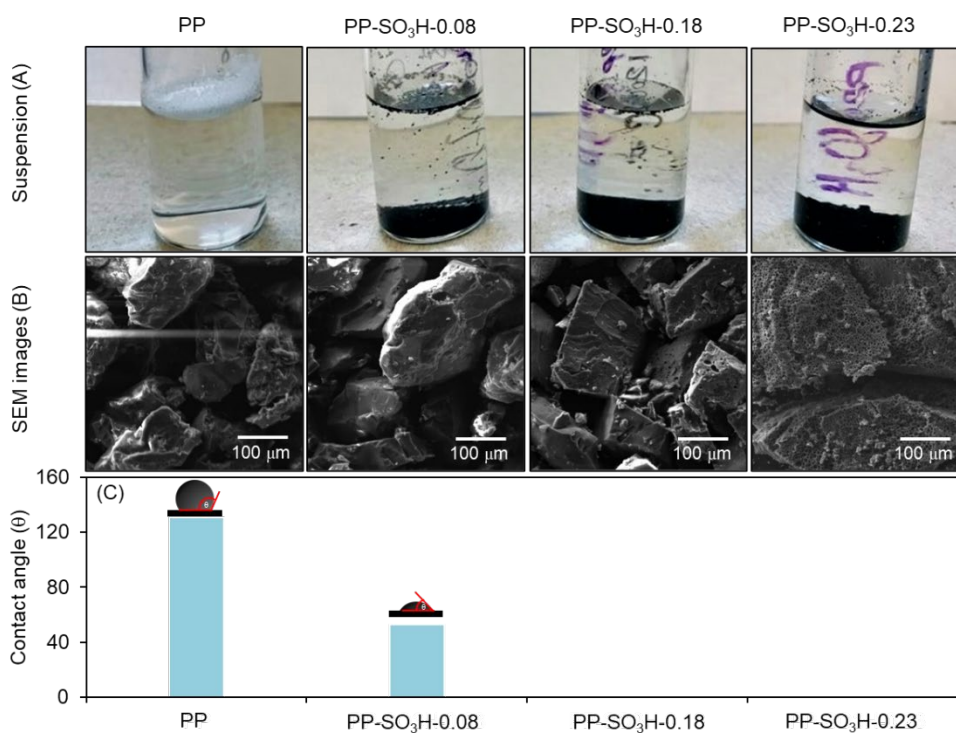


**Figure 8.2.** Physical characteristics of the modified polypropylene with different sulfonate loadings by suspension in water (A), SEM images (B), and contact angle (C).

### 3.3. Catalytic performance of PP-SO<sub>3</sub>H in the esterification of levulinic acid

To examine the catalytic activity of PP-SO<sub>3</sub>H catalysts, we performed esterification of levulinic acid with methanol using the same loading for each catalyst (**Fig. 8.3**). As a control, a blank (no added catalyst) experiment showed a low conversion of levulinic acid of 10% after 1 h. This catalyst-free low conversion of levulinic acid suggested that levulinic acid catalyzed its own conversion, in agreement with studies by Shu et al.[559] and Fernandes et al.[539]. We used Amberlyst-36, a commercial solid Brønsted acid catalyst, as an additional control. Amberlyst-36 catalyzed a progressive increase in conversion of levulinic acid, which reached 65% selectivity to methyl levulinate at 38% conversion of levulinic acid after 0.5 h. A prolonged reaction time of 1.0 h increased the conversion of levulinic acid to 60%; however, the selectivity to methyl levulinate remained constant at 67%. We postulated that the constant selectivity of methyl levulinate with the increasing conversion of levulinic acid was due to the formation of by-product water [437, 438], which poisoned the Amberlyst-36.

When we used PP-SO<sub>3</sub>H catalysts of varying sulfonate contents, all catalysts showed a progressive increase in conversion of levulinic acid. PP-SO<sub>3</sub>H-0.08, -0.18, and -0.23 reached 69, 83, and 94% conversion of levulinic acid after 1 h. Interestingly, PP-SO<sub>3</sub>H catalysts were highly selective and reached 78, 81, and 88% selectivity to methyl levulinate after 0.5 h. The PP-SO<sub>3</sub>H-0.23 had the highest selectivity of methyl levulinate of 96% at 94% conversion after 1 h. To assess the quality of active sites, we plotted levulinic acid conversion vs. selectivity to methyl levulinate (**Fig. 8.3C**). We found that selectivity to methyl levulinate at similar conversion was in the order of PP-SO<sub>3</sub>H-0.23 > PP-SO<sub>3</sub>H-0.18 > PP-SO<sub>3</sub>H-0.08 > Amberlyst-36. This order of selectivity to methyl levulinate was the same order as Brønsted acid strength measured by pH change (**Table 8.1**). Overall, these results showed that PP-SO<sub>3</sub>H catalyst with a high S/C ratio improved levulinic acid conversion and selectivity to methyl levulinate.

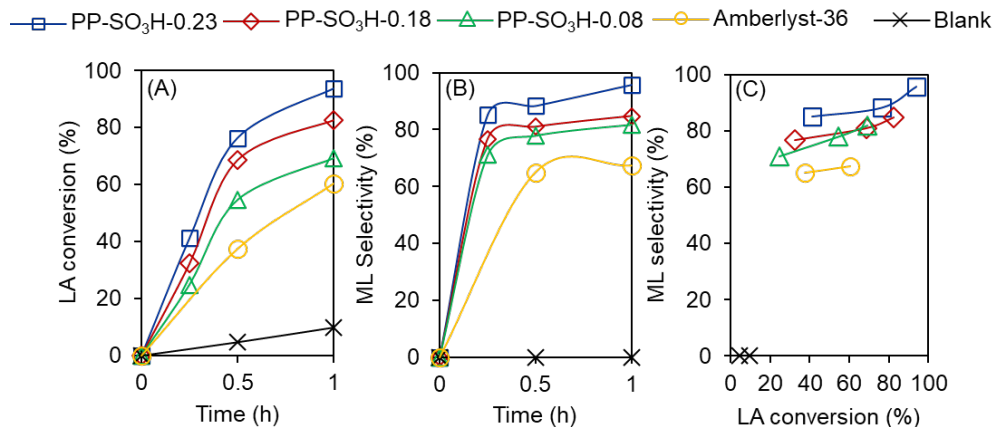


**Figure 8.3.** Catalytic performance of PP-SO<sub>3</sub>H catalysts for levulinic acid esterification with methanol. Evolution of levulinic acid conversion (A), methyl levulinate selectivity (B), and conversion vs. selectivity (C). Reaction condition: levulinic acid (100 mg): methanol (0.7 g) = 1:25 (molar ratio), 10 mg PP-SO<sub>3</sub>H, 65 °C.

### 3.4. Influence of different alcohols

To determine the effect of alcohol carbon chain length on catalyst activity, we performed esterification of levulinic acid with ethanol, n-propanol, and n-butanol using PP-SO<sub>3</sub>H-0.23 catalyst (Fig. 8.4). The PP-SO<sub>3</sub>H-0.23 exhibited high selectivity to the ester (>93%) at >91% conversion of levulinic acid in methanol, ethanol, n-propanol, and n-butanol. With 2-butanol, the ester selectivity was 21.4% at a low conversion of levulinic acid (46%), significantly lower performance compared with the primary alcohols. Our findings were similar to those of Enumula et al.[560] who concluded that, compared with primary alcohols, the inferior performance of WO<sub>3</sub>-SBA-16 catalyst for esterification of levulinic acid with 2-butanol was due to steric hindrance that reduced the nucleophilic attack by the hydroxyl group of alcohol.

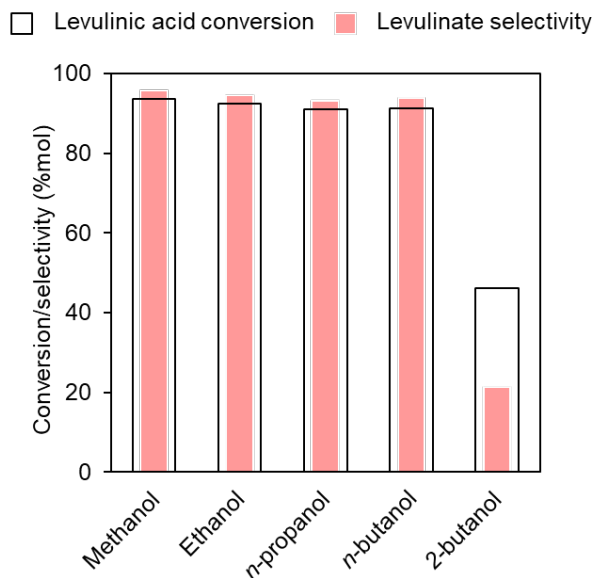


**Figure 8.4.** Effect of alcohols on esterification of levulinic acid. Reaction condition: levulinic acid: alcohol = 1:25 (molar ratio), 10 mg PP-SO<sub>3</sub>H-0.23, 65 °C, 1 h.

### 3.5. Stability and reusability of PP-SO<sub>3</sub>H catalysts

The ability to reuse catalysts is important for their practical use. We recycled the PP-SO<sub>3</sub>H-0.23 catalyst by centrifugation and washing with ethyl acetate to remove the residual products, intermediates, and unreacted levulinic acid. The catalyst was then dried in a vacuum oven at 120 °C. The PP-SO<sub>3</sub>H catalyst maintained its high selectivity to ester with a <8% drop in levulinic acid conversion and retained its selectivity to methyl levulinate (95%) for four cycles (**Fig. 8.5A**).

To evaluate catalyst stability, we conducted the esterification of levulinic acid using PP-SO<sub>3</sub>H-0.23 catalyst over 0.5 h at 65 °C, then filtered the PP-SO<sub>3</sub>H-0.23 catalyst from the reaction mixture and heated the liquid phase under the same reaction condition (65 °C) for 2.5 h (**Fig. 8.5B**). We sampled the mixture three times during 2.5 h and measured levulinic acid conversion and methyl levulinate yield. The levulinic acid conversion increased slightly during the prolonged 2.5 h (likely by self-catalysis), whereas the yield of methyl levulinate remained constant. These results demonstrated

that the PP-SO<sub>3</sub>H-0.23 catalyst was structurally stable and did not release any catalytic material during the reaction.

Further, after the 4<sup>th</sup> reuse cycle, we characterized the PP-SO<sub>3</sub>H-0.23 catalyst by EDS, XRD, and FTIR (**Fig. 8.6**). The S/C ratio of the used catalyst, measured by EDS, was 0.18, compared with 0.23 for fresh catalyst. Thus, a slight loss of the sulfonate group occurred during reuse. We postulated that this decrease in the S content was due to the loss of weakly functionalized sulfonate groups. Nevertheless, the catalyst maintained a high selectivity to an ester (95%) during four reuse cycles. Furthermore, the XRD and FTIR spectra of the used catalyst confirmed its chemical structure and functionality similar to the fresh PP-SO<sub>3</sub>H-0.23 catalyst. Together, these filtration and characterization results suggested catalyst stability under the present experimental conditions. Overall, PP-SO<sub>3</sub>H catalyst maintained high selectivity to desired products for all the cycles and structural integrity after four reuses, as evidenced by its performance in the esterification of levulinic acid.

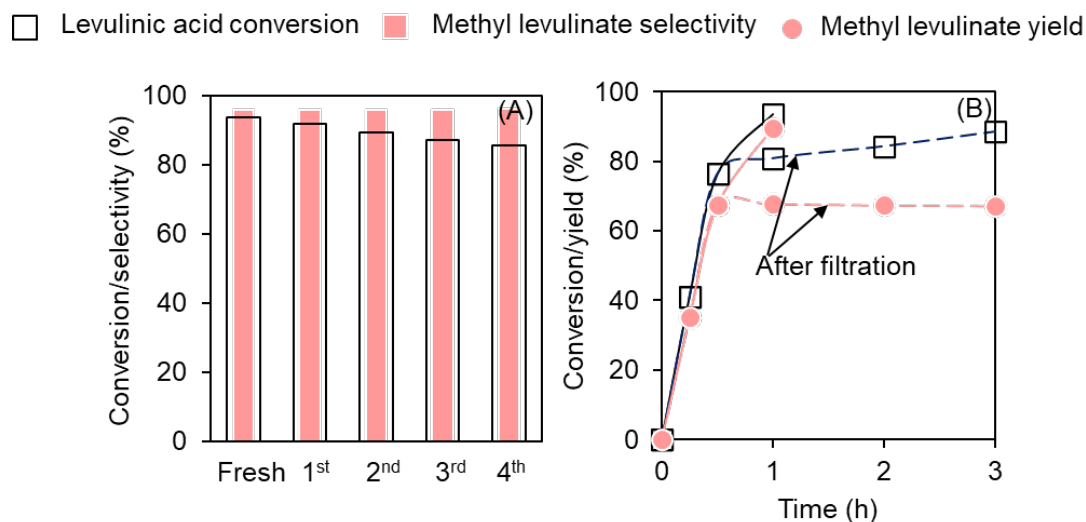


**Figure 8.5.** Reusability (A) and stability (B) of PP-SO<sub>3</sub>H-0.23 catalysts for levulinic acid esterification with methanol. Reaction condition: levulinic acid (100 mg): methanol (0.7 g) = 1:25 (molar ratio), 10 mg PP-SO<sub>3</sub>H, 65 °C, 1 h.

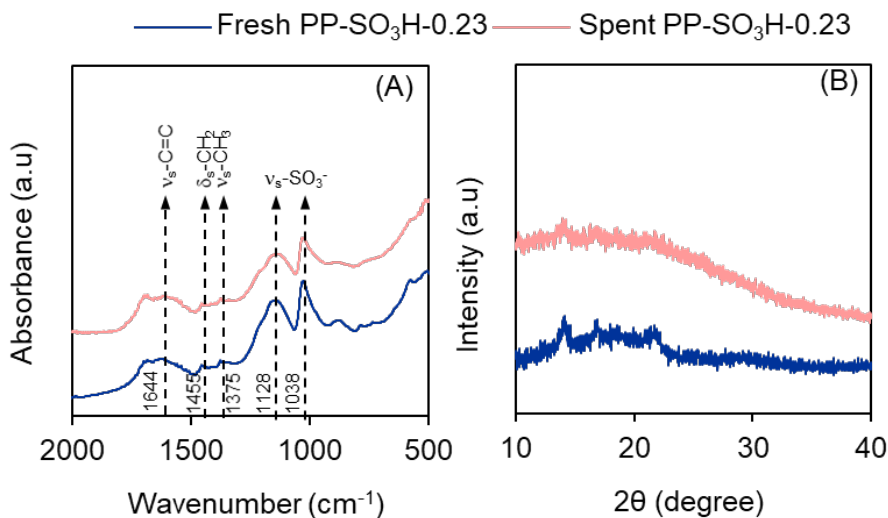


**Figure 8.6.** FTIR spectra (A) and X-ray diffraction pattern (B) of spent PP-SO<sub>3</sub>H-0.23 catalyst.

#### 4. Discussion

The development of active, selective, and recyclable solid Brønsted acidic catalysts is a major challenge in the production of levulinate esters [540]. Here, we devised a simple strategy to synthesize solid Brønsted acidic PP-SO<sub>3</sub>H catalysts by grafting sulfonate groups onto polypropylene. The Brønsted acid strength increased as the S/C ratio of PP-SO<sub>3</sub>H catalyst increased, which was responsible for high esterification activity and selectivity to esters. The PP-SO<sub>3</sub>H catalyst with an S/C of 0.23 had the highest Brønsted acid strength and enabled the 96% selectivity of methyl levulinate at 94% conversion of levulinic acid. Moreover, PP-SO<sub>3</sub>H catalysts were stable and reusable.

Our most significant finding was the creation of the active Brønsted acidic PP-SO<sub>3</sub>H catalysts with tunable acid strength that were selective to esters. First, the strength of Brønsted acid facilitated the esterification. Cirujano et al.[422, 561] used UiO-66(Zr) metal-organic frameworks (MOFs) to catalyze the esterification of levulinic acid with ethanol at 80 °C. They found that the Brønsted acid sites of UiO-66(Zr) were the active sites for esterification of levulinic acid, which enabled >93% selectivity to an ester at a near-complete conversion. Mbaraka et al.[562] reported a strong dependence of esterification of fatty acids on the strength of Brønsted acid, a result that agrees

with our findings. Second, the sulfonate ( $\text{SO}_3\text{H}$ )-containing solid catalysts possessed a strong Brønsted acidity. Melero et al.[563] reported that sulfonate sites were important in the catalytic activity of sulfonate-modified SBA-15 catalysts. Although commercially available  $\text{SO}_3\text{H}$ -containing ion-exchange resins (e.g., Amberlyst, Amberlite, Dowex, and Purolite) have been used in the chemical industry [564], these resins swell in solvents. The relationship between the swelling property and catalytic activity is still under debate. For example, aliphatic and aromatic alcohols swell sulfonated polystyrene resins (i.e., Amberlyst) and diffuse through the swollen polymer gel to bulk acid sites[565][566]. Tejero et al.[541] found that swollen gel-type polystyrene-divinylbenzene (PS-DVB) resins had a low acid site density, which resulted in high catalytic activity for esterification of levulinic acid. Bihani et al.[567] reported the catalytic activity of Amberlyst-21 was independent of its swelling properties for the synthesis of pyran annulated heterocycles. Our PP- $\text{SO}_3\text{H}$  catalysts retained high selectivity to the ester at a high conversion, which was indicative of the high stability of the PP- $\text{SO}_3\text{H}$  catalyst in the presence of various aliphatic alcohols. Compared with commercial ion-exchange resins, our PP- $\text{SO}_3\text{H}$  catalysts were superior to ion-exchange resins in terms of Brønsted acid strength, stability in alcoholic solvents, and selectivity to esters.

On the basis of experimental results, we proposed the chemical pathway for esterification of levulinic acid with methanol by PP- $\text{SO}_3\text{H}$  catalysts (**Fig. 8.7**). The reaction mechanism proceeded through three steps. First, levulinic acid was adsorbed on Brønsted acidic protons from the  $-\text{SO}_3\text{H}$  groups of PP- $\text{SO}_3\text{H}$  catalysts, created a protonated levulinate intermediate, and increased the electrophilicity of carbonyl carbon. Next, this electrophilic carbonyl carbon underwent the nucleophilic attack by the oxygen atom of methanol and formed an oxonium ion. Then, a proton transfer and dehydration in the oxonium ion occurred, followed by deprotonation to form the ester and regenerate the Brønsted acid sites on the catalyst surface. Studies by Corma et al.[534], Osatiashtiani et al.[568], and Koo et al.[569] showed that the esterification activity of carboxylic acids depended on acid strength, which corroborated our findings. The high strength of the Brønsted acid sites of PP- $\text{SO}_3\text{H}$ -0.23 catalyst facilitated the activation of the carbonyl group and resulted in the high conversion of levulinic acid and selectivity to the ester.

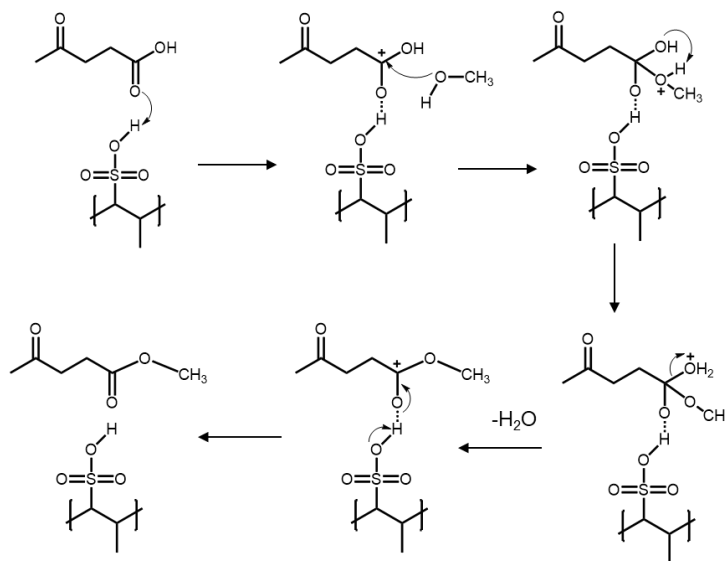


**Figure 8.7.** Proposed chemical pathway for esterification of levulinic acid with methanol by PP-SO<sub>3</sub>H catalyst

These findings demonstrated that polypropylene-derived Brønsted acidic catalysts were active, selective, and stable for the esterification of levulinic acid. Furthermore, the ability to tune the Brønsted acid strength provides opportunities to use these catalysts in various organic reactions, such as acetalization [444, 570, 571], dehydration [443, 572, 573], condensation [398], isomerization [304, 574], and hydrolysis [446, 575, 576]. The additional benefit of these catalysts is that they are based on polypropylene, which is significant because polypropylene is one of the top three most poorly recycled waste plastics consigned to landfills [577]. Thus, the use of polypropylene-derived catalysts for the chemical industry potentially increases plastic recycling rates and mitigates plastic pollution.

Although our results show the PP-SO<sub>3</sub>H catalysts were promising for levulinic acid esterification, we have not yet extensively investigated the interaction and stability between the -SO<sub>3</sub>H groups and solvents that affect their physicochemical properties and catalytic performance. Moreover, the economic and environmental impact of using waste plastic should be assessed to understand how developing catalysts from waste plastic impacts chemical production cost and the environment.



The knowledge gained will help in designing stable and selective catalysts and systems for the esterification of acids and other organic reactions.

## **5. Conclusion**

This work illustrates a feasible route to synthesize Brønsted acidic PP-SO<sub>3</sub>H catalysts from polypropylene for levulinic acid esterification. The synthesized catalysts addressed the inferior catalytic esterification performance of commercial ion-exchange resins. The synthesized PP-SO<sub>3</sub>H catalysts had a high strength of Brønsted acidity, which provided high selectivity to esters at a high conversion for levulinic acid esterification. Moreover, the degree of sulfonation controlled the strength of Brønsted acid, which will enable applications of the catalysts in various organic reactions. The use of polypropylene as a precursor for catalyst synthesis in biomass conversion will promote biorefineries and plastic upcycling. Future work will focus on investigating the stability of the sulfonate groups in various solvents and reaction temperatures.

## **Acknowledgment**

A part of this material is based upon work supported by the National Science Foundation under Cooperative Agreement No. 1355438 and Internal Research Grant, Office of the Executive Vice President for Research, University of Louisville. This work was performed in part at the Conn Center for Renewable Energy Research at the University of Louisville, which belongs to the National Science Foundation NNCI KY Manufacturing and Nano Integration Node, supported by ECCS-1542174. The authors would like to thank Dr. Howard Fried for his valuable comments and suggestions on the manuscript.

## 6. Supplementary Information

| Table 8.S1. List of chemicals/reagents used in this study |   |                  |            |
|---|---|------------------|------------|
| Material/Chemical   | Supplier  | Purity           | CAS Number |
| Polypropylene powder<br>135-168 $\mu\text{m}$             | Haihang Industry Co, Ltd.<br>(Shangdong, China) | 99.5%            | 9003-07-0  |
| 1,1,2,2-Tetrachloroethane                                 | Beantown Chemical Corporation<br>(Hudson, NH)   | 98%              | 79-34-5    |
| Chlorosulfonic acid                                       | Beantown Chemical Corporation                   | 99%              | 7790-94-5  |
| Dichloromethane   | Avantor (Radnor Township, PA)                   | $\geq 99.5\%$    | 75-09-2    |
| Levulinic acid  | Sigma-Aldrich, St. Louis, MO, USA               | 98%              | 123-76-2   |
| Methyl levulinate   | Sigma-Aldrich, St. Louis, MO, USA               | $>98\%$          | 624-45-3   |
| Methanol  | Ward's science                                  | Lab grade        | 67-56-1    |
| Amberlyst-36*   | Sigma-Aldrich, St. Louis, MO, USA               | Industrial grade | 39389-20-3 |

\*from manufacturer: solid sulfonic acid resin with macropores, acid site concentration 5.4

equivalent/kg,  $S_{\text{BET}} = 33 \text{ m}^2/\text{g}$ ,  $V_p = 0.2 \text{ cc/g}$ ,  $d_p = 24 \text{ nm}$ , particle diameter = 550-700  $\mu\text{m}$ ,

maximum operating temperature = 150  $^\circ\text{C}$ .

## CHAPTER 9

### UPCYCLING POLYPROPYLENE TO SULFONIC ACID CATALYSTS FOR CONVERSION OF BIOMASS-DERIVED COMPOUNDS TO SUSTAINABLE CHEMICALS

#### 1. Introduction

Fossil fuels are primary feedstocks for the chemical industry [578]. However, fossil fuels are non-renewable, and processing fossil fuels generate a large number of greenhouse gases (CO<sub>2</sub> and CH<sub>4</sub>), which contribute to climate change [579, 580]. Therefore, the ability to use renewable feedstock, such as lignocellulose, for the production of chemicals will revolutionize the chemical industry and promote sustainable chemical manufacturing. Furfural is a versatile precursor for plastics, adhesives, fungicides, fertilizers, pharmaceutical intermediates, flavoring compounds, and fuel additives [581]. For example, furfural can be catalyzed into 2,5-furandicarboxylic acid (FDCA) [582, 583],  $\gamma$ -valerolactone [584, 585], and 1,5-pentanediol [586, 587]. We can obtain furfural from dehydration of xylose using acid catalysts [588, 589]. Homogeneous acid catalysts, such as HCl, H<sub>2</sub>SO<sub>4</sub>, H<sub>3</sub>PO<sub>4</sub>, and HNO<sub>3</sub>, are effective for xylose dehydration [590]. Mazar et al. used H<sub>2</sub>SO<sub>4</sub> to catalyze xylose to furfural, generating 78% furfural yield at 240 °C after 60 min for the industrial scale [591]. However, homogeneous Brønsted acid is corrosive, hazardous, hard to separate and reuse, which contributes to production, equipment maintenance, safety problems, and waste management costs [531].

Solid heterogeneous Brønsted acid catalysts, such as zeolites [592], Amberlyst [593], MCM-41 [594], Nafion [595], have been used for xylose conversion. However, they obtained low xylose conversion and selectivity of furfural. Kim et al. [596] used H-zeolites for xylose dehydration in

DMSO and obtained 39% selectivity of furfural at 62% conversion at 140 °C. Wu et al. [597] used lignosulfonic acid and got an 18% furfural yield in ionic liquid. Weingarten et al. [598] used Amberlyst-70 and achieved 25% xylose conversion with 55 % furfural selectivity at 160 °C. Although these solid acid catalysts were a promising catalyst for xylose dehydration to furfural, their low selectivity and high price limit their use in large-scale industrial applications [599]. Clearly, we need to develop selective, efficient, and reusable solid Brønsted acid catalysts to address these issues.

Here, we developed solid Brønsted acidic catalysts by sulfonating polypropylene to create sulfonated polypropylene (PP-SO<sub>3</sub>H) for xylose dehydration. We varied the content of the sulfonate group and determined the relationship between the sulfonate group, acid strength, and catalytic performance for xylose dehydration. The PP-SO<sub>3</sub>H with the highest S/C ratio had the highest Brønsted acid strength and selectivity of furfural of 88% at 85% xylose conversion at 120 °C after 2 h. In addition, we recycled PP-SO<sub>3</sub>H catalyst five times which retained catalytic activity without significant loss in furfural yield.

## 2. Materials and Methods

**2.1. Materials.** All chemicals were used as received unless otherwise noted. Their CAS numbers, purity, and manufacturers are listed in **Table 9.S1**.

**2.2. Synthesis of SO<sub>3</sub>H-functionalized polypropylene (PP-SO<sub>3</sub>H).** PP-SO<sub>3</sub>H was synthesized by the previously described method with a slight modification [543, 544]. Briefly, 1.00 g of polypropylene (PP) powder was dispersed in 25 mL of 1,1,2,2-tetrachloroethane with stirring (300 rpm) under reflux at 65 °C for 30 min. Next, we mixed different vol. % (10 - 33%) of chlorosulfonic acid into dichloromethane and kept the total volume of 15 mL fixed. Finally, we added the mixture of dichloromethane and chlorosulfonic acid into the solution dropwise over 30 min. The resulting mixture was kept for an additional 2 h, and the solvents were removed by distillation. The black precipitate was obtained by centrifugation and washed with deionized water until the supernatant became colorless, and the solids were dried in a vacuum oven at 120 °C overnight.

**2.3. Characterization of the PP-SO<sub>3</sub>H.** The structural characteristics and morphologies of the catalysts were determined by X-ray diffraction (XRD), N<sub>2</sub> adsorption-desorption, Diffuse reflectance infrared Fourier transform spectroscopy (DRIFTS), Fourier-transform infrared spectroscopy (FTIR), and scanning electron microscopy (SEM) with energy dispersive X-ray spectrometry (EDS).

**2.3.1. X-ray diffraction.** X-ray diffraction (XRD) analysis of samples was carried out on a Bruker AXS Model D8 Advance A28 diffractometer (Germany) using CuK<sub>α</sub> radiation in the 2θ range from 5° to 40° with 0.02 degree/step. 200 mg of samples were used in each analysis.

**2.3.2. N<sub>2</sub> adsorption-desorption.** The N<sub>2</sub> adsorption-desorption was measured by a Micromeritics Tristar (Norcross, GA, USA) instrument to calculate the surface area, pore size, and pore volume. The function of TriStar was verified with reference materials (Micromeritics). Prior to the measurement, the sample was pretreated at 130 °C for 4 h using a Micromeritics FlowPrep with sample degasser (Norcross, GA, USA). The surface area, S<sub>BET</sub>, was determined from N<sub>2</sub> isotherms by Brunauer–Emmett–Teller equation (BET) at -196.1°C [174, 175]. BET surface area was calculated over the range of relative pressures between 0.05 and 0.3. The pore volume was estimated from the N<sub>2</sub> desorption values according to the Barrett–Joyner–Halenda (BJH) model [178]. The pore volume was calculated as the uptake (cm<sup>3</sup>/g) at a relative pressure of 0.95. We measured the average pore size of the samples by the BJH model [179, 180].

**2.3.3. Scanning electron microscopy.** To determine the microstructure and elemental distribution of the samples, scanning electron microscopy (HRTEM) was performed using a Tescan Vega V3 SEM microscope with energy dispersive X-ray spectrometry (EDS).

**2.3.4. Fourier transforms infrared spectroscopy.** Infrared spectra of samples were recorded on a JASCO Fourier transform infrared (FTIR) spectrometer (Easton, MD, USA), equipped with an attenuated total reflection stage (ATR). 5 mg of samples were used in each analysis. The samples

were scanned between 400 and 4000  $\text{cm}^{-1}$  at a 4  $\text{cm}^{-1}$  resolution. Spectra were collected using deuterated triglycine sulfate (DTGS) detector averaging 256 scans.

**2.3.5. Measurement of acid properties by pH change in methanol.** The Brønsted acid properties of synthesized catalysts were determined by measuring the pH change of methanol upon suspending catalysts inside, as described by previous studies [199, 600, 601]. In short, 8 mg catalysts were suspended in 24 mL methanol and kept stirring at ambient temperature before pH measurement. This amount was selected because previous experiments, which varied the amount of catalysts, revealed that it was high enough, so the measured pH was independent of the solid amount. The pH was measured with a gel-filled, double junction electrode (Milwaukee Instruments, Inc., Rocky Mount, NC, USA). The electrode was calibrated with the pH 4, 7, and 9 buffers. All measurements were conducted in triplicate.

**2.4. Xylose dehydration to furfural.** Xylose dehydration experiments were conducted using 15 mL pressure tubes in an oil bath. Typically, 50 mg xylose, 1 g DMSO, and 30 mg catalysts were added into 15 mL pressure tube, sealed, and stirred at 120 °C unless otherwise noted. Xylitol was used as an internal standard. The reaction was stopped by quenching in the cold water bath, followed by adding water (~5 mL) to dissolve those reaction products, intermediates, and unreacted xylose. The solution was centrifuged, and the solid catalysts were removed. The liquid sample was then plugged into HPLC for the analysis of the product distribution and xylose conversion.

**2.5. Product analysis and quantification.** The reactants and products were analyzed by High-Performance Liquid Chromatography (HPLC, Agilent Technology, Santa Clara, CA, USA) equipped with a refractive index detector (RID) and diode array detector (DAD). The Aminex HPX-87H (300 x 7.8 mm, Bio-Rad®, Hercules, CA, USA) was used for reactants and products separation at 60 °C with 0.6 ml/min of 4mM  $\text{H}_2\text{SO}_4$  as a mobile phase. The concentration of the product was determined by the peak area from the RID signals. Reaction products were calibrated against certified

standards (Absolute Standards, Inc., Hamden, CT, USA). The reactant conversion, product yield, and product selectivity were calculated as follows:

$$\text{Reactant conversion (\%)} = \frac{\text{reactant reacted (mol)}}{\text{initial reactant (mol)}} \times 100$$

$$\text{Product yield (\%)} = \frac{\text{product generated (mol)}}{\text{initial reactant (mol)}} \times 100$$

$$\text{Product selectivity (\%)} = \frac{\text{product yield}}{\text{reactant conversion}} \times 100$$

### 3. Results

We modified polypropylene (PP) with a chemical donating agent to graft sulfonate groups on the polymer surface and formed sulfonated polypropylene (PP-SO<sub>3</sub>H). We varied the amount of chemical donating agent from 10 - 33 vol.% during synthesis to affect the concentration of sulfonate group in PP-SO<sub>3</sub>H catalysts. We referred these catalysts to S/C ratios as PP-SO<sub>3</sub>H-0.08, PP-SO<sub>3</sub>H-0.18, and PP-SO<sub>3</sub>H-0.23. Then, we investigated the effect of sulfonate concentration on catalysts' physicochemical properties. We expected that PP-SO<sub>3</sub>H materials exhibited Brønsted acidity and evaluated the catalytic performance of PP-SO<sub>3</sub>H catalysts in xylose dehydration. We used dimethyl sulfoxide (DMSO) as a solvent for xylose dehydration because it minimizes the furfural degradation by providing a shielding effect in the acid-catalyzed reaction [602]. DMSO showed high catalytic activity for furfural production compared to other solvents such as water, alcohols, ketones, toluene, alkylphenol, N, N dimethylformamide, and ionic liquids [602].

#### 3.1. Physicochemical properties of sulfonated polypropylene at different sulfonate loading

To evaluate the physicochemical properties of PP-SO<sub>3</sub>H catalysts, we characterized them by scanning electron microscope (SEM), contact angle measurement, X-ray diffraction, Fourier-transform infrared spectroscopy (FTIR), N<sub>2</sub> adsorption-desorption and acidity.

First, N<sub>2</sub> adsorption-desorption was examined to measure surface area, pore-volume, and pore size (**Table 9.1**). The calculated surface area of unmodified PP was 0.65 m<sup>2</sup>/g with 0.0011 cc/g. An increase in sulfonate loading slightly increased the surface area from 0.65 and reached 1.14 m<sup>2</sup>/g,

pore volume from 0.0011 to 0.0027 cm<sup>3</sup>/g, and pore size from 6.49 to 9.47 nm. These results suggested that sulfonation did not significantly affect the surface area, pore size, and pore volume of polypropylene.

We used SEM and contact angle measurement to characterize the PP-SO<sub>3</sub>H catalysts for wettability, water suspension, and morphology (**Fig. 9.1A - C**). Surprisingly, we started to observe pores on the surface of the PP-SO<sub>3</sub>H catalyst by SEM, and PP-SO<sub>3</sub>H-0.23 was porous (**Fig. 9.1A**). As a control, PP was hydrophobic with an estimated contact angle of 131°, in agreement with that of PP membrane (~139 - 149°) (**Fig. 9.1C**) [558, 603]. The PP sample floated on water and was non-porous. PP-SO<sub>3</sub>H-0.08 had a contact angle of 53°. Therefore, most PP-SO<sub>3</sub>H-0.08 sank at the bottom of the water (**Fig. 9.1B**). An increase in SO<sub>3</sub>H concentration made the materials PP-SO<sub>3</sub>H-0.18 and PP-SO<sub>3</sub>H-0.23 become completely hydrophilic and suspended in water. Unmodified PP had 0.92 g/mL density, which was in agreement with previous studies (**Table 9.1**) [546]. The density of PP-SO<sub>3</sub>H increased from 0.92 to 1.14 g/mL with an increasing S/C ratio from 0 to 0.23, which was higher than the density of water (~1 g/mL). Increased hydrophilicity and density of PP-SO<sub>3</sub>H catalysts enhanced their dispersion in liquid phases and increased the mass transfer between catalysts and reactants.

**Table 9.1.** Surface area, density, total pore volume, average pore size, carbon to sulfur ratio, and pH in methanol of the PP-SO<sub>3</sub>H

| Polymer                   | S <sub>BET</sub><br>(m <sup>2</sup> /g) | Density <sup>a</sup><br>(g/mL) | V <sub>p</sub><br>(cm <sup>3</sup> /g) | d <sub>p</sub><br>(nm) | S/C ratio<br>(w/w) | pH in methanol <sup>b</sup> |          |
|---------------------------|---|--------------------------------|--|------------------------|--------------------|-----------------------------|----------|
|                           |   |                                |  |                        |                    | Suspension                  | Filtrate |
| PP                        | 0.65                                    | 0.92                           | 0.0011                                 | 6.49                   | -                  | 6.0                         | 6.0      |
| PP-SO <sub>3</sub> H-0.08 | 0.76                                    | 1.01                           | 0.0014                                 | 7.11                   | 0.08               | 2.4                         | 6.0      |
| PP-SO <sub>3</sub> H-0.18 | 0.88                                    | 1.09                           | 0.0018                                 | 8.16                   | 0.18               | 2.1                         | 5.9      |
| PP-SO <sub>3</sub> H-0.23 | 1.14                                    | 1.14                           | 0.0027                                 | 9.47                   | 0.23               | 1.9                         | 5.9      |
| Amberlyst-36              | -                                       | -                              | -                                      | -                      | -                  | 3.7                         | 6.0      |



---

Note.  $S_{\text{BET}}$  = surface area determined by BET,  $V_p$  = pore volume determined by from the  $N_2$  desorption values according to the Barrett–Joyner–Halenda (BJH) model,  $d_p$  = average pore diameter determined by the BJH model, <sup>a</sup>Density calculated by the water displacement method through a graduated cylinder. <sup>b</sup> pH of a stirred suspension of 3 mg of catalysts in 12 mL of methanol at 25 °C. Methanol pH (blank) was 6.0, which was in agreement with previous reports [600, 601].

To evaluate the change in chemical properties of PP-SO<sub>3</sub>H, we characterized PP-SO<sub>3</sub>H by X-ray diffraction (**Fig. 9.1D**) and FTIR spectra (**Fig. 9.1E**). X-ray diffraction of virgin polypropylene showed the characteristic peaks of (110), (040), (130), (111), and (041) at 14.0, 16.9, 18.5, 21.7, and 21.9°, respectively, suggested the monoclinic  $\alpha$ -crystalline phase of PP [555, 556]. An increase in sulfonate concentration lowered the peak intensity. These results suggested that an increase in sulfonate groups on polypropylene decreased the degree of crystallinity. As a control, unmodified PP showed the characteristic FTIR peaks of CH<sub>2</sub> bending and CH<sub>3</sub> stretching 1455 and 1375 cm<sup>-1</sup>, respectively (**Fig. 9.1E**). These two peaks were polypropylene backbone, reported by the literature [549-551]. In addition, PP-SO<sub>3</sub>H catalysts showed sulfonate bending at 1128 and 1038 cm<sup>-1</sup>, respectively. These results confirmed the formation of sulfonate groups on the polypropylene backbone [543, 552, 553]. Interestingly, we observed C=C bending at 1644 cm<sup>-1</sup> suggested that introducing the sulfonate group triggered the formation of C=C bonds in the polypropylene backbone [554]. Moreover, an increase in SO<sub>3</sub>H concentration (an increase in S/C ratio) showed a stronger intensity of this band.

### 3.2. Brønsted acid properties of modified polypropylene

To determine the Brønsted acidity of PP-SO<sub>3</sub>H catalysts, we measured the pH change of the filtrate after suspending PP-SO<sub>3</sub>H in methanol (**Table 9.1**). In the presence of solid catalysts, we measured the polarizing power of the solid catalyst on the methanol molecules [601]. As a control, blank (bare methanol) showed a pH of 6.0. The pH of the solution after suspension with PP was similar to that

of blank, which suggested PP had no Brønsted acidity. Another control of Amberlyst-36 showed a pH of 3.6, which suggested that Amberlyst-36 was Brønsted acidic.

Interestingly, the suspension of PP-SO<sub>3</sub>H in methanol showed a decrease in pH from 6.0 to 1.9 - 2.4, which suggested the Brønsted acidity of PP-SO<sub>3</sub>H samples. The pH of methanol with PP-SO<sub>3</sub>H samples was 2.4, 2.1, and 1.9 for PP-SO<sub>3</sub>H-0.08, PP-SO<sub>3</sub>H-0.18, and PP-SO<sub>3</sub>H-0.23, respectively. A significant decrease in pH of methanol of PP-SO<sub>3</sub>H-0.23 compared with blank indicated the high polarizing power of PP-SO<sub>3</sub>H-0.23 on the methanol molecules and the high strength of Brønsted acid. These results suggested that the increasing sulfonate content of PP-SO<sub>3</sub>H samples enhanced the strength of Brønsted acid. After filtering all solid out, the pH of methanol became ~5.9 - 6.0, close to the blank (methanol). These results suggested that the Brønsted acidic proton was on the surface of Amberlyst-36 and PP-SO<sub>3</sub>H catalysts.

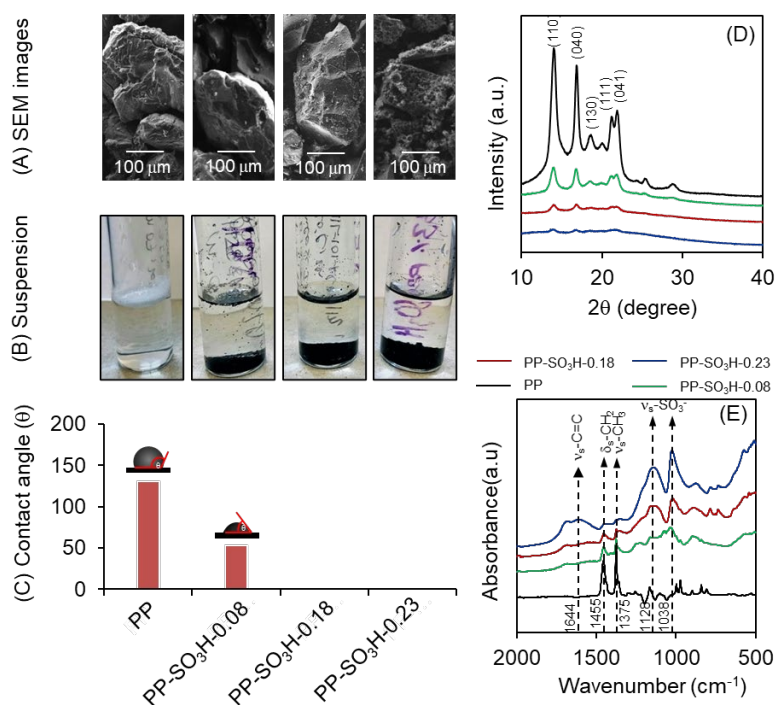


**Figure 9.1.** Characterization of functionalized polypropylene with sulfonate at different loading, SEM images (A), suspension (B), contact angle (C), XRD spectra (D) and FTIR spectra (E).

### 3.3. Catalytic performance of PP-SO<sub>3</sub>H in xylose dehydration

To evaluate the catalytic performance of PP-SO<sub>3</sub>H, we performed xylose dehydration in DMSO at 120 °C by using the same amount of catalyst (30 mg in all sulfonate loading) (**Fig. 9.2**). A blank (no added catalyst) experiment showed a low xylose conversion (20%) with no furfural yield after 2 h. These blank results suggested xylose was slightly degraded by heat conversion and xylose dehydration to furfural required Brønsted acid catalyst. As a control, we used Amberlyst-36, a commercial solid Brønsted acid catalyst. We observed a progressive increase in conversion of xylose and reached 30% selectivity to furfural at 60% conversion of xylose after 2 h. Although the conversion of xylose increased from 27 to 60% within 0.5 to 2 h, the selectivity to furfural remained low (22 - 30%). We postulated that the low selectivity of furfural with the increasing conversion of xylose was due to the lower strength of Brønsted acid in Amberlyst-36, which was observed during the pH test of methanol (**Table 9.1**).

Then, we tested the catalytic activity of PP-SO<sub>3</sub>H for xylose dehydration in DMSO. An increase in sulfonate loading from 10 to 33% improved xylose conversion from 25 to 40 % after 0.5 h under the same amount of catalyst. PP-SO<sub>3</sub>H-0.08, -0.18, and -0.23 reached 65, 75 and 85 % conversion of xylose after 2 h, respectively. The PP-SO<sub>3</sub>H-0.23 gave the highest furfural selectivity of 88% at 85% conversion after 2 h. Finally, we compare the quality of active sites through the performance of catalysts by plotting conversion vs. selectivity. We found that furfural selectivity at similar conversion was in the order of PP-SO<sub>3</sub>H-0.23 > PP-SO<sub>3</sub>H-0.18 > PP-SO<sub>3</sub>H-0.08 > Amberlyst-36, corresponding to the same order as Brønsted acid strength measured by pH change (**Table 9.1**). Overall, these results suggested that PP-SO<sub>3</sub>H catalyst with a high S/C ratio improved xylose conversion and selectivity to furfural.

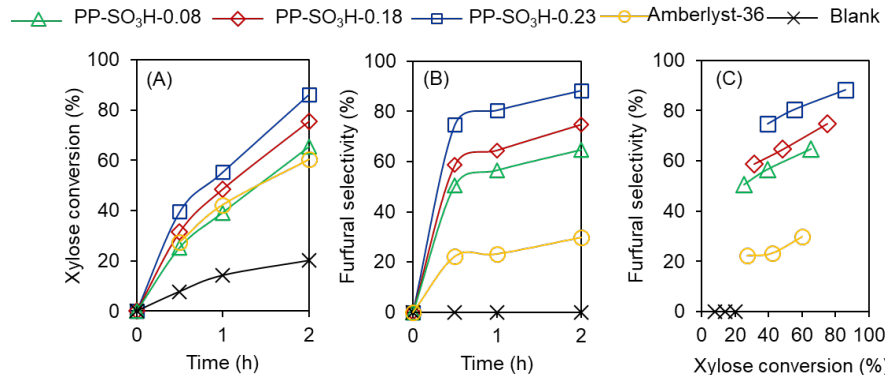


**Figure 9.2.** Catalytic performance of PP-SO<sub>3</sub>H catalysts for xylose dehydration. Evolution of xylose conversion (A), furfural selectivity (B), and conversion vs. selectivity (C). Reaction condition: 50 mg xylose, 30 mg PP-SO<sub>3</sub>H, 1 g DMSO, 120 °C.

### 3.4. Stability and reusability of PP-SO<sub>3</sub>H catalysts

The recyclability of catalysts is important for their practical use and commercialization. To examine the catalyst reusability, we recycled the PP-SO<sub>3</sub>H-0.23 catalyst by centrifugation and washing with water to remove the residual products, intermediates, and unreacted xylose. The catalyst was then dried in a vacuum oven at 130 °C to remove moisture for 6 h. The PP-SO<sub>3</sub>H-0.23 catalyst maintained its activity with a < 11% drop in xylose conversion and retained its high furfural selectivity (>85%) for four cycles (**Fig. 9.3A**).

To evaluate the catalyst stability under the reaction condition, we performed the filtration experiments by conducting the xylose dehydration using PP-SO<sub>3</sub>H-0.23 catalyst over 1 h at 120 °C, filtering the PP-SO<sub>3</sub>H-0.23 catalyst from the reaction mixture, and heating the filtrate under the same reaction condition (120 °C) for 4 h (**Fig. 9.3B**). We sampled the reaction mixture 3 times during 3 h and measured xylose conversion and furfural yield. The xylose conversion increased during the prolonged 3 h. At the same time, the yield of furfural remained constant. These results suggested that the Brønsted acid site was only on the surface of PP-SO<sub>3</sub>H-0.23 and stable.

Further, we characterized the spent PP-SO<sub>3</sub>H-0.23 catalyst after the 4<sup>th</sup> reuse cycle by EDS, XRD, and FTIR (**Fig. 9.4**). The S/C ratio of the spent catalyst, measured by EDS, was 0.19, compared with 0.23 of the fresh catalyst. These results suggested a slight loss of the sulfonate group during reuse. We postulated that this decrease in the S/C ratio of the spent PP-SO<sub>3</sub>H-0.23 was due to the weakly functionalized sulfonate groups during modification. The XRD and FTIR spectra of the spent catalyst exhibited similar chemical structure and functionality to those of fresh PP-SO<sub>3</sub>H-0.23 catalyst, which suggested minimal changes in the chemical structure after reuse. These filtration and characterization results suggested catalyst stability under the present experimental conditions. Overall, PP-SO<sub>3</sub>H catalyst maintained high selectivity to desired products for all the cycles and structural integrity after four recycles, as evidenced by its performance in xylose dehydration.

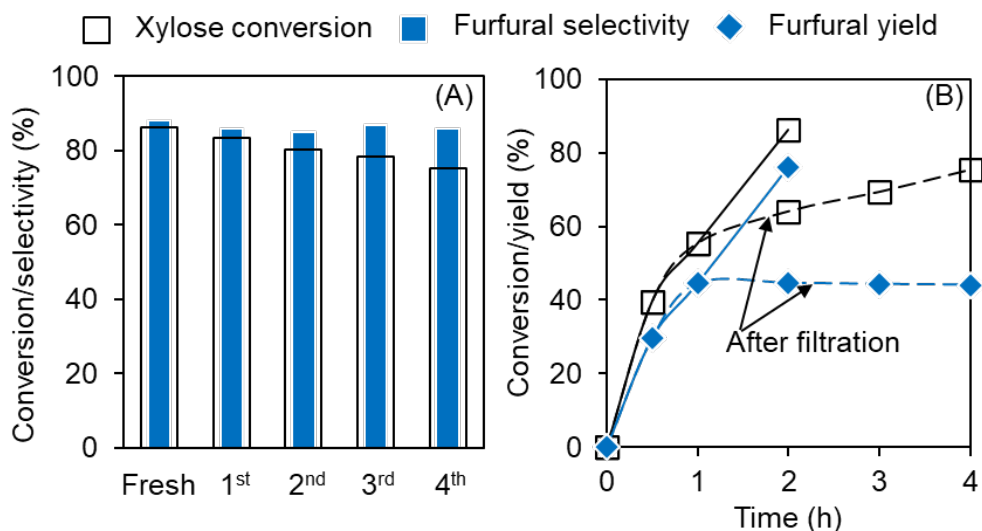


**Figure 9.3.** Catalyst recyclability (A) and stability (B) of PP-SO<sub>3</sub>H-0.23 for xylose dehydration.

Reaction condition: 50 mg xylose, 30 mg PP-SO<sub>3</sub>H-0.23, 1 g DMSO, 120 °C, 2 h.

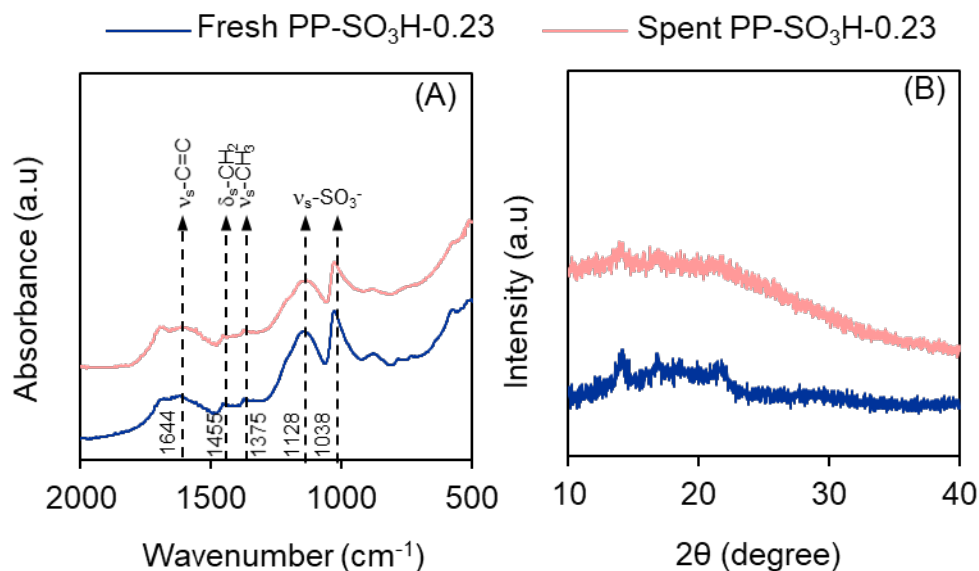


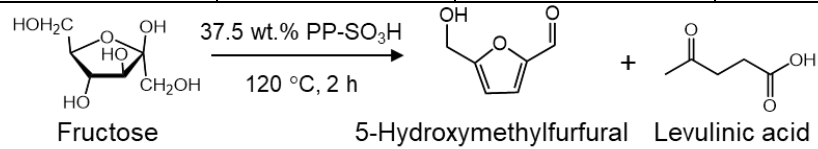
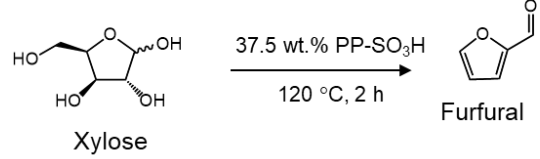
**Figure 9.4.** FTIR spectra (A) and X-ray diffraction pattern (B) of spent PP-SO<sub>3</sub>H-0.23.

### 3.5. Applications of acidic PP-SO<sub>3</sub>H catalysts for conversion of biomass-derived compounds

To further evaluate the feasibility of this Brønsted acid PP-SO<sub>3</sub>H catalyst, we applied the PP-SO<sub>3</sub>H catalysts to catalyze selected biomass-derived reactions in different solvents. We summarized the results in **Table 9.2**. We applied PP-SO<sub>3</sub>H catalyst for fructose dehydration to HMF and obtained high HMF selectivity 78 - 88% with ~98% fructose conversion in DMSO and [C<sub>4</sub>C<sub>1</sub>im]Cl at 120 °C. We observed low HMF selectivity (46 %) in *p*-dioxane. These results suggested that HMF was not stable in *p*-dioxane and degraded to humin and corresponded to the previous study [604]. Unlike fructose dehydration to HMF, [C<sub>4</sub>C<sub>1</sub>im]Cl gave low furfural selectivity (18 %) with 74 % xylose conversion at 120 °C. These results suggested that furfural was not stable and degraded to humin in [C<sub>4</sub>C<sub>1</sub>im]Cl. Previous studies demonstrated that ionic liquid acted as both solvent and catalyst, which could catalyze xylose dehydration furfural and side reaction of furfural degradation to humin [604-606]. To minimize humin formation and maximize furfural yield, the selection of solvents and a reactive furfural extraction process should be considered [211]. However, the further study of solvent effect on PP-SO<sub>3</sub>H-catalyzed dehydration of xylose to furfural is ongoing.

Brønsted acid catalysts are an active catalyst for glycerol acetalization, producing solketal, an expensive fuel additive. We also applied this PP-SO<sub>3</sub>H catalyst for glycerol acetalization reaction and obtained 93% selectivity of solketal at 95% glycerol conversion at 30 °C. Wang et al. [531] added Brønsted acid sites to Sn-containing β-zeolites for glycerol acetalization. Rahaman et al. [395] used organic surfactant functionalized HY zeolites for glycerol acetalization and obtained 95% selectivity of solketal at 89% glycerol conversion at 30 °C. Overall, our Brønsted acidic PP-SO<sub>3</sub>H catalysts showed outstanding performance in glycerol acetalization, fructose, and xylose dehydration.

**Table 9.2.** Applications of PP-SO<sub>3</sub>H catalysts in the conversion of selected biomass-derived molecules.

| Conversion   | Solvent                               | Yield/selectivity      | Yield/selectivity      |
|--|---------------------------------------|------------------------|------------------------|
|  <p>Fructose</p> <p>5-Hydroxymethylfurfural    Levulinic acid</p> |                                       |                        |                        |
| X = 97.3%  | DMSO                                  | Y = 85.3%<br>S = 87.7% | Y = 3.3%<br>S = 3.4%   |
| X = 98.5%  | <i>p</i> -Dioxane                     | Y = 45.6%<br>S = 46.3% | Y = 12.9%<br>S = 13.1% |
| X = 98.6%  | [C <sub>4</sub> C <sub>1</sub> im]Cl* | Y = 77.2%<br>S = 78.3% | Y = 1.3%<br>S = 1.3%   |
|  <p>Xylose</p> <p>Furfural</p>                                    |                                       |                        |                        |
| X = 84.9%  | DMSO                                  | Y = 74.5%<br>S = 87.8% |                        |

|   |                                       |           |          |
|---|---------------------------------------|-----------|----------|
| X = 74.6%   | [C <sub>4</sub> C <sub>1</sub> im]Cl* | Y = 13.2% |          |
|   |                                       | S = 17.7% |          |
| <p style="text-align: center;">Glycerol <span style="margin-left: 100px;">Soketal</span> + <span style="margin-left: 50px;">Acetal</span></p> |                                       |           |          |
| X = 95.1%   | Acetone                               | Y = 88.2% | Y = 6.3% |
|   |                                       | S = 92.7% | S = 7.1% |

\*[C<sub>4</sub>C<sub>1</sub>im]Cl = 1-butyl-3-methylimidazolium chloride

### 3.6. Proposed mechanism of xylose dehydration to furfural by PP-SO<sub>3</sub>H

On the basis of experimental results, we proposed the chemical pathway for xylose dehydration by PP-SO<sub>3</sub>H catalysts (**Fig. 9.5**). The reaction mechanism proceeded through protonation of the C2 hydroxyl group and dehydration. As a result, the carbenium ion was generated and formed a bond with the ring oxygen (O1). Subsequently, the bond between the anomeric carbon (C1) and the ring oxygen was broken to form the 2,5-anhydroxylose intermediate. This intermediate was dehydrated twice to form furfural [607-609].

We further described the chemical pathways of fructose dehydration and glycerol acetalization by acidic PP-SO<sub>3</sub>H catalyst (**Fig. 9.5**). For the conversion of fructose to HMF, the reaction is started by protonating the fructose hydroxyl group and leaves the ring as water. Then, the 2,5-anhydro-d-mannose intermediate is formed via the tautomerization reaction. The process is followed by the water loss to form the HMF. The glycerol acetalization with acetone proceeds in the first step with the protonation of acetone by the acidic proton of PP-SO<sub>3</sub>H catalyst, which at the same time forms the C-O bond between carbon of acetone and hydroxyl oxygen of glycerol to give a hemiketal intermediate. Then, the dehydration process is followed to form a tertiary carbenium ion. Finally, the nucleophilic secondary or terminal hydroxyl group can attack the carbenium ion with the deprotonation process to generate the solketal and acetal, respectively [513, 610]. Overall, these



results suggested the potential use of acidic PP-SO<sub>3</sub>H catalyst for conversion of biomass-derived compounds.

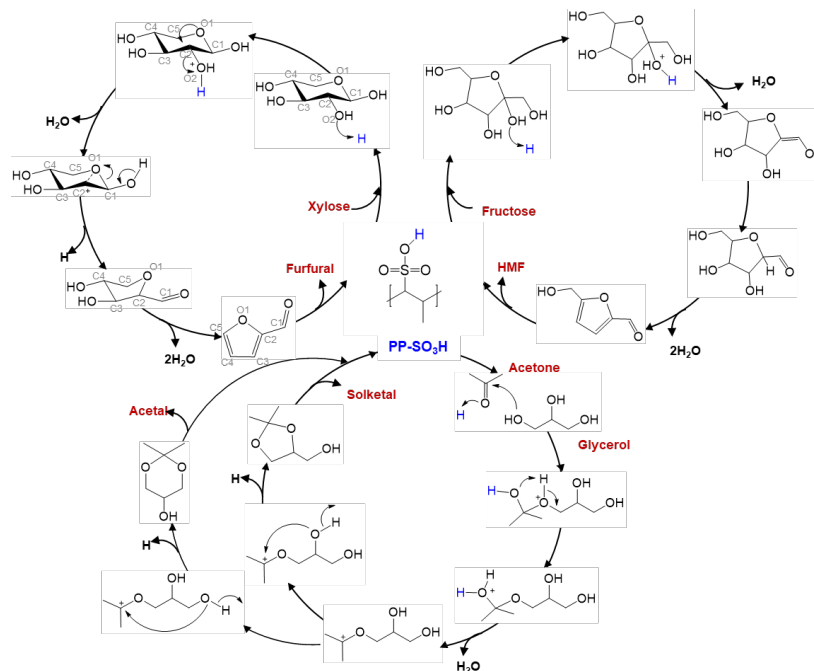


**Figure 9.5.** Proposed reaction pathways for conversion of biomass-derived compounds by acidic PP-SO<sub>3</sub>H catalyst.

#### 4. Discussion

Developing cost-effective, active, selective, and recyclable solid Brønsted acidic catalysts is a major challenge in converting biomass-derived molecules [531]. Here, we proposed a simple strategy to synthesize solid Brønsted acidic catalysts by grafting sulfonate groups onto polypropylene to form solid PP-SO<sub>3</sub>H catalysts. Then, we investigated the relationship of the sulfonate group concentration in PP-SO<sub>3</sub>H to their physicochemical properties and catalytic activities. High sulfonate group loading (high S/C ratio) in PP-SO<sub>3</sub>H catalysts increased wettability and density, promoting the mass transfer between catalysts and reactants and catalytic activity and furfural selectivity in DMSO. Moreover, the results demonstrated that PP-SO<sub>3</sub>H catalysts were stable and reusable up to four times.

Our most significant finding was that PP-SO<sub>3</sub>H catalysts were active and selective Brønsted acidic catalysts for furfural production better than the commercial Brønsted acid (Amberlyst). The superior selectivity and conversion attributed the high Brønsted acid strength, corresponding to previous studies [611-613]. Krzelj et al. developed foam catalyst derived from sulfonation of polypropylene and polystyrene foam for xylose dehydration to furfural [613]. The foam catalyst showed high furfural selectivity (70 – 80 %) in a continuous process at 160 – 200 °C in water-toluene biphasic due to high acid strength and mass transfer. Although effective, high operating temperature and pressure led to high operating costs, and catalyst synthesis was complicated.

These findings demonstrated that polypropylene-derived Brønsted acidic catalysts were active, selective, and stable catalysts for xylose dehydration reactions. Furthermore, the ability to tune the Brønsted acid strength provides opportunities to use these catalysts in various organic reactions, such as Isomerization [304, 393, 574], Meerwein–Ponndorf–Verley reduction [394], acetalization [395], esterification [397], condensation [398], and hydrolysis [446, 575, 576]. The additional benefit of these catalysts is the utilization of polypropylene as a starting material, which is significant because polypropylene is one of the top three most common waste plastic found in landfills with a low recycling rate [577]. Thus, using polypropylene-derived catalysts for the chemical industry potentially increases plastic recycling rates and mitigates plastic pollution.

Although our results show the PP-SO<sub>3</sub>H catalysts were promising for xylose dehydration, the interaction and stability between the -SO<sub>3</sub>H groups and solvents that affect their physicochemical properties and catalytic performance have not been extensively investigated. Moreover, the economic and environmental impact of using waste plastic should be investigated to understand how developing catalysts from waste plastic impacts chemical production cost and the environment. These results are essential in designing active, selective, and reusable solid Brønsted acid catalysts for biomass conversion reactions. In addition, the knowledge gained will help design stable and selective catalysts and systems for biomass dehydration and other organic reactions.

## **5. Conclusion**

Our work described a feasible route to synthesize Brønsted acidic PP-SO<sub>3</sub>H catalysts from polypropylene for xylose dehydration. The synthesized PP-SO<sub>3</sub>H catalysts had a high strength of Brønsted acidity, which provided high selectivity to furfural at the high conversion of xylose. Moreover, the degree of sulfonation controlled the strength of Brønsted acid and enabled the conversion of biomass-derived molecules into value-added chemicals. Applications of polypropylene as a precursor for solid acid catalyst synthesis would promote biorefineries and plastic upcycling. Further studies will focus on investigating the stability of the sulfonate groups in various solvents and reaction temperatures.

## **Acknowledgment**

A part of this material is based upon work supported by the National Science Foundation under Cooperative Agreement No. 1355438 and Internal Research Grant, Office of the Executive Vice President for Research, University of Louisville. This work was performed in part at the Conn Center for Renewable Energy Research at the University of Louisville, which belongs to the National Science Foundation NNCI KY Manufacturing and Nano Integration Node, supported by ECCS-1542174. The authors would like to thank Dr. Howard Fried for his valuable comments and suggestions on the manuscript.

## 6. Supplementary Information

| <b>Table 9.S1.</b> List of chemicals/reagents used in this study |   |               |                   |  |
|--|---|---------------|-------------------|--|
| <b>Material/Chemical</b>   | <b>Supplier</b>                                 | <b>Purity</b> | <b>CAS Number</b> |  |
| Polypropylene powder<br>135-168 $\mu\text{m}$                    | Haihang Industry Co, Ltd.<br>(Shangdong, China) | 99.5%         | 9003-07-0         |  |
| 1,1,2,2-Tetrachloroethane  | Beantown Chemical Corporation<br>(Hudson, NH)   | 98%           | 79-34-5           |  |
| Chlorosulfonic acid  | Beantown Chemical Corporation                   | 99%           | 7790-94-5         |  |
| Dichloromethane  | Avantor (Radnor Township, PA)                   | $\geq 99.5\%$ | 75-09-2           |  |
| D-xylose   | Acros Organics                                  | 99+%          | 58-86-6           |  |
| Furfural   | Alfa Aesar, USA                                 | 98%           | 98-01-1           |  |
| D-fructose   | Ward's science (NY, USA)                        | 100%          | 57-48-7           |  |
| Levulinic acid   | Sigma-Aldrich, St. Louis, MO                    | 98%           | 123-76-2          |  |
| Xylitol  | Acros Organics                                  | 99+%          | 87-99-0           |  |
| Glycerol   | Fisher Scientific                               | 99.5%         | 56-81-5           |  |
| Methanol   | Ward's science                                  | Lab grade     | 67-56-1           |  |
| Ethanol  | Decon Laboratories, Inc.                        | 200 Proof     | 64-17-5           |  |
| Amberlyst-36*  | Sigma-Aldrich, St. Louis, MO                    | lab grade     | 39389-20-3        |  |
| Dimethyl sulfoxide   | Sigma-Aldrich, USA                              | 99.9%         | 67-68-5           |  |
| 1,4-dioxane  | VWR, USA  | $>99.9\%$     | 123-91-1          |  |
| BMIMCl   | Alfa Aesar, USA                                 | 96%           | 79917-90-1        |  |
| Acetone  | Electron Microscopy Sciences                    | 99.8%         | 67-64-1           |  |

\*from manufacturer: solid sulfonic acid resin with macropores, acid site concentration 5.4 equivalent/kg, surface area (BET) = 33  $\text{m}^2/\text{g}$ ,  $V_p = 0.2 \text{ cc/g}$ ,  $d_p = 24 \text{ nm}$ , particle diameter = 550-700  $\mu\text{m}$ , maximum operating temperature = 150  $^\circ\text{C}$ .

## CONCLUSION AND FUTURE WORK

This dissertation has investigated the methodology to develop the porous solid acid catalysts and tested their performance for the lignocellulosic biomass and waste plastic upgrading. At first, we modified the surface of zeolite with a long-chain organic surfactant which improved the contact between glycerol and acetone for glycerol acetalization and resulted in high catalytic activity. Later, we focused our study on MOFs' tuning and linker engineering. We developed the bi-functional Lewis-Brønsted acidic MOFs and tested the effect of functional groups on the framework. We also created the surface defect on the MOFs framework. We found that defective UiO-66 MOFs have Lewis and Brønsted acidity, which exhibited superior catalytic performance. We also combined experimental results and density functional theory to elucidate how Hf- and Zr-containing MOFs activated carbonyl compounds during transfer hydrogenation. Finally, we developed the novel solid Brønsted acidic catalysts by sulfonating polypropylene to create sulfonated polypropylene (PP-SO<sub>3</sub>H). We applied these PP-SO<sub>3</sub>H catalysts to convert selected biomass-derived molecules and achieved high selectivity towards desired products. Although we developed the solid acid catalysts with high catalytic activity, there are several research areas/directions that we could further expand the work presented in this dissertation.

**Re-design "thermal catalysis" into "electrification-driven catalysis"**: Most plastics are discarded in landfills, and they pollute waterways and food chains, negatively affecting human health and the environment [614, 615]. Mechanical processes recycle about 30% of discarded plastics globally. However, mechanical recycling alone is insufficient to keep pace with the ever-growing accumulation of discarded plastics. Current combustion and pyrolysis technologies eliminate discarded plastics and produce energy/chemical feedstocks. However, the pyrolysis

process requires high temperatures (300-900 °C), lacks product selectivity [616-618], and generates CO<sub>2</sub>, contributing to greenhouse gases. Thus, a critical need is to develop a cost-effective electrification process to break plastic waste into valuable chemicals for a circular economy. In recent years, electricity-driven reactions have been of interest because we can obtain electricity from renewable wind, tide, and solar. In addition, plasma at the gas/water interface generates reactive oxygen species, such as H<sub>2</sub>O<sub>2</sub> and radicals (superoxide (O<sub>2</sub><sup>·-</sup>), hydrogen-free (H<sup>·</sup>), and hydroxyl (OH<sup>·</sup>) radicals) without added oxidants. The ability to use plasma-derived reactive oxygen species in plastic upcycling to chemicals would revolutionize the plastic and chemical industry.

**Engineering Plasma Catalysis at ambient atmosphere for Plastic Upcycling:** A key challenge in upgrading plastics is their hydrophobicity which hinders dissolution in solvents, resulting in low contact efficiency with catalysts. A strategy to overcome the nonreactivity of polyolefins would involve the introduction of polar functionalities onto the polymer chains. Recently, nonthermal atmospheric plasma processes have been of great interest in wastewater treatment and chemical processing because they can use renewable solar and wind-generated electricity [619]. Moreover, plasma processes allow low-temperature operations to initiate chemical reactions [620]. In the case of plastic upcycling, plasma discharge can generate active radicals, which could contribute to oxidative depolymerization and overcome the limited reactivity of plastic conversion into organic acids.

**Application of MOFs for oxidative depolymerization of plastic:** Metal-organic frameworks (MOFs) are promising catalytic materials because of their high surface area, high porosity, tunable functionalities. Furthermore, many accessible metal sites make MOFs ideal catalytic materials, especially for oxidation reactions [621]. The accessible metal nodes promote oxidation activity; the transition metal nodes act as a Lewis acid and/or change oxidation states [622-624]. Among MOFs that catalyze oxidation reactions, Zr-containing MOFs (i.e., UiO-66(Zr)) catalysts [625] have been investigated because of their high thermal stability [626], chemical stability in the presence of

oxidizing agents [627-629], and plasma [630-633]. Therefore, we could apply MOFs as a catalyst for the plasma oxidation of plastics.

**Plastic wastes as feedstock for making biodegradable plastics:** We can develop the plasma catalytic process to synthesize biodegradable plastics. Oxidative depolymerization by plasma would generate organic acids. These acids could be treated to *Pseudomonas putida* and *Ralstonia eutropha*. These bacterial species naturally biodegrade organic acids to produce medium-chain-length polyhydroxyalkanoates (mcl-PHAs), which are potential bioplastic alternatives to petroleum-derived plastics.

## REFERENCES

- [1] M.M. Rojas-Downing, A.P. Nejadhashemi, T. Harrigan, S.A. Woznicki, Climate change and livestock: Impacts, adaptation, and mitigation, *Clim. Risk Manage.*, 16 (2017) 145-163.
- [2] A. Paquette, J. Vayreda, L. Coll, C. Messier, J. Retana, Climate change could negate positive tree diversity effects on forest productivity: a study across five climate types in Spain and Canada, *Ecosystems*, 21 (2018) 960-970.
- [3] C. Nolan, J.T. Overpeck, J.R. Allen, P.M. Anderson, J.L. Betancourt, H.A. Binney, S. Brewer, M.B. Bush, B.M. Chase, R. Cheddadi, Past and future global transformation of terrestrial ecosystems under climate change, *Science*, 361 (2018) 920-923.
- [4] O. Edenhofer, *Climate change 2014: mitigation of climate change*, Cambridge University Press 2015.
- [5] T.A. Boden, R.J. Andres, G. Marland, Global, regional, and national fossil-fuel CO<sub>2</sub> emissions (1751-2014)(v. 2017), *Environmental System Science Data Infrastructure for a Virtual Ecosystem ...*, 2017.
- [6] K. Anderson, G. Peters, The trouble with negative emissions, *Science*, 354 (2016) 182-183.
- [7] R.W. Howarth, Ideas and perspectives: is shale gas a major driver of recent increase in global atmospheric methane, *Biogeosciences*, 16 (2019) 3033-3046.
- [8] R. Shogren, D. Wood, W. Orts, G. Glenn, Plant-based materials and transitioning to a circular economy, *Sustainable Prod. Consumption*, 19 (2019) 194-215.
- [9] C. Wu, M. Hu, F. Ni, Supporting a circular economy: Insights from Taiwan's plastic waste sector and lessons for developing countries, *Sustainable Prod. Consumption*, 26 (2020) 228-238.
- [10] Y.C. Lin, G.W. Huber, The critical role of heterogeneous catalysis in lignocellulosic biomass conversion, *Energy Environ. Sci.*, 2 (2009) 68-80.



- [11] Z. Xue, Advances in the conversion of glucose and cellulose to 5-hydroxymethylfurfural over heterogeneous catalysts, *RSC Adv.*, 6 (2016) 98874-98892.
- [12] C. Li, Direct conversion of glucose and cellulose to 5-hydroxymethylfurfural in ionic liquid under microwave irradiation, *Tetrahedron Lett.*, 50 (2009) 5403-5405.
- [13] B. Girisuta, Green chemicals: A kinetic study on the conversion of glucose to levulinic acid, *Chem. Eng. Res. Des.*, 84 (2006) 339-349.
- [14] K.L. Wasewar, A.A. Yawalkar, J.A. Moulijn, V.G. Pangarkar, Fermentation of glucose to lactic acid coupled with reactive extraction: a review, *Ind. Eng. Chem. Res.*, 43 (2004) 5969-5982.
- [15] M.E. Ligthelm, The oxygen requirements of yeasts for the fermentation of D-xylose and D-glucose to ethanol, *Appl. Microbiol. Biotechnol.*, 28 (1988) 63-68.
- [16] M. Chidambaram, A two-step approach for the catalytic conversion of glucose to 2, 5-dimethylfuran in ionic liquids, *Green Chem.*, 12 (2010) 1253-1262.
- [17] L. Peng, Solid acid catalyzed glucose conversion to ethyl levulinate, *Appl. Catal., A*, 397 (2011) 259-265.
- [18] M. Balakrishnan, Etherification and reductive etherification of 5-(hydroxymethyl) furfural: 5-(alkoxymethyl) furfurals and 2, 5-bis (alkoxymethyl) furans as potential bio-diesel candidates, *Green Chem.*, 14 (2012) 1626-1634.
- [19] A. Illanes, Reactor design for the enzymatic isomerization of glucose to fructose, *Bioprocess. Eng.*, 7 (1992) 199-204.
- [20] J.P. Casey, High fructose corn syrup. A case history of innovation, *Starch-Stärke*, 29 (1977) 196-204.
- [21] J.S. White, Sucrose, HFCS, and fructose: history, manufacture, composition, applications, and production, *Fructose, high fructose corn syrup, sucrose and health*, Springer2014, pp. 13-33.
- [22] S.H. Bhosale, Molecular and industrial aspects of glucose isomerase, *Microbiological reviews*, 60 (1996) 280-300.
- [23] J. Lee, O.K. Farha, J. Roberts, K.A. Scheidt, S.T. Nguyen, J.T. Hupp, Metal-organic framework materials as catalysts, *Chem. Soc. Rev.*, 38 (2009) 1450-1459.

- [24] D. Farrusseng, S. Aguado, C. Pinel, Metal–organic frameworks: opportunities for catalysis, *Angew. Chem. Int. Ed.*, 48 (2009) 7502-7513.
- [25] J. Hall, P. Bollini, Metal–Organic Framework MIL-100 Catalyzed Acetalization of Benzaldehyde with Methanol: Lewis or Brønsted Acid Catalysis?, *ACS Catal.*, 10 (2020) 3750-3763.
- [26] F. Zhang, J. Shi, Y. Jin, Y. Fu, Y. Zhong, W. Zhu, Facile synthesis of MIL-100 (Fe) under HF-free conditions and its application in the acetalization of aldehydes with diols, *Chem. Eng. J.*, 259 (2015) 183-190.
- [27] A. Valekar, M. Lee, J. Yoon, J. Kwak, D.-Y. Hong, K.-R. Oh, G.-Y. Cha, Y.-U. Kwon, J. Jung, J.-S. Chang, Catalytic transfer hydrogenation of furfural to furfuryl alcohol under mild conditions over Zr-MOFs: Exploring the role of metal node coordination and modification, *ACS Catal.*, 10 (2020) 3720-3732.
- [28] S. Rojas-Buzo, P. García-García, A. Corma, Catalytic Transfer Hydrogenation of Biomass-Derived Carbonyls over Hafnium-Based Metal–Organic Frameworks, *ChemSusChem*, 11 (2018) 432-438.
- [29] F. Wang, Z. Chen, H. Chen, T. Goetjen, P. Li, X. Wang, S. Alayoglu, K. Ma, Y. Chen, T. Wang, T. Islamoglu, Y. GFang, R. Snurr, O. Farha, Interplay of Lewis and Brønsted Acid Sites in Zr-Based Metal–Organic Frameworks for Efficient Esterification of Biomass-Derived Levulinic Acid, *ACS Appl. Mater. Interfaces*, 11 (2019) 32090-32096.
- [30] F. Cirujano, A. Corma, F. Xamena, Zirconium-containing metal organic frameworks as solid acid catalysts for the esterification of free fatty acids: Synthesis of biodiesel and other compounds of interest, *Catal Today*, 257 (2015) 213-220.
- [31] H. Furukawa, K.E. Cordova, M. O’Keeffe, O.M. Yaghi, The chemistry and applications of metal-organic frameworks, *Science*, 341 (2013) 1230444.
- [32] H. Furukawa, The chemistry and applications of metal-organic frameworks, *Science*, 341 (2013) 1230444.
- [33] R. Pravettoni, Plastic waste produced and mismanaged, Grid Arendal <http://www.grida.no/resources/6931>, (2018).

- [34] R. Geyer, J.R. Jambeck, K.L. Law, Production, use, and fate of all plastics ever made, *Sci. Adv.*, 3 (2017) e1700782.
- [35] L. Neufeld, F. Stassen, R. Sheppard, T. Gilman, The new plastics economy: rethinking the future of plastics, *World Economic Forum*, 2016.
- [36] T.F. Degnan, Applications of zeolites in petroleum refining, *Top. Catal.*, 13 (2000) 349-356.
- [37] A. Primo, H. Garcia, Zeolites as catalysts in oil refining, *Chem. Soc. Rev.*, 43 (2014) 7548-7561.
- [38] D. Kubička, O. Kikhtyanin, Opportunities for zeolites in biomass upgrading—Lessons from the refining and petrochemical industry, *Catal. Today*, 243 (2015) 10-22.
- [39] A. Aho, N. Kumar, A. Lashkul, K. Eränen, M. Ziolek, P. Decyk, T. Salmi, B. Holmbom, M. Hupa, D.Y. Murzin, Catalytic upgrading of woody biomass derived pyrolysis vapours over iron modified zeolites in a dual-fluidized bed reactor, *Fuel*, 89 (2010) 1992-2000.
- [40] D.M. Bibby, R.F. Howe, G.D. McLellan, Coke formation in high-silica zeolites, *Appl. Catal., A*, 93 (1992) 1-34.
- [41] S. Bailleul, I. Yarulina, A.E. Hoffman, A. Dokania, E. Abou-Hamad, A.D. Chowdhury, G. Pieters, J. Hajek, K. De Wispelaere, M. Waroquier, A supramolecular view on the cooperative role of Brønsted and Lewis acid sites in zeolites for methanol conversion, *J. Am. Chem. Soc.*, 141 (2019) 14823-14842.
- [42] L. Yang, G. Tsilomelekis, S. Caratzoulas, D.G. Vlachos, Mechanism of Brønsted Acid-Catalyzed Glucose Dehydration, *ChemSusChem*, 8 (2015) 1334-1341.
- [43] Y. Román-Leshkov, M. Moliner, J.A. Labinger, M.E. Davis, Mechanism of glucose isomerization using a solid Lewis acid catalyst in water, *Angew. Chem. Int. Ed.*, 49 (2010) 8954-8957.
- [44] J.S. Kruger, V. Nikolakis, D.G. Vlachos, Aqueous-phase fructose dehydration using Brønsted acid zeolites: Catalytic activity of dissolved aluminosilicate species, *Appl. Catal., A*, 469 (2014) 116-123.

- [45] U.S. Environmental Protection Agency, Inventory of U.S. Greenhouse Gas Emissions and Sinks: 1990-2017, Executive Summary, <https://www.epa.gov/ghgemissions/inventory-us-greenhouse-gas-emissions-and-sinks-1990-2017> (access Nov 19, 2019), 2019.
- [46] C. Nolan, J.T. Overpeck, J.R. Allen, P. Anderson, J. Betancourt, H. Binney, S. Brewer, M. Bush, B. Chase, R. Cheddadi, Past and future global transformation of terrestrial ecosystems under climate change, *Science*, 361 (2018) 920-923.
- [47] T. Boden, R. Andres, G. Marland, Global, regional, and national fossil-fuel CO<sub>2</sub> emissions (1751-2014)(v. 2017), Oak Ridge, TN: Carbon Dioxide Information Analysis Center (CDIAC), Oak Ridge National Laboratory (ORNL). 2017.
- [48] R.W. Howarth, Ideas and perspectives: is shale gas a major driver of recent increase in global atmospheric methane?, *Biogeosci.*, 16 (2019) 3033-3046.
- [49] U.S.E.I. Administration, Monthly Biodiesel Production Survey, 2018.
- [50] F. Yang, M.A. Hanna, R.C. Sun, Value-added uses for crude glycerol--a byproduct of biodiesel production, *Biotechnol. Biofuels*, 5 (2012) 13.
- [51] M. Ayoobi, I. Schoegl, Non-catalytic conversion of glycerol to syngas at intermediate temperatures: Numerical methods with detailed chemistry, *Fuel*, 195 (2017) 190-200.
- [52] M.R.K. Estahbanati, M. Feilizadeh, M.C. Iliuta, Photocatalytic valorization of glycerol to hydrogen: Optimization of operating parameters by artificial neural network, *Appl. Catal. B*, 209 (2017) 483-492.
- [53] S. García-Fernández, I. Gandarias, J. Requies, F. Soulimani, P. Arias, B. Weckhuysen, The role of tungsten oxide in the selective hydrogenolysis of glycerol to 1, 3-propanediol over Pt/WO<sub>3</sub>/Al<sub>2</sub>O<sub>3</sub>, *Appl. Catal., B*, 204 (2017) 260-272.
- [54] M. Massa, A. Andersson, E. Finocchio, G. Busca, Gas-phase dehydration of glycerol to acrolein over Al<sub>2</sub>O<sub>3</sub>-, SiO<sub>2</sub>-, and TiO<sub>2</sub>-supported Nb- and W-oxide catalysts, *J. Catal.*, 307 (2013) 170-184.
- [55] C.H. Zhou, J.N. Beltramini, Y.X. Fan, G.Q. Lu, Chemoselective catalytic conversion of glycerol as a biorenewable source to valuable commodity chemicals, *Chem Soc Rev*, 37 (2008) 527-549.

- [56] D.C. de Carvalho, A.C. Oliveira, O.P. Ferreira, J.M. Filho, S. Tehuacanero-Cuapa, A.C. Oliveira, Titanate nanotubes as acid catalysts for acetalization of glycerol with acetone: Influence of the synthesis time and the role of structure on the catalytic performance, *Chem. Eng. J.*, 313 (2017) 1454-1467.
- [57] G.P. da Silva, M. Mack, J. Contiero, Glycerol: A promising and abundant carbon source for industrial microbiology, *Biotechnol. Adv.*, 27 (2009) 30-39.
- [58] V.K. Garlapati, U. Shankar, A. Budhiraja, Bioconversion technologies of crude glycerol to value added industrial products, *Biotechnol. Rep.*, 9 (2016) 9-14.
- [59] M. da Silva, F. de Ávila Rodrigues, A. Júlio, SnF<sub>2</sub>-catalyzed glycerol ketalization: A friendly environmentally process to synthesize solketal at room temperature over on solid and reusable Lewis acid, *Chem. Eng. J.*, 307 (2017) 828-835.
- [60] T.N. Pham, T. Sooknoi, S.P. Crossley, D.E. Resasco, Ketonization of carboxylic acids: mechanisms, catalysts, and implications for biomass conversion, *Acs Catal.*, 3 (2013) 2456-2473.
- [61] M.R. Nanda, Y. Zhang, Z. Yuan, W. Qin, H.S. Ghaziaskar, C. Xu, Catalytic conversion of glycerol for sustainable production of solketal as a fuel additive: A review, *Renew. Sustain. Energy Rev.*, 56 (2016) 1022-1031.
- [62] S. Gadamsetti, N.P. Rajan, G.S. Rao, K. V. R. Chary, Acetalization of glycerol with acetone to bio fuel additives over supported molybdenum phosphate catalysts, *J. Mol. Cat. A Chem.*, 410 (2015) 49-57.
- [63] M. Gonçalves, R. Rodrigues, T.S. Galhardo, W.A. Carvalho, Highly selective acetalization of glycerol with acetone to solketal over acidic carbon-based catalysts from biodiesel waste, *Fuel*, 181 (2016) 46-54.
- [64] C.J.A. Mota, C.X.A. da Silva, N. Rosenbach, J. Costa, F. da Silva, Glycerin Derivatives as Fuel Additives: The Addition of Glycerol/Acetone Ketal (Solketal) in Gasolines, *Energy Fuel.*, 24 (2010) 2733-2736.
- [65] P.H.R. Silva, V.L.C. Gonçalves, C.J.A. Mota, Glycerol acetals as anti-freezing additives for biodiesel, *Bioresour. Technol.*, 101 (2010) 6225-6229.

- [66] L. Fertier, M. Ibert, C. Buffe, R. Saint-Loup, C. Joly-Duhamel, J.J. Robin, O. Giani, New biosourced UV curable coatings based on isosorbide, *Prog. Org. Coat.*, 99 (2016) 393-399.
- [67] B.A.J. Noordover, A. Heise, P. Malanowski, D. Senatore, M. Mak, L. Molhoek, R. Duchateau, C.E. Koning, R.A.T.M. van Benthem, Biobased step-growth polymers in powder coating applications, *Prog. Org. Coat.*, 65 (2009) 187-196.
- [68] M. Durand, V. Molinier, T. Féron, J.-M. Aubry, Isosorbide mono- and di-alkyl ethers, a new class of sustainable coalescents for water-borne paints, *Prog. Org. Coat.*, 69 (2010) 344-351.
- [69] J.I. Garcia, H. Garcia-Marin, E. Pires, Glycerol based solvents: synthesis, properties and applications, *Green Chem.*, 16 (2014) 1007-1033.
- [70] C. Chen, J.-T. Hu, Y.-J. Tu, J.-C. Wu, J. Liang, L.-L. Gao, Z.-G. Wang, B.-F. Yang, D.-L. Dong, Effects of isosorbide mononitrate on the restoration of injured artery in mice in vivo, *Eur. J. Pharm.*, 640 (2010) 150-156.
- [71] Z.Q. Li, X. He, X. Gao, Y.Y. Xu, Y.-F. Wang, H. Gu, R.-F. Ji, S.-J. Sun, Study on dissolution and absorption of four dosage forms of isosorbide mononitrate: Level A in vitro–in vivo correlation, *Eur. J. Pharm. Biopharm.*, 79 (2011) 364-371.
- [72] S.-A. Park, J. Choi, S. Ju, J. Jegal, K.M. Lee, S.Y. Hwang, D.X. Oh, J. Park, Copolycarbonates of bio-based rigid isosorbide and flexible 1,4-cyclohexanedimethanol: Merits over bisphenol-A based polycarbonates, *Polymer*, 116 (2017) 153-159.
- [73] C. da Silva, V. Gonçalves, C. Mota, Water-tolerant zeolite catalyst for the acetalisation of glycerol, *Green Chem.*, 11 (2009) 38-41.
- [74] C. Ferreira, A. Araujo, V. Calvino-Casilda, M. Cutrufello, E. Rombi, A. Fonseca, M. Bañares, I.C. Neves, Y zeolite-supported niobium pentoxide catalysts for the glycerol acetalization reaction, *Microporous Mesoporous Mater.*, 271 (2018) 243-251.
- [75] C.-N. Fan, C.-H. Xu, C.-Q. Liu, Z.-Y. Huang, J.-Y. Liu, Z.-X. Ye, Catalytic acetalization of biomass glycerol with acetone over TiO<sub>2</sub>–SiO<sub>2</sub> mixed oxides, *Reac. Kinet. Mech. Cat.*, 107 (2012) 189-202.

- [76] A. Behr, D. Obst, B. Turkowski, Isomerizing hydroformylation of trans-4-octene to n-nonanal in multiphase systems: acceleration effect of propylene carbonate, *J. Mol. Catal. A: Chem.*, 226 (2005) 215-219.
- [77] C. Sievers, Y. Noda, L. Qi, E. Albuquerque, R. Rioux, S. Scott, Phenomena affecting catalytic reactions at solid–liquid interfaces, *ACS Catal.*, 6 (2016) 8286-8307.
- [78] N. Weeranoppanant, Enabling tools for continuous-flow biphasic liquid–liquid reaction, *React. Chem. Eng.*, 4 (2019) 235-243.
- [79] M. Moreira, R. Faria, A. Ribeiro, A. Rodrigues, Solketal Production from Glycerol Ketalization with Acetone: Catalyst Selection and Thermodynamic and Kinetic Reaction Study, *Ind. Eng. Chem. Res.*, 58 (2019) 17746-17759.
- [80] H.C. Genuino, S. Thiyagarajan, J.C. van der Waal, E. de Jong, J. van Haveren, D.S. van Es, B.M. Weckhuysen, P. Bruijninx, Selectivity Control in the Tandem Aromatization of Bio-Based Furanics Catalyzed by Solid Acids and Palladium, *ChemSusChem*, 10 (2017) 277-286.
- [81] P.A. Zapata, Y. Huang, M.A. Gonzalez-Borja, D.E. Resasco, Silylated hydrophobic zeolites with enhanced tolerance to hot liquid water, *J. Catal.*, 308 (2013) 82-97.
- [82] H. Wang, H. Ruan, M. Feng, Y. Qin, H. Job, L. Luo, C. Wang, M. Engelhard, E. Kuhn, X. Chen, M. Tucker, B. Yang, One-Pot Process for Hydrodeoxygenation of Lignin to Alkanes Using Ru-Based Bimetallic and Bifunctional Catalysts Supported on Zeolite Y, *ChemSusChem*, 10 (2017) 1846-1856.
- [83] P. Prinsen, R. Luque, C. González-Arellano, Zeolite catalyzed palmitic acid esterification, *Microporous Mesoporous Mater.*, 262 (2018) 133-139.
- [84] E. Pires, J. Magalhães, U. Schuchardt, Effects of oxidant and solvent on the liquid-phase cyclohexane oxidation catalyzed by Ce-exchanged zeolite Y, *Appl. Catal., A*, 203 (2000) 231-237.
- [85] E. Astorino, J.B. Peri, R.J. Willey, G. Busca, Spectroscopic Characterization of Silicalite-1 and Titanium Silicalite-1, *J. Catal.*, 157 (1995) 482-500.
- [86] T.K. Phung, M.M. Carnasciali, E. Finocchio, G. Busca, Catalytic conversion of ethyl acetate over faujasite zeolites, *Appl. Catal. A*, 470 (2014) 72-80.

- [87] M. Junaidi, C. Khoo, C. Leo, A. Ahmad, The effects of solvents on the modification of SAPO-34 zeolite using 3-aminopropyl trimethoxy silane for the preparation of asymmetric polysulfone mixed matrix membrane in the application of CO<sub>2</sub> separation, *Microporous Mesoporous Mater.*, 192 (2014) 52-59.
- [88] D. Flinn, D. Guzonas, R.-H. Yoon, Characterization of silica surfaces hydrophobized by octadecyltrichlorosilane, *Colloids Surf., A*, 87 (1994) 163-176.
- [89] A. Kumar, J. Richter, J. Tywoniak, P. Hajek, S. Adamopoulos, U. Šegedin, M. Petrič, Surface modification of Norway spruce wood by octadecyltrichlorosilane (OTS) nanosol by dipping and water vapour diffusion properties of the OTS-modified wood, *Holzforschung*, 72 (2017) 45-56.
- [90] K. Yamagishi, S. Namba, T. Yashima, Defect sites in highly siliceous HZSM-5 zeolites: a study performed by alumination and IR spectroscopy, *The Journal of Physical Chemistry*, 95 (1991) 872-877.
- [91] T. Montanari, E. Finocchio, G. Busca, Infrared spectroscopy of heterogeneous catalysts: acidity and accessibility of acid sites of faujasite-type solid acids, *The Journal of Physical Chemistry C*, 115 (2010) 937-943.
- [92] T. Korányi, F. Moreau, V. Rozanov, E. Rozanova, Identification of SH groups in zeolite-supported HDS catalysts by FTIR spectroscopy, *J. Mol. Struct.*, 410-411 (1997) 103-110.
- [93] M. Makarova, A. Ojo, K. Karim, M. Hunger, J. Dwyer, FTIR study of weak hydrogen bonding of Brønsted hydroxyls in zeolites and aluminophosphates, *J. Phys. Chem.*, 98 (1994) 3619-3623.
- [94] I. Tsuchiya, Infrared spectroscopic study of hydroxyl groups on silica surfaces, *J. Phys. Chem.*, 86 (1982) 4107-4112.
- [95] I.-S. Chuang, G.E. Maciel, Probing hydrogen bonding and the local environment of silanols on silica surfaces via nuclear spin cross polarization dynamics, *JACS*, 118 (1996) 401-406.
- [96] S. Mirji, S. Halligudi, D.P. Sawant, N.E. Jacob, K. Patil, A. Gaikwad, S. Pradhan, Adsorption of octadecyltrichlorosilane on mesoporous SBA-15, *Appl. Surf. Sci.*, 252 (2006) 4097-4103.



- [97] J. Parise, D. Corbin, L. Abrams, D. Cox, Structure of dealuminated Linde Y-zeolite; Si139. 7Al52. 3O384 and Si173. 1Al18. 9O384: presence of non-framework Al species, *Acta Crystallogr., Sect. C: Cryst. Struct. Commun.*, 40 (1984) 1493-1497.
- [98] V. Felice, A.C. Tavares, Faujasite zeolites as solid electrolyte for low temperature fuel cells, *Solid State Ionics*, 194 (2011) 53-61.
- [99] P.A. Zapata, J. Faria, M.P. Ruiz, R.E. Jentoft, D.E. Resasco, Hydrophobic zeolites for biofuel upgrading reactions at the liquid–liquid interface in water/oil emulsions, *JACS*, 134 (2012) 8570-8578.
- [100] N.-Y. Topsøe, K. Pedersen, E.G. Derouane, Infrared and temperature-programmed desorption study of the acidic properties of ZSM-5-type zeolites, *J. Catal.*, 70 (1981) 41-52.
- [101] B. Binks, S. Lumsdon, Catastrophic phase inversion of water-in-oil emulsions stabilized by hydrophobic silica, *Langmuir*, 16 (2000) 2539-2547.
- [102] B. Binks, J. Rodrigues, W. Frith, Synergistic interaction in emulsions stabilized by a mixture of silica nanoparticles and cationic surfactant, *Langmuir*, 23 (2007) 3626-3636.
- [103] S. Arditty, C. Whitby, B. Binks, V. Schmitt, F. Leal-Calderon, Some general features of limited coalescence in solid-stabilized emulsions, *Eur. Phys. J. E*, 11 (2003) 273-281.
- [104] B. Binks, J. Clint, Solid wettability from surface energy components: relevance to Pickering emulsions, *Langmuir*, 18 (2002) 1270-1273.
- [105] S. Pickering, *Chem. J. Chem. Soc., Trans.*, 91 (1907) 2001-2021.
- [106] M. Pera-Titus, L. Leclercq, J.M. Clacens, F. De Campo, V. Nardello-Rataj, Pickering interfacial catalysis for biphasic systems: from emulsion design to green reactions, *Angew. Chem. Int. Ed.*, 54 (2015) 2006-2021.
- [107] A. Cornejo, M. Campoy, I. Barrio, B. Navarrete, J. Lázaro, Solketal production in a solvent-free continuous flow process: scaling from laboratory to bench size, *React. Chem. Eng.*, (2019).
- [108] I. Agirre, I. Garcia, J. Requies, V. Barrio, M. Güemez, J. Cambra, P. Arias, Glycerol acetals, kinetic study of the reaction between glycerol and formaldehyde, *Biomass Bioenergy*, 35 (2011) 3636-3642.

- [109] I. Agirre, M. Güemez, A. Ugarte, J. Requies, V. Barrio, J. Cambra, P. Arias, Glycerol acetals as diesel additives: Kinetic study of the reaction between glycerol and acetaldehyde, *Fuel Process. Technol.*, 116 (2013) 182-188.
- [110] J. Yu, N. Grossiord, C.E. Koning, J. Loos, Controlling the dispersion of multi-wall carbon nanotubes in aqueous surfactant solution, *Carbon*, 45 (2007) 618-623.
- [111] M. Nanda, Z. Yuan, W. Qin, H. Ghaziaskar, M.-A. Poirier, C. Xu, Thermodynamic and kinetic studies of a catalytic process to convert glycerol into solketal as an oxygenated fuel additive, *Fuel*, 117 (2014) 470-477.
- [112] J. Deutsch, A. Martin, H. Lieske, Investigations on heterogeneously catalysed condensations of glycerol to cyclic acetals, *J. Catal.*, 245 (2007) 428-435.
- [113] M. Mehmood, A. Sanawar, N. Siddiqui, T. Yasin, Quantification of silane grafting efficacy, weak IR vibration bands and percentage crystallinity in post e-beam irradiated UHMWPE, *Polym. Bull.*, 74 (2017) 213-227.
- [114] E. Astorino, J. Peri, R. Willey, G. Busca, Spectroscopic characterization of silicalite-1 and titanium silicalite-1, *J. Catal.*, 157 (1995) 482-500.
- [115] T.K. Phung, M.M. Carnasciali, E. Finocchio, G. Busca, Catalytic conversion of ethyl acetate over faujasite zeolites, *Appl. Catal., A* 470 (2014) 72-80.
- [116] Y. He, T. Hoff, L. Emdadi, Y. Wu, J. Bouraima, D. Liu, Catalytic consequences of micropore topology, mesoporosity, and acidity on the hydrolysis of sucrose over zeolite catalysts, *Catal. Sci. Technol.*, 4 (2014) 3064-3073.
- [117] H. Nur, A. Manan, L. Wei, M. Muhid, H. Hamdan, Simultaneous adsorption of a mixture of paraquat and dye by NaY zeolite covered with alkylsilane, *J. Hazard. Mater.*, 117 (2005) 35-40.
- [118] E. Regnier, Oil and energy price volatility, *Energy Econ.*, 29 (2007) 405-427.
- [119] O.B. Awodumi, A.O. Adewuyi, The role of non-renewable energy consumption in economic growth and carbon emission: Evidence from oil producing economies in Africa, *Energy Strategy Rev.*, 27 (2020) 100434.
- [120] B.F.M. Kuster, 5-Hydroxymethylfurfural (HMF). A review focussing on its manufacture, *Starch-Stärke*, 42 (1990) 314-321.

- [121] C. Fan, H. Guan, H. Zhang, J. Wang, S. Wang, X. Wang, Conversion of fructose and glucose into 5-hydroxymethylfurfural catalyzed by a solid heteropolyacid salt, *Biomass and bioenergy*, 35 (2011) 2659-2665.
- [122] G. Yong, Y. Zhang, J.Y. Ying, Efficient catalytic system for the selective production of 5-hydroxymethylfurfural from glucose and fructose, *Angew. Chem. Int. Ed.*, 47 (2008) 9345-9348.
- [123] H. Xu, Z. Wang, J. Huang, Y. Jiang, Thermal Catalytic Conversion of Biomass-Derived Glucose to Fine Chemicals, *Energy Fuels*, 35 (2021) 8602-8616.
- [124] P. Wrigstedt, J. Keskiäli, M. Leskelä, T. Repo, The Role of Salts and Brønsted Acids in Lewis Acid-Catalyzed Aqueous-Phase Glucose Dehydration to 5-Hydroxymethylfurfural, *ChemCatChem*, 7 (2015) 501-507.
- [125] R.J. van Putten, J. Soetedjo, E. Pidko, J. van der Waal, E. Hensen, E. de Jong, H. Heeres, Dehydration of different ketoses and aldoses to 5-hydroxymethylfurfural, *ChemSusChem*, 6 (2013) 1681-1687.
- [126] V. Ordonsky, V. Sushkevich, J. Schouten, J. Van Der Schaaf, T. Nijhuis, Glucose dehydration to 5-hydroxymethylfurfural over phosphate catalysts, *J. Catal.*, 300 (2013) 37-46.
- [127] J. Shen, C.E. Wyman, Hydrochloric acid-catalyzed levulinic acid formation from cellulose: data and kinetic model to maximize yields, *AIChE J.*, 58 (2012) 236-246.
- [128] Y.J. Pagan-Torres, T. Wang, J.M.R. Gallo, B.H. Shanks, J.A. Dumesic, Production of 5-hydroxymethylfurfural from glucose using a combination of Lewis and Brønsted acid catalysts in water in a biphasic reactor with an alkylphenol solvent, *ACS Catal.*, 2 (2012) 930-934.
- [129] S.S. Chen, T. Maneerung, D.C.W. Tsang, Y.S. Ok, C.H. Wang, Valorization of biomass to hydroxymethylfurfural, levulinic acid, and fatty acid methyl ester by heterogeneous catalysts, *Chem. Eng. J.*, 328 (2017) 246-273.
- [130] C.E. Bounoukta, C. Megías-Sayago, F. Ammari, S. Ivanova, A. Monzon, M.A. Centeno, J.A. Odriozola, Dehydration of glucose to 5-hydroxymethylfurfural on bifunctional carbon catalysts, *Appl. Catal., B*, 286 (2021) 119938.

- [131] J.L. Vieira, M. Almeida-Trapp, A. Mithöfer, W. Plass, J.M.R. Gallo, Rationalizing the conversion of glucose and xylose catalyzed by a combination of Lewis and Brønsted acids, *Catal. Today*, 344 (2020) 92-101.
- [132] T.D. Swift, H. Nguyen, A. Anderko, V. Nikolakis, D.G. Vlachos, Tandem Lewis/Brønsted homogeneous acid catalysis: conversion of glucose to 5-hydroxymethylfurfural in an aqueous chromium (III) chloride and hydrochloric acid solution, *Green Chem.*, 17 (2015) 4725-4735.
- [133] E. Nikolla, Y. Román-Leshkov, M. Moliner, M. Davis, "One-pot" synthesis of 5-(hydroxymethyl) furfural from carbohydrates using tin-beta zeolite, *ACS Catal.*, 1 (2011) 408-410.
- [134] D.J. Cole-Hamilton, Homogeneous catalysis--new approaches to catalyst separation, recovery, and recycling, *Science*, 299 (2003) 1702-1706.
- [135] G. Férey, Hybrid porous solids: past, present, future, *Chem. Soc. Rev.*, 37 (2008) 191-214.
- [136] H. Li, M. Eddaoudi, M. O'Keeffe, O.M. Yaghi, Design and synthesis of an exceptionally stable and highly porous metal-organic framework, *Nature*, 402 (1999) 276-279.
- [137] S. Kitagawa, R. Kitaura, S.-I. Noro, Functional porous coordination polymers, *Angew. Chem. Int. Ed.*, 43 (2004) 2334-2375.
- [138] A. Dhakshinamoorthy, M. Alvaro, H. Garcia, Commercial metal-organic frameworks as heterogeneous catalysts, *Chem. Commun.*, 48 (2012) 11275-11288.
- [139] Y. Chen, Y. Zhou, H. Wang, J. Lu, T. Uchida, Q. Xu, S. Yu, H. Jiang, Multifunctional PdAg@ MIL-101 for one-pot cascade reactions: combination of host-guest cooperation and bimetallic synergy in catalysis, *ACS Catal.*, 5 (2015) 2062-2069.
- [140] A. Henschel, K. Gedrich, R. Kraehnert, S. Kaskel, Catalytic properties of MIL-101, *Chem. Commun.*, (2008) 4192-4194.
- [141] L. Bromberg, X. Su, T.A. Hatton, Heteropolyacid-functionalized aluminum 2-aminoterephthalate metal-organic frameworks as reactive aldehyde sorbents and catalysts, *ACS Appl. Mater. Interfaces*, 5 (2013) 5468-5477.
- [142] T. Toyao, M. Fujiwaki, Y. Horiuchi, M. Matsuoka, Application of an amino-functionalised metal-organic framework: an approach to a one-pot acid-base reaction, *Rsc Adv.*, 3 (2013) 21582-21587.

- [143] P. Serra-Crespo, E.V. Ramos-Fernandez, J. Gascon, F. Kapteijn, Synthesis and characterization of an amino functionalized MIL-101 (Al): separation and catalytic properties, *Chem. Mater.*, 23 (2011) 2565-2572.
- [144] R. Srirambalaji, S. Hong, R. Natarajan, M. Yoon, R. Hota, Y. Kim, Y.H. Ko, K. Kim, Tandem catalysis with a bifunctional site-isolated Lewis acid–Brønsted base metal–organic framework, NH<sub>2</sub>-MIL-101(Al), *Chem. Commun.*, 48 (2012) 11650-11652.
- [145] E.V. Ramos-Fernandez, C. Pieters, B. van der Linden, J. Juan-Alcañiz, P. Serra-Crespo, M. Verhoeven, H. Niemantsverdriet, J. Gascon, F. Kapteijn, Highly dispersed platinum in metal organic framework NH<sub>2</sub>-MIL-101 (Al) containing phosphotungstic acid–Characterization and catalytic performance, *J. Catal.*, 289 (2012) 42-52.
- [146] L. Ma, C. Abney, W. Lin, Enantioselective catalysis with homochiral metal–organic frameworks, *Chem. Soc. Rev.*, 38 (2009) 1248-1256.
- [147] A. Corma, H. García, F.X. Llabrés i Xamena, Engineering metal organic frameworks for heterogeneous catalysis, *Chem. Rev.*, 110 (2010) 4606-4655.
- [148] M. Yoon, R. Srirambalaji, K. Kim, Homochiral metal–organic frameworks for asymmetric heterogeneous catalysis, *Chem. Rev.*, 112 (2012) 1196-1231.
- [149] J. Jiang, O.M. Yaghi, Brønsted acidity in metal–organic frameworks, *Chem. Rev.*, 115 (2015) 6966-6997.
- [150] M.R. Horn, A. Singh, S. Alomari, S. Goberna-Ferrón, R. Benages-Vilau, N. Chodankar, N. Motta, K. Ostrikov, J. MacLeod, P. Sonar, P. Gomez-Romero, D. Dubal, Polyoxometalates (POMs): from electroactive clusters to energy materials, *Energy Environ. Sci.*, 14 (2021) 1652-1700.
- [151] N.I. Gumerova, A. Rompel, Synthesis, structures and applications of electron-rich polyoxometalates, *Nat. Rev. Chem.*, 2 (2018) 0112.
- [152] L.P. Kazanskij, V.I. Spitsyn, Proton-acceptor capacity and energy of oxygen 1s-electrons of heteropolyanions, *Dokl. Akad. Nauk SSSR*, 227 (1976) 140-143.
- [153] M. Misono, Recent progress in the practical applications of heteropolyacid and perovskite catalysts: Catalytic technology for the sustainable society, *Catal. Today*, 144 (2009) 285-291.

- [154] S.S. Wang, G.Y. Yang, Recent advances in polyoxometalate-catalyzed reactions, *Chem. Rev.*, 115 (2015) 4893-4962.
- [155] W. Deng, Q. Zhang, Y. Wang, Polyoxometalates as efficient catalysts for transformations of cellulose into platform chemicals, *Dalton Trans.*, 41 (2012) 9817-9831.
- [156] I.A. Weinstock, R.E. Schreiber, R. Neumann, Dioxygen in polyoxometalate mediated reactions, *Chem. Rev.*, 118 (2017) 2680-2717.
- [157] A. Enferadi-Kerenkan, T.O. Do, S. Kaliaguine, Heterogeneous catalysis by tungsten-based heteropoly compounds, *Catal. Sci. Technol.*, 8 (2018) 2257-2284.
- [158] J. Zhong, J. Perez-Ramirez, N. Yan, Biomass valorisation over polyoxometalate-based catalysts, *Green Chem.*, 23 (2021) 18-36.
- [159] C. Wang, L. Zhang, T. Zhou, J. Chen, F. Xu, Synergy of Lewis and Brønsted acids on catalytic hydrothermal decomposition of carbohydrates and corncob acid hydrolysis residues to 5-hydroxymethylfurfural, *Sci. Rep.*, 7 (2017) 40908.
- [160] Z. Wang, Q. Chen, Conversion of 5-hydroxymethylfurfural into 5-ethoxymethylfurfural and ethyl levulinate catalyzed by MOF-based heteropolyacid materials, *Green Chem.*, 18 (2016) 5884-5889.
- [161] G. Zhan, H.C. Zeng, Integrated nanocatalysts with mesoporous silica/silicate and microporous MOF materials, *Coord. Chem. Rev.*, 320 (2016) 181-192.
- [162] D.D. Liang, S.X. Liu, F.J. Ma, F. Wei, Y.G. Chen, A crystalline catalyst based on a porous metal-organic framework and 12-tungstosilicic acid: Particle size control by hydrothermal synthesis for the formation of dimethyl ether, *Adv. Synth. Catal.*, 353 (2011) 733-742.
- [163] Y. Zhang, V. Degirmenci, C. Li, E.J.M. Hensen, Phosphotungstic acid encapsulated in metal-organic framework as catalysts for carbohydrate dehydration to 5-hydroxymethylfurfural, *ChemSusChem*, 4 (2011) 59-64.
- [164] J. Juan-Alcañiz, E.V. Ramos-Fernandez, U. Lafont, J. Gascon, F. Kapteijn, Building MOF bottles around phosphotungstic acid ships: One-pot synthesis of bi-functional polyoxometalate-MIL-101 catalysts, *J. Catal.*, 269 (2010) 229-241.

- [165] M. Sun, A PTA@MIL-101(Cr)-diatomite composite as catalyst for efficient oxidative desulfurization, *Inorg. Chem. Commun.*, 87 (2018) 30-35.
- [166] N.V. Maksimchuk, K.A. Kovalenko, S.S. Arzumanov, Y.A. Chesalov, M.S. Melgunov, A.G. Stepanov, V.P. Fedin, O.A. Kholdeeva, Hybrid polyoxotungstate/MIL-101 materials: synthesis, characterization, and catalysis of H<sub>2</sub>O<sub>2</sub>-based alkene epoxidation, *Inorg. Chem.*, 49 (2010) 2920-2930.
- [167] Y. Su, G. Chang, Z. Zhang, H. Xing, B. Su, Q. Yang, Q. Ren, Y. Yang, Z. Bao, Catalytic dehydration of glucose to 5-hydroxymethylfurfural with a bifunctional metal-organic framework, *AIChE J.*, 62 (2016) 4403-4417.
- [168] A.P. Das, S. Mishra, Hexavalent chromium (VI): Environment pollutant and health hazard, *J. Environ. Res. Dev.*, 2 (2008) 386-392.
- [169] S. Tulaphol, M.A. Hossain, M.S. Rahaman, L.Y. Liu, T.K. Phung, S. Renneckar, N. Grisdanurak, N. Sathitsuksanoh, Direct production of levulinic acid in one pot from hemp hurd by dilute acid in ionic liquids, *Energy Fuels*, 32 (2019) 1764-1772.
- [170] N. Sun, H. Liu, N. Sathitsuksanoh, V. Stavila, M. Sawant, A. Bonito, K. Tran, A. George, K.L. Sale, S. Singh, B.A. Simmons, B.A. Holmes, Production and extraction of sugars from switchgrass hydrolyzed in ionic liquids, *Biotechnol. Biofuels*, 6 (2013) 1-15.
- [171] D. Groff, A. George, N. Sun, N. Sathitsuksanoh, G. Bokinsky, B.A. Simmons, B.M. Holmes, J.D. Keasling, Acid enhanced ionic liquid pretreatment of biomass, *Green Chem.*, 15 (2013) 1264-1267.
- [172] I.V. Kozhevnikov, Advances in catalysis by heteropolyacids, *Russ. Chem. Rev.*, 56 (1987) 811.
- [173] L. Bromberg, Heteropolyacid-functionalized aluminum 2-aminoterephthalate metal-organic frameworks as reactive aldehyde sorbents and catalysts, *ACS Appl. Mater. Interfaces*, 5 (2013) 5468-5477.
- [174] R. Haul, SJ Gregg, KSW Sing: adsorption, surface area and porosity. 2. auflage, academic press, London 1982. 303 Seiten, Preis: \$49.50, Wiley Online Library, 1982.

- [175] K.S.W. Sing, Reporting physisorption data for gas/solid systems with special reference to the determination of surface area and porosity (Recommendations 1984), *Pure Appl. Chem.*, 57 (1985) 603-619.
- [176] M. Jaroniec, M. Kruk, A. Sayari, Adsorption methods for characterization of surface and structural properties of mesoporous molecular sieves, *Stud. Surf. Sci. Catal.*, Elsevier 1998, pp. 325-332.
- [177] D. Dollimore, P. Spooner, A. Turner, The BET method of analysis of gas adsorption data and its relevance to the calculation of surface areas, *Surf. Technol.*, 4 (1976) 121-160.
- [178] E.P. Barrett, L.G. Joyner, P.P. Halenda, The determination of pore volume and area distributions in porous substances. I. Computations from nitrogen isotherms, *J. Am. Chem. Soc.*, 73 (1951) 373-380.
- [179] J. Xu, J. Liu, Z. Li, X. Wang, Z. Wang, Synthesis, structure and properties of Pd@ MOF-808, *J. Mater. Sci.*, 54 (2019) 12911-12924.
- [180] S.K. Jana, R. Nishida, K. Shindo, T. Kugita, S. Namba, Pore size control of mesoporous molecular sieves using different organic auxiliary chemicals, *Microporous Mesoporous Mater.*, 68 (2004) 133-142.
- [181] J.C. Groen, L.A.A. Peffer, J. Pérez-Ramírez, Pore size determination in modified micro-and mesoporous materials. Pitfalls and limitations in gas adsorption data analysis, *Microporous Mesoporous Mater.*, 60 (2003) 1-17.
- [182] A.I. Osman, J.K. Abu-Dahrieh, D.W. Rooney, S.A. Halawy, M.A. Mohamed, A. Abdelkader, Effect of precursor on the performance of alumina for the dehydration of methanol to dimethyl ether, *Appl. Catal., B*, 127 (2012) 307-315.
- [183] K.M. Santos, E.M. Albuquerque, G. Innocenti, L.E. Borges, C. Sievers, M.A. Fraga, The role of brønsted and water-tolerant Lewis acid sites in the cascade aqueous-phase reaction of triose to lactic acid, *ChemCatChem*, (2019).
- [184] D. Yu, M. Wu, Q. Hu, L. Wang, C. Lv, L. Zhang, Iron-based metal-organic frameworks as novel platforms for catalytic ozonation of organic pollutant: Efficiency and mechanism, *J. Hazard. Mater.*, 367 (2019) 456-464.



- [185] S.W. Li, W. Wang, J.S. Zhao, Effective and reusable oxidative desulfurization of dibenzothiophene via magnetic amino-MIL-101 supported  $H_3PMo_6W_6O_{40}$  components: comparison influence on various types of MIL-101, *Energy Fuels*, 34 (2020) 4837-4848.
- [186] L. Qin, Z. Li, Q. Hu, Z. Xu, X. Guo, G. Zhang, One-pot assembly of metal/organic-acid sites on amine-functionalized ligands of MOFs for photocatalytic hydrogen peroxide splitting, *Chem. Commun.*, 52 (2016) 7110-7113.
- [187] J. Wang, Y. Liu, X. Guo, H. Qu, R. Chang, J. Ma, Efficient Adsorption of Dyes Using Polyethyleneimine-Modified  $NH_2$ -MIL-101 (Al) and its Sustainable Application as a Flame Retardant for an Epoxy Resin, *ACS omega*, 5 (2020) 32286-32294.
- [188] J. Jae, G.A. Tompsett, A.J. Foster, K.D. Hammond, S.M. Auerbach, R.F. Lobo, G.W. Huber, Investigation into the shape selectivity of zeolite catalysts for biomass conversion, *J. Catal.*, 279 (2011) 257-268.
- [189] Z.J. Lin, H.Q. Zheng, J. Chen, W.E. Zhuang, Y.X. Lin, J.W. Su, Y.B. Huang, R. Cao, Encapsulation of phosphotungstic acid into metal-organic frameworks with tunable window sizes: Screening of PTA@MOF catalysts for efficient oxidative desulfurization, *Inorg. Chem.*, 57 (2018) 13009-13019.
- [190] L. Bromberg, Y. Diao, H. Wu, S.A. Speakman, T.A. Hatton, Chromium(III) Terephthalate Metal Organic Framework (MIL-101): HF-Free Synthesis, Structure, Polyoxometalate Composites, and Catalytic Properties, *Chem. Mater.*, 24 (2012) 1664-1675.
- [191] J. Navarro-Sánchez, N. Almora-Barrios, B. Lerma-Berlanga, J.J. Ruiz-Pernía, V.A. Lorenz-Fonfria, I. Tuñón, C. Martí-Gastaldo, Translocation of enzymes into a mesoporous MOF for enhanced catalytic activity under extreme conditions, *Chem. Sci.*, 10 (2019) 4082-4088.
- [192] N.V. Maksimchuk, M.N. Timofeeva, M.S. Melgunov, A.N. Shmakov, Y.A. Chesalov, D.N. Dybtsev, V.P. Fedin, O.A. Kholdeeva, Heterogeneous selective oxidation catalysts based on coordination polymer MIL-101 and transition metal-substituted polyoxometalates, *J. Catal.*, 257 (2008) 315-323.

- [193] C. Sun, S. Liu, D. Liang, K. Shao, Y. Ren, Z. Su, Highly stable crystalline catalysts based on a microporous metal– organic framework and polyoxometalates, *J. Am. Chem. Soc.*, 131 (2009) 1883-1888.
- [194] X. Li, W. Guo, X. Gao, X. Yue, Phosphotungstic acid encapsulated in MIL-53(Fe) as efficient visible-light photocatalyst for rhodamine B degradation, *Environ. Prog. Sustainable Energy*, 36 (2017) 1342-1350.
- [195] J.N. Hall, P. Bollini, Metal–organic framework MIL-100 catalyzed acetalization of benzaldehyde with methanol: Lewis or Brønsted acid catalysis?, *ACS Catal.*, 10 (2020) 3750-3763.
- [196] X.X. Zheng, Z.P. Fang, Z.J. Dai, J.M. Cai, L.J. Shen, Y.F. Zhang, C.T. Au, L.L. Jiang, Iron-based metal–organic frameworks as platform for H<sub>2</sub>S selective conversion: Structure-dependent desulfurization activity, *Inorg. Chem.*, 59 (2020) 4483-4492.
- [197] C. Volkringer, H. Leclerc, J.C. Lavalley, T. Loiseau, G. Férey, M. Daturi, A. Vimont, Infrared spectroscopy investigation of the acid sites in the metal–organic framework aluminum trimesate MIL-100 (Al), *J. Phys. Chem. C*, 116 (2012) 5710-5719.
- [198] H. Leclerc, A. Vimont, J.C. Lavalley, M. Daturi, A.D. Wiersum, P.L. Llewellyn, P. Horcajada, G. Férey, C. Serre, Infrared study of the influence of reducible iron (III) metal sites on the adsorption of CO, CO<sub>2</sub>, propane, propene and propyne in the mesoporous metal–organic framework MIL-100, *Phys. Chem. Chem. Phys.*, 13 (2011) 11748-11756.
- [199] A. Herbst, A. Khutia, C. Janiak, Brønsted instead of Lewis acidity in functionalized MIL-101Cr MOFs for efficient heterogeneous (nano-MOF) catalysis in the condensation reaction of aldehydes with alcohols, *Inorg. Chem.*, 53 (2014) 7319-7333.
- [200] A. Vimont, J.-M. Goupil, J.-C. Lavalley, M. Daturi, S. Surblé, C. Serre, F. Millange, G. Férey, N. Audebrand, Investigation of acid sites in a zeotypic giant pores chromium (III) carboxylate, *J. Am. Chem. Soc.*, 128 (2006) 3218-3227.
- [201] J. Juan-Alcañiz, M. Goesten, E. Ramos-Fernandez, J. Gascon, F. Kapteijn, Towards efficient polyoxometalate encapsulation in MIL-100 (Cr): Influence of synthesis conditions, *New J. Chem.*, 36 (2012) 977-987.

- [202] S. Patil, C. Lund, Formation and growth of humins via aldol addition and condensation during acid-catalyzed conversion of 5-hydroxymethylfurfural, *Energy Fuels*, 25 (2011) 4745-4755.
- [203] N. Maksimchuk, O. Kholdeeva, K. Kovalenko, V. Fedin, MIL-101 Supported Polyoxometalates: Synthesis, Characterization, and Catalytic Applications in Selective Liquid-Phase Oxidation, *Isr. J. Chem.*, 51 (2011) 281-289.
- [204] J. Song, Z. Luo, D. Britt, H. Furukawa, O. Yaghi, K. Hardcastle, C. Hill, A multiunit catalyst with synergistic stability and reactivity: a polyoxometalate–metal organic framework for aerobic decontamination, *J. Am. Chem. Soc.*, 133 (2011) 16839-16846.
- [205] Q. Hou, W. Li, M. Zhen, L. Liu, Y. Chen, Q. Yang, F. Huang, S. Zhang, M. Ju, An ionic liquid–organic solvent biphasic system for efficient production of 5-hydroxymethylfurfural from carbohydrates at high concentrations, *RSC Adv.*, 7 (2017) 47288-47296.
- [206] P. Zhao, H. Cui, Y. Zhang, Y. Zhang, Y. Wang, Y. Zhang, Y. Xie, W. Yi, Synergetic Effect of Brønsted/Lewis Acid Sites and Water on the Catalytic Dehydration of Glucose to 5-Hydroxymethylfurfural by Heteropolyacid-Based Ionic Hybrids, *ChemistryOpen*, 7 (2018) 824-832.
- [207] H. Li, S. Yang, Catalytic Transformation of Fructose and Sucrose to HMF with Proline-Derived Ionic Liquids under Mild Conditions, *Int. J. Chem. Eng.*, 2014 (2014) 978708.
- [208] K. Kumar, A. Dahiya, T. Patra, S. Upadhyayula, Upgrading of HMF and Biomass-Derived Acids into HMF Esters Using Bifunctional Ionic Liquid Catalysts under Solvent Free Conditions, *ChemistrySelect*, 3 (2018) 6242-6248.
- [209] Z. Xu, Y. Yang, P. Yan, Z. Xia, X. Liu, Z.C. Zhang, Mechanistic understanding of humin formation in the conversion of glucose and fructose to 5-hydroxymethylfurfural in [BMIM]Cl ionic liquid, *RSC Adv.*, 10 (2020) 34732-34737.
- [210] G. Tsilomelekis, M.J. Orella, Z. Lin, Z. Cheng, W. Zheng, V. Nikolakis, D.G. Vlachos, Molecular structure, morphology and growth mechanisms and rates of 5-hydroxymethyl furfural (HMF) derived humins, *Green Chem.*, 18 (2016) 1983-1993.

- [211] Q. Hou, X. Qi, M. Zhen, H. Qian, Y. Nie, C. Bai, S. Zhang, X. Bai, M. Ju, Biorefinery roadmap based on catalytic production and upgrading 5-hydroxymethylfurfural, *Green Chem.*, 23 (2021) 119-231.
- [212] E. Pidko, V. Degirmenci, R. van Santen, E. Hensen, Glucose activation by transient Cr<sup>2+</sup> dimers, *Angew. Chem. Int. Ed.*, 122 (2010) 2584-2588.
- [213] E. Pidko, V. Degirmenci, E. Hensen, On the mechanism of Lewis acid catalyzed glucose transformations in ionic liquids, *ChemCatChem*, 4 (2012) 1263-1271.
- [214] G. Yang, E. Pidko, E. Hensen, The mechanism of glucose isomerization to fructose over Sn-BEA zeolite: a periodic density functional theory study, *ChemSusChem*, 6 (2013) 1688-1696.
- [215] V. Tangsermit, T. Pila, B. Boekfa, V. Somjit, W. Klysubun, J. Limtrakul, S. Horike, K. Kongpatpanich, Incorporation of Al<sup>3+</sup> Sites on Brønsted Acid Metal–Organic Frameworks for Glucose-to-Hydroxymethylfurfural Transformation, *Small*, 17 (2021) 2006541.
- [216] F. Newth, The formation of furan compounds from hexoses, *Adv. Carbohydr. Chem.*, 6 (1951) 83-106.
- [217] M. Antal Jr, W. Mok, G. Richards, Mechanism of formation of 5-(hydroxymethyl)-2-furaldehyde from D-fructose and sucrose, *Carbohydr. Res.*, 199 (1990) 91-109.
- [218] S.P. Teong, G. Yi, Y. Zhang, Hydroxymethylfurfural production from bioresources: past, present and future, *Green Chem.*, 16 (2014) 2015-2026.
- [219] X. Li, K. Peng, X. Liu, Q. Xia, Y. Wang, Comprehensive Understanding of the Role of Brønsted and Lewis Acid Sites in Glucose Conversion into 5-Hydroxymethylfurfural, *ChemCatChem*, 9 (2017) 2739-2746.
- [220] V. Tangsermit, T. Pila, B. Boekfa, V. Somjit, W. Klysubun, J. Limtrakul, S. Horike, K. Kongpatpanich, Incorporation of Al<sup>3+</sup> sites on Brønsted acid metal–organic frameworks for glucose-to-hydroxymethylfurfural transformation, *Small*, (2021) 2006541.
- [221] V. Choudhary, S.H. Mushrif, C. Ho, A. Anderko, V. Nikolakis, N.S. Marinkovic, A.I. Frenkel, S.I. Sandler, D.G. Vlachos, Insights into the interplay of Lewis and Brønsted acid catalysts in glucose and fructose conversion to 5-(hydroxymethyl) furfural and levulinic acid in aqueous media, *JACS*, 135 (2013) 3997-4006.

- [222] G. Férey, C. Mellot-Draznieks, C. Serre, F. Millange, J. Dutour, S. Surblé, I. Margiolaki, A chromium terephthalate-based solid with unusually large pore volumes and surface area, *Science*, 309 (2005) 2040-2042.
- [223] Q.X. Luo, X.D. Song, M. Ji, S.E. Park, C. Hao, Y.Q. Li, Molecular size- and shape-selective Knoevenagel condensation over microporous  $\text{Cu}_3(\text{BTC})_2$  immobilized amino-functionalized basic ionic liquid catalyst, *Appl. Catal., A*, 478 (2014) 81-90.
- [224] Y.K. Hwang, D.Y. Hong, J.S. Chang, S.H. Jung, Y.K. Seo, J. Kim, A. Vimont, M. Daturi, C. Serre, G. Férey, Amine grafting on coordinatively unsaturated metal centers of MOFs: consequences for catalysis and metal encapsulation, *Angew. Chem. Int. Ed.*, 120 (2008) 4144-4148.
- [225] Y. Qu, Y. Zhao, S. Xiong, C. Wang, S. Wang, L. Zhu, L. Ma, Conversion of Glucose into 5-Hydroxymethylfurfural and Levulinic Acid Catalyzed by  $\text{SO}_4^{2-}/\text{ZrO}_2$  in a Biphasic Solvent System, *Energy Fuels*, 34 (2020) 11041-11049.
- [226] J. Dijkmans, D. Gabriëls, M. Dusselier, F. de Clippel, P. Vanelderen, K. Houthoofd, A. Malfliet, Y. Pontikes, B.F. Sels, Productive sugar isomerization with highly active Sn in dealuminated  $\beta$  zeolites, *Green Chem.*, 15 (2013) 2777-2785.
- [227] M. Tao, L. Xue, Z. Sun, S. Wang, X. Wang, J. Shi, Tailoring the synergistic Brønsted-Lewis acidic effects in heteropolyacid catalysts: Applied in esterification and transesterification reactions, *Sci. Rep.*, 5 (2015) 13764.
- [228] N. Liu, X. Pu, X. Wang, L. Shi, Study of alkylation on a Lewis and Brønsted acid hybrid catalyst and its industrial test, *J. Ind. Eng. Chem.*, 20 (2014) 2848-2857.
- [229] B. Li, K. Leng, Y. Zhang, J.J. Dynes, J. Wang, Y. Hu, D. Ma, Z. Shi, L. Zhu, D. Zhang, Y. Sun, M. Chrzanowski, S. Ma, Metal-organic framework based upon the synergy of a Brønsted acid framework and Lewis acid centers as a highly efficient heterogeneous catalyst for fixed-bed reactions, *J. Am. Chem. Soc.*, 137 (2015) 4243-4248.
- [230] K. Gupta, K. Zhang, J. Jiang, Glucose recovery from aqueous solutions by adsorption in metal-organic framework MIL-101: a molecular simulation study, *Sci. Rep.*, 5 (2015) 1-9.

- [231] Z. Zeng, J. Lyu, P. Bai, X. Guo, Adsorptive separation of fructose and glucose by metal–organic frameworks: Equilibrium, kinetic, thermodynamic, and adsorption mechanism studies, *Ind. Eng. Chem. Res.*, 57 (2018) 9200-9209.
- [232] Y. Zhang, J. Wan, Y. Wang, Y. Ma, Synthesis of phosphotungstic acid-supported versatile metal–organic framework PTA@ MIL-101 (Fe)–NH<sub>2</sub>–Cl, *RSC adv.*, 5 (2015) 97589-97597.
- [233] J. Li, S. Zhao, Z. Li, D. Liu, Y. Chi, C. Hu, Efficient Conversion of Biomass-Derived Levulinic Acid to  $\gamma$ -Valerolactone over Polyoxometalate@Zr-Based Metal–Organic Frameworks: The Synergistic Effect of Bronsted and Lewis Acidic Sites, *Inorg. Chem.*, DOI: 10.1021/acs.inorgchem.1c00185 (2021).
- [234] K. Sabyrov, J. Jiang, O. Yaghi, G. Somorjai, Hydroisomerization of n-Hexane using acidified metal–organic framework and platinum nanoparticles, *JACS*, 139 (2017) 12382-12385.
- [235] Y. Lu, C. Yue, B. Liu, M. Zhang, Y. Li, W. Yang, Y. Lin, Y. Pan, D. Sun, Y. Liu, The encapsulation of POM clusters into MIL-101 (Cr) at molecular level: LaW10O36@ MIL-101 (Cr), an efficient catalyst for oxidative desulfurization, *Microporous Mesoporous Mater.*, 311 (2021) 110694.
- [236] D. Julião, A. Gomes, M. Pillinger, L. Cunha-Silva, B. de Castro, I. Gonçalves, S. Balula, Desulfurization of model diesel by extraction/oxidation using a zinc-substituted polyoxometalate as catalyst under homogeneous and heterogeneous (MIL-101 (Cr) encapsulated) conditions, *Fuel Process. Technol.*, 131 (2015) 78-86.
- [237] L. Wee, F. Bonino, C. Lamberti, S. Bordiga, J. Martens, Cr-MIL-101 encapsulated Keggin phosphotungstic acid as active nanomaterial for catalysing the alcoholysis of styrene oxide, *Green Chem.*, 16 (2014) 1351-1357.
- [238] G. Ye, L. Hu, Y. Gu, C. Lancelot, A. Rives, C. Lamonier, N. Nuns, M. Marinova, W. Xu, Y. Sun, Synthesis of polyoxometalate encapsulated in UiO-66 (Zr) with hierarchical porosity and double active sites for oxidation desulfurization of fuel oil at room temperature, *J. Mater. Chem. A.*, 8 (2020) 19396-19404.

- [239] X. Song, D. Hu, X. Yang, H. Zhang, W. Zhang, J. Li, M. Jia, J. Yu, Polyoxomolybdic cobalt encapsulated within Zr-based metal–organic frameworks as efficient heterogeneous catalysts for olefins epoxidation, *ACS Sustainable Chem. Eng.*, 7 (2019) 3624-3631.
- [240] W. Shah, A. Waseem, M. Nadeem, P. Kögerler, Leaching-free encapsulation of cobalt-polyoxotungstates in MIL-100 (Fe) for highly reproducible photocatalytic water oxidation, *Appl. Catal., A*, 567 (2018) 132-138.
- [241] X. Hu, Y. Lu, F. Dai, C. Liu, Y. Liu, Host–guest synthesis and encapsulation of phosphotungstic acid in MIL-101 via “bottle around ship”: an effective catalyst for oxidative desulfurization, *Microporous Mesoporous Mater.*, 170 (2013) 36-44.
- [242] F. Zhang, Y. Jin, J. Shi, Y. Zhong, W. Zhu, M. El-Shall, Polyoxometalates confined in the mesoporous cages of metal–organic framework MIL-100 (Fe): efficient heterogeneous catalysts for esterification and acetalization reactions, *Chem. Eng. J.*, 269 (2015) 236-244.
- [243] X. Zhong, Y. Lu, F. Luo, Y. Liu, X. Li, S. Liu, A nanocrystalline POM@ MOFs catalyst for the degradation of phenol: effective cooperative catalysis by metal nodes and POM guests, *Chem. Eur. J.*, 24 (2018) 3045-3051.
- [244] Z. Saedi, S. Tangestaninejad, M. Moghadam, V. Mirkhani, I. Mohammadpoor-Baltork, The effect of encapsulated Zn-POM on the catalytic activity of MIL-101 in the oxidation of alkenes with hydrogen peroxide, *J. Coord. Chem.*, 65 (2012) 463-473.
- [245] P. Wei, Y. Yang, W. Li, G. Li, Keggin-POM@ rht-MOF-1 composite as heterogeneous catalysts towards ultra-deep oxidative fuel desulfurization, *Fuel*, 274 (2020) 117834.
- [246] H. Wan, C. Chen, Z. Wu, Y. Que, Y. Feng, W. Wang, L. Wang, G. Guan, X. Liu, Encapsulation of heteropolyanion-based ionic liquid within the metal–organic framework MIL-100 (Fe) for biodiesel production, *ChemCatChem*, 7 (2015) 441-449.
- [247] C. Buru, M. Wasson, O. Farha, H5PV2Mo10O40 polyoxometalate encapsulated in NU-1000 metal–organic framework for aerobic oxidation of a mustard gas simulant, *ACS Appl. Nano Mater.*, 3 (2019) 658-664.

- [248] W. Shah, L. Noureen, M. Nadeem, P. Kögerler, Encapsulation of Keggin-type manganese-polyoxomolybdates in MIL-100 (Fe) for efficient reduction of p-nitrophenol, *J. Solid State Chem.*, 268 (2018) 75-82.
- [249] A. Marandi, S. Tangestaninejad, M. Moghadam, V. Mirkhani, A. Mechler, I. Mohammadpoor-Baltork, F. Zadehahmadi, Dodecatungstocobaltate heteropolyanion encapsulation into MIL-101 (Cr) metal–organic framework scaffold provides a highly efficient heterogeneous catalyst for methanolysis of epoxides, *Appl. Organomet. Chem.*, 32 (2018) e4065.
- [250] F. Liang, D. Chen, H. Liu, W. Liu, M. Xian, D. Feng, One-pot synthesis of 5-hydroxymethylfurfural from glucose by Brønsted acid-free bifunctional porous coordination polymers in water, *ACS Omega*, 4 (2019) 9316-9323.
- [251] R. Oozeerally, D. Burnett, T. Chamberlain, R. Kashtiban, S. Huband, R. Walton, V. Degirmenci, Systematic modification of UiO-66 metal-organic frameworks for glucose conversion into 5-hydroxymethyl furfural in water, *ChemCatChem*, (2021).
- [252] J. Gong, M.J. Katz, F.M. Kerton, Catalytic conversion of glucose to 5-hydroxymethylfurfural using zirconium-containing metal–organic frameworks using microwave heating, *RSC Adv.*, 8 (2018) 31618-31627.
- [253] Y. Su, G. Chang, Z. Zhang, H. Xing, B. Su, Q. Yang, Q. Ren, Y. Yang, Z. Bao, Catalytic dehydration of glucose to 5-hydroxymethylfurfural with a bifunctional metal-organic framework, *AIChE Journal*, 62 (2016) 4403-4417.
- [254] M. Yabushita, P. Li, T. Islamoglu, H. Kobayashi, A. Fukuoka, O.K. Farha, A. Katz, Selective metal–organic framework catalysis of glucose to 5-Hydroxymethylfurfural using phosphate-modified NU-1000, *Ind. Eng. Chem. Res.*, 56 (2017) 7141-7148.
- [255] Y. Zhang, V. Degirmenci, C. Li, E.J. Hensen, Phosphotungstic acid encapsulated in metal–organic framework as catalysts for carbohydrate dehydration to 5-hydroxymethylfurfural, *ChemSusChem*, 4 (2011) 59-64.
- [256] J. Chen, K. Li, L. Chen, R. Liu, X. Huang, D. Ye, Conversion of fructose into 5-hydroxymethylfurfural catalyzed by recyclable sulfonic acid-functionalized metal–organic frameworks, *Green Chem.*, 16 (2014) 2490-2499.



- [257] H. Yang, Q. Guo, P. Yang, X. Liu, Y. Wang, Synthesis of hierarchical Sn-Beta zeolite and its catalytic performance in glucose conversion, *Catal. Today*, 367 (2021) 117-123.
- [258] B. Torres-Olea, C. García-Sancho, J.A. Cecilia, M. Oregui-Bengoechea, P.L. Arias, R. Moreno-Tost, P. Maireles-Torres, Influence of Lewis acidity and CaCl<sub>2</sub> on the direct transformation of glucose to 5-hydroxymethylfurfural, *Mol. Catal.*, 510 (2021) 111685.
- [259] E. Nikolla, Y. Román-Leshkov, M. Moliner, M.E. Davis, "One-Pot" Synthesis of 5-(Hydroxymethyl)furfural from Carbohydrates using Tin-Beta Zeolite, *ACS Cat.*, 1 (2011) 408-410.
- [260] Y. Park, E. Yetley, Intakes and food sources of fructose in the United States, *Am. J. Clin. Nutr.*, 58 (1993) 737S-747S.
- [261] B. Kamm, Production of platform chemicals and synthesis gas from biomass, *Angew. Chem. Int. Ed.*, 46 (2007) 5056-5058.
- [262] N. Rodriguez Quiroz, A. Norton, H. Nguyen, E. Vasileiadou, D. Vlachos, Homogeneous Metal Salt Solutions for Biomass Upgrading and Other Select Organic Reactions, *ACS Catal.*, 9 (2019) 9923-9952.
- [263] L.Q. Jin, X.X. Chen, Y.T. Jin, J.K. Shentu, Z.Q. Liu, Y.G. Zheng, Immobilization of recombinant *Escherichia coli* cells expressing glucose isomerase using modified diatomite as a carrier for effective production of high fructose corn syrup in packed bed reactor, *Bioprocess. Biosyst. Eng.*, 44 (2021) 1781-1792.
- [264] Y.C. Lee, C.T. Chen, Y.T. Chiu, K.C.W. Wu, An effective Cellulose-to-Glucose-to-Fructose conversion sequence by using Enzyme immobilized Fe<sub>3</sub>O<sub>4</sub>-loaded mesoporous silica nanoparticles as recyclable biocatalysts, *ChemCatChem*, 5 (2013) 2153-2157.
- [265] D.X. Jia, L. Zhou, Y.G. Zheng, Properties of a novel thermostable glucose isomerase mined from *Thermus oshimai* and its application to preparation of high fructose corn syrup, *Enzyme Microb. Technol.*, 99 (2017) 1-8.
- [266] N. Zhang, X.G. Meng, Y.Y. Wu, H.J. Song, H. Huang, F. Wang, J. Lv, Highly selective isomerization of glucose into fructose catalyzed by a mimic glucose isomerase, *ChemCatChem*, 11 (2019) 2355-2361.

- [267] L.Q. Jin, Q. Xu, Z.Q. Liu, D.X. Jia, C.J. Liao, D.S. Chen, Y.G. Zheng, Immobilization of recombinant glucose isomerase for efficient production of high fructose corn syrup, *Appl. Biochem. Biotechnol.*, 183 (2017) 293-306.
- [268] V. Jensen, S. Rugh, Industrial-scale production and application of immobilized glucose isomerase, *Methods Enzymol.*, 136 (1987) 356-370.
- [269] Y. Tewari, Thermodynamics of industrially-important, enzyme-catalyzed reactions, *Appl. Biochem. Biotechnol.*, 23 (1990) 187-203.
- [270] R. Messing, A. Filbert, Immobilized glucose isomerase for the continuous conversion of glucose to fructose, *J. Agric. Food. Chem.*, 23 (1975) 920-923.
- [271] M. Moliner, Y. Román-Leshkov, M.E. Davis, Tin-containing zeolites are highly active catalysts for the isomerization of glucose in water, *PNAS*, 107 (2010) 6164-6168.
- [272] Y. Román-Leshkov, M. Moliner, J.A. Labinger, M.E. Davis, Mechanism of glucose isomerization using a solid Lewis acid catalyst in water, *Angew. Chem. Int. Ed.*, 49 (2010) 8954-8957.
- [273] Q. Guo, L. Ren, S. Alhassan, M. Tsapatsis, Glucose isomerization in dioxane/water with Sn- $\beta$  catalyst: improved catalyst stability and use for HMF production, *Chem. Commun.*, 55 (2019) 14942-14945.
- [274] L. Ren, Q. Guo, P. Kumar, M. Orazov, D. Xu, S. Alhassan, K. Mkhoyan, M. Davis, M. Tsapatsis, Self-Pillared, Single-Unit-Cell Sn-MFI Zeolite Nanosheets and Their Use for Glucose and Lactose Isomerization, *Angew. Chem. Int. Ed.*, 127 (2015) 10998-11001.
- [275] J. Pimenta Lorenti, E. Scolari, N. Cabral, C. Bisio, J. Gallo, Isomerization and Epimerization of Glucose Catalyzed by Sn-Containing Mesoporous Silica, *Ind. Eng. Chem. Res.*, 60 (2021) 12821-12833.
- [276] W. van der Graaff, C. Tempelman, E. Pidko, E. Hensen, Influence of pore topology on synthesis and reactivity of Sn-modified zeolite catalysts for carbohydrate conversions, *Catal. Sci. Technol.*, 7 (2017) 3151-3162.

- [277] R. Oozeerally, D.L. Burnett, T.W. Chamberlain, R.I. Walton, V. Degirmenci, Exceptionally efficient and recyclable heterogeneous metal–organic framework catalyst for glucose isomerization in water, *ChemCatChem*, 10 (2018) 706-709.
- [278] M.D. de Mello, M. Tsapatsis, Selective Glucose-to-Fructose Isomerization over Modified Zirconium UiO-66 in Alcohol Media, *ChemCatChem*, 10 (2018) 2417-2423.
- [279] G. Akiyama, R. Matsuda, H. Sato, S. Kitagawa, Catalytic glucose isomerization by porous coordination polymers with open metal sites, *Chemistry–An Asian Journal*, 9 (2014) 2772-2777.
- [280] R. Oozeerally, Exceptionally Efficient and Recyclable Heterogeneous Metal–Organic Framework Catalyst for Glucose Isomerization in Water, *ChemCatChem*, 10 (2018) 706-709.
- [281] M.D. de Mello, Selective Glucose-to-Fructose Isomerization over Modified Zirconium UiO-66 in Alcohol Media, *ChemCatChem*, 10 (2018) 2417-2423.
- [282] G. Akiyama, Catalytic glucose isomerization by porous coordination polymers with open metal sites, *Chemistry–An Asian Journal*, 9 (2014) 2772-2777.
- [283] Q. Guo, L. Ren, P. Kumar, V.J. Cybulskis, K.A. Mkhoyan, M.E. Davis, M. Tsapatsis, A Chromium Hydroxide/MIL-101 (Cr) MOF Composite Catalyst and Its Use for the Selective Isomerization of Glucose to Fructose, *Angew. Chem. Int. Ed.*, 130 (2018) 5020-5024.
- [284] R. Oozeerally, S.D.K. Ramkhelawan, D.L. Burnett, C.H.L. Tempelman, V. Degirmenci, ZIF-8 metal organic framework for the conversion of glucose to fructose and 5-hydroxymethyl furfural, *Catalysts*, 9 (2019) 812.
- [285] V. Choudhary, A. Pinar, R. Lobo, D. Vlachos, S. Sandler, Comparison of homogeneous and heterogeneous catalysts for glucose-to-fructose isomerization in aqueous media, *ChemSusChem*, 6 (2013) 2369-2376.
- [286] A. Norton, H. Nguyen, N. Xiao, D. Vlachos, Direct speciation methods to quantify catalytically active species of AlCl<sub>3</sub> in glucose isomerization, *RSC Adv.*, 8 (2018) 17101-17109.
- [287] C. Rasrendra, I. Makertihartha, S. Adisasmito, H. Heeres, Green Chemicals from d-glucose: Systematic Studies on Catalytic Effects of Inorganic Salts on the Chemo-Selectivity and Yield in Aqueous Solutions, *Top. Catal.*, 53 (2010) 1241-1247.
- [288] S. Kozuch, J. Martin, “Turning over” definitions in catalytic cycles, *ACS Catal.*, (2012).

- [289] M. Yabushita, N. Shibayama, K. Nakajima, A. Fukuoka, Selective glucose-to-fructose isomerization in ethanol catalyzed by hydrotalcites, *ACS Catal.*, 9 (2019) 2101-2109.
- [290] T. Vuorinen, E. Sjöström, Kinetics of alkali-catalyzed isomerization of D-glucose and D-fructose in ethanol-water solutions, *Carbohydr. Res.*, 108 (1982) 23-29.
- [291] K. Visuri, A. Klivanov, Enzymatic production of high fructose corn syrup (HFCS) containing 55% fructose in aqueous ethanol, *Biotechnol Bioeng.*, 30 (1987) 917-920.
- [292] T. Zhao, I. Boldog, V. Spasojevic, A. Rotaru, Y. Garcia, C. Janiak, Solvent-triggered relaxative spin state switching of [Fe (HB (pz) 3) 2] in a closed nano-confinement of NH<sub>2</sub>-MIL-101 (Al), *J. Mater. Chem. C*, 4 (2016) 6588-6601.
- [293] M. Sánchez-Sánchez, N. Getachew, K. Díaz, M. Díaz-García, Y. Chebude, I. Díaz, Synthesis of metal-organic frameworks in water at room temperature: salts as linker sources, *Green Chem.*, 17 (2015) 1500-1509.
- [294] Y. Luan, Y. Qi, H. Gao, R.S. Andriamitantsoa, N. Zheng, G. Wang, A general post-synthetic modification approach of amino-tagged metal-organic frameworks to access efficient catalysts for the Knoevenagel condensation reaction, *J. Mater. Chem. A*, 3 (2015) 17320-17331.
- [295] D.V. Patil, P.B.S. Rallapalli, G.P. Dangi, R.J. Tayade, R.S. Somani, H.C. Bajaj, MIL-53 (Al): an efficient adsorbent for the removal of nitrobenzene from aqueous solutions, *Ind. Eng. Chem. Res.*, 50 (2011) 10516-10524.
- [296] C. Li, Z. Xiong, J. Zhang, C. Wu, The strengthening role of the amino group in metal-organic framework MIL-53 (Al) for methylene blue and malachite green dye adsorption, *J. Chem. Eng. Data*, 60 (2015) 3414-3422.
- [297] R. Huang, X. Guo, S. Ma, J. Xie, J. Xu, J. Ma, Novel phosphorus-nitrogen-containing ionic liquid modified metal-organic framework as an effective flame retardant for epoxy resin, *Polymers*, 12 (2020) 108.
- [298] V.I. Isaeva, A.L. Tarasov, L.E. Starannikova, Y.P. Yampol'skii, A.Y. Alent'ev, L.M. Kustov, Microwave-assisted synthesis of mesoporous metal-organic framework NH<sub>2</sub>-MIL-101 (Al), *Russ. Chem. Bull.*, 64 (2015) 2791-2795.

- [299] B. Seoane, C. Téllez, J. Coronas, C. Staudt, NH<sub>2</sub>-MIL-53 (Al) and NH<sub>2</sub>-MIL-101 (Al) in sulfur-containing copolyimide mixed matrix membranes for gas separation, *Sep. Purif. Technol.*, 111 (2013) 72-81.
- [300] X.-X. Zheng, Z.-P. Fang, Z.-J. Dai, J.-M. Cai, L.-J. Shen, Y.-F. Zhang, C.-T. Au, L.-L. Jiang, Iron-Based Metal–Organic Frameworks as Platform for H<sub>2</sub>S Selective Conversion: Structure-Dependent Desulfurization Activity, *Inorg. Chem.*, 59 (2020) 4483-4492.
- [301] C. Volkringer, H. Leclerc, J.-C. Lavalley, T. Loiseau, G. Férey, M. Daturi, A. Vimont, Infrared spectroscopy investigation of the acid sites in the metal–organic framework aluminum trimesate MIL-100 (Al), *J. Phys. Chem. C*, 116 (2012) 5710-5719.
- [302] H. Leclerc, A. Vimont, J.-C. Lavalley, M. Daturi, A. Wiersum, P. Llwellyn, P. Horcajada, G. Férey, C. Serre, Infrared study of the influence of reducible iron (III) metal sites on the adsorption of CO, CO<sub>2</sub>, propane, propene and propyne in the mesoporous metal–organic framework MIL-100, *Phys. Chem. Chem. Phys.*, 13 (2011) 11748-11756.
- [303] Y.P. Xu, Z.Q. Wang, H.Z. Tan, K.Q. Jing, Z.N. Xu, G.C. Guo, Lewis acid sites in MOFs supports promoting the catalytic activity and selectivity for CO esterification to dimethyl carbonate, *Catal. Sci. Technol.*, 10 (2020) 1699-1707.
- [304] M.A. Hossain, K.N. Mills, A.M. Molley, M.S. Rahaman, S. Tulaphol, S.B. Lalvani, J. Dong, M.K. Sunkara, N. Sathitsuksanoh, Catalytic isomerization of dihydroxyacetone to lactic acid by heat treated zeolites, *Appl. Catal., A*, 611 (2021) 117979.
- [305] S. Roy, K. Bakhmutsky, E. Mahmoud, R.F. Lobo, R.J. Gorte, Probing Lewis Acid Sites in Sn-Beta Zeolite, *ACS Catal.*, 3 (2013) 573-580.
- [306] T. Montanari, E. Finocchio, G. Busca, Infrared Spectroscopy of Heterogeneous Catalysts: Acidity and Accessibility of Acid Sites of Faujasite-Type Solid Acids, *J. Phys. Chem. C*, 115 (2011) 937-943.
- [307] T.K. Phung, M.M. Carnasciali, E. Finocchio, G. Busca, Catalytic conversion of ethyl acetate over faujasite zeolites, *Appl. Catal., A*, 470 (2014) 72-80.
- [308] K. Góra-Marek, K. Tarach, M. Choi, 2,6-Di-tert-butylpyridine Sorption Approach to Quantify the External Acidity in Hierarchical Zeolites, *J. Phys. Chem. C*, 118 (2014) 12266-12274.

- [309] B. Chakraborty, B. Viswanathan, Surface acidity of MCM-41 by in situ IR studies of pyridine adsorption, *Catal. Today*, 49 (1999) 253-260.
- [310] G. Akiyama, R. Matsuda, H. Sato, S. Kitagawa, Catalytic Glucose Isomerization by Porous Coordination Polymers with Open Metal Sites, *Chemistry – An Asian Journal*, 9 (2014) 2772-2777.
- [311] S.J. Angyal, The composition and conformation of sugars in solution, *Angew. Chem. Int. Ed.*, 8 (1969) 157-166.
- [312] K. Visuri, Enzymatic production of high fructose corn syrup (HFCS) containing 55% fructose in aqueous ethanol, *Biotechnol. Bioeng.*, 30 (1987) 917-920.
- [313] G. Xingchu, Solid-liquid equilibria of D-glucose, D-fructose and sucrose in the mixture of ethanol and water from 273.2 K to 293.2 K, *Chin. J. Chem. Eng.*, 19 (2011) 217-222.
- [314] M. Yabushita, Selective Glucose-to-Fructose Isomerization in Ethanol Catalyzed by Hydrotalcites, *ACS Catal.*, 9 (2019) 2101-2109.
- [315] M. Timofeeva, V. Panchenko, J. Jun, Z. Hasan, M. Matrosova, S. Jung, Effects of linker substitution on catalytic properties of porous zirconium terephthalate UiO-66 in acetalization of benzaldehyde with methanol, *Appl. Catal.,A*, 471 (2014) 91-97.
- [316] F. Vermoortele, M. Vandichel, B. Van de Voorde, R. Ameloot, M. Waroquier, V. Van Speybroeck, D. De Vos, Electronic effects of linker substitution on Lewis acid catalysis with metal–organic frameworks, *Angew. Chem. Int. Ed.*, 51 (2012) 4887-4890.
- [317] J. Moreno, A. Velty, U. Díaz, A. Corma, Synthesis of 2D and 3D MOFs with tuneable Lewis acidity from preformed 1D hybrid sub-domains, *Chem. Sci.*, 10 (2019) 2053-2066.
- [318] C. Caratelli, J. Hajek, F. Cirujano, M. Waroquier, F. Xamena, V. Speybroeck, Nature of active sites on UiO-66 and beneficial influence of water in the catalysis of Fischer esterification, *J. Catal.*, 352 (2017) 401-414.
- [319] J. Hajek, M. Vandichel, B. Van de Voorde, B. Bueken, D. De Vos, M. Waroquier, V. Van Speybroeck, Mechanistic studies of aldol condensations in UiO-66 and UiO-66-NH<sub>2</sub> metal organic frameworks, *J. Catal.*, 331 (2015) 1-12.

- [320] V. Panchenko, M. Matrosova, J. Jeon, J. Jun, M. Timofeeva, S. Jhung, Catalytic behavior of metal–organic frameworks in the Knoevenagel condensation reaction, *J. Catal.*, 316 (2014) 251-259.
- [321] L. Shen, R. Liang, M. Luo, F. Jing, L. Wu, Electronic effects of ligand substitution on metal–organic framework photocatalysts: the case study of UiO-66, *Phys. Chem. Chem. Phys.*, 17 (2015) 117-121.
- [322] T. Devic, P. Horcajada, C. Serre, F. Salles, G. Maurin, B. Moulin, D. Heurtaux, G. Clet, A. Vimont, J.-M. Greneche, Functionalization in flexible porous solids: effects on the pore opening and the host– guest interactions, *JACS*, 132 (2010) 1127-1136.
- [323] W. Liang, C.J. Coghlan, F. Ragon, M. Rubio-Martinez, D.M. D'Alessandro, R. Babarao, Defect engineering of UiO-66 for CO<sub>2</sub> and H<sub>2</sub>O uptake—a combined experimental and simulation study, *Dalton Trans.*, 45 (2016) 4496-4500.
- [324] A. Schaate, Modulated synthesis of Zr-based metal–organic frameworks: from nano to single crystals, *Chemistry—A European Journal*, 17 (2011) 6643-6651.
- [325] F. Vermoortele, Synthesis modulation as a tool to increase the catalytic activity of metal–organic frameworks: the unique case of UiO-66 (Zr), *JACS*, 135 (2013) 11465-11468.
- [326] A. Dhakshinamoorthy, A. Santiago-Portillo, A.M. Asiri, H. Garcia, Engineering UiO-66 Metal Organic Framework for Heterogeneous Catalysis, *ChemCatChem*, 11 (2019) 899-923.
- [327] A. Corma, H. García, Lewis Acids: From Conventional Homogeneous to Green Homogeneous and Heterogeneous Catalysis, *Chem. Rev.*, 103 (2003) 4307-4366.
- [328] P. Vermeeren, M.D. Tiezza, M. van Dongen, I. Fernández, F. Bickelhaupt, T. Hamlin, Lewis Acid-Catalyzed Diels-Alder Reactions: Reactivity Trends across the Periodic Table, *ChemCatChem*, 27 (2021) 10610-10620.
- [329] Y. Lin, Q. Bu, J. Xu, X. Liu, X. Zhang, G.-P. Lu, B. Zhou, Hf-MOF catalyzed Meerwein–Ponndorf–Verley (MPV) reduction reaction: Insight into reaction mechanism, *Mol. Catal.*, 502 (2021) 111405.

- [330] A. Corma, M. Domine, L. Nemeth, S. Valencia, Al-free Sn-beta zeolite as a catalyst for the selective reduction of carbonyl compounds (Meerwein– Ponndorf– Verley reaction), *J. Am. Chem. Soc.*, 124 (2002) 3194-3195.
- [331] P. Tarakeshwar, J. Lee, K. Kim, Role of Lewis acid ( $\text{AlCl}_3$ )– aromatic ring interactions in Friedel– Craft's reaction: an ab InitiosStudy, *J. Phys. Chem. A*, 102 (1998) 2253-2255.
- [332] E. Hall, L. Redfern, M. Wang, K. Scheidt, Lewis acid activation of a hydrogen bond donor metal–organic framework for catalysis, *ACS Catal.*, 6 (2016) 3248-3252.
- [333] M. Rahaman, S. Tulaphol, K. Mills, A. Molley, M. Hossain, S. Lalvani, T. Maihom, M. Crocker, N. Sathitsuksanoh, Aluminum based metal-organic framework as water-tolerant Lewis acid catalyst for selective dihydroxyacetone isomerization to lactic acid, *ChemCatChem*, (2022) DOI: 10.1002/cctc.202101756.
- [334] J. Tang, X. Guo, L. Zhu, C. Hu, Mechanistic study of glucose-to-fructose isomerization in water catalyzed by  $[\text{Al}(\text{OH})_2(\text{aq})]^+$ , *ACS Catal.*, 5 (2015) 5097-5103.
- [335] A.A. Marianou, C.M. Michailof, A. Pineda, E.F. Iliopoulou, K.S. Triantafyllidis, A.A. Lappas, Glucose to Fructose Isomerization in Aqueous Media over Homogeneous and Heterogeneous Catalysts, *ChemCatChem*, 8 (2016) 1100-1110.
- [336] C.D. Malonzo, S.M. Shaker, L. Ren, S.D. Prinslow, A.E. Platero-Prats, L.C. Gallington, J. Borycz, A.B. Thompson, T.C. Wang, O.K. Farha, J.T. Hupp, C.C. Lu, K.W. Chapman, J.C. Myers, R.L. Penn, L. Gagliardi, M. Tsapatsis, A. Stein, Thermal Stabilization of Metal–Organic Framework-Derived Single-Site Catalytic Clusters through Nanocasting, *Journal of the American Chemical Society*, 138 (2016) 2739-2748.
- [337] P. Rallapalli, D. Patil, K.P. Prasanth, R.S. Somani, R.V. Jasra, H.C. Bajaj, An alternative activation method for the enhancement of methane storage capacity of nanoporous aluminium terephthalate, MIL-53 (Al), *J. Porous Mater.*, 17 (2010) 523-528.
- [338] M. Dusselier, P. Van Wouwe, A. Dewaele, E. Makshina, B.F. Sels, Lactic acid as a platform chemical in the biobased economy: the role of chemocatalysis, *Energy & Environmental Science*, 6 (2013) 1415-1442.



- [339] P. Ponchai, K. Adpakpang, S. Thongratkaew, K. Chaipojjana, S. Wannapaiboon, S. Siwaipram, K. Faungnawakij, S. Bureekaew, Engineering zirconium-based UiO-66 for effective chemical conversion of d-xylose to lactic acid in aqueous condition, *Chem. Commun.*, 56 (2020) 8019-8022.
- [340] S. Kiatphuengporn, A. Junkaew, C. Luadthong, S. Thongratkaew, C. Yimsukanan, S. Songtawee, T. Butburee, P. Khemthong, S. Namuangruk, M. Kunaseth, Roles of acidic sites in alumina catalysts for efficient d-xylose conversion to lactic acid, *Green Chem.*, 22 (2020) 8572-8583.
- [341] L. Yang, J. Su, S. Carl, J.G. Lynam, X. Yang, H. Lin, Catalytic conversion of hemicellulosic biomass to lactic acid in pH neutral aqueous phase media, *Appl. Catal., B*, 162 (2015) 149-157.
- [342] Y. Zhang, H. Luo, L. Kong, X. Zhao, G. Miao, L. Zhu, S. Li, Y. Sun, Highly efficient production of lactic acid from xylose using Sn-beta catalysts, *Green Chem.*, 22 (2020) 7333-7336.
- [343] C. Kosri, S. Kiatphuengporn, T. Butburee, S. Youngjun, S. Thongratkaew, K. Faungnawakij, C. Yimsukanan, N. Chanlek, P. Kidkhunthod, J. Wittayakun, Selective conversion of xylose to lactic acid over metal-based Lewis acid supported on  $\gamma$ -Al<sub>2</sub>O<sub>3</sub> catalysts, *Catal. Today*, 367 (2021) 205-212.
- [344] M. Morales, P.Y. Dapsens, I. Giovinazzo, J. Witte, C. Mondelli, S. Papadokonstantakis, K. Hungerbühler, J. Pérez-Ramírez, Environmental and economic assessment of lactic acid production from glycerol using cascade bio-and chemocatalysis, *Energy Environ. Sci.*, 8 (2015) 558-567.
- [345] P.Y. Dapsens, B.T. Kusema, C. Mondelli, J. Pérez-Ramírez, Gallium-modified zeolites for the selective conversion of bio-based dihydroxyacetone into C<sub>1</sub>–C<sub>4</sub> alkyl lactates, *J. Mol. Catal. A: Chem.*, 388 (2014) 141-147.
- [346] C.B. Rasrendra, B.A. Fachri, I.G.B.N. Makertihartha, S. Adisasmito, H.J. Heeres, Catalytic conversion of dihydroxyacetone to lactic acid using metal salts in water, *ChemSusChem*, 4 (2011) 768-777.

- [347] M. Xia, W. Dong, M. Gu, C. Chang, Z. Shen, Y. Zhang, Synergetic effects of bimetallics in modified beta zeolite for lactic acid synthesis from biomass-derived carbohydrates, *RSC Adv.*, 8 (2018) 8965-8975.
- [348] E. Jolimaitre, D. Delcroix, N. Essayem, C. Pinel, M. Besson, Dihydroxyacetone conversion into lactic acid in an aqueous medium in the presence of metal salts: influence of the ionic thermodynamic equilibrium on the reaction performance, *Catal. Sci. Technol.*, 8 (2018) 1349-1356.
- [349] Y. Sun, L. Shi, H. Wang, G. Miao, L. Kong, S. Li, Y. Sun, Efficient production of lactic acid from sugars over Sn-Beta zeolite in water: catalytic performance and mechanistic insights, *Sustainable Energy Fuels*, 3 (2019) 1163-1171.
- [350] L. Kong, Z. Shen, W. Zhang, M. Xia, M. Gu, X. Zhou, Y. Zhang, Conversion of sucrose into lactic acid over functionalized sn-beta zeolite catalyst by 3-Aminopropyltrimethoxysilane, *ACS omega*, 3 (2018) 17430-17438.
- [351] P.Y. Dapsens, C. Mondelli, J. Pérez-Ramírez, Highly selective Lewis acid sites in desilicated MFI zeolites for dihydroxyacetone isomerization to lactic acid, *ChemSusChem*, 6 (2013) 831-839.
- [352] M.K. Wardani, G.T. Kadja, A.T. Fajar, I. Makertihartha, M.L. Gunawan, V. Suendo, R.R. Mukti, Highly crystalline mesoporous SSZ-13 zeolite obtained via controlled post-synthetic treatment, *RSC Adv.*, 9 (2019) 77-86.
- [353] M. Gackowski, K. Tarach, J. Podobiński, S. Jarczewski, P. Kuśtrowski, J. Datka, Hierarchical zeolites Y obtained by desilication: Porosity, acidity and catalytic properties, *Microporous Mesoporous Mater.*, 263 (2018) 282-288.
- [354] S. Horike, D. Umeyama, S. Kitagawa, Ion conductivity and transport by porous coordination polymers and metal-organic frameworks, *Acc. Chem. Res.*, 46 (2013) 2376-2384.
- [355] H.B. Wu, X.W.D. Lou, Metal-organic frameworks and their derived materials for electrochemical energy storage and conversion: Promises and challenges, *Sci. Adv.*, 3 (2017) eaap9252.

- [356] K. Sumida, D.L. Rogow, J.A. Mason, T.M. McDonald, E.D. Bloch, Z.R. Herm, T. Bae, J.R. Long, Carbon dioxide capture in metal–organic frameworks, *Chem. Rev.*, 112 (2012) 724-781.
- [357] I.A. Lazaro, R.S. Forgan, Application of zirconium MOFs in drug delivery and biomedicine, *Coord. Chem. Rev.*, 380 (2019) 230-259.
- [358] H. Furukawa, F. Gandara, Y. Zhang, J. Jiang, W.L. Queen, M.R. Hudson, O.M. Yaghi, Water adsorption in porous metal–organic frameworks and related materials, *J. Am. Chem. Soc.*, 136 (2014) 4369-4381.
- [359] J. Canivet, A. Fateeva, Y. Guo, B. Coasne, D. Farrusseng, Water adsorption in MOFs: fundamentals and applications, *Chem. Soc. Rev.*, 43 (2014) 5594-5617.
- [360] N.C. Burtch, H. Jasuja, K.S. Walton, Water stability and adsorption in metal–organic frameworks, *Chem. Rev.*, 114 (2014) 10575-10612.
- [361] M. Ding, X. Cai, H. Jiang, Improving MOF stability: approaches and applications, *Chem. Sci.*, 10 (2019) 10209-10230.
- [362] M. Ding, H. Jiang, Improving water stability of metal–organic frameworks by a general surface hydrophobic polymerization, *CCS Chem.*, 3 (2021) 2740-2748.
- [363] S. Yuan, L. Feng, K. Wang, J. Pang, M. Bosch, C. Lollar, Y. Sun, J. Qin, X. Yang, P. Zhang, Stable metal–organic frameworks: design, synthesis, and applications, *Adv. Mater.*, 30 (2018) 1704303.
- [364] J.E. Samad, J. Blanchard, C. Sayag, C. Louis, J.R. Regalbutto, The controlled synthesis of metal-acid bifunctional catalysts: Selective Pt deposition and nanoparticle synthesis on amorphous aluminosilicates, *J. Catal.*, 342 (2016) 213-225.
- [365] J. Jiang, O. Yaghi, Brønsted acidity in metal–organic frameworks, *Chem. Rev.*, 115 (2015) 6966-6997.
- [366] S. Yamaguchi, M. Yabushita, M. Kim, J. Hirayama, K. Motokura, A. Fukuoka, K. Nakajima, Catalytic Conversion of Biomass-Derived Carbohydrates to Methyl Lactate by Acid–Base Bifunctional  $\gamma$ -Al<sub>2</sub>O<sub>3</sub>, *ACS Sustainable Chem. Eng.*, 6 (2018) 8113-8117.

- [367] G.R. Jenness, M.A. Christiansen, S. Caratzoulas, D.G. Vlachos, R.J. Gorte, Site-dependent Lewis acidity of  $\gamma$ -Al<sub>2</sub>O<sub>3</sub> and its impact on ethanol dehydration and etherification, *The Journal of Physical Chemistry C*, 118 (2014) 12899-12907.
- [368] T.K. Phung, C. Herrera, M.Á. Larrubia, M. García-Diéguez, E. Finocchio, L.J. Alemany, G. Busca, Surface and catalytic properties of some  $\gamma$ -Al<sub>2</sub>O<sub>3</sub> powders, *Appl. Catal., A*, 483 (2014) 41-51.
- [369] A. Takagaki, J.C. Jung, S. Hayashi, Solid Lewis acidity of boehmite  $\gamma$ -AlO (OH) and its catalytic activity for transformation of sugars in water, *RSC Adv.*, 4 (2014) 43785-43791.
- [370] R.M. West, M.S. Holm, S. Saravanamurugan, J. Xiong, Z. Beversdorf, E. Taarning, C.H. Christensen, Zeolite H-USY for the production of lactic acid and methyl lactate from C<sub>3</sub>-sugars, *J. Catal.*, 269 (2010) 122-130.
- [371] A. Feliczak-Guzik, M. Sprynskyy, I. Nowak, B. Buszewski, Catalytic isomerization of dihydroxyacetone to lactic acid and alkyl lactates over hierarchical zeolites containing tin, *Catalysts*, 8 (2018) 31.
- [372] X. Wang, F. Liang, C. Huang, Y. Li, B. Chen, Siliceous tin phosphates as effective bifunctional catalysts for selective conversion of dihydroxyacetone to lactic acid, *Catal. Sci. Technol.*, 6 (2016) 6551-6560.
- [373] S. Kobayashi, Water-stable rare-earth Lewis-acid catalysis in aqueous and organic solvents, *Organic synthesis in water*, Springer1998, pp. 262-305.
- [374] T. Ollevier, Bismuth-mediated organic reactions, Springer Science & Business Media2012.
- [375] E. Taarning, S. Saravanamurugan, M.S. Holm, J. Xiong, R.M. West, C.H. Christensen, Zeolite-catalyzed isomerization of triose sugars, *Conversion of Oxygenates over Zeolite Catalysts: Structure-Activity Relations*, (2009) 90.
- [376] M.W. Logan, S. Langevin, Z. Xia, Reversible atmospheric water harvesting using metal-organic frameworks, *Sci. Rep.*, 10 (2020) 1-11.
- [377] N. Hanikel, M.S. Prévot, F. Fathieh, E.A. Kapustin, H. Lyu, H. Wang, N.J. Diercks, T.G. Glover, O.M. Yaghi, Rapid cycling and exceptional yield in a metal-organic framework water harvester, *ACS Cent. Sci.*, 5 (2019) 1699-1706.

- [378] K. Tan, N. Nijem, Y. Gao, S. Zuluaga, J. Li, T. Thonhauser, Y.J. Chabal, Water interactions in metal organic frameworks, *CrystEngComm*, 17 (2015) 247-260.
- [379] N. ul Qadir, S.A.M. Said, H.M. Bahaidarah, Structural stability of metal organic frameworks in aqueous media—controlling factors and methods to improve hydrostability and hydrothermal cyclic stability, *Microporous Mesoporous Mater.*, 201 (2015) 61-90.
- [380] T. Wu, L. Shen, M. Luebbers, C. Hu, Q. Chen, Z. Ni, R.I. Masel, Enhancing the stability of metal–organic frameworks in humid air by incorporating water repellent functional groups, *Chem. Commun.*, 46 (2010) 6120-6122.
- [381] M. Bosch, M. Zhang, H. Zhou, Increasing the stability of metal-organic frameworks, *Adv. Chem.*, 2014 (2014) 1155.
- [382] E. Mangano, J. Kahr, P.A. Wright, S. Brandani, Accelerated degradation of MOFs under flue gas conditions, *Faraday Discuss.*, 192 (2016) 181-195.
- [383] Y. Ming, N. Kumar, D.J. Siegel, Water adsorption and insertion in MOF-5, *ACS omega*, 2 (2017) 4921-4928.
- [384] H. Li, W. Shi, K. Zhao, H. Li, Y. Bing, P. Cheng, Enhanced hydrostability in Ni-doped MOF-5, *Inorg. Chem.*, 51 (2012) 9200-9207.
- [385] J.G. Nguyen, S.M. Cohen, Moisture-resistant and superhydrophobic metal– organic frameworks obtained via postsynthetic modification, *J. Am. Chem. Soc.*, 132 (2010) 4560-4561.
- [386] Y. Sun, L. Shi, H. Wang, G. Miao, L. Kong, S. Li, Y. Sun, Efficient production of lactic acid from sugars over Sn-Beta zeolite in water: catalytic performance and mechanistic insights, *Sustainable Energy & Fuels*, 3 (2019) 1163-1171.
- [387] W. Dong, Z. Shen, B. Peng, M. Gu, X. Zhou, B. Xiang, Y. Zhang, Selective chemical conversion of sugars in aqueous solutions without alkali to lactic acid over a Zn-Sn-Beta Lewis acid-base catalyst, *Sci. Rep.*, 6 (2016) 1-8.
- [388] Y. Liu, Y. Xiao, C. Xia, X. Yi, Y. Zhao, J. Yuan, K. Huang, B. Zhu, A. Zheng, M. Lin, Insight into the effects of acid characteristics on the catalytic performance of Sn-MFI zeolites in the transformation of dihydroxyacetone to methyl lactate, *J. Catal.*, 391 (2020) 386-396.

- [389] K. Kim, Z. Wang, Y. Jiang, M. Hunger, J. Huang, The cooperative effect of Lewis and Brønsted acid sites on Sn-MCM-41 catalysts for the conversion of 1, 3-dihydroxyacetone to ethyl lactate, *Green Chem.*, 21 (2019) 3383-3393.
- [390] K. Santos, E. Albuquerque, G. Innocenti, L. Borges, C. Sievers, M. Fraga, The role of Brønsted and water-tolerant Lewis acid sites in the cascade aqueous-phase reaction of triose to lactic acid, *ChemCatChem*, 11 (2019) 3054-3063.
- [391] C. Rasrendra, B. Fachri, I. Makertihartha, S. Adisasmito, H. Heeres, Catalytic conversion of dihydroxyacetone to lactic acid using metal salts in water, *ChemSusChem*, 4 (2011) 768-777.
- [392] Y. Hayashi, Y. Sasaki, Tin-catalyzed conversion of trioses to alkyl lactates in alcohol solution, *Chem. Commun.*, (2005) 2716-2718.
- [393] S. Saravanamurugan, M. Paniagua, J.A. Melero, A. Riisager, Efficient isomerization of glucose to fructose over zeolites in consecutive reactions in alcohol and aqueous media, *JACS*, 135 (2013) 5246-5249.
- [394] A.H. Valekar, M. Lee, J.W. Yoon, J. Kwak, D. Hong, K. Oh, G. Cha, Y. Kwon, J. Jung, J. Chang, Catalytic transfer hydrogenation of furfural to furfuryl alcohol under mild conditions over Zr-MOFs: Exploring the role of metal node coordination and modification, *ACS Catal.*, 10 (2020) 3720-3732.
- [395] M.S. Rahaman, T.K. Phung, M.A. Hossain, E. Chowdhury, S. Tulaphol, S.B. Lalvani, M. O'Toole, G.A. Willing, J.B. Jasinski, M. Crocker, Hydrophobic functionalization of HY zeolites for efficient conversion of glycerol to solketal, *Appl. Catal., A*, 592 (2020) 117369.
- [396] S. Tulaphol, M.A. Hossain, M.S. Rahaman, L. Liu, T.K. Phung, S. Renneckar, N. Gridanurak, N. Sathitsuksanoh, Direct Production of Levulinic Acid in One Pot from Hemp Hurd by Dilute Acid in Ionic Liquids, *Energy & Fuels*, 34 (2019) 1764-1772.
- [397] Y. Xu, Z. Wang, H. Tan, K. Jing, Z. Xu, G. Guo, Lewis acid sites in MOFs supports promoting the catalytic activity and selectivity for CO esterification to dimethyl carbonate, *Catal. Sci. Technol.*, (2020).
- [398] M.S. Rahaman, S. Tulaphol, M.A. Hossain, C.N. Evrard, L.M. Thompson, N. Sathitsuksanoh, Kinetics of phosphotungstic acid-catalyzed condensation of levulinic acid with

phenol to diphenolic acid: Temperature-controlled regioselectivity, *Mol. Catal.*, 514 (2021) 111848.

[399] L. Briand, J.-M. Jehng, L. Cornaglia, A. Hirt, I. Wachs, Quantitative determination of the number of surface active sites and the turnover frequency for methanol oxidation over bulk metal vanadates, *Catal Today*, 78 (2003) 257-268.

[400] M. Boudart, Turnover rates in heterogeneous catalysis, *Chem. Rev.*, 95 (1995) 661-666.

[401] D.J. Cole-Hamilton, R.P. Tooze, *Catalyst separation, recovery and recycling: chemistry and process design*, Springer Science & Business Media 2006.

[402] Á. Molnár, A. Papp, Catalyst recycling—A survey of recent progress and current status, *Coord. Chem. Rev.*, 349 (2017) 1-65.

[403] G. Innocenti, E. Papadopoulos, G. Fornasari, F. Cavani, A.J. Medford, C. Sievers, Continuous Liquid-Phase Upgrading of Dihydroxyacetone to Lactic Acid over Metal Phosphate Catalysts, *ACS Catal.*, 10 (2020) 11936-11950.

[404] A. Takagaki, H. Goto, R. Kikuchi, S.T. Oyama, Silica-supported chromia-titania catalysts for selective formation of lactic acid from a triose in water, *Appl. Catal., A*, 570 (2019) 200-208.

[405] S. Lux, M. Siebenhofer, Synthesis of lactic acid from dihydroxyacetone: use of alkaline-earth metal hydroxides, *Catal. Sci. Technol.*, 3 (2013) 1380-1385.

[406] L. Lomba, B. Giner, I. Bandrés, C. Lafuente, M.R. Pino, Physicochemical properties of green solvents derived from biomass, *Green chem.*, 13 (2011) 2062-2070.

[407] P.D. Bloom, Levulinic acid ester derivatives as reactive plasticizers and coalescent solvents, Google Patents, 2010.

[408] S. Cousinet, A. Ghadban, I. Allaoua, F. Lortie, D. Portinha, E. Drockenmuller, J.P. Pascault, Biobased vinyl levulinate as styrene replacement for unsaturated polyester resins, *J. Polym. Sci., Part A: Polym. Chem.*, 52 (2014) 3356-3364.

[409] X. Liu, W. Yang, Q. Zhang, C. Li, H. Wu, Current approaches to alkyl levulinates via efficient valorization of biomass derivatives, *Front. Chem.*, (2020) 794.

[410] A. Mukherjee, M.J. Dumont, V. Raghavan, Sustainable production of hydroxymethylfurfural and levulinic acid: Challenges and opportunities, *Biomass Bioenerg.*, 72 (2015) 143-183.

- [411] A. Démolis, N. Essayem, F. Rataboul, Synthesis and applications of alkyl levulinates, *ACS Sustainable Chem. Eng.*, 2 (2014) 1338-1352.
- [412] L. Yan, Q. Yao, Y. Fu, Conversion of levulinic acid and alkyl levulinates into biofuels and high-value chemicals, *Green Chem.*, 19 (2017) 5527-5547.
- [413] A. Schaate, P. Roy, A. Godt, J. Lippke, F. Waltz, M. Wiebcke, P. Behrens, Modulated synthesis of Zr-based metal–organic frameworks: from nano to single crystals, *Chem. Eur. J.*, 17 (2011) 6643-6651.
- [414] F. Vermoortele, B. Bueken, G. Le Bars, B. Van de Voorde, M. Vandichel, K. Houthoofd, A. Vimont, M. Daturi, M. Waroquier, V. Van Speybroeck, Synthesis modulation as a tool to increase the catalytic activity of metal–organic frameworks: the unique case of UiO-66 (Zr), *JACS*, 135 (2013) 11465-11468.
- [415] C. Atzori, G.C. Shearer, L. Maschio, B. Civalleri, F. Bonino, C. Lamberti, S. Svelle, K.P. Lillerud, S. Bordiga, Effect of benzoic acid as a modulator in the structure of UiO-66: an experimental and computational study, *J. Phys. Chem. C*, 121 (2017) 9312-9324.
- [416] W. Morris, S. Wang, D. Cho, E. Auyeung, P. Li, O.K. Farha, C.A. Mirkin, Role of modulators in controlling the colloidal stability and polydispersity of the UiO-66 metal–organic framework, *ACS Appl. Mater. Interfaces*, 9 (2017) 33413-33418.
- [417] X. Zheng, Z. Fang, Z. Dai, J. Cai, L. Shen, Y. Zhang, C. Au, L. Jiang, Iron-Based Metal–Organic Frameworks as Platform for H<sub>2</sub>S Selective Conversion: Structure-Dependent Desulfurization Activity, *Inorg. Chem.*, 59 (2020) 4483-4492.
- [418] C. Volkringer, H. Leclerc, J. Lavalley, T. Loiseau, G. Ferey, M. Daturi, A. Vimont, Infrared spectroscopy investigation of the acid sites in the metal–organic framework aluminum trimesate MIL-100 (Al), *The Journal of Physical Chemistry C*, 116 (2012) 5710-5719.
- [419] F. Wang, Z. Chen, H. Chen, T.A. Goetjen, P. Li, X. Wang, S. Alayoglu, K. Ma, Y. Chen, T. Wang, Interplay of Lewis and Brønsted acid sites in Zr-based metal–organic frameworks for efficient esterification of biomass-derived levulinic acid, *ACS Appl. Mater. Interfaces*, 11 (2019) 32090-32096.



- [420] Y. Xu, Z. Wang, H. Tan, K. Jing, Z. Xu, G. Guo, Lewis acid sites in MOFs supports promoting the catalytic activity and selectivity for CO esterification to dimethyl carbonate, *Catal. Sci. Technol.*, 10 (2020) 1699-1707.
- [421] J. Guarinos, F. Cirujano, A. Rapeyko, F. Llabrés i Xamena, Conversion of levulinic acid to  $\gamma$ -valerolactone over Zr-containing metal-organic frameworks: Evidencing the role of Lewis and Brønsted acid sites, *Mol. Catal.*, 515 (2021) 111925.
- [422] F. Cirujano, F. Llabrés i Xamena, Tuning the Catalytic Properties of UiO-66 Metal–Organic Frameworks: From Lewis to Defect-Induced Brønsted Acidity, *J. Phys. Chem. Lett.*, 11 (2020) 4879-4890.
- [423] R. Wu, X. Qian, K. Zhou, H. Liu, B. Yadian, J. Wei, H. Zhu, Y. Huang, Highly dispersed Au nanoparticles immobilized on Zr-based metal–organic frameworks as heterostructured catalyst for CO oxidation, *J. Mater. Chem. A*, 1 (2013) 14294-14299.
- [424] B. Mirhosseini-Eshkevari, M. Esnaashari, M.A. Ghasemzadeh, Novel Brønsted Acidic Ionic Liquids Confined in UiO-66 Nanocages for the Synthesis of Dihydropyrido [2, 3-d] Pyrimidine Derivatives under Solvent-Free Conditions, *ACS omega*, 4 (2019) 10548-10557.
- [425] V.V. Butova, A.P. Budnyk, A.A. Guda, K.A. Lomachenko, A.L. Bugaev, A.V. Soldatov, S.M. Chavan, S. Øien-Ødegaard, U. Olsbye, K.P. Lillerud, Modulator Effect in UiO-66-NDC (1, 4-Naphthalenedicarboxylic Acid) Synthesis and Comparison with UiO-67-NDC Isoreticular Metal–Organic Frameworks, *Cryst. Growth Des.*, 17 (2017) 5422-5431.
- [426] P. Piszczek, A. Radtke, A. Grodzicki, A. Wojtczak, J. Chojnacki, The new type of  $[Zr_6(\mu_3-O)_4(\mu_3-OH)_4]$  cluster core: Crystal structure and spectral characterization of  $[Zr_6O_4(OH)_4(OOCR)_{12}]$ (R= But, C(CH<sub>3</sub>)<sub>2</sub>Et), *Polyhedron*, 26 (2007) 679-685.
- [427] Y. Jiao, Y. Liu, G. Zhu, J.T. Hungerford, S. Bhattacharyya, R.P. Lively, D.S. Sholl, K.S. Walton, Heat-treatment of defective UiO-66 from modulated synthesis: Adsorption and stability studies, *J. Phys. Chem. C*, 121 (2017) 23471-23479.
- [428] J.H. Cavka, S. Jakobsen, U. Olsbye, N. Guillou, C. Lamberti, S. Bordiga, K.P. Lillerud, A new zirconium inorganic building brick forming metal organic frameworks with exceptional stability, *J. Am. Chem. Soc.*, 130 (2008) 13850-13851.

- [429] R.G. Faria, D. Julião, S.S. Balula, L. Cunha-Silva, Hf-Based UiO-66 as Adsorptive Compound and Oxidative Catalyst for Denitrogenation Processes, *Compounds*, 1 (2021) 3-14.
- [430] X. Zhang, P. Huang, A. Liu, M. Zhu, A metal–organic framework for oxidative desulfurization: UiO-66 (Zr) as a catalyst, *Fuel*, 209 (2017) 417-423.
- [431] M. Qiu, T. Guo, R. Xi, D. Li, X. Qi, Highly efficient catalytic transfer hydrogenation of biomass-derived furfural to furfuryl alcohol using UiO-66 without metal catalysts, *Appl. Catal., A*, 602 (2020) 117719.
- [432] X. Cai, J. Pan, G. Tu, Y. Fu, F. Zhang, W. Zhu, Pd/UiO-66 (Hf): A highly efficient heterogeneous catalyst for the hydrogenation of 2, 3, 5-trimethylbenzoquinone, *Catal. Commun.*, 113 (2018) 23-26.
- [433] G.C. Shearer, S.M. Chavan, J. Ethiraj, J.G. Vitillo, S. Svelle, U. Olsbye, C. Lamberti, S. Bordiga, K.P. Lillerud, Tuned to perfection: ironing out the defects in metal–organic framework UiO-66, *Chem. Mater.*, 26 (2014) 4068-4071.
- [434] H. Jiang, Q. Gao, S. Wang, Y. Chen, M. Zhang, The synergistic effect of Pd NPs and UiO-66 for enhanced activity of carbon dioxide methanation, *J. CO<sub>2</sub> Util.*, 31 (2019) 167-172.
- [435] W. Xu, M. Dong, L. Di, X. Zhang, A facile method for preparing UiO-66 encapsulated Ru catalyst and its application in plasma-assisted CO<sub>2</sub> methanation, *Nanomaterials*, 9 (2019) 1432.
- [436] L. Valenzano, B. Civaleri, S. Chavan, S. Bordiga, M. Nilsen, S. Jakobsen, K. Lillerud, C. Lamberti, Disclosing the complex structure of UiO-66 metal organic framework: a synergic combination of experiment and theory, *Chem. Mater.*, 23 (2011) 1700-1718.
- [437] D. Song, S. An, B. Lu, Y. Guo, J. Leng, Arylsulfonic acid functionalized hollow mesoporous carbon spheres for efficient conversion of levulinic acid or furfuryl alcohol to ethyl levulinate, *Appl. Catal. B.*, 179 (2015) 445-457.
- [438] D. Song, S. An, Y. Sun, Y. Guo, Efficient conversion of levulinic acid or furfuryl alcohol into alkyl levulinates catalyzed by heteropoly acid and ZrO<sub>2</sub> bifunctionalized organosilica nanotubes, *J. Catal.*, 333 (2016) 184-199.

- [439] R. Wei, C.A. Gaggioli, G. Li, T. Islamoglu, Z. Zhang, P. Yu, O.K. Farha, C.J. Cramer, L. Gagliardi, D. Yang, Tuning the properties of Zr<sub>6</sub>O<sub>8</sub> nodes in the metal organic framework UiO-66 by selection of node-bound ligands and linkers, *Chem. Mater.*, 31 (2019) 1655-1663.
- [440] S. Dharne, V.V. Bokade, Esterification of levulinic acid to n-butyl levulinate over heteropolyacid supported on acid-treated clay, *J. Nat. Gas Chem.*, 20 (2011) 18-24.
- [441] F.G. Cirujano, F.X. Llabrés i Xamena, Tuning the Catalytic Properties of UiO-66 Metal–Organic Frameworks: From Lewis to Defect-Induced Brønsted Acidity, *J. Phys. Chem. Lett.*, 11 (2020) 4879-4890.
- [442] R.C. Klet, Y. Liu, T.C. Wang, J.T. Hupp, O.K. Farha, Evaluation of Brønsted acidity and proton topology in Zr-and Hf-based metal–organic frameworks using potentiometric acid–base titration, *J. Mater. Chem. A*, 4 (2016) 1479-1485.
- [443] M. Rahaman, S. Tulaphol, M. Hossain, J. Jasinski, N. Sun, A. George, B. Simmons, T. Maihom, M. Crocker, N. Sathitsuksanoh, Cooperative Brønsted-Lewis acid sites created by phosphotungstic acid encapsulated metal–organic frameworks for selective glucose conversion to 5-hydroxymethylfurfural, *Fuel*, 310 (2022) 122459.
- [444] M. Rahaman, T. Phung, M.A. Hossain, E. Chowdhury, S. Tulaphol, S. Lalvani, M. O'Toole, G. Willing, J. Jasinski, M. Crocker, N. Sathitsuksanoh, Hydrophobic functionalization of HY zeolites for efficient conversion of glycerol to solketal, *Appl. Catal., A*, (2020) 117369.
- [445] M. Hossain, K. Mills, A. Molley, M. Rahaman, S. Tulaphol, S. Lalvani, J. Dong, M. Sunkara, N. Sathitsuksanoh, Catalytic isomerization of dihydroxyacetone to lactic acid by heat treated zeolites, *Appl. Catal. A.*, 611 (2021) 117979.
- [446] S. Tulaphol, M.A. Hossain, M. Rahaman, L.-Y. Liu, T. Phung, S. Rennekar, N. Gridanurak, N. Sathitsuksanoh, Direct Production of Levulinic Acid in One Pot from Hemp Hurd by Dilute Acid in Ionic Liquids, *Energy Fuels*, 32 (2019) 1764-1772.
- [447] H.K. Sharma, C. Xu, W. Qin, Biological pretreatment of lignocellulosic biomass for biofuels and bioproducts: an overview, *Waste and Biomass Valorization*, 10 (2019) 235-251.
- [448] D.R. Cohn, L. Bromberg, J.B. Heywood, Direct Injection Ethanol Boosted Gasoline Engines: Biofuel Leveraging For Cost Effective Reduction of Oil Dependence and CO<sub>2</sub>Emissions, (2006).

- [449] A. Galletti, C. Antonetti, V. De Luise, M. Martinelli, A sustainable process for the production of  $\gamma$ -valerolactone by hydrogenation of biomass-derived levulinic acid, *Green Chem.*, 14 (2012) 688-694.
- [450] R. Alamillo, M.G. Tucker, M. Chia, Y. Pagán-Torres, J. Dumesic, The selective hydrogenation of biomass-derived 5-hydroxymethylfurfural using heterogeneous catalysts, *Green Chem.*, 14 (2012) 1413-1419.
- [451] H. Xia, C. Chen, P. Liu, M. Zhou, J. Jiang, Selective hydrogenation of furfural for high-value chemicals: effect of catalysts and temperature, *Sustain. Energy Fuels*, 4 (2020) 5709-5720.
- [452] M.J. Ahmed, B.H. Hameed, Hydrogenation of glucose and fructose into hexitols over heterogeneous catalysts: A review, *J. Taiwan Inst. Chem. Eng.*, 96 (2019) 341-352.
- [453] S. Li, X. Wang, X. Liu, G. Xu, S. Han, X. Mu, Aqueous-phase hydrogenation of biomass-derived itaconic acid to methyl- $\gamma$ -butyrolactone over Pd/C catalysts: Effect of pretreatments of active carbon, *Catal. Commun.*, 61 (2015) 92-96.
- [454] Z. Yan, L. Lin, S. Liu, Synthesis of  $\gamma$ -valerolactone by hydrogenation of biomass-derived levulinic acid over Ru/C catalyst, *Energy Fuels*, 23 (2009) 3853-3858.
- [455] B.M. Matsagar, C.Y. Hsu, S.S. Chen, T. Ahamad, S.M. Alshehri, D.C.W. Tsang, K.C.W. Wu, Selective hydrogenation of furfural to tetrahydrofurfuryl alcohol over a Rh-loaded carbon catalyst in aqueous solution under mild conditions, *Sustain. Energy Fuels*, 4 (2020) 293-301.
- [456] Y. Nakagawa, K. Tomishige, Total hydrogenation of furan derivatives over silica-supported Ni-Pd alloy catalyst, *Catal. Commun.*, 12 (2010) 154-156.
- [457] J. Ohyama, A. Esaki, Y. Yamamoto, S. Arai, A. Satsuma, Selective hydrogenation of 2-hydroxymethyl-5-furfural to 2, 5-bis (hydroxymethyl) furan over gold sub-nano clusters, *RSC Adv.*, 3 (2013) 1033-1036.
- [458] K. Hengst, D.M. Ligthart, D.E. Doronkin, K.M. Walter, W. Kleist, E.J.M. Hensen, J. Grunwaldt, Continuous synthesis of  $\gamma$ -valerolactone in a trickle-bed reactor over supported nickel catalysts, *Ind. Eng. Chem. Res.*, 56 (2017) 2680-2689.
- [459] I. Obregón, E. Corro, U. Izquierdo, J. Requies, P.L. Arias, Levulinic acid hydrogenolysis on Al<sub>2</sub>O<sub>3</sub>-based Ni-Cu bimetallic catalysts, *Chin. J. Catal.*, 35 (2014) 656-662.

- [460] J.Y. Yeh, B.M. Matsagar, S.S. Chen, H.L. Sung, D.C.W. Tsang, Y.P. Li, K.C.W. Wu, Synergistic effects of Pt-embedded, MIL-53-derived catalysts (Pt@ Al<sub>2</sub>O<sub>3</sub>) and NaBH<sub>4</sub> for water-mediated hydrogenolysis of biomass-derived furfural to 1, 5-pentanediol at near-ambient temperature, *J. Catal.*, 390 (2020) 46-56.
- [461] M. Balakrishnan, E.R. Sacia, A.T. Bell, Etherification and reductive etherification of 5-(hydroxymethyl) furfural: 5-(alkoxymethyl) furfurals and 2, 5-bis (alkoxymethyl) furans as potential bio-diesel candidates, *Green Chem.*, 14 (2012) 1626-1634.
- [462] H. Cai, C. Li, A. Wang, T. Zhang, Biomass into chemicals: One-pot production of furan-based diols from carbohydrates via tandem reactions, *Catal. Today*, 234 (2014) 59-65.
- [463] W. Jin, L. Pastor-Pérez, J. Yu, J. Odriozola, S. Gu, T. Reina, Cost-effective routes for catalytic biomass upgrading, *Curr. Opin. Green Sustain. Chem.*, 23 (2020) 1-9.
- [464] P. Panagiotopoulou, D. Vlachos, Liquid phase catalytic transfer hydrogenation of furfural over a Ru/C catalyst, *Appl. Catal. A.*, 480 (2014) 17-24.
- [465] P. Panagiotopoulou, N. Martin, D.G. Vlachos, Effect of hydrogen donor on liquid phase catalytic transfer hydrogenation of furfural over a Ru/RuO<sub>2</sub>/C catalyst, *J. Mol. Catal. A: Chem.*, 392 (2014) 223-228.
- [466] A. Corma, M.E. Domine, L. Nemeth, S. Valencia, Al-Free Sn-Beta Zeolite as a Catalyst for the Selective Reduction of Carbonyl Compounds (Meerwein-Ponndorf-Verley Reaction), *J. Am. Chem. Soc.*, 124 (2002) 3194-3195.
- [467] R. Johnstone, A. Wilby, I. Entwistle, Heterogeneous catalytic transfer hydrogenation and its relation to other methods for reduction of organic compounds, *Chem. Rev.*, 85 (1985) 129-170.
- [468] R. Assary, L. Curtiss, J. Dumesic, Exploring Meerwein-Ponndorf-Verley reduction chemistry for biomass catalysis using a first-principles approach, *ACS Catal.*, 3 (2013) 2694-2704.
- [469] Y. Injongkol, T. Maihom, P. Treesukul, J. Sirijaraensre, B. Boekfa, J. Limtrakul, Theoretical study on the reaction mechanism of hydrogenation of furfural to furfuryl alcohol on Lewis acidic BEA zeolites: effects of defect structure and tetravalent metals substitution, *Phys. Chem. Chem. Phys.*, 19 (2017) 24042-24048.

- [470] B. Johnson, J. Di Iorio, Y. Román-Leshkov, Identification and quantification of distinct active sites in Hf-Beta zeolites for transfer hydrogenation catalysis, *J. Catal.*, 404 (2021) 607-619.
- [471] J. Lewis, S. Van de Vyver, A. Crisci, W. Gunther, V. Michaelis, R. Griffin, Y. Román-Leshkov, A Continuous Flow Strategy for the Coupled Transfer Hydrogenation and Etherification of 5-(Hydroxymethyl) furfural using Lewis Acid Zeolites, *ChemSusChem*, 7 (2014) 2255-2265.
- [472] A. Prasertsab, T. Maihom, M. Probst, C. Wattanakit, J. Limtrakul, Furfural to furfuryl alcohol: Computational study of the hydrogen transfer on Lewis acidic BEA zeolites and effects of cation exchange and tetravalent metal substitution, *Inorg. Chem.*, 57 (2018) 6599-6605.
- [473] B. Tang, S. Li, W.-C. Song, E.-C. Yang, X.-J. Zhao, N. Guan, L. Li, Hierarchical FAU-Type Hafnosilicate Zeolite as a Robust Lewis Acid Catalyst for Catalytic Transfer Hydrogenation, *ACS Sustain. Chem. Eng.*, 7 (2019) 16329-16343.
- [474] A. Corma, M.E. Domine, S. Valencia, Water-resistant solid Lewis acid catalysts: Meerwein-Ponndorf-Verley and Oppenauer reactions catalyzed by tin-beta zeolite, *J. Catal.*, 215 (2003) 294-304.
- [475] W. Hu, Y. Wan, L. Zhu, X. Cheng, S. Wan, J. Lin, Y. Wang, A Strategy for the Simultaneous Synthesis of Methyl Alcohol and Diethyl Acetal with Sn- $\beta$ , *ChemSusChem*, 10 (2017) 4715-4724.
- [476] C.-C. Chang, Z. Wang, P. Dornath, H. Je Cho, W. Fan, Rapid synthesis of Sn-Beta for the isomerization of cellulosic sugars, *RSC Adv.*, 2 (2012) 10475-10477.
- [477] C. Hammond, S. Conrad, I. Hermans, Simple and Scalable Preparation of Highly Active Lewis Acidic Sn- $\beta$ , *Angew. Chem. Int. Ed.*, 51 (2012) 11736-11739.
- [478] H.-H. Mautschke, F. Drache, I. Senkovska, S. Kaskel, F. Llabrés i Xamena, Catalytic properties of pristine and defect-engineered Zr-MOF-808 metal organic frameworks, *Catal. Sci. Technol.*, 8 (2018) 3610-3616.
- [479] S. Rojas-Buzo, P. García-García, A. Corma, Hf-based metal-organic frameworks as acid-base catalysts for the transformation of biomass-derived furanic compounds into chemicals, *Green Chem.*, 20 (2018) 3081-3091.

- [480] Y. Kuwahara, H. Kango, H. Yamashita, Catalytic transfer hydrogenation of biomass-derived levulinic acid and its esters to  $\gamma$ -valerolactone over sulfonic acid-functionalized UiO-66, *ACS Sustainable Chem. Eng.*, 5 (2017) 1141-1152.
- [481] T. Wang, A. Hu, G. Xu, C. Liu, H. Wang, Y. Xia, Porous Zr–thiophenedicarboxylate hybrid for catalytic transfer hydrogenation of bio-based furfural to furfuryl alcohol, *Catal. Lett.*, 149 (2019) 1845-1855.
- [482] A.H. Valekar, K. Cho, S.K. Chitale, D. Hong, G. Cha, U. Lee, D.W. Hwang, C. Serre, J. Chang, Y.K. Hwang, Catalytic transfer hydrogenation of ethyl levulinate to  $\gamma$ -valerolactone over zirconium-based metal–organic frameworks, *Green Chem.*, 18 (2016) 4542-4552.
- [483] Z. Cai, W. Li, F. Wang, X. Zhang, Zirconium/hafnium-DUT67 for catalytic transfer hydrogenation of ethyl levulinate to  $\gamma$ -valerolactone, *J. Taiwan Inst. Chem. Eng.*, 93 (2018) 374-378.
- [484] E. Plessers, D.E. De Vos, M.B. Roeffaers, Chemoselective reduction of  $\alpha$ ,  $\beta$ -unsaturated carbonyl compounds with UiO-66 materials, *J. Catal.*, 340 (2016) 136-143.
- [485] Z. Ma, C. Li, H. Fan, J. Wan, Y. Luo, B.-G. Li, Polyhydroxyurethanes (PHUs) derived from diphenolic acid and carbon dioxide and their application in solvent-and water-borne PHU coatings, *Ind. Eng. Chem. Res.*, 56 (2017) 14089-14100.
- [486] M.J. Cliffe, W. Wan, X. Zou, P.A. Chater, A.K. Kleppe, M.G. Tucker, H. Wilhelm, N.P. Funnell, F. Coudert, A.L. Goodwin, Correlated defect nanoregions in a metal–organic framework, *Nat. Commun.*, 5 (2014) 1-8.
- [487] M.R. Momeni, C.J. Cramer, Dual role of water in heterogeneous catalytic hydrolysis of sarin by zirconium-based metal–organic frameworks, *ACS Appl. Mater. Interfaces*, 10 (2018) 18435-18439.
- [488] Y. Zhao, D.G. Truhlar, Density functionals with broad applicability in chemistry, *Acc. Chem. Res.*, 41 (2008) 157-167.
- [489] M. Frisch, G. Trucks, H. Schlegel, G. Scuseria, M. Robb, J. Cheeseman, G. Scalmani, V. Barone, G. Petersson, H. Nakatsuji, *Gaussian 16*, Gaussian, Inc. Wallingford, CT, 2016.

- [490] A. Reed, L. Curtiss, F. Weinhold, Intermolecular interactions from a natural bond orbital, donor-acceptor viewpoint, *Chem. Rev.*, 88 (1988) 899-926.
- [491] J. Colmenares, R. Luque, Heterogeneous photocatalytic nanomaterials: prospects and challenges in selective transformations of biomass-derived compounds, *Chem. Soc. Rev.*, 43 (2014) 765-778.
- [492] W. Gong, Y. Lin, C. Chen, M. Al-Mamun, H.S. Lu, G. Wang, H. Zhang, H. Zhao, Nitrogen-Doped Carbon Nanotube Confined Co–Nx Sites for Selective Hydrogenation of Biomass-Derived Compounds, *Adv. Mater.*, 31 (2019) 1808341.
- [493] V. Bakuru, S. Churipard, S. Maradur, S. Kalidindi, Exploring the Brønsted acidity of UiO-66 (Zr, Ce, Hf) metal–organic frameworks for efficient solketal synthesis from glycerol acetalization, *Dalton Trans.*, 48 (2019) 843-847.
- [494] X. Feng, J. Hajek, H. Jena, G. Wang, S. Veerapandian, R. Morent, N. De Geyter, K. Leyssens, A. Hoffman, V. Meynen, Engineering a highly defective stable UiO-66 with tunable Lewis-Brønsted acidity: the role of the hemilabile linker, *J. Am. Chem. Soc.*, 142 (2020) 3174-3183.
- [495] B. Villoria-del-Álamo, S. Rojas-Buzo, P. García García, A. Corma, Zr-MOF-808 as Catalyst for Amide Esterification, *Chem. Eur. J.*, 27 (2020) 4588–4598.
- [496] A.S. Lawrence, B. Sivakumar, A. Dhakshinamoorthy, Detecting Lewis acid sites in metal-organic frameworks by density functional theory, *Mol. Catal.*, 517 (2022) 112042.
- [497] S. Garg, D.K. Unruh, C. Krempner, Zirconium and hafnium polyhedral oligosilsesquioxane complexes–green homogeneous catalysts in the formation of bio-derived ethers via a MPV/etherification reaction cascade, *Catal. Sci. Technol.*, 11 (2021) 211-218.
- [498] B. Hernández, J. Iglesias, G. Morales, M. Paniagua, C. López-Aguado, J.L.G. Fierro, P. Wolf, I. Hermans, J.A. Melero, One-pot cascade transformation of xylose into  $\gamma$ -valerolactone (GVL) over bifunctional Brønsted–Lewis Zr–Al-beta zeolite, *Green Chem.*, 18 (2016) 5777-5781.
- [499] J.D. Lewis, S. Van de Vyver, A.J. Crisci, W.R. Gunther, V.K. Michaelis, R.G. Griffin, Y. Román-Leshkov, A Continuous Flow Strategy for the Coupled Transfer Hydrogenation and



- Etherification of 5-(Hydroxymethyl) furfural using Lewis Acid Zeolites, *ChemSusChem*, 7 (2014) 2255-2265.
- [500] X. Tang, X. Zeng, Z. Li, W. Li, Y. Jiang, L. Hu, S. Liu, Y. Sun, L. Lin, In situ generated catalyst system to convert biomass-derived levulinic acid to  $\gamma$ -valerolactone, *ChemCatChem*, 7 (2015) 1372-1379.
- [501] P. Vasanthakumar, D. Sindhuja, D.S. Raja, C.-H. Lin, R. Karvembu, Iron and chromium MOFs as sustainable catalysts for transfer hydrogenation of carbonyl compounds and biomass conversions, *New J. Chem.*, 44 (2020) 8223-8231.
- [502] E. Plessers, G. Fu, C.Y.X. Tan, D.E. De Vos, M.B. Roeffaers, Zr-based MOF-808 as Meerwein–Ponndorf–Verley reduction catalyst for challenging carbonyl compounds, *Catalysts*, 6 (2016) 104.
- [503] Y. Lin, Q. Bu, J. Xu, X. Liu, X. Zhang, G. Lu, B. Zhou, Hf-MOF catalyzed Meerwein–Ponndorf–Verley (MPV) reduction reaction: Insight into reaction mechanism, *Mol. Catal.*, 502 (2021) 111405.
- [504] M. Koehle, R. Lobo, Lewis acidic zeolite Beta catalyst for the Meerwein–Ponndorf–Verley reduction of furfural, *Catal. Sci. Technol.*, 6 (2016) 3018-3026.
- [505] J. Sittiwong, S. Boonmark, W. Nunthakitguson, T. Maihom, C. Wattanakit, J. Limtrakul, Density Functional Investigation of the Conversion of Furfural to Furfuryl Alcohol by Reaction with *i*-Propanol over UiO-66 Metal–Organic Framework, *Inorg. Chem.*, 60 (2021) 4860-4868.
- [506] A. Das, N. Anbu, A. Dhakshinamoorthy, S. Biswas, A highly catalytically active Hf (IV) metal-organic framework for Knoevenagel condensation, *Microporous Mesoporous Mater.*, 284 (2019) 459-467.
- [507] A. Das, N. Anbu, C. Gogoi, A. Dhakshinamoorthy, S. Biswas, Amino Group Functionalized Hf-Based Metal-Organic Framework for Knoevenagel-Doebner Condensation, *Eur. J. Inorg. Chem.*, 2021 (2021) 3396-3403.
- [508] A. Das, N. Anbu, P. Varalakshmi, A. Dhakshinamoorthy, S. Biswas, A hydrazine functionalized UiO-66 (Hf) metal–organic framework for the synthesis of quinolines via Friedländer condensation, *New J. Chem.*, 44 (2020) 10982-10988.

- [509] Z. Hu, A. Nalaparaju, Y. Peng, J. Jiang, D. Zhao, Modulated hydrothermal synthesis of UiO-66 (Hf)-type metal–organic frameworks for optimal carbon dioxide separation, *Inorg. Chem.*, 55 (2016) 1134-1141.
- [510] W. Li, Z. Cai, H. Li, Y. Shen, Y. Zhu, H. Li, X. Zhang, F. Wang, Hf-based metal organic frameworks as bifunctional catalysts for the one-pot conversion of furfural to  $\gamma$ -valerolactone, *Mol. Catal.*, 472 (2019) 17-26.
- [511] J. Xu, J. Liu, Z. Li, X. Wang, Y. Xu, S. Chen, Z. Wang, Optimized synthesis of Zr (IV) metal organic frameworks (MOFs-808) for efficient hydrogen storage, *New J. Chem.*, 43 (2019) 4092-4099.
- [512] B.H. Park, Y. Jung, S. Kim, Particle Size Control Influence on the Electrochemical Properties of Sulfur Deposited on Metal Organic Frameworks Host Electrodes, *J. Inorg. Organomet. Polym Mater.*, 31 (2021) 1931-1938.
- [513] V.R. Bakuru, S.R. Churipard, S.P. Maradur, S.B. Kalidindi, Exploring the Brønsted acidity of UiO-66 (Zr, Ce, Hf) metal–organic frameworks for efficient solketal synthesis from glycerol acetalization, *Dalton Trans.*, 48 (2019) 843-847.
- [514] S. Waitschat, D. Fröhlich, H. Reinsch, H. Terraschke, K. Lomachenko, C. Lamberti, H. Kummer, T. Helling, M. Baumgartner, S. Henninger, Synthesis of M-UiO-66 (M= Zr, Ce or Hf) employing 2, 5-pyridinedicarboxylic acid as a linker: defect chemistry, framework hydrophilisation and sorption properties, *Dalton Trans.*, 47 (2018) 1062-1070.
- [515] J. Halpern, Homogeneous catalytic activation of molecular hydrogen by metal ions and complexes, *J. Phys. Chem.*, 63 (1959) 398-403.
- [516] G.M. Chambers, E.S. Wiedner, R.M. Bullock, H<sub>2</sub> Oxidation Electrocatalysis Enabled by Metal-to-Metal Hydrogen Atom Transfer: A Homolytic Approach to a Heterolytic Reaction, *Angew. Chem. Int. Ed.*, 130 (2018) 13711-13715.
- [517] F.D. Pileidis, M.M. Titirici, Levulinic acid biorefineries: new challenges for efficient utilization of biomass, *ChemSusChem*, 9 (2016) 562-582.
- [518] M. Climent, A. Corma, S. Iborra, Conversion of biomass platform molecules into fuel additives and liquid hydrocarbon fuels, *Green Chem*, 16 (2014) 516-547.

- [519] D.A.G. Aranda, R.T.P. Santos, N.C.O. Tapanes, A.L.D. Ramos, O.A.C. Antunes, Acid-Catalyzed Homogeneous Esterification Reaction for Biodiesel Production from Palm Fatty Acids, *Catal. Lett.*, 122 (2008) 20-25.
- [520] H. Joshi, B. Moser, J. Toler, W. Smith, T. Walker, Ethyl levulinate: A potential bio-based diluent for biodiesel which improves cold flow properties, *Biomass Bioenergy*, 35 (2011) 3262-3266.
- [521] G. Pasquale, P. Vázquez, G. Romanelli, G. Baronetti, Catalytic upgrading of levulinic acid to ethyl levulinate using reusable silica-included Wells-Dawson heteropolyacid as catalyst, *Catal. Commun.*, 18 (2012) 115-120.
- [522] X. Chen, Y. Zhang, T. Hou, L. Han, W. Xiao, Catalysis performance comparison of a Brønsted acid  $H_2SO_4$  and a Lewis acid  $Al_2(SO_4)_3$  in methyl levulinate production from biomass carbohydrates, *J. Energy Chem*, 27 (2018) 552-558.
- [523] H. Bart, J. Reidetschlager, K. Schatka, A. Lehmann, Kinetics of esterification of levulinic acid with n-butanol by homogeneous catalysis, *Ind. Eng. Chem. Res*, 33 (1994) 21-25.
- [524] I. Lucena, R. Saboya, J. Oliveira, M. Rodrigues, A. Torres, C. Cavalcante Jr, E. Parente Jr, G. Silva, F. Fernandes, Oleic acid esterification with ethanol under continuous water removal conditions, *Fuel*, 90 (2011) 902-904.
- [525] E. Fischer, A. Speier, Darstellung der ester, *Ber. Dtsch. Chem. Ges.*, 28 (1924) 3252-3258.
- [526] C.-H. Su, Kinetic study of free fatty acid esterification reaction catalyzed by recoverable and reusable hydrochloric acid, *Biores Technol.*, 130 (2013) 522-528.
- [527] W.-M. Xiong, M.-Z. Zhu, L. Deng, Y. Fu, Q.-X. Guo, Esterification of organic acid in bio-oil using acidic ionic liquid catalysts, *Energy Fuels*, 23 (2009) 2278-2283.
- [528] A. Masri, M. Mutalib, W. Yahya, N. Aminuddin, J. Leveque, Rapid esterification of fatty acid using dicationic acidic ionic liquid catalyst via ultrasonic-assisted method, *Ultrason. Sonochem.*, 60 (2020) 104732.
- [529] J. Keogh, M. Tiwari, H. Manyar, Esterification of glycerol with acetic acid using nitrogen-based brønsted-acidic ionic liquids, *Ind. Eng. Chem. Res*, 58 (2019) 17235-17243.

- [530] C. Chiappe, S. Rajamani, F. D'Andrea, A dramatic effect of the ionic liquid structure in esterification reactions in protic ionic media, *Green Chem*, 15 (2013) 137-143.
- [531] L. Wang, J. Zhang, X. Wang, B. Zhang, W. Ji, X. Meng, J. Li, D. Su, X. Bao, F.-S. Xiao, Creation of Brønsted acid sites on Sn-based solid catalysts for the conversion of biomass, *J. Mater. Chem. A*, 2 (2014) 3725-3729.
- [532] S. Kirumakki, N. Nagaraju, K. Chary, Esterification of alcohols with acetic acid over zeolites H $\beta$ , HY and HZSM5, *Appl. Catal. A.*, 299 (2006) 185-192.
- [533] A. Corma, H. Garcia, Organic reactions catalyzed over solid acids, *Catal Today*, 38 (1997) 257-308.
- [534] A. Corma, H. Garcia, S. Iborra, J. Primo, Modified faujasite zeolites as catalysts in organic reactions: Esterification of carboxylic acids in the presence of HY zeolites, *J. Catal.*, 120 (1989) 78-87.
- [535] M. Laspèras, P. Graffin, P. Geneste, One-Pot Selective Synthesis of Ethyl Esters from Aromatic Nitriles Using Acid Faujasites as Catalysts, *J. Catal.*, 139 (1993) 362-370.
- [536] K. Rodponthukwaji, C. Wattanakit, T. Yutthalekha, S. Assavapanumat, C. Warakulwit, W. Wannapakdee, J. Limtrakul, Catalytic upgrading of carboxylic acids as bio-oil models over hierarchical ZSM-5 obtained via an organosilane approach, *RSC Adv.*, 7 (2017) 35581-35589.
- [537] J. Pavlovic, M. Popova, R. Mihalyi, M. Mazaj, G. Mali, J. Kovač, H. Lazarova, N. Rajic, Catalytic activity of SnO<sub>2</sub>-and SO<sub>4</sub>/SnO<sub>2</sub>-containing clinoptilolite in the esterification of levulinic acid, *Microporous Mesoporous Mater.*, 279 (2019) 10-18.
- [538] N. Mansir, Y. Taufiq-Yap, U. Rashid, I. Lokman, Investigation of heterogeneous solid acid catalyst performance on low grade feedstocks for biodiesel production: A review, *Energy Convers. Manage.*, 141 (2017) 171-182.
- [539] D. Fernandes, A. Rocha, E. Mai, C. Mota, V. Da Silva, Levulinic acid esterification with ethanol to ethyl levulinate production over solid acid catalysts, *Appl. Catal. A.*, 425 (2012) 199-204.

- [540] D. Chaffey, T. Bere, T. Davies, D. Apperley, S. Taylor, A. Graham, Conversion of levulinic acid to levulinate ester biofuels by heterogeneous catalysts in the presence of acetals and ketals, *Appl. Catal., B*, 293 (2021) 120219.
- [541] M. Tejero, E. Ramírez, C. Fité, J. Tejero, F. Cunill, Esterification of levulinic acid with butanol over ion exchange resins, *Appl. Catal. A.*, 517 (2016) 56-66.
- [542] V. Trombettoni, L. Bianchi, A. Zupanic, A. Porciello, M. Cuomo, O. Piermatti, A. Marrocchi, L. Vaccaro, Efficient catalytic upgrading of levulinic acid into alkyl levulinates by resin-supported acids and flow reactors, *Catalysts*, 7 (2017) 235.
- [543] C.F. Chow, C.S. Chan, A Study on Fenton Technology for Polypropylene Waste Degradation and Recovery of High-Value Chemicals, *Environmental Sustainability and Education for Waste Management*, Springer2019, pp. 223-239.
- [544] C.F. Chow, W.L. Wong, K.Y. Ho, C.S. Chan, C.B. Gong, Combined Chemical Activation and Fenton Degradation to Convert Waste Polyethylene into High-Value Fine Chemicals, *Chemistry—A European Journal*, 22 (2016) 9513-9518.
- [545] J.M. Guarinos, F.G. Cirujano, A. Rapeyko, F.X.L. i Xamena, Conversion of levulinic acid to  $\gamma$ -valerolactone over Zr-containing metal-organic frameworks: Evidencing the role of Lewis and Brønsted acid sites, *Mol. Catal.*, 515 (2021) 111925.
- [546] M. Muniyadi, T. Ng, Y. Munusamy, Z. Ooi, Mimusops elengi seed shell powder as a new bio-filler for polypropylene-based bio-composites, *BioRes.*, 13 (2018) 272-289.
- [547] L. Ciddor, J. Bennett, J. Hunns, K. Wilson, A. Lee, Catalytic upgrading of bio-oils by esterification, *J. Chem. Technol. Biotechnol.*, 90 (2015) 780-795.
- [548] M. Marczewski, M. Aleksandrowicz, E. Brzezińska, M. Podlewska, M. Rychlik, S. Żmuda, U. Ulkowska, M. Gliński, O. Osawaru, Acid strength measurements of Amberlyst 15 resin, p-xylene-2-sulfonic acid and chlorosulfonic and sulfuric acid treated SiO<sub>2</sub>, Al<sub>2</sub>O<sub>3</sub>, TiO<sub>2</sub> and MgO, *React. Kinet. Mech. Catal.*, 126 (2019) 1081-1096.
- [549] F. Darvish, N.M. Sarkari, M. Khani, E. Eslami, B. Shokri, M.o. Mohseni, M. Ebrahimi, M. Alizadeh, C.F. Dee, Direct plasma treatment approach based on non-thermal gliding arc for

surface modification of biaxially-oriented polypropylene with post-exposure hydrophilicity improvement and minus aging effects, *Appl. Surf. Sci.*, 509 (2020) 144815.

[550] M.R. Jung, F.D. Horgen, S.V. Orski, V. Rodriguez, K.L. Beers, G.H. Balazs, T.T. Jones, T.M. Work, K.C. Brignac, S. Royer, Validation of ATR FT-IR to identify polymers of plastic marine debris, including those ingested by marine organisms, *Mar. Pollut. Bull.*, 127 (2018) 704-716.

[551] M. Raji, M.E.M. Mekhzoum, D. Rodrigue, R. Bouhfid, Effect of silane functionalization on properties of polypropylene/clay nanocomposites, *Composites, Part B*, 146 (2018) 106-115.

[552] C.F. Chow, W.L. Wong, K.Y. Ho, C.S. Chan, C.B. Gong, Combined Chemical Activation and Fenton Degradation to Convert Waste Polyethylene into High-Value Fine Chemicals, *Chem. Eur. J.*, 22 (2016) 9513-9518.

[553] M. Kaneko, S. Kumagai, T. Nakamura, H. Sato, Study of sulfonation mechanism of low-density polyethylene films with fuming sulfuric acid, *J. Appl. Polym. Sci.*, 91 (2004) 2435-2442.

[554] N. Gomathi, S. Neogi, Surface modification of polypropylene using argon plasma: Statistical optimization of the process variables, *Appl. Surf. Sci.*, 255 (2009) 7590-7600.

[555] J. Qian, G. Cheng, H. Zhang, Y. Xu, Preparation and characterization of polypropylene/silica nanocomposites by gamma irradiation via ultrafine blend, *J. Polym. Res.*, 18 (2011) 409-417.

[556] R.H. Somani, B.S. Hsiao, A. Nogales, H. Fruitwala, S. Srinivas, A.H. Tsou, Structure Development during Shear Flow Induced Crystallization of i-PP: In Situ Wide-Angle X-ray Diffraction Study, *Macromolecules*, 34 (2001) 5902-5909.

[557] Z. Changani, A. Razmjou, A. Taheri-Kafrani, M. Warkiani, M. Asadnia, Surface modification of polypropylene membrane for the removal of iodine using polydopamine chemistry, *Chemosphere*, 249 (2020) 126079.

[558] J. Matoušek, N. Bendlová, Z. Kolská, P. Čapková, J. Pavlík, M. Kormunda, Time dependence of the surface chemistry of the plasma treated polypropylene powder, *Adv. Powder Technol.*, 27 (2016) 262-267.

[559] C.-K. Shu, B. Lawrence, Formation of 4-alkoxy- $\gamma$ -valerolactones from levulinic acid and alcohols during storage at room temperature, *J. Agric. Food. Chem.*, 43 (1995) 782-784.

- [560] S.S. Enumula, V.R.B. Gurram, R.R. Chada, D.R. Burri, S.R.R. Kamaraju, Clean synthesis of alkyl levulinates from levulinic acid over one pot synthesized WO<sub>3</sub>-SBA-16 catalyst, *J. Mol. Catal. A: Chem.*, 426 (2017) 30-38.
- [561] F. Cirujano, A. Corma, F. Llabrés i Xamena, Conversion of levulinic acid into chemicals: synthesis of biomass derived levulinate esters over Zr-containing MOFs, *Chem. Eng. Sci.*, 124 (2015) 52-60.
- [562] I. Mbaraka, D. Radu, V.-Y. Lin, B. Shanks, Organosulfonic acid-functionalized mesoporous silicas for the esterification of fatty acid, *J. Catal.*, 219 (2003) 329-336.
- [563] J. Melero, G. Morales, J. Iglesias, M. Paniagua, B. Hernández, S. Penedo, Efficient conversion of levulinic acid into alkyl levulinates catalyzed by sulfonic mesostructured silicas, *Appl. Catal. A.*, 466 (2013) 116-122.
- [564] L. Konwar, P. Mäki-Arvela, J.-P. Mikkola, SO<sub>3</sub>H-containing functional carbon materials: synthesis, structure, and acid catalysis, *Chem. Rev.*, 119 (2019) 11576-11630.
- [565] P.F. Siril, H.E. Cross, D.R. Brown, New polystyrene sulfonic acid resin catalysts with enhanced acidic and catalytic properties, *J. Mol. Catal. A: Chem.*, 279 (2008) 63-68.
- [566] R. Bringué, M. Iborra, J. Tejero, J.F. Izquierdo, F. Cunill, C. Fité, V.J. Cruz, Thermally stable ion-exchange resins as catalysts for the liquid-phase dehydration of 1-pentanol to di-n-pentyl ether (DNPE), *J. Catal.*, 244 (2006) 33-42.
- [567] M. Bihani, P. Bora, G. Bez, H. Askari, Amberlyst A21: A reusable solid catalyst for green synthesis of pyran annulated heterocycles at room temperature, *C. R. Chimie*, 16 (2013) 419-426.
- [568] A. Osatiashtiani, B. Puértolas, C. Oliveira, J. Manayil, B. Barbero, M. Isaacs, C. Michailof, E. Heracleous, J. Pérez-Ramírez, A. Lee, On the influence of Si: Al ratio and hierarchical porosity of FAU zeolites in solid acid catalysed esterification pretreatment of bio-oil, *Biomass Conv. Bioref.*, 7 (2017) 331-342.
- [569] H. Koo, J. Lee, T.-S. Chang, Y.-W. Suh, D. Lee, J. Bae, Esterification of acetic acid with methanol to methyl acetate on Pd-modified zeolites: effect of Brønsted acid site strength on activity, *Reac Kinet Mech Cat*, 112 (2014) 499-510.

- [570] K. Stawicka, A. Diaz-Alvarez, V. Calvino-Casilda, M. Trejda, M. Banares, M. Ziolk, The role of brønsted and lewis acid sites in acetalization of glycerol over modified mesoporous cellular foams, *J. Phys. Chem. C*, 120 (2016) 16699-16711.
- [571] S. Shylesh, S. Sharma, S. Mirajkar, A. Singh, Silica functionalised sulphonic acid groups: synthesis, characterization and catalytic activity in acetalization and acetylation reactions, *J. Mol. Catal. A: Chem.*, 212 (2004) 219-228.
- [572] L. Yang, G. Tsilomelekis, S. Caratzoulas, D. Vlachos, Mechanism of Brønsted Acid-Catalyzed Glucose Dehydration, *ChemSusChem*, 8 (2015) 1334-1341.
- [573] R. Weingarten, G. Tompsett, W. Conner Jr, G. Huber, Design of solid acid catalysts for aqueous-phase dehydration of carbohydrates: The role of Lewis and Brønsted acid sites, *J. Catal.*, 279 (2011) 174-182.
- [574] M.S. Rahaman, S. Tulaphol, K.N. Mills, A.M. Molley, M.A. Hossain, S.B. Lalvani, T. Maihom, M. Crocker, N. Sathitsuksanoh, Aluminum based metal-organic framework as water-tolerant Lewis acid catalyst for selective dihydroxyacetone isomerization to lactic acid, *ChemCatChem*, 14 (2022).
- [575] K.-i. Shimizu, H. Furukawa, N. Kobayashi, Y. Itaya, A. Satsuma, Effects of Brønsted and Lewis acidities on activity and selectivity of heteropolyacid-based catalysts for hydrolysis of cellobiose and cellulose, *Green Chem*, 11 (2009) 1627-1632.
- [576] J. Tian, J. Wang, S. Zhao, C. Jiang, X. Zhang, X. Wang, Hydrolysis of cellulose by the heteropoly acid  $H_3PW_{12}O_{40}$ , *Cellulose*, 17 (2010) 587-594.
- [577] U.S. Environmental Protection Agency, Advancing sustainable materials management: 2018 tables and figures, 2020.
- [578] J. Steinbuks, B.G. Narayanan, Fossil fuel producing economies have greater potential for industrial interfuel substitution, *Energy Econ.*, 47 (2015) 168-177.
- [579] E. Abokyi, P. Appiah-Konadu, F. Abokyi, E.F. Oteng-Abayie, Industrial growth and emissions of CO<sub>2</sub> in Ghana: The role of financial development and fossil fuel consumption, *Energy Rep.*, 5 (2019) 1339-1353.



- [580] D.J. Wuebbles, A.K. Jain, Concerns about climate change and the role of fossil fuel use, *Fuel Process. Technol.*, 71 (2001) 99-119.
- [581] M. Kabbour, R. Luque, Furfural as a platform chemical: From production to applications, *Biomass, Biofuels, Biochemicals*, (2020) 283-297.
- [582] S. Zhang, G. Shen, Y. Deng, Y. Lei, J.-W. Xue, Z. Chen, G. Yin, Efficient Synthesis of 2,5-Furandicarboxylic Acid from Furfural Based Platform through Aqueous-Phase Carbonylation, *ACS Sustainable Chem. Eng.*, 6 (2018) 13192-13198.
- [583] T. Pan, J. Deng, Q. Xu, Y. Zuo, Q.-X. Guo, Y. Fu, Catalytic Conversion of Furfural into a 2,5-Furandicarboxylic Acid-Based Polyester with Total Carbon Utilization, *ChemSusChem*, 6 (2013) 47-50.
- [584] Q. Peng, H. Wang, Y. Xia, X. Liu, One-pot conversion of furfural to gamma-valerolactone in the presence of multifunctional zirconium alizarin red S hybrid, *Appl. Catal., A*, 621 (2021) 118203.
- [585] S. Zhu, Y. Xue, J. Guo, Y. Cen, J. Wang, W. Fan, Integrated Conversion of Hemicellulose and Furfural into  $\gamma$ -Valerolactone over Au/ZrO<sub>2</sub> Catalyst Combined with ZSM-5, *ACS Catal.*, 6 (2016) 2035-2042.
- [586] Y. Shao, M. Guo, J. Wang, K. Sun, L. Zhang, S. Zhang, G. Hu, L. Xu, X. Yuan, X. Hu, Selective Conversion of Furfural into Diols over Co-Based Catalysts: Importance of the Coordination of Hydrogenation Sites and Basic Sites, *Ind. Eng. Chem. Res.*, 60 (2021) 10393-10406.
- [587] W. Xu, H. Wang, X. Liu, J. Ren, Y. Wang, G. Lu, Direct catalytic conversion of furfural to 1,5-pentanediol by hydrogenolysis of the furan ring under mild conditions over Pt/Co<sub>2</sub>AlO<sub>4</sub> catalyst, *Chem. Commun.*, 47 (2011) 3924-3926.
- [588] V. Choudhary, S.I. Sandler, D.G. Vlachos, Conversion of xylose to furfural using Lewis and Brønsted acid catalysts in aqueous media, *ACS Catal.*, 2 (2012) 2022-2028.
- [589] K. Lamminpää, J. Ahola, J. Tanskanen, Acid-catalysed xylose dehydration into furfural in the presence of kraft lignin, *Bioresour. Technol.*, 177 (2015) 94-101.

- [590] O. Yemiş, G. Mazza, Acid-catalyzed conversion of xylose, xylan and straw into furfural by microwave-assisted reaction, *Bioresource Technology*, 102 (2011) 7371-7378.
- [591] A. Mazar, N. Jemaa, W. Wafa Al Dajani, M. Marinova, M. Perrier, Furfural production from a pre-hydrolysate generated using aspen and maple chips, *Biomass Bioenergy*, 104 (2017) 8-16.
- [592] R. O'Neill, M.N. Ahmad, L. Vanoye, F. Aiouache, Kinetics of Aqueous Phase Dehydration of Xylose into Furfural Catalyzed by ZSM-5 Zeolite, *Ind. Eng. Chem. Res.*, 48 (2009) 4300-4306.
- [593] I. Agirrezabal-Telleria, A. Larreategui, J. Requies, M.B. Güemez, P.L. Arias, Furfural production from xylose using sulfonic ion-exchange resins (Amberlyst) and simultaneous stripping with nitrogen, *Bioresour. Technol.*, 102 (2011) 7478-7485.
- [594] C. García-Sancho, I. Sádaba, R. Moreno-Tost, J. Mérida-Robles, J. Santamaría-González, M. López-Granados, P. Maireles-Torres, Dehydration of Xylose to Furfural over MCM-41-Supported Niobium-Oxide Catalysts, *ChemSusChem*, 6 (2013) 635-642.
- [595] E. Lam, E. Majid, A.C.W. Leung, J.H. Chong, K.A. Mahmoud, J.H.T. Luong, Synthesis of Furfural from Xylose by Heterogeneous and Reusable Nafion Catalysts, *ChemSusChem*, 4 (2011) 535-541.
- [596] S.B. Kim, S.J. You, Y.T. Kim, S.M. Lee, H. Lee, K. Park, E.D. Park, Dehydration of D-xylose into furfural over H-zeolites, *Korean J. Chem. Eng.*, 28 (2011) 710-716.
- [597] C. Wu, W. Chen, L. Zhong, X. Peng, R. Sun, J. Fang, S. Zheng, Conversion of xylose into furfural using lignosulfonic acid as catalyst in ionic liquid, *J. Agric. Food. Chem.*, 62 (2014) 7430-7435.
- [598] R. Weingarten, G.A. Tompsett, W.C. Conner Jr, G.W. Huber, Design of solid acid catalysts for aqueous-phase dehydration of carbohydrates: The role of Lewis and Brønsted acid sites, *J. Catal.*, 279 (2011) 174-182.
- [599] Y. Zhu, W. Li, Y. Lu, T. Zhang, H. Jameel, H.-M. Chang, L. Ma, Production of furfural from xylose and corn stover catalyzed by a novel porous carbon solid acid in  $\gamma$ -valerolactone, *RSC Adv.*, 7 (2017) 29916-29924.

- [600] J.M. Guarinos, F.G. Cirujano, A. Rapeyko, F.X. Llabrés i Xamena, Conversion of levulinic acid to  $\gamma$ -valerolactone over Zr-containing metal-organic frameworks: Evidencing the role of Lewis and Brønsted acid sites, *Mol. Catal.*, 515 (2021) 111925.
- [601] F.G. Cirujano, F.X. Llabrés i Xamena, Tuning the Catalytic Properties of UiO-66 Metal–Organic Frameworks: From Lewis to Defect-Induced Brønsted Acidity, *J. Phys. Chem. Lett.*, 11 (2020) 4879-4890.
- [602] X. Hu, R.J. Westerhof, D. Dong, L. Wu, C. Li, Acid-catalyzed conversion of xylose in 20 solvents: insight into interactions of the solvents with xylose, furfural, and the acid catalyst, *ACS Sustainable Chem. Eng.*, 2 (2014) 2562-2575.
- [603] Z. Changani, A. Razmjou, A. Taheri-Kafrani, M.E. Warkiani, M. Asadnia, Surface modification of polypropylene membrane for the removal of iodine using polydopamine chemistry, *Chemosphere*, 249 (2020) 126079.
- [604] M.S. Rahaman, S. Tulaphol, M.A. Hossain, J.B. Jasinski, N. Sun, A. George, B.A. Simmons, T. Maihom, M. Crocker, N. Sathitsuksanoh, Cooperative Brønsted-Lewis acid sites created by phosphotungstic acid encapsulated metal–organic frameworks for selective glucose conversion to 5-hydroxymethylfurfural, *Fuel*, 310 (2022) 122459.
- [605] B. Matsagar, S. Hossain, T. Islam, H. Alamri, Z. Alothman, Y. Yamauchi, P. Dhepe, K.-W. Wu, Direct production of furfural in one-pot fashion from raw biomass using Brønsted acidic ionic liquids, *Sci. Rep.*, 7 (2017) 1-7.
- [606] S. Peleteiro, A.M. da Costa Lopes, G. Garrote, J.C. Parajó, R. Bogel-Lukasik, Simple and Efficient Furfural Production from Xylose in Media Containing 1-Butyl-3-Methylimidazolium Hydrogen Sulfate, *Ind. Eng. Chem. Res.*, 54 (2015) 8368-8373.
- [607] K.R. Enslow, A.T. Bell, The kinetics of Brønsted acid-catalyzed hydrolysis of hemicellulose dissolved in 1-ethyl-3-methylimidazolium chloride, *RSC Adv.*, 2 (2012) 10028-10036.
- [608] M.R. Nimlos, X. Qian, M. Davis, M.E. Himmel, D.K. Johnson, Energetics of Xylose Decomposition as Determined Using Quantum Mechanics Modeling, *J. Phys. Chem. A*, 110 (2006) 11824-11838.

- [609] B. Danon, G. Marcotullio, W. de Jong, Mechanistic and kinetic aspects of pentose dehydration towards furfural in aqueous media employing homogeneous catalysis, *Green Chem.*, 16 (2014) 39-54.
- [610] P. Ferreira, I.M. Fonseca, A.M. Ramos, J. Vital, J.E. Castanheiro, Valorisation of glycerol by condensation with acetone over silica-included heteropolyacids, *Appl. Catal., B*, 98 (2010) 94-99.
- [611] M.R. Nolan, G. Sun, B.H. Shanks, On the selective acid-catalysed dehydration of 1,2,6-hexanetriol, *Catal. Sci. Technol.*, 4 (2014) 2260-2266.
- [612] V. Krzelj, J. Ferreira Liberal, M. Papaioannou, J. van der Schaaf, M.F. Neira d'Angelo, Kinetic Model of Xylose Dehydration for a Wide Range of Sulfuric Acid Concentrations, *Ind. Eng. Chem. Res.*, 59 (2020) 11991-12003.
- [613] V. Krzelj, D.P. Ferrandez, M.F. Neira D'Angelo, Sulfonated foam catalysts for the continuous dehydration of xylose to furfural in biphasic media, *Catal. Today*, 365 (2021) 274-281.
- [614] L. Mark, M. Cendejas, I. Hermans, The Use of Heterogeneous Catalysis in the Chemical Valorization of Plastic Waste, *ChemSusChem*, (2020).
- [615] B. Weckhuysen, Creating value from plastic waste, *Science*, 370 (2020) 400-401.
- [616] J. Zeaiter, A process study on the pyrolysis of waste polyethylene, *Fuel*, 133 (2014) 276-282.
- [617] R. Miandad, M. Rehan, M. Barakat, A. Aburizaiza, H. Khan, I. Ismail, J. Dhavamani, J. Gardy, A. Hassanpour, A.-S. Nizami, Catalytic pyrolysis of plastic waste: moving toward pyrolysis based biorefineries, *Front. Energy Res.*, 7 (2019) 27, doi: 10.3389/fenrg.2019.00027.
- [618] X. Chen, Y. Wang, L. Zhang, Recent Progresses in the Chemical Upcycling of Plastic Wastes, *ChemSusChem*, 14 (2021) 4137-4151.
- [619] A. Bogaerts, X. Tu, J. Whitehead, G. Centi, L. Lefferts, O. Guaitella, F. Azzolina-Jury, H.-H. Kim, A. Murphy, W. Schneider, The 2020 plasma catalysis roadmap, *J. Phys. D: Appl. Phys.*, 53 (2020) 443001.
- [620] E. Neyts, K. Ostrikov, M. Sunkara, A. Bogaerts, Plasma catalysis: synergistic effects at the nanoscale, *Chem. Rev.*, 115 (2015) 13408-13446.

- [621] A. Dhakshinamoorthy, A. Asiri, H. Garcia, Metal–organic frameworks as catalysts for oxidation reactions, *Chem. Eur. J.*, 22 (2016) 8012-8024.
- [622] A. Corma, H. García, Lewis acids as catalysts in oxidation reactions: from homogeneous to heterogeneous systems, *Chem. Rev.*, 102 (2002) 3837-3892.
- [623] A. Dhakshinamoorthy, A.M. Asiri, H. Garcia, Metal–organic frameworks as catalysts for oxidation reactions, *Chem. Eur. J.*, 22 (2016) 8012-8024.
- [624] O. Kholdeeva, N. Maksimchuk, Metal-organic frameworks in oxidation catalysis with hydrogen peroxide, *Catalysts*, 11 (2021) 283.
- [625] F. Bi, X. Zhang, J. Chen, Y. Yang, Y. Wang, Excellent catalytic activity and water resistance of UiO-66-supported highly dispersed Pd nanoparticles for toluene catalytic oxidation, *Appl. Catal., B*, 269 (2020) 118767.
- [626] K. Leus, T. Bogaerts, J. De Decker, H. Depauw, K. Hendrickx, H. Vrielinck, V. Van Speybroeck, P. Van Der Voort, Systematic study of the chemical and hydrothermal stability of selected “stable” Metal Organic Frameworks, *Microporous Mesoporous Mater.*, 226 (2016) 110-116.
- [627] H.G.T. Nguyen, L. Mao, A.W. Peters, C.O. Audu, Z.J. Brown, O.K. Farha, J.T. Hupp, S.T. Nguyen, Comparative study of titanium-functionalized UiO-66: support effect on the oxidation of cyclohexene using hydrogen peroxide, *Catal. Sci. Technol.*, 5 (2015) 4444-4451.
- [628] H.Q. Zheng, Y.N. Zeng, J. Chen, R.G. Lin, W.E. Zhuang, R. Cao, Z.J. Lin, Zr-based metal–organic frameworks with intrinsic peroxidase-like activity for ultradeep oxidative desulfurization: mechanism of H<sub>2</sub>O<sub>2</sub> decomposition, *Inorg. Chem.*, 58 (2019) 6983-6992.
- [629] M. Zhou, C. Zhou, D. Chen, H. Wu, Z. Zhang, H. Yang, W. Ruan, Y. Zhou, Z. Tan, Mn decorated UIO-66 catalyst for gaseous toluene removal: Synergistic effect of enhanced hydroxyl from H<sub>2</sub>O<sub>2</sub>, *Fuel*, 309 (2022) 122229.
- [630] H. Chen, Y. Mu, Y. Shao, S. Chansai, H. Xiang, Y. Jiao, C. Hardacre, X. Fan, Nonthermal plasma (NTP) activated metal–organic frameworks (MOFs) catalyst for catalytic CO<sub>2</sub> hydrogenation, *AIChE J.*, 66 (2020) e16853.

- [631] X. Feng, C. Chen, C. He, S. Chai, Y. Yu, J. Cheng, Non-thermal plasma coupled with MOF-74 derived Mn-Co-Ni-O porous composite oxide for toluene efficient degradation, *J. Hazard. Mater.*, 383 (2020) 121143.
- [632] R. Vakili, R. Gholami, C. Stere, S. Chansai, H. Chen, S. Holmes, Y. Jiao, C. Hardacre, X. Fan, Plasma-assisted catalytic dry reforming of methane (DRM) over metal-organic frameworks (MOFs)-based catalysts, *Appl. Catal., B*, 260 (2020) 118195.
- [633] J. Shah, T. Wu, J. Lucero, M. Carreon, M. Carreon, Nonthermal Plasma Synthesis of Ammonia over Ni-MOF-74, *ACS Sustain. Chem. Eng.*, 7 (2019) 377-383.

APPENDIX  
COPYRIGHTS FOR ARTICLES

**Chapter 2:** Hydrophobic functionalization of HY zeolites for efficient conversion of glycerol to solketal.

<https://doi.org/10.1016/j.apcata.2019.117369>

CCC | RightsLink®

Home ? Help Email Support Sign in Create Account

 **Hydrophobic functionalization of HY zeolites for efficient conversion of glycerol to solketal**

**Author:** Mohammad Shahinur Rahaman, Thanh Khoa Phung, Md. Anwar Hossain, Emtias Chowdhury, Sartrawut Tulaphol, Shashi B. Lalvani, Martin O'Toole, Gerald A. Willing, Jacek B. Jasinski, Mark Crocker, Noppadon Sathitsuksanoh

**Publication:** Applied Catalysis A: General

**Publisher:** Elsevier

**Date:** 25 February 2020

© 2020 Elsevier B.V. All rights reserved.

**Journal Author Rights**

Please note that, as the author of this Elsevier article, you retain the right to include it in a thesis or dissertation, provided it is not published commercially. Permission is not required, but please ensure that you reference the journal as the original source. For more information on this and on your other retained rights, please visit: <https://www.elsevier.com/about/our-business/policies/copyright#Author-rights>

BACK CLOSE WINDOW


© 2022 Copyright - All Rights Reserved | Copyright Clearance Center, Inc. | Privacy statement | Terms and Conditions  
Comments? We would like to hear from you. E-mail us at [customer@copyright.com](mailto:customer@copyright.com)

### Chapter 3: Cooperative Brønsted-Lewis acid sites created by phosphotungstic acid encapsulated metal–organic frameworks for selective glucose conversion to 5-hydroxymethylfurfural

<https://doi.org/10.1016/j.fuel.2021.122459>

CCC | RightsLink®

Home ? Help Email Support Sign in Create Account

 Cooperative Brønsted-Lewis acid sites created by phosphotungstic acid encapsulated metal–organic frameworks for selective glucose conversion to 5-hydroxymethylfurfural

**Author:**  
Mohammad Shahinur Rahaman, Sartrawut Tulaphol, Md Anwar Hossain, Jacek B. Jasinski, Ning Sun, Anthe George, Blake A. Simmons, Thana Maihom, Mark Crocker, Noppadon Sathitsuksanoh

**Publication:** Fuel

**Publisher:** Elsevier

**Date:** 15 February 2022

© 2021 Elsevier Ltd. All rights reserved.

**Journal Author Rights**

Please note that, as the author of this Elsevier article, you retain the right to include it in a thesis or dissertation, provided it is not published commercially. Permission is not required, but please ensure that you reference the journal as the original source. For more information on this and on your other retained rights, please visit: <https://www.elsevier.com/about/our-business/policies/copyright#Author-rights>


BACK CLOSE WINDOW

© 2022 Copyright - All Rights Reserved | Copyright Clearance Center, Inc. | Privacy statement | Terms and Conditions  
Comments? We would like to hear from you. E-mail us at [customer-care@copyright.com](mailto:customer-care@copyright.com)



## Chapter 5: Aluminum-based Metal-Organic Framework as Water-tolerant Lewis Acid Catalyst for Selective Dihydroxyacetone Isomerization to Lactic Acid.

<https://doi.org/10.1002/cctc.202101756>



**Aluminum-based Metal-Organic Framework as Water-tolerant Lewis Acid Catalyst for Selective Dihydroxyacetone Isomerization to Lactic Acid**  
Author: Mohammad Shahinur Rahaman, Sartravut Tulaphol, Kyle Mills, et al  
Publication: ChemCatChem  
Publisher: John Wiley and Sons  
Date: Jan 21, 2022  
© 2021 Wiley-VCH GmbH

---

**Order Completed**

Thank you for your order.

This Agreement between Mohammad Shahinur Rahaman ("You") and John Wiley and Sons ("John Wiley and Sons") consists of your license details and the terms and conditions provided by John Wiley and Sons and Copyright Clearance Center.

Your confirmation email will contain your order number for future reference.

|                |               |                                   |
|----------------|---------------|-----------------------------------|
| License Number | 5266671112104 | <a href="#">Printable Details</a> |
| License date   | Mar 12, 2022  |                                   |

| Licensed Content             |  | Order Details            |                              |
|------------------------------|--|--------------------------|------------------------------|
| Licensed Content Publisher   | John Wiley and Sons  | Type of use              | Dissertation/Thesis          |
| Licensed Content Publication | ChemCatChem  | Requestor type           | Author of this Wiley article |
| Licensed Content Title       | Aluminum-based Metal-Organic Framework as Water-tolerant Lewis Acid Catalyst for Selective Dihydroxyacetone Isomerization to Lactic Acid | Format                   | Print and electronic         |
| Licensed Content Author      | Mohammad Shahinur Rahaman, Sartravut Tulaphol, Kyle Mills, et al   | Portion                  | Full article                 |
| Licensed Content Date        | Jan 21, 2022   | Will you be translating? | No                           |
| Licensed Content Volume      | 14   |                          |                              |
| Licensed Content Issue       | 4  |                          |                              |
| Licensed Content Pages       | 10   |                          |                              |


| About Your Work            |   | Additional Data |  |
|----------------------------|---|-----------------|--|
| Title                      | DEVELOPMENT OF POROUS SOLID ACID CATALYSTS FOR LIGNOCELLULOSE AND PLASTIC UPCYCLING |                 |  |
| Institution name           | UNIVERSITY OF LOUISVILLE  |                 |  |
| Expected presentation date | Apr 2022  |                 |  |

## Chapter 7: Mechanism of transfer hydrogenation of carbonyl compounds by zirconium and hafnium-containing metal-organic frameworks

<https://doi.org/10.1016/j.mcat.2022.112247>

CCC RightsLink®

Home Help Live Chat Sign in Create Account

 **Mechanism of transfer hydrogenation of carbonyl compounds by zirconium and hafnium-containing metal-organic frameworks**  
Author: Mohammad Shahinur Rahaman, Sarttrawut Tulaphol, Md. Anwar Hossain, Matthew C. Mulvehill, Joshua M. Spurgeon, Thana Maihom, Noppadon Sathitsuksanoh  
Publication: Molecular Catalysis  
Publisher: Elsevier  
Date: April 2022  
© 2022 Elsevier B.V. All rights reserved.

**Journal Author Rights**  
Please note that, as the author of this Elsevier article, you retain the right to include it in a thesis or dissertation, provided it is not published commercially. Permission is not required, but please ensure that you reference the journal as the original source. For more information on this and on your other retained rights, please visit: <https://www.elsevier.com/about/our-business/policies/copyright#author-rights>

BACK CLOSE WINDOW

© 2022 Copyright - All Rights Reserved | Copyright Clearance Center, Inc. | Privacy statement | Terms and Conditions  
Comments? We would like to hear from you. E-mail us at [customercare@copyright.com](mailto:customercare@copyright.com)

## CURRICULUM VITAE

Mohammad Shahinur Rahaman  
502-554-0025 | m0raha01@louisville.edu

### Summary of Qualifications

---

- 5+ years of research experience in heterogeneous catalyst synthesis, materials characterization, biofuel production, biomass & plastic upcycling, product development.
- 16 peer-reviewed articles published in scientific journals
- 3 years of industrial experience as process engineer in gas and chemical industry
- Energetic team player, able to communicate effectively with people from diverse backgrounds
- Multidisciplinary project management with flexible and adaptable problem-solving skills

### Research Skills

---

- **Instrumentation techniques:** GC-MS/FID, HPLC, TPD, TPR, TGA, DSC, BET, SEM, EDX, FTIR, XRD, DRIFT, UV-Vis spectroscopy, Raman.
- **Experimental skills:** Catalyst synthesis (zeolites, MOFs), Analytical separation & characterization, Surface modification of polymers & catalysts, Biomass & plastic upgrading, Reactor design & operation, Production of value-added chemicals
- **Computer and software skills:** MS Office, MS Excel, Origin, ChemStation
- **Process simulation and data analysis:** ASPEN PLUS, ChemDraw, Design of Experiments

### Research and Professional Experience

---

|   |                    |
|---|--------------------|
| <b>University of Louisville</b>   | Louisville, KY     |
| Research Associate/Ph.D. Candidate  | 08/2016 to 04/2022 |
| <ul style="list-style-type: none"><li>• Led a team to conduct research in the synthesis, characterization, and application of catalyst.</li><li>• Experienced in operating and troubleshooting chromatographic equipment (GC-MS, HPLC)</li><li>• Developed suitable methods to upgrade biomass and plastic into value-added chemicals</li></ul> |                    |
| <b>Hyundai Engineering Co., Ltd.</b>  | Bangladesh         |
| Operation Engineer  | 01/2015 to 06/2016 |
| <ul style="list-style-type: none"><li>• Monitored smooth operation of gas compressor and supervised the process operation.</li><li>• Increased the 20% gas flow capacity throughout Bangladesh.</li></ul>   |                    |
| <b>Tasnim Chemical Complex Ltd.</b>   | Bangladesh         |
| Assistant Process Engineer  | 08/2013 to 12/2014 |
| <ul style="list-style-type: none"><li>• Responsible for the uninterrupted production of caustic soda, and liquid chlorine,</li><li>• Finished the commissioning work and increased the 50% production capacity.</li></ul>   |                    |

## Education

---

|   |                           |
|---|---------------------------|
| <b>University of Louisville</b><br>Ph.D., Chemical Engineering  | Louisville, KY<br>04/2022 |
| <b>University of Louisville</b><br>M.S., Chemical Engineering   | Louisville, KY<br>08/2020 |
| <b>Shahjalal University of Science and Technology</b><br>B.S., Chemical Engineering & Polymer Science | Bangladesh<br>12/2012     |

## Publications

---

1. **M. S. Rahaman**, S. Tulaphol, M. A. Hossain, J. B. Jasinski, S. Lalvani, M. Crocker, T. Maihom, N. Sathitsuksanoh, "Aluminum-containing metal organic frameworks as selective and reusable catalysts for glucose isomerization to fructose" *ChemCatChem* (2022) *Accepted*
2. **M. S. Rahaman**, S. Tulaphol, M. A. Hossain, M. C. Mulvehill, J. M. Spurgeon, T. Maihom, N. Sathitsuksanoh, "Mechanism of transfer hydrogenation of carbonyl compounds by zirconium and hafnium-containing metal-organic frameworks" *Molecular Catalysis* 522 (2022): 112247
3. **M. S. Rahaman**, S. Tulaphol, K. Mills, A. Molley, M.A. Hossain, S. Lalvani, T. Maihom, M. Crocker, N. Sathitsuksanoh, "Aluminum based metal-organic framework as water-tolerant Lewis acid catalyst for selective dihydroxyacetone isomerization to lactic acid" *ChemCatChem* 14 (2022): e202101756
4. **M. S. Rahaman**, S. Tulaphol, M. A. Hossain, J. B. Jasinski, N. Sun, et al., "Cooperative Brønsted-Lewis acid sites created by phosphotungstic acid encapsulated metal-organic frameworks for selective glucose conversion to 5-hydroxymethylfurfural." *Fuel* 310 (2022): 122459
5. **M. S. Rahaman**, S. Tulaphol, A. Molley, K. Mills, M. A. Hossain, D. Yelle, T. Maihom, N. Sathitsuksanoh, "Metal triflates formation of C12-C22 phenolic compounds by simultaneous C-O breaking and C-C coupling of benzyl phenyl ether." *Dalton Transactions* 50 (2021): 17390-17396
6. **M. S. Rahaman**, S. Tulaphol, M. A. Hossain, L. M. Thompson, N. Sathitsuksanoh, "Kinetics of phosphotungstic acid catalyzed condensation of levulinic acid with phenol to diphenolic acid: Temperature-controlled regioselectivity." *Molecular Catalysis* 514 (2021): 111848
7. M. A. Hossain, L. Mushill, **M. S. Rahaman**, S. M. Mains, et al. "Upcycling agricultural waste to biodegradable polyhydroxyalkanoates by combined ambient alkaline treatment and bacterial fermentation." *Industrial Crops and Products*(2022) *Accepted*
8. E. Chowdhury, **M. S. Rahaman**, N. Sathitsuksanoh, C. A. Grapperhaus, M. G. O'Toole. "DNA-mediated hierarchical organization of gold nanoprisms into 3D aggregates and their application in surface-enhanced Raman scattering." *Physical Chemistry Chemical Physics* 23 (2021): 25256
9. M. A. Hossain, **M. S. Rahaman**, D. Yelle, H. Shang, Z. Sun, S. Renneckar, J. Dong, S. Tulaphol, N. Sathitsuksanoh. "Effects of polyol-based deep eutectic solvents on the efficiency of rice straw enzymatic hydrolysis." *Industrial Crops and Products* 167 (2021): 113480
10. M.A. Hossain, S. Tulaphol, A.K. Thapa, **M. S. Rahaman**, J. Jasinski, H. Wang, M.K. Sunkara, J. Syzdek; R. Ozdemir, J. Ornstein; N. Sathitsuksanoh, "Metal-organic framework separator as polyselenide filter for high-performance lithium-selenium batteries" *ACS Applied Energy Materials* 4 (2021): 13450-13460

11. M. A. Hossain, K. N. Mills., A. M. Molley, **M. S. Rahaman**, S. Tulaphol, S. B. Lalvani, J. Dong, M. K. Sunkara, N. Sathitsuksanoh. "Catalytic isomerization of dihydroxyacetone to lactic acid by heat treated zeolites." *Applied Catalysis A: General* 611 (2021): 117979.
12. **M. S. Rahaman**, T. K. Phung, M. A. Hossain, et al. "Hydrophobic functionalization of HY zeolites for efficient conversion of glycerol to solketal." *Applied Catalysis A: General* 592 (2020): 117369.
13. E. Chowdhury, **M. S. Rahaman**, N. Sathitsuksanoh, C. A. Grapperhaus, M. G O'Toole. "DNA-induced assembly of gold nanoprisms and polystyrene beads into 3D plasmonic SERS substrates." *Nanotechnology* 32, no. 2 (2020): 025506.
14. M. A. Hossain, **M. S. Rahaman**, D. Lee, T. K. Phung, et al. "Enhanced softwood cellulose accessibility by H3PO4 pretreatment: high sugar yield without compromising lignin integrity." *Industrial & Engineering Chemistry Research* 59, no. 2 (2019): 1010- 1024.
15. S. Tulaphol, M. A. Hossain, **M. S. Rahaman**, L. Liu, T. K. Phung, S. Renneckar, N. Grisdanurak & N. Sathitsuksanoh. "Direct Production of Levulinic Acid in One Pot from Hemp Hurd by Dilute Acid in Ionic Liquids." *Energy & Fuels* 34, no. 2 (2019): 1764-1772.
16. M. A. Hossain, T. K. Phung, **M. S. Rahaman**, S. Tulaphol, J. Jasinski, N. Sathitsuksanoh, "Catalytic cleavage of the  $\beta$ -O-4 aryl ether bonds of lignin model compounds by Ru/C catalyst." *Applied Catalysis A: General* 582 (2019): 117100.
17. S. A. Iqbal, **M. S. Rahaman**, M. Rahman, A. Yousuf. "Anaerobic digestion of kitchen waste to produce biogas." *Procedia Engineering* 90 (2014): 657-662.

#### **Manuscript Under Review:**

1. **M. S. Rahaman**, S. Tulaphol, M. A. Hossain, S. B. Lalvani, T. Maihom, N. Sathitsuksanoh, "Creation of Brønsted acid sites on plastic for esterification of levulinic acid: A plastic-to-biorefinery circular economy" (Submitted to *Molecular Catalysis*)
2. **M. S. Rahaman**, M. A. Hossain, T. Maihom, S. Tulaphol, N. Sathitsuksanoh, "Upcycling polypropylene to sulfonic acid catalysts for efficient conversion of xylose to furfural" (Submitted to *Chemistry: An Asian Journal*)
3. M. A. Hossain, T. Saelee, S. Tulaphol, **M. S. Rahaman**, T. K. Phung, T. Maihom, P. Prasertthdam, D. J. Yelle, S. Prasertthdam, N. Sathitsuksanoh, "Unlocking self-hydrogen for hydrogenolysis of lignin by a dual function Ru/RuOx/C catalyst." (Submitted to *Applied Catalysis A: General*)

#### **Manuscript in-preparation:**

1. **M. S. Rahaman**, S. Tulaphol, M. A. Hossain, D. J. Yelle, T. Maihom, J. Dong, N. Sathitsuksanoh, "Plasma-mediated chemical upcycling of lignin to biodegradable polyhydroxyalkanoates by combined oxidation and bacterial fermentation"
2. **M. S. Rahaman**, S. Tulaphol, M. A. Hossain, T. Maihom, N. Sathitsuksanoh, "Cooperative effect of Lewis and Brønsted acidity in UiO-66(Zr) metal-organic frameworks for esterification of levulinic acid with methanol"
3. **M. S. Rahaman**, L. Mushill, S. Tulaphol, M. A. Hossain, S. Lalvani, T. Vickers, J. Dong, N. Sathitsuksanoh, "Plasma-mediated chemical upcycling of plastic into biodegradable polyhydroxyalkanoates by combined oxidative depolymerization and bacterial fermentation"
4. **M. S. Rahaman**, S. Tulaphol, M. A. Hossain, Q. Zhou, J. Dong, W. Paxton, M. Sunkara, S. Renneckar, N. Sathitsuksanoh, "Functionalization triggered plasma-mediated C-C bond cleavage of polypropylene into commodity chemicals"

## Conference Presentations

---

1. **M. S. Rahaman**, S. Tulaphol, M. A. Hossain, T. Maihom, and N. Sathitsuksanoh, "Production of C<sub>12</sub>-C<sub>22</sub> phenolic compounds by simultaneous C-O breaking and C-C coupling of lignin-derived benzyl phenyl ether" ACS Spring meeting, San Diego, CA, March 20 – 24, 2022.
2. M. A. Hossain, S. Tulaphol, **M. S. Rahaman**, S. Renneckar, J. Dong, and N. Sathitsuksanoh, "Catalytic production of biodegradable polymers from hemp hurd for a circular bioeconomy" ACS Spring meeting, San Diego, CA, March 20 – 24, 2022.
3. **M. S. Rahaman**, S. Tulaphol, M. A. Hossain, J. Dong, and N. Sathitsuksanoh, "Oxidative depolymerization of lignin at ambient temperature for production of biodegradable plastic", The 27th North American Catalysis Society Meeting, New York, NY, May 22-27, 2022
4. L. Mushill, **M. S. Rahaman**, N. Sathitsuksanoh, J. Dong, "Biodegradable Polyhydroxyalkanoate Production from Plasma Oxidized Non-Degradable Polypropylene", 2021 AIChE Annual Meeting, Boston, MA, November 7-12, 2021.
5. **M. S. Rahaman**, S. Viswanathan, K. Mills, A. Molley, M.A. Hossain, and N. Sathitsuksanoh, "Synthesis of Metal-Organic Framework from the plastic wastes", Graduate Student Regional Research Conference (GSRR), February 27-28, 2020
6. **M. S. Rahaman**, M. A. Hossain, T. K. Phung, S. Tulaphol, M. Crocker, & N. Sathitsuksanoh, "Enhanced Glucose Dehydration to 5-Hydroxymethyl Furfural through Encapsulated Phosphotungstic Acid in MOF", 2019 AIChE Annual Meeting", Orlando, FL, November 11-15, 2019.
7. M. A. Hossain, **M. S. Rahaman**, & N. Sathitsuksanoh, "Enhancing Lactic Acid Production from the Dihydroxyacetone by Extra Framework Alumina", 2019 AIChE Annual Meeting, Orlando, FL, November 11-15, 2019.
8. **M. S. Rahaman**, T. K. Phung, M. A. Hossain, S. Tulaphol, M. Crocker, J. B. Jasinski, & N. Sathitsuksanoh, "Hydrophobic HY zeolites enabling acetalization of crude glycerol", Tri State Catalysis Society Symposium, Louisville, KY, April 30, 2019
9. M. A. Hossain, K. N. Mills, **M. S. Rahaman**, S. Tulaphol, N. Krisadanurak, L. Liu, S. Renneckar, N. Sathitsuksanoh, "Hemp processing: From weed to values", Tri State Catalysis Society Symposium, Louisville, KY, April 30, 2019
10. **M. S. Rahaman**, T. K. Phung, M. A. Hossain, S. Tulaphol, M. Crocker, J. B. Jasinski, & N. Sathitsuksanoh, "Hydrophobic HY zeolites enabling acetalization of crude glycerol", KY NSF EPSCoR Annual Meeting, Lexington, KY, April 19, 2019.
11. **M. S. Rahaman**, T. K. Phung, M. A. Hossain, & N. Sathitsuksanoh, Mechanistic insights of the acid-catalyzed diphenolic acid production from renewable biomass, Frontiers in Biorefining 2018, St. Simons Island, GA, November 5-8, 2018
12. **M. S. Rahaman**, T. K. Phung, M. A. Hossain, S. Tulaphol, M. Crocker, J. B. Jasinski, & N. Sathitsuksanoh, "Hydrophobic HY zeolites enabling acetalization of crude glycerol", Frontiers in Biorefining 2018, St. Simons Island, GA, November 5-8, 2018
13. **M. S. Rahaman**, N. Sathitsuksanoh, "Mechanistic insights of the acid-catalyzed synthesis of diphenolic acid as a plastic precursor for 3D printing", KY Nano Symposium 2018, University of Louisville, Louisville, KY, August 2nd, 2018.
14. **M. S. Rahaman**, M. A. Hossain, T. K. Phung, & N. Sathitsuksanoh, "Mechanistic insights of the acid-catalyzed synthesis of diphenolic acid", Kentucky NSF EPSCoR Super Collider 2018, University of Kentucky, Lexington, KY, February 23, 2018.
15. **M. S. Rahaman**, M. A. Hossain, T. K. Phung, S. Tulaphol, & N. Sathitsuksanoh, "Efficient Saccharification of Softwoods by an Integrated Thermochemical and Biological Process", 2017 AIChE Annual Meeting, Minneapolis, MN, October 29-November 03, 2017

## Scholarship and Awards

---

- **Graduate Dean's Citation**, University of Louisville, 2022
- **Doctoral Dissertation Completion Award**, University of Louisville, 2021
- **1<sup>st</sup> prize winner**, Graduate Student Regional Research Conference (GSRRC), UofL, 2020
- **Graduate School Travel Grant**, Graduate Student Council, University of Louisville, 2019
- **Graduate Research Grant**, Graduate Student Council, University of Louisville, 2019
- **Graduate Student Travel Award**, Southeastern SunGrant Center, UTK, 2018
- **Graduate School Travel Grant**, Graduate Student Council, University of Louisville, 2017
- **Grosscurth Fellowship**, University of Louisville, 2017
- **Pullin Fellowship**, University of Louisville, 2016

## Leadership and Voluntary Service

---

- **President**, Bangladeshi Student Association, UofL, 2020-2021
- **Vice President**, Bangladeshi Student Association, UofL, 2019-2020
- **Vice President**, Chemical Engineering Graduate Student Association, UofL, 2019-2021
- **Executive Member**, Research Grant Committee, GSC, UofL, 2020-2021
- **Social Media Coordinator**, American Institute of Chemical Engineers (AIChE), 2019-20
- **Department Representative**, Graduate Student Council, UofL, 2019-2021
- **Public Relation Secretary**, Bangladeshi Student Association, UofL, 2018-2019
- **Volunteer**, Oasis-Organization Assisting and Serving International Students, 2017-2020
- **Judge for Undergraduate Student Poster Competition**, 2017 AIChE annual meeting, MN

## Teaching Experience

---

- **Instructor/Teaching Assistant (TA)**: worked as a TA for multiple courses such as Materials Science, Heat & Mass Transfer, Health, Environment & Safety, Modeling and Transport Phenomena, Computer Applications in Chemical Engineering, Polymer Processing in the department of chemical engineering at the University of Louisville. My responsibilities include giving lectures and encouraging students to apply the classroom concepts into lab experiments.
- **Mentoring**: Supervised >40 graduate and undergraduate students for their research projects by encouraging them to develop a sound hypothesis and validate their findings. I also trained two high school students from DuPont Manual (Louisville, KY) to develop their school projects, and both won the 2<sup>nd</sup> prize in the Kentucky regional science fair competition.